STATES IN ^{176}Hf POPULATED BY THE (α,2n) REACTION

by

TENG LEK KHOO, B.Sc., M.Sc.

A Thesis

Submitted to the School of Graduate Studies

in Partial Fulfilment of the Requirements

for the Degree

Doctor of Philosophy

McMaster University

March 1972

DOCTOR OF PHILOSOPHY (1972) (Physics)

McMASTER UNIVERSITY, Hamilton, Ontario

TITLE: States in ^{176}Hf populated by the (α,2n) reaction

AUTHOR: Teng Lek KHOO, B.Sc. (Hons.), M.Sc. (Dalhousie)

SUPERVISOR: Dr. M. W. Johns

NUMBER OF PAGES: x, 336

SCOPE AND CONTENTS:

The level structure of the even-even deformed nucleus ^{176}Hf has been studied by means of the ^{174}Yb (α,2n) ^{176}Hf reaction through γ-ray singles, conversion electron and extensive prompt and delayed γ-γ coincidence measurements. The half-lives of the isomeric states at 1333 and 1559 keV have been measured as 9.5 and 9.8 μsec, respectively.

Besides the ground state rotational band, the following ten rotational bands have been established: two $K=0^+$ bands at 1150 keV and 1293 keV, a $K=2^+$ band at 1341.1 keV, a $K=3^+$ band at 1577.3 keV, a $K=2^-$ octupole band at 1247.5 keV, two $K=6^+$ bands of mixed neutron and proton character at 1333.1 keV and 1761.5 keV, a $K=8^-$ band at 1559.4 keV, a $K=8^-$ and/or 7^- band at 1860.3 keV and a $K=7^-$ and/or 6^- band at 1798.0 keV. The de-excitation of the high K states proceeds through either of the two isomers, and were studied by novel experimental techniques which involved pulsing the alpha beam.

The intrinsic structure and decay properties of the states are understood in terms of the unified model. In some cases it has been necessary to make use of unpublished McMaster results from the single neutron and proton transfer reactions.

ACKNOWLEDGEMENTS

It has been an educational experience to be part of the initial development of the McMaster Tandem Accelerator Laboratory. The cooperative attitude of different groups and their willingness in making available the "fruits" of their labour have been greatly appreciated. It hardly needs to be pointed out that in the course of this work, the skills, expertise and ideas of many have been called upon.

I should, however, like to offer specific thanks to the following:-

Dr. M. W. Johns, my supervisor, for his interest in all phases of the research project, his help in the preparation of this thesis, and his efforts on my behalf;

Drs. D. G. Burke and G. L. Keech, the other members of my supervising committee for their advice;

Dr. Zygmunt Preibisz , for help in the experimental "runs" and in some of the data analysis;

Phil Gregory, for tending to many of the experiments;

Brian Cook, for providing the original versions of many of the data analysis computer programmes and for many helpful conversations;

Dr. Hamish Robertson, who first developed the delayed coincidence technique, for instructive discussions concerning the method;

Bob O'Neil, for his collaboration in the nucleon transfer studies;

Bev Kenyon and Dave Kelly for help with computer programming;

the staff of the McMaster Tandem Accelerator Laboratory;

Mrs. Helen Kennelly, for expertly and with incredible speed transcribing "microscopic" scribble into type;

Trevane, for the many hours she willingly devoted to the assembly of this thesis and cheerful support during its preparation;

Dr. Jim Waddington, teacher and colleague, who has been a well-spring of insight and ideas. I wish to pay special tribute to his rare gift for communicating his enthusiasm and sense of excitement, which have provided the stimulus for this work.

Finally, I wish to acknowledge with gratitude a Colombo Plan Scholarship provided by the Canadian International Development Agency.

TABLE OF CONTENTS

CHAPTER 1

INTRODUCTION

An enormous expansion of our knowledge of nuclear level properties has occurred in recent years. This has been largely due to technological advances in detectors, data acquisition systems and accelerators. The advent of solid-state radiation detectors, and the development of sophisticated data acquisition made nearly all the data gathered before 1960 obsolete. When used along with the modern successive versions of charged particle accelerators, these techniques have made it possible to make precise studies of a wide variety of level properties, using a range of nuclear reactions not possible to earlier workers. In recent years, on-line reaction studies have replaced in importance the radioactive decay studies which for many years had formed the backbone of nuclear spectroscopy.

Many of the properties of deformed nuclei in the rare-earth mass region ($150<A<190$) may be now explained with remarkable success in terms of a unified model, which combines single nucleon motions with pairing correlations and collective effects. A great wealth of experimental information exists on the odd-A nuclei. On the other hand,

except for the properties of the ground state band, there is a decided lack of data concerning even-even nuclei. As a case in point we note that, whereas many odd-A nuclei have been fruitfully studied by means of (particle,xn) reactions, this method has not yet been used to carry out extensive studies of the excited states of even-even deformed nuclei (with the exception of ground state bands and lower lying vibrational bands). This thesis represents an attempt to remedy this situation through the study of a doubly even system in the deformed region. As one might expect, the high level density makes the problem extremely complicated. However, the work in this thesis shows that the problem can be profitably studied with the techniques which are now available and that such studies should make possible a considerable extension in the applicability of the unified model.

The ^{176}Hf nucleus offers several advantages for a study of highly excited states in even-even nuclei. It lies in a region where most of the Nilsson orbitals near the Fermi surface have large values of Ω. Consequently, the low-lying two quasi-particle states are likely to have high-K with no lower energy states of low K values to "short-circuit" their decay to the ground state. This situation is responsible for the existence of $K = 6^+$ and $K = 8^-$ isomers at 1333 and 1559 keV, respectively. Other high K states are expected which should decay preferentially to these isomers, and their identification presented a challenging problem. In addition,

this work will remedy, in some small way, the paucity of experimental data on the beta, gamma and octupole bands in this mass region. In fact, the original intent of this study, when first suggested by Dr. Z. Preibisz, was focussed on the excited $K = 0^+$ states.

When this work was begun, very little was known about the level structure of ^{176}Hf. The existence of the 1333 keV isomer had been discovered from (γ,n) studies by Brandi et al in 1964, and a second isomer at 1559 keV was later found by Borgreen et al. (1967) by means of the (p,n) reaction. Harmatz et al (1960) had studied the levels of ^{176}Hf through the decay of ^{176}Ta using a magnetic spectrograph to examine the conversion electrons, but were unable to construct a level scheme. Other early attempts to do so, using NaI(Tl) detectors, were also largely unsuccessful (Verheul et al 1963; Hashizume and Tandow 1963) because of the complexity of the problem. More recently, Boddendijk et al (1969), Broda et al. (1970) and, in particular, Bernthal et al. (1969,1971) successfully employed Ge(Li) detectors to develop a secure level scheme. However, since the ground state spin of ^{176}Ta is 1^- (Valentin and Santoni, 1967) only the states with spin ≤ 3 are generally populated by the ^{176}Ta decay.

On the other hand, the (α,2n) reaction employed in the present work tends to populate higher spin states and thus complements the previous work admirably. We have recently

become aware that groups in Stockholm (Ryde et al) and in Copenhagen (Hammer and Hagemann) are also currently using this reaction to study ^{176}Hf.

Although the bulk of the thesis describes a study of ^{176}Hf by means of the (α,2n) reaction, the results of unpublished single nucleon transfer data have also been examined as an aid to the interpretation of the observed states. The ^{175}Lu(α,t), ^{175}Lu(^{3}He,d), ^{177}Hf(^{3}He,α)^{176}Hf reaction studies were carried out in collaboration with O'Neil and Burke of this laboratory, while the ^{177}Hf(d,t)^{176}Hf data were kindly communicated by R. Casten. The data from the transfer reactions are not presented in this thesis.

CHAPTER 2

HEAVY ION, xn REACTIONS

2.1 Introduction

Heavy ion, xn reactions (HI,xn) have been applied, with considerable success, to the spectroscopic study of nuclei since the initial study of Morinaga and Gugelot (1963). With the increasing availability of heavy ions from the new generation of tandem accelerators and sector focussed cyclotrons, nuclear spectroscopy employing such reactions has become a rapidly growing field. An excellent review on the subject has recently been written by Newton (1969), from which is derived some of the material presented here.

In this chapter the concept of the compound nuclear reaction is first introduced, with particular emphasis on HI,xn reactions. In the next section the reaction mechanism is then elaborated upon; succeeding sections will then outline the statistical calculations describing such reactions and discuss excitation functions, spin distributions in the product nuclei, and angular distributions in the emitted gamma rays.

2.2 Compound Nuclear Reactions; HI,xn Reactions

Nuclear reactions at moderate energies (typically < 30 MeV per nucleon) can be conveniently classified into direct reactions and compound nuclear reactions. In the former the time between particle incidence and particle emission is of

the order of the transit time of the projectile across the nucleus ($\sim 10^{-22}$ sec.), while in the latter the particle emission is greatly retarded.

The formation of a compound nucleus was first proposed by Bohr (1936), in order to account for the long half life implied by the narrow resonance widths observed in slow neutron absorption experiments. He suggested that the incident particle and target combine to form a compound system in which the energy was shared by all nucleons in a completely random manner, until one particle acquired sufficient energy to escape.

When the average level spacing in the compound nucleus is large compared to the average level width, a resonance treatment applies. However, in many cases the opposite situation is obtained and many overlapping states are populated both in the compound nucleus and in the residual nucleus following particle evaporation. In this case the reaction may then be treated in a statistical manner. Details of statistical theory first formulated by Weisskopf (1937) may be found in Grover and Gilat (1967a,b,c) and Jagäre (1967) or in the review articles by Feshbach (1960) and Bodansky (1962). An outline of this model will be found in section 2.4.

The particular situation of a heavy ion incident on a target will now be considered. The term heavy ion will be construed broadly to include protons, alphas and heavier

particles such as ^{10}Bo, ^{16}O, and ^{40}Ar. In general, compound nucleus formation and direct reaction processes are in competition; typical cross-sections for the two processes are 500 and 5 mb respectively.

When a compound nucleus is formed in a highly excited state it decays with the evaporation of several neutrons or charged particles. With light nuclei, in which the Coulomb barrier is low, or in very neutron-deficient nuclei, which have large neutron binding energies, a variety of reactions are possible with proton and alpha emission competing favorably with neutron emission. With the medium and heavy nuclei where the Coulomb barrier inhibits the emission of charged particles, the dominant process is neutron emission. For very heavy nuclei, the fission process becomes competitive with neutron evaporation. In short, the (HI,xn) reaction has a relatively large cross-section in the mass range from 100 to 220.

One advantage of the (HI,xn) reaction is that it populates a wide variety of states. Because of the statistical nature of the process, the compound nucleus retains no memory of the process by which it was formed and the states populated are restricted only by the limits imposed by the conservation laws. Since the probability of populating a final state is roughly independent of its configuration a large number of levels not normally accessible by other methods may thus be studied. The two and three quasi-particle high spin states

known to exist in the rare earth region are among these.

2.3 Reaction Mechanisms

In this section the various steps by which a typical HI,xn reaction proceeds will be described. It will also be shown that with medium or heavy target nuclei it is possible, by proper choice of projectile energy, to make a product nucleus almost uniquely.

For illustration, the scheme of a ^{4}He,xn reaction induced in a rare earth target is shown in Fig. 2.1. After the incident ^{4}He ion has been captured by the target (A-4, Z-2), the compound nucleus (A,Z) resides at an excitation energy of about 25 MeV. One neutron is then 'boiled' off; the energy spectrum of the evaporated neutron is shown in the insert. It will be noted that the mean energy carried away by the neutron is about 2 MeV, much less than the neutron binding energy. The intermediate nucleus (A-1,Z) thus formed is still at a high excitation energy and one more neutron is emitted. Most of the states formed in this nucleus will be stable against further particle emission and will decay by gamma emission to the ground state. Hence at this alpha energy, most of the cross-section is associated with (A-2,Z) production with relatively small cross-sections for (A-1,Z) and (A-3,Z).

As the number, x, of evaporated neutrons increases, the spread in A of the produced nuclei will increase because

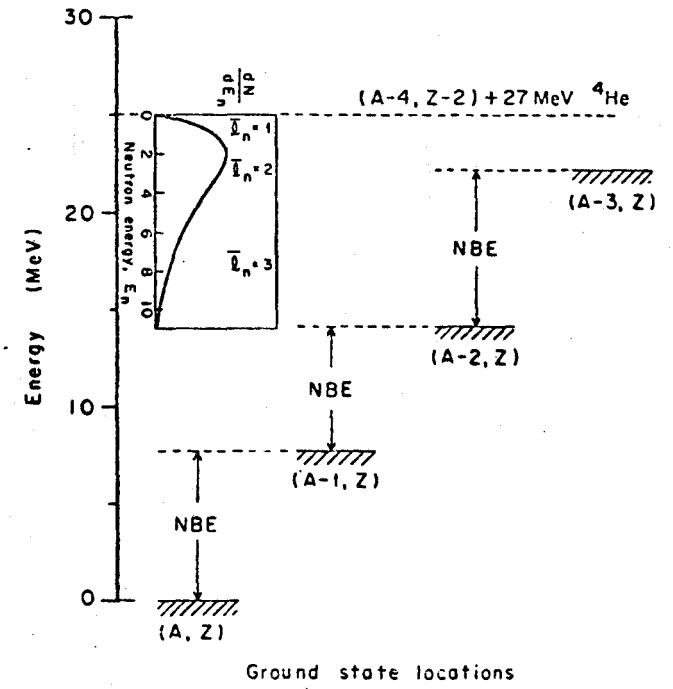

Figure 2.1

Scheme of α,xn reaction

(Reproduced from Newton et al.1967)

of the finite width of the neutron spectrum. The number of neutrons evaporated increases as the bombarding energy is increased. The excitation functions for a sequence of reaction products thus appear as a series of successive peaks, one for every product nucleus. This is illustrated in Fig. 2.2 by the calculated excitation functions in a $^{181}Ta(^{16}O,xn)^{197-x}Tl$ reaction.

In the simple description of the last paragraph the effects of angular momentum have not been considered. When this is done it is found that the effective threshold for producing a state of a given spin is the sum of the normal threshold energy plus the so-called Yrast energy for that spin. In addition, the peak of the excitation function for that level will be shifted upwards for increasing ℓ. The angular momentum effect, therefore, causes the excitation function peaks of different nuclei to overlap more and more as the angular momentum brought into the system increases. It thus becomes less and less possible to produce the desired final nucleus clearly. The best way to overcome this problem is to perform such reactions at a bombarding energy which is at the Coulomb barrier energy, since the rate of increase of the cross-section with incoming angular momentum is greatest in this region. At this energy the minimum practical number of neutrons will be emitted and thus the broadening of the peak due to the finite width of the neutron spectrum will also be at a minimum.

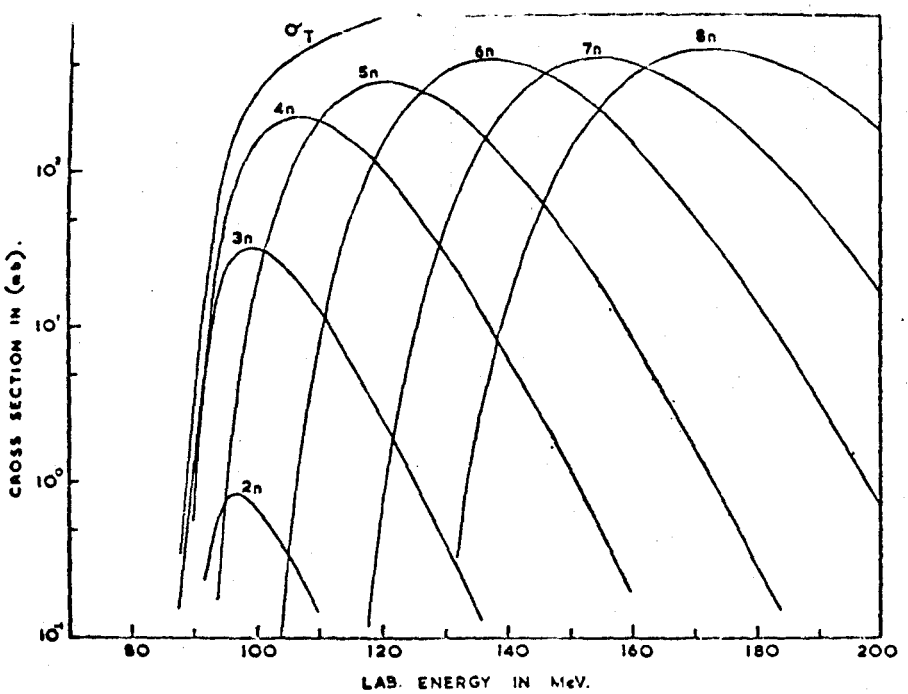

Figure 2.2

Calculated excitation functions for the $^{181}Ta(^{16}O,xn)^{197-x}Tl$ reactions (reproduced from Newton (1969))

There is, moreover, a further advantage to be gained from this feature since the excitation function for a particular state may provide information abouts its spin. Since the yield of a state of higher spin increases more sharply with increasing projectile energy than the yield for a state of low spin, a comparison of yield curves for different states may be a rough indicator of spin.

2.4 The γ-deexcitation Scheme

The gamma deexcitation in the final product nucleus is illustrated in Fig. 2.3, which has been reproduced from a recent paper by Newton et al (1970). In this paper many features of the deexcitation process are described, based on a scheme first formulated by Grover and Gilat (1967 a,b,c) and Grover (1967). In the figure, excitation energy is plotted against angular momentum. The long thin line represents the states of lowest energy, excluding the members of the ground state band (g.s.b.), for each spin value and is commonly referred to as the yrast line. The short dashes and dots indicate the g.s.b. members for a rotor like ^{160}Er and ^{190}Hg respectively and are obviously the yrast levels for low angular momentum values. The dark heavy lines indicate the range of excitation energies and spins of the states populated in the final nucleus following (^{40}Ar,4n) and (^{4}He,4n) reactions. (Only the lower spin states, up to $\sim$ 14, are

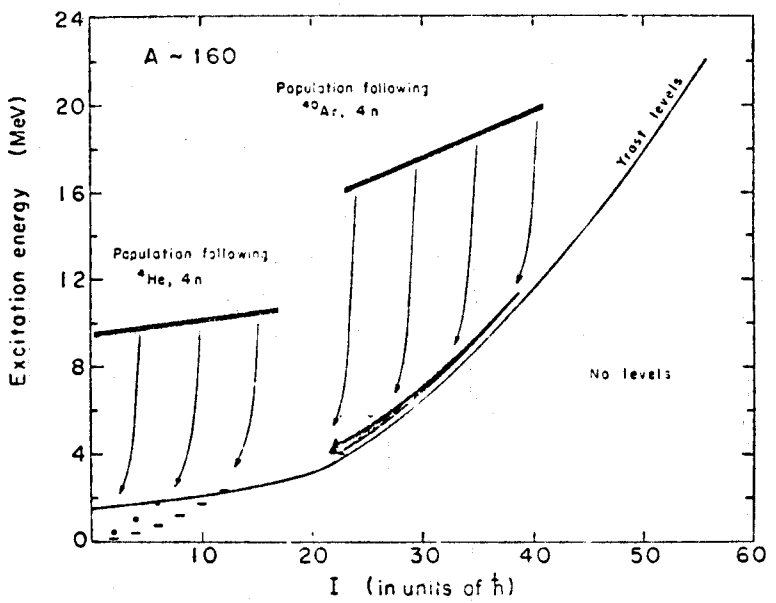

Figure 2.3

Schematic figure showing the energy levels in a nucleus of mass $\approx$ 160 versus angular momentum. Indicated on the figure are (i) the lowest non-g.s.b. energy levels for each spin (yrast levels), (ii) the regions of populated states following (He,4n) and (Ar,4n) reactions, and (iii) the g.s.b. levels of a typical vibrator (dots) and rotor (dashes).

populated in the (^{4}He,2n) reaction.) The average excitation energies are about one neutron binding energy above the yrast level.

The gamma deexcitation proceeds via mainly dipole radiation to the yrast region, which is a region, 200-300 keV wide, lying above the yrast line. In (^{40}Ar,4n) reactions, where a large amount of angular momentum (up to 40 $\hbar$) is brought into the system, the yrast levels are populated above the g.s.b. members. The depopulation then proceeds by a cascade down the yrast line through a series of mainly E2 transitions (Newton et al 1970). The g.s.b. is then populated at the point where its members become the yrast levels. Thus, with very heavy ions, transitions down the g.s.b. are very prominent and few others are resolved. On the other hand, in ^{4}He-induced reactions the high-energy transitions proceed directly to the g.s.b. members, since these comprise the yrast levels over the populated angular momentum range. However, on the average, several transitions occur and there is also considerable feeding of other excited states. This results in several units of angular momentum being lost prior to entry into the g.s.b.

Several features commonly observed in ^{4}He-induced

reactions may now be readily understood. The continuous gamma background that is invariably observed consists of the multitude of unresolvable transitions associated with the deexcitation of the residual nucleus and only the strongest of these which stand out from the continuum can be effectively used in spectroscopic studies. In an odd residual nucleus the rotational members of several intrinsic states comprise the lowest lying levels. Consequently, these are quite strongly fed and the cascades within each band are very prominent. This explains why ^{4}He,xn reactions have been particularly successful in studying odd mass nuclei Newton (1968), Løvhøiden et al. (1970), Winter et al. (1970)), prompting the observation that "the alpha particle is the tool of the side-band hunter". In odd-odd and even-even nuclei the situation is not so favourable. In the former the abundance of low-lying states makes the problem quite complicated. Even so the method can be successfully applied to odd-odd nuclei as indicated by the preliminary work of Leigh et al (1970). In even-even nuclei the g.s.b.'s are the lowest lying states and transitions within this band are the strongest. As a result, previous work has mainly been focussed on them, in many cases with the purpose of investigating details of the reaction mechanism (Williamson et al (1968)). The β and γ vibrational states are often appreciably populated and have also been profitably studied

with these reactions. (Graetzer et al (1966), Lönsjö and Hagemann (1966); Ejiri and Hagemann (1971). Population of the numerous "two quasi-particle" states, expected to occur above the pairing energy gap of $\sim$ 1 MeV, is also to be expected. These give rise to numerous transitions, many of high energy, and therefore lead to very complex spectra. It is therefore not surprising that very few studies of such states have been made.

2.5 Outline of Statistical Model Calculations

In order to understand the other factors that affect the population of identifiable states in the product nucleus, an outline of a statistical model calculation used to predict this population will now be presented. Such computations have been undertaken by Jagäre (1967), Grover and Gilat (1967) and Halpern et al (1968). In essence, a typical calculation consists of first determining the spin distribution in the original compound nucleus and then computing the modification of this initial spin distribution brought about by the emission of the appropriate number of particles (only neutrons assumed) and photons. In the description below the original compound nucleus is denoted by '0' and subsequent nuclei in the evaporation process by i = 1,2... .

The initial distribution in the compound nucleus is determined from an expression of the form

$$P_o(J_o,E_o) = \frac{\pi(\hbar^2)}{2m_bE_b}\ \frac{2J_o+1}{(2S_b+1)(2I+1)} \sum_{S=|J_o+S_b|}^{J_o+S} \sum_{\ell=|J_o-S|} T_b(\ell,E_b),$$

where m_b, S_b and E_b are the mass, spin and energy of the projectile, b.

I = spin of target nucl.

$E_o = E_b - |Q|$ = energy of compound nucleus

J_o = spin of the excited compound nucleus

$T_b(\ell, E_b)$ = transmission coefficient for the ℓ^{th} partial wave.

$T_b(\ell, E_b)$ accounts for the fact that the projectile has to overcome both a Coulomb and a centrifugal barrier, and is usually calculated using an optical model.

The probability of populating a state $(E_1 J_1)$ in the first intermediate nucleus is then obtained by summing the probability $P(E_o J_o \rightarrow E_1 J_1)$ over the distribution for J_o. $P(E_o J_o \rightarrow E_1 J_1)$ is the probability of the state $E_o J_o$ decaying to the state $E_1 J_1$ via neutron emission and may be expressed in terms of the inverse reaction by

$$P_o(E_o J_o \rightarrow E_1 J_1) = \frac{\omega(E_1 J_1) T_o(E_o J_o \leftarrow E_1 J_1)}{h\omega(E_o J_o)}$$

where $T_o(E_o J_o \leftarrow E_1 J_1)$ is the transmission coefficient for a neutron to be absorbed by the nucleus $E_1 J_1$ to form the nucleus $E_o J_o$. The formalism may be extended to subsequent stages in the evaporation process by replacing $E_o J_o$ by $E_i J_i$ and $E_1 J_1$ by $E_{i+1} J_{i+1}$.

$\omega(E_i J_i)$ is the level density in the nucleus i and may be estimated from the expression (Newton 1969)

$$\omega(EJ) \propto (2J+1)(E+\delta)^{-2} \times \exp 2[a(E-E_J+\delta)]^{1/2},$$

where the parameter $\delta = 0$ for even-even, Δ for odd-even and 2Δ for odd-odd nuclei (Δ, the pairing energy, is $\sim$ 1 MeV for the rare earth region), where

$$a = (A/7.24)\ \text{MeV}^{-1},$$

and where

$$E_J = \frac{\hbar^2}{2\mathcal{I}} J(J+1).$$

$\mathcal{I}$ is an effective moment of inertia, usually taken to be that of a rigid rotor. This last equation for E_J roughly describes the yrast line.

When the system no longer has sufficient energy to emit a neutron, gamma emission occurs and the resultant population is given by

$$P_\gamma = \sum_{J'} \sum_{L} P_{\gamma L},$$

where

$$P_{\gamma L}(E'J' \rightarrow EJ) \propto \varepsilon^{2L+1} \frac{\omega(EJ)}{\omega(E'J')}$$

represents the probability of gamma deexcitation from a state of excitation and spin E',J' to one of excitation and spin E,J. ε is the energy of the photon emitted and L is the multipolarity. In general, several photons are emitted before the ground state is reached.

Statistical calculations of this type indicate that for a highly excited ($\sim$ 8 MeV) residual nucleus the spin distribution is not significantly different from the original

distribution in the compound nucleus. This has not been borne out in experiments (Williamson et al 1968), probably because the gamma deexcitation process is not entirely statistical. As has been previously indicated (section 2.4), details of nuclear structure in the yrast region have a large influence on the last few steps of the decay.

2.6 Angular distribution

In a HI,xn reaction the residual nucleus is strongly aligned because the incoming particle brings in angular momentum in the m=0 substate only, the beam direction being taken as the quantization axis. Since the orbital angular momentum brought in by the heavy ions ranges from 15 to 60 $\hbar$ units this greatly exceeds the spins of both the projectiles and targets. Consequently the angular momentum vector of the resulting system is aligned almost perpendicular to the beam direction. The evaporation of several neutrons broadens the distribution in m, but only slightly since the evaporated neutrons are not correlated in direction and their angular momentum vectors tend to cancel out. Besides, the angular momentum carried off by each neutron is quite small ($\ell \lesssim 2$).

This alignment means that the gamma rays emitted will have pronounced anisotropies. Conversion electrons following proton and alpha induced reactions have also been shown to exhibit anisotropy by Ejiri et al (1965). The

angular distribution $W(\theta)$ is symmetric about 90° (with respect to the beam axis) and may be expressed in the usual form:

$$W(\theta) = \sum_{\nu} b_{2\nu}\ a_{2\nu}\ (I)\ A_{2\nu}\ P_{2\nu}\ (\cos\theta).$$

The $A_{2\nu}$'s are the appropriate coefficients of the Legendre polynomials for states with complete alignment. The $a_{2\nu}$'s are the attenuation factors which take into account the fact that the alignment, after the various deexcitation steps, is in fact not complete. The $b_{2\nu}$'s are the usual particle parameters; $b_{2\nu} = 1$ for gamma emission. This feature offers a powerful spectroscopic tool with which to determine the nature of the emitted gamma ray, (Løvhøiden et al. (1970), Ejiri and Hagemann (1970)).

In extreme cases (i.e. when the decaying state is highly aligned) variations as a function of angle up to a factor of 4 in the gamma ray intensity may be obtained. In general, however, factors of less than 1.5 are more common. This anisotropy must be taken into account in measuring electron conversion coefficients and branching ratios.

CHAPTER 3

THEORY

3.1 Introduction

Nuclear structure phenomena are currently interpreted in terms of models. Undoubtedly the most significant, and successful, of these has been the shell model (Mayer and Jensen 1955). Basically this model treats each nucleon as if it were moving independently, in a quantised orbit, in a common average potential. For a particular nucleon this represents its interaction with all other nucleons in the nucleus. The model was originally applied to spherical nuclei with a central potential.

The discovery of unusually large quadrupole moments shows that some nuclei are ellipsoidal in shape with deformations corresponding to radial differences $\Delta R/R$ as large as 30%. These deformed nuclei, which exhibit distinct rotational band structure, are found in the mass regions $18 \leq A \leq 28$, $150 \leq A \leq 190$, $A > 224$.

Such nuclei are characterized by collective motions in which the nuclear matter rotates about an axis perpendicular to the symmetry axis, or in which the shape of the nuclear surface undergoes periodic variation. These systems are mathematically more tractable if a non-spherical potential is used. The collective nuclear model, first proposed by Bohr (1952)

and Bohr and Mottelson (1953), describes both the collective and particle modes of motion. The appropriate description of the single particle motion in a non-spherical potential was first developed by Nilsson (1955), in a model which represents a logical extension of the shell model.

In this study we are concerned with the deformed nucleus ^{176}Hf. It is therefore appropriate to outline the accepted theoretical description of non-spherical nuclei. The following three sections cover the collective model, the Nilsson model, the residual interactions, and the excited states of even-even nuclei. This is followed by a discussion in section 3.5 of electromagnetic transitions, and in section 3.6 by a section on internal conversion electrons with particular emphasis on monopole transitions. Finally, there is a treatment of the gyromagnetic ratios (g_K) of intrinsic states (section 3.7) and a discussion of band-mixing (section 3.8).

3.2 The Unified Model for Odd Mass Nuclei

In the unified model as applied to a deformed nucleus, the main features of the level structure are accounted for by coupling the motion of the single particle to the rotational motion of the core. The vector relations in this description are shown in Fig. 3.1. In this figure $\underline{j}$ and $\underline{R}$ are the angular

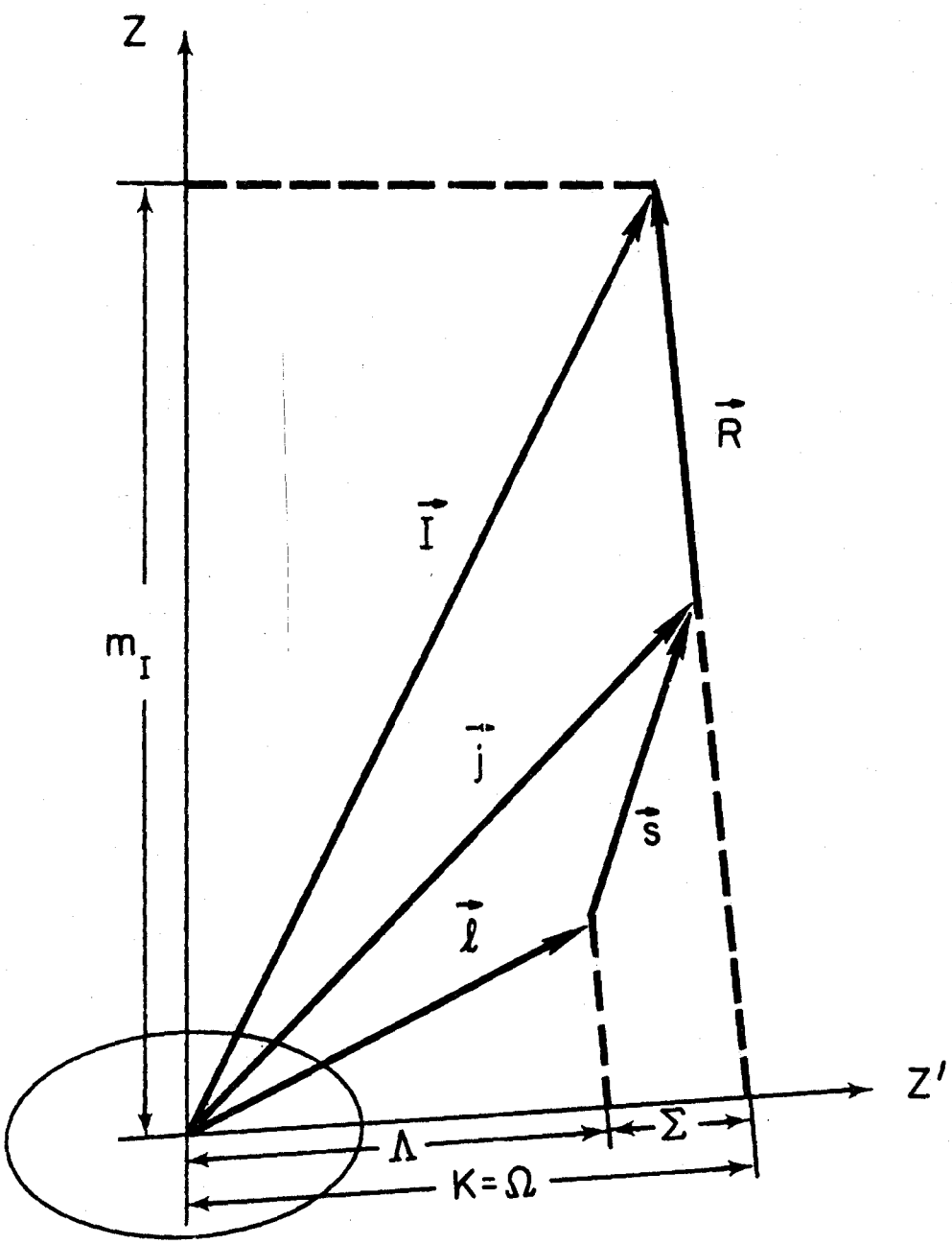

Figure 3.1

Angular momentum vector diagram for a deformed rotating nucleus

momenta of the particle and core respectively. These combine to form the total angular momentum of the nucleus, $\underline{I}$. The figure also shows the value of K, the projection of $\underline{I}$ on the axis of nuclear symmetry, z'; and the projection, Ω,of $\underline{j}$ on the same axis. M is the projection of $\underline{I}$ on the space fixed axis z. If the nucleus is symmetric about the z' axis, R is perpendicular to this axis, so that $K = \Omega$.

The Schrödinger equation is

$$H\psi = (T_{rot} + \sum_{p} H_{p})\psi = E\psi, \qquad (3.1)$$

where the summation p is over all the particles involved (if there are more than one) and where the wave function ψ has the form

$$\psi = \chi_{particle}\, \phi_{vib}\, \mathcal{D}_{rot}. \qquad (3.2)$$

A product wave function of this form implies that the intrinsic nucleonic motion is considered independent of the collective rotational and vibrational motion. The Hamiltonian may then be written as

$$H = H_{rotation} + H_{intrinsic} + H_{coupling} + H_{vibration} \qquad (3.3)$$

where the third term accounts for the rotation-particle coupling (RPC).

If, besides rotational symmetry around the nuclear axis, there is also reflection symmetry through a plane perpendicular to this axis, the appropriately symmetrised wave function may be written

$$|IMK\Omega\rangle = \sqrt{\frac{2I+1}{16\pi^2}}\,\phi_{vib}[\chi_\Omega D^I_{MK} + (-)^{I-j}\chi_{-\Omega}D^I_{M-K}] \qquad (3.4)$$

Using this wave function to solve equation (3.1) for the rotational energy, one obtains

$$T_{rot} = \sum_{i=1}^{3} \frac{\hbar^2}{2\mathcal{J}_i}\langle R_i^2\rangle = \sum_{i=1}^{3} \frac{\hbar^2}{2\mathcal{J}_i}\langle (I_i-j_i)^2\rangle \qquad (3.5)$$

where the indices i refer to the body-centred axes. For rotational symmetry around the 3-axis $\mathcal{J}_1 = \mathcal{J}_2 = \mathcal{J}$ and $\mathcal{J}_3$ is zero equation 3.5 may be re-written

$$\langle T_{rot}\rangle = \frac{\hbar 2}{2\mathcal{J}}[\langle(\underline{I}-\underline{j})^2\rangle - (I_3-j_3)^2] + \frac{\hbar^2}{2\mathcal{J}_3}(I_3-j_3)^2$$

$$= \frac{\hbar^2}{2\mathcal{J}}[I(I+1)+\langle j^2\rangle - 2\langle \underline{I}\cdot\underline{j}\rangle - (K-\Omega)^2] + \frac{\hbar}{2\mathcal{J}_3}(K-\Omega)^2$$

$$= \frac{\hbar^2}{2\mathcal{J}}[I(I+1)-K^2-\Omega^2] + \frac{\hbar^2}{2\mathcal{J}_3}(K-\Omega)^2 - \frac{\hbar^2}{2\mathcal{J}}(I_+j_- + I_-j_+)$$

$$+ \frac{\hbar^2}{2\mathcal{J}}\langle j^2\rangle \quad , \qquad (3.6)$$

where use has been made of the relation

$$I\cdot j = I_3j_3 + I_2j_2 + I_1j_1 = K\Omega + (I_+j_- + I_-j_+)/2 \qquad (3.7)$$

The last term in 3.6 involves only particle motion and is usually grouped with that portion of the Hamiltonian. The first two terms contain the diagonal contributions to the rotational energy and are constants of motion because of axial symmetry. The remaining so-called RPC term, $-\frac{\hbar^2}{2\mathcal{J}}(I_+j_- + I_-j_+)$, has a diagonal contribution only if

$K = 1/2$ (giving rise to the well known "a" decoupling parameter) and has non-zero off-diagonal matrix elements only between states differing in K by ±1:

$$\langle IK|I_{\pm}|IK\pm1\rangle = \sqrt{(I\mp K)(I\pm K+1)} \tag{3.8a}$$

$$\langle j\Omega|j_{\mp}|j\Omega\pm1\rangle = \sqrt{(j\mp\Omega)(j\pm\Omega+1)} \tag{3.8b}$$

This RPC term, usually referred to as the Coriolis interaction, in analogy with the classical case, is responsible for many of the observed deviations from the adiabatic theory (in which only the diagonal matrix elements are considered). We shall consider the effects of the Coriolis interaction in more detail in section 3.3.

3.3 Single Particle States in a Deformed Nucleus - the Nilsson Model

The success of the unified model described above depends on the proper choice of the average potential experienced by the single odd particle. This choice of potential in turn defines the single particle wave functions. The relatively simple potential chosen by Nilsson (1955) led to rather simple wave functions, which in turn made it fairly easy to calculate matrix elements. Thus, while a number of more physically realistic potentials have been suggested as improvements, they have proven to be much less tractable for calculations. Since the predictions obtained from these alternative potentials have not been significantly better than those from the

simpler Nilsson potential, the Nilsson model continues to be almost exclusively used to describe the properties of deformed nuclei.

The Nilsson model accounts for the properties of an odd-A nucleus in terms of a single particle moving, independently of the other nucleons, in a spheroidal harmonic oscillator potential with axial symmetry. The Hamiltonian is expressed as

$$H_{sp} = H_o + H_\delta + C\cdot\underline{\ell}\cdot\underline{s} + D\underline{\ell}\cdot\underline{\ell}$$

or alternatively as

$$H_{sp} = \frac{p^2}{2m} + \frac{m}{2}\{\omega_\perp^2(x^2+y^2) + \omega_z^2 z^2]\}$$

$$- \kappa\hbar\omega_o(2\underline{\ell}\cdot\underline{s} + \mu\ell^2) \qquad (3.9)$$

In this expression $H_o + H_\delta$ represents the spheroidal harmonic oscillator potential which has been split into two parts, one of which is spherically symmetric and one of which is a function of the deformation, δ. The $\underline{\ell}\cdot\underline{s}$ term takes care of the spin orbit coupling and the ℓ^2 term is introduced empirically to account for the experimental fact that high angular momentum states are reduced in energy with respect to the values predicted by the simple harmonic oscillator potential.

The frequencies $\omega_\perp$ and ω_z are defined by the equations

$$\omega_\perp^2 = \omega_o(\delta)^2\ [1 + \frac{2\delta}{3}]$$

$$\omega_z^2 = \omega_o(\delta)^2\ [1 - \frac{4\delta}{3}]$$

where $\omega_o(\delta) = \omega_{oo}(1 - \frac{4\delta^2}{3} - \frac{16\delta^3}{27})^{-1/6}$ and

$\hbar\omega_{oo} = \hbar\omega_o(o) \simeq 41\ A^{-1/3}$ MeV.

The parameter δ, which is approximately the ratio of the difference between the major and minor axes of the ellipsoid to the mean diameter (i.e., $\frac{\Delta R}{R_o}$), is related to the quantities η and β (used by Nilsson (1955) and Bohr and Mottelson (1953), respectively) by the expressions

$$\delta = 0.95\ \beta$$

and

$$\eta = \frac{\delta}{\kappa}\left[1 - \frac{4}{3}\delta^2 - \frac{16}{27}\delta^3\right]^{-1/6} .$$

For the rare earth nuclei δ is positive which means that the nuclei are stretched along their symmetry axis (prolate).

The constants κ and μ were adjusted to reproduce the sequence of shell model states already established for spherical nuclei (i.e., those with $\delta = 0$). Since the Hamiltonian of equation 3.9 does not possess spherical symmetry, the total angular momentum of the particle, $\underline{j}$, is not conserved. However, the projection, Ω, of the particle angular momentum on the symmetry axis is still a good quantum number.

The eigenfunctions of 3.9 may be expanded as a linear combination of the base vectors $|N\ell\Lambda\Sigma\rangle$ by means of the relation

$$\chi_\Omega = \sum_{\ell\Lambda\Sigma} a^{\Omega}_{\ell\Lambda\Sigma} |N\ell\Lambda\Sigma\rangle \qquad (3.10)$$

where Λ and Σ are the projections of the orbital and spin angular momenta of the odd particle on the symmetry axis and

$$\Lambda + \Sigma = \Omega \ .$$

Although the summation should in principle also occur over N, the total number of oscillator quanta, the contribution from the N-2 and N+2 shells are usually so small that they can be ignored. Exceptions to this general rule have been documented (Bunker and Reich, 1971).

Alternatively, one may express χ_Ω in terms of the spherical harmonic oscillator base vectors $|N\ell j\Omega\rangle$ through the equation

$$\chi_\Omega = \sum_{j\ell} C^{\Omega}_{j\ell} |N\ell j\Omega\rangle \ . \qquad (3.11)$$

The amplitudes $a_{\ell\Lambda\Sigma}$ and $C_{j\ell}$ are related to the Clebsch-Gordan transformation

$$C^{\Omega}_{j\ell} = \sum_{\Lambda\Sigma} \langle \ell \tfrac{1}{2} \Lambda\Sigma | j\Omega\rangle \, a^{\Omega}_{\ell\Lambda\Sigma} \qquad (3.12)$$

Values of $a_{\ell\Lambda\Sigma}$ are tabulated by Nilsson (1955) and values of $C_{j\ell}$ have been given by Chi (1966, 1967).

At zero deformation the states reduce to the shell model states and are (2j+1)-fold degenerate. As the deformation increases from zero, each shell model state splits into $j + \frac{1}{2}$ levels; for $\delta > 0$, the low Ω states are depressed while the high Ω states are raised. This gives rise to the well-known Nilsson energy level diagram, parts of which are shown in Fig. 3.2 and Fig. 3.3. Each level can accommodate two particles corresponding to the projections $\pm \Omega$ of j on the

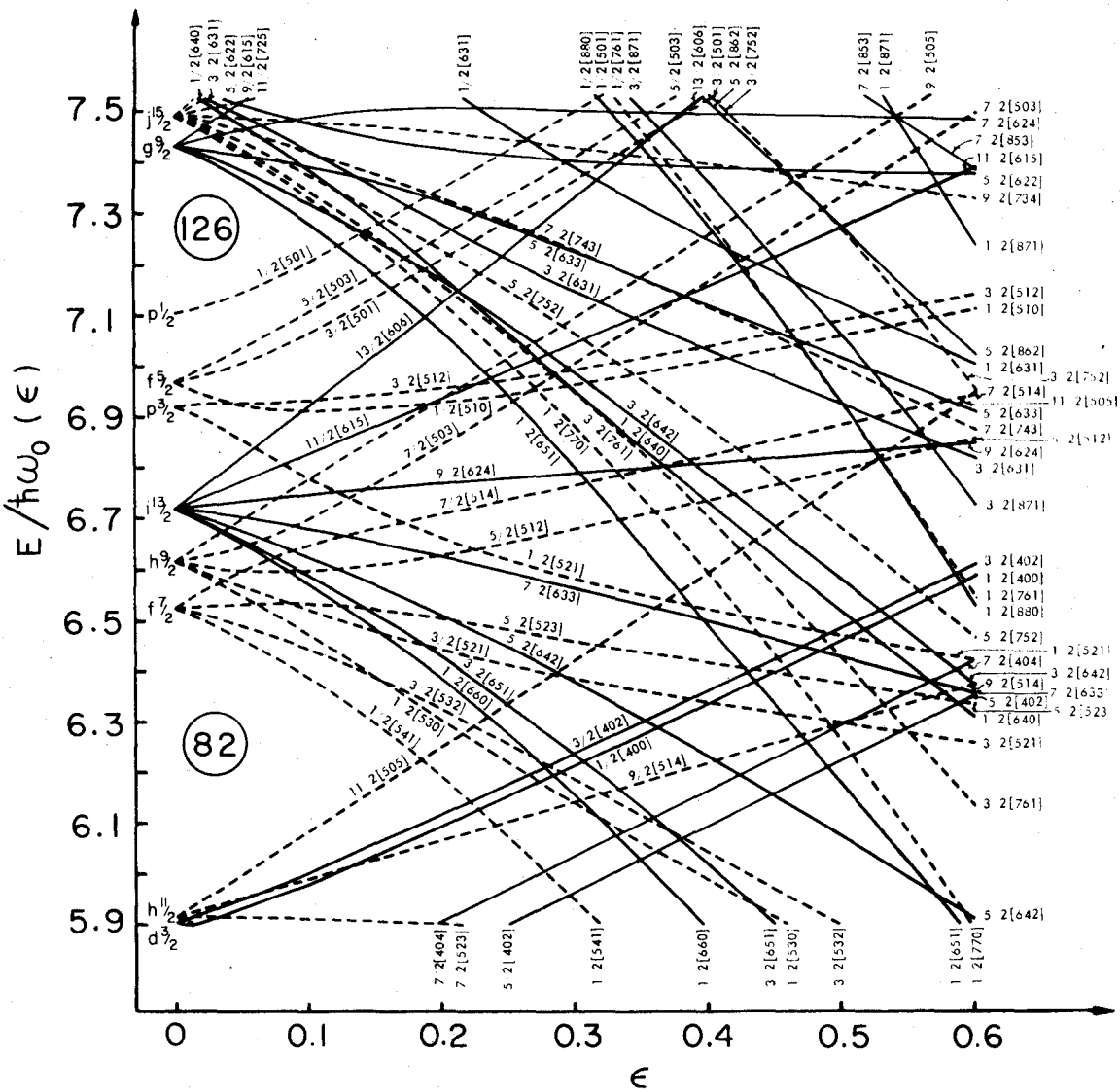

Figure 3.2

Nilsson diagram for neutron states, $82 \leq N \leq 126$
(Note: In this diagram the deformation parameter $\varepsilon = \delta + \frac{1}{6}\delta^2 + \ldots$, where δ is defined in the text.)
(Reproduced from Lederer et al 1968)

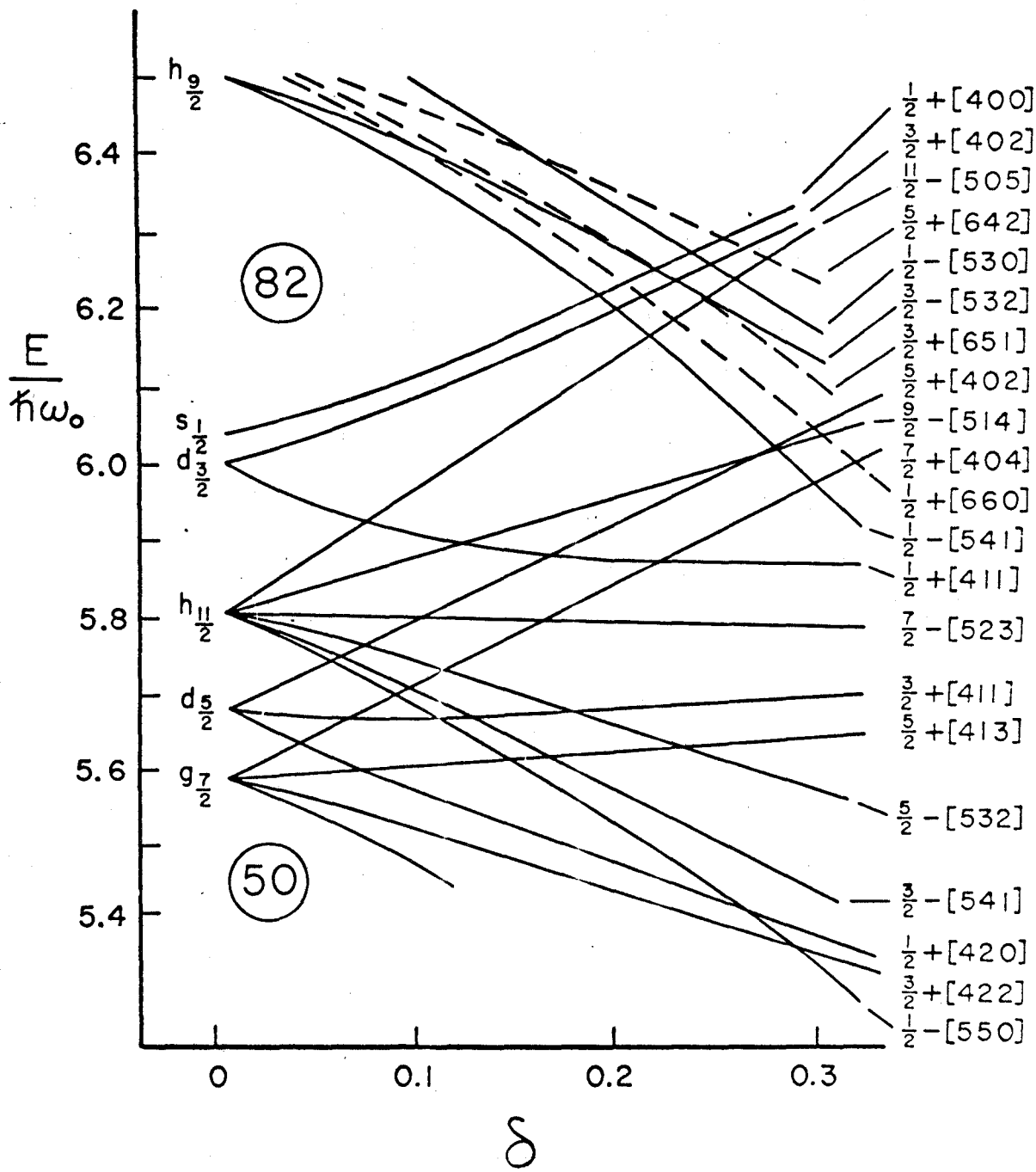

Figure 3.3

Nilsson diagram for proton states, $50 \leq Z \leq 82$
(Reproduced from O'Neil et al 1971)

symmetry axis. Each of the levels is labelled by $\Omega\pi[N\ n_z\ \Lambda]$, where n_z is the number of oscillator quanta along the symmetry axis and π is the parity, equal to $(-)^N$. The symbols inside the square brackets are used to identify a given Nilsson state. They are termed the "asymptotic" quantum numbers since N, n_z and Λ are constants of motion only for very large deformations. For the usual range of deformation encountered ($0.2 \leq \delta \leq 0.3$) in the rare-earth region, this is only approximately so.

In the Nilsson model, Ω is a good quantum number. Since for axial symmetry $K = \Omega$, we may then characterise each intrinsic state with its K value. On each intrinsic state there is built a rotational band with the members having spins $I = K, K + 1$, etc. and energy

$$E_{IK} = \varepsilon_K + \frac{\hbar^2}{2\mathcal{J}} [I(I+1) - 2K^2 + \delta_{K\frac{1}{2}}\, a(-)^{I+\frac{1}{2}}(I+\tfrac{1}{2})] \qquad (3.13)$$

ε_K is the intrinsic state energy (including the contribution from the $\underline{j}^2$ term in eqn. (3.6)) and "a" is the decoupling parameter, non zero only for $K = \frac{1}{2}$, which arises from the diagonal contribution of the Coriolis interaction referred to above.

The off-diagonal contribution from the Coriolis force also mixes states that differ in K by ± 1. In this case, K is no longer a good quantum number. The effect of this interaction is that states of the same spin "push" on each other. In the simple case involving two bands, the lower band is

consequently compressed, while the upper one is expanded. For weak to moderate coupling, the rotational structure is approximately preserved and results only in a renormalization of the rotational parameter. In extreme cases, however, the band structure may not be recognizable (see, for example, Hjorth et al. (1970)). The strongest Coriolis couplings involve orbitals arising from the same shell model state. The strength of this unhindered coupling increases with the value of j of the spherical state from which the orbital originates. As a consequence these effects are most pronounced among orbitals from the $h_{11/2}$ and $i_{13/2}$ shell model states.

3.4 Residual interactions - pairing and multipole-multipole interactions

The simple picture of independent nucleon motion in a deformed potential is modified by the influence of the interactions which produce effects that cannot be described in terms of the average field potential well. These residual forces, which approximate the nucleon-nucleon interactions, are usually divided into a short-range and a long-range part. Thus, the intrinsic Hamiltonian of eq. 3.3 may be written as

$$H_{\text{intrinsic}} = H_{\text{av potl}} + H_{\text{short r}} + H_{\text{long r}} . \quad (3.14)$$

The short-range interaction is simulated by a pairing force which accounts for the empirical fact that nucleons prefer to exist as correlated pairs which continuously scatter from one

orbit to another. The adaptation of the B.C.S. theory of superconductivity (Bardeen, Cooper and Schrïeffer 1957) to the nuclear problem provided the mathematical formalism for describing the pairing phenomenon. In this section we shall not attempt to develop this formalism, but restrict the presentation to describing some of its more important consequences. A more detailed discussion of the pairing theory may be found in the recent papers of Nathan and Nilsson (1965) or Ogle et al. (1971).

The deepest lying states in an even-even nucleus are filled with nucleons which pairwise occupy the Ω-degenerate orbitals. Near the Fermi level, however, the levels are only partially occupied, so that the Fermi surface is diffuse. Each level ν has a probability V_ν^2 of being filled by a pair of nucleons, and a probability U_ν^2 of being empty, with $U_\nu^2 + V_\nu^2 = 1$.

In an odd nucleus, the odd nucleon occupies a definite level ν. This nucleon has the properties of a particle to the extent U^2 that the level ν was empty in the even-even nucleus, and the properties of a hole to the extent V^2 that the orbital was already occupied. This dual nature gives rise to the concept of a "quasi-particle" and, as a consequence single particle excitations in odd A nuclei must be thought of as "quasi-particle" excitations. For excitations far above the Fermi energy, the state becomes "particle-like" while for excitations far below this energy it becomes "hole-like" in character.

The observed intrinsic excitation in an odd nucleus is the difference between the ground state quasi-particle energy and the quasi-particle energy of the excited nucleon. The ground state quasi particle energy is given by

$$E_\nu = \sqrt{(\varepsilon_\nu - \lambda)^2 + \Delta^2} \qquad (3.15)$$

where ε_ν is the single particle energy (e.g. the Nilsson energy), λ the Fermi energy and 2Δ the energy gap. Thus the excitation energy of a quasi-particle occupying the level ν', is given by

$$E_{exc.} = \sqrt{(\varepsilon_\nu' - \lambda)^2 + \Delta^2} - \sqrt{(\varepsilon_\nu - \lambda)^2 + \Delta^2} \ .$$

Since $(\varepsilon_\nu - \lambda)$ is $<<$ Δ, this can be written as

$$E_{exc} = \sqrt{(\varepsilon_\nu' - \lambda)^2 + \Delta^2} - \Delta \ . \qquad (3.16)$$

The general effect of the pairing is to compress the levels near the ground state, the high lying states being lowered by approximately Δ.

The gap parameter Δ, whose magnitude is determined by the strength of the pairing force, also provides a measure of the extent of diffuseness of the Fermi surface. The gap parameter may be determined empirically from the separation energies, S. Since in an odd A nucleus the odd nucleon has more energy Δ than if it were paired, it requires 2Δ more energy to remove a nucleon from an even-even nucleus than from an odd-even nucleus. The proton gap is thus given by

$$\Delta_p = \frac{1}{4}\{2S(Z,N) - S(Z+1,N) - S(Z-1,N)\}. \qquad (3.18)$$

The neutron gap is similarly defined. S(Z,N) refers to the separation energy in the even-even system. Values of S(Z,N) obtained from the 1971 atomic mass evaluation (Wapstra and Gove 1971) give, for ^{176}Hf

$$\Delta_p = 863 \text{ keV}$$
$$\Delta_n = 736 \text{ keV}.$$

The quantities V^2 and U^2 referred to above are defined by

$$V_\nu^2 = \frac{1}{2}\left[1 - \frac{\varepsilon_\nu - \lambda}{\sqrt{(\varepsilon_\nu - \lambda)^2 + \Delta^2}}\right] \qquad (3.18)$$

$$U_\nu^2 = \frac{1}{2}\left[1 + \frac{\varepsilon_\nu - \lambda}{\sqrt{(\varepsilon_\nu - \lambda)^2 + \Delta^2}}\right] \qquad (3.19)$$

The model described provides a much more realistic prediction of transfer reaction cross-sections, β-transition rates, and gamma transition probabilities than is possible without pairing. The effect on the latter may be taken into account by a multiplication pairing factor P_γ:

$$T_\gamma(i \to f) = P_\gamma \, T_{\gamma\ \text{single-particle}} \,. \qquad (3.20)$$

P_γ is defined as follows:

$$P_\gamma \sim [U_i U_f \pm V_i V_f]^2 \qquad (3.21a)$$

where there is no change in the number of quasi particles

or

$$P_\gamma \sim [U_i V_f \mp U_f V_i]^2 \qquad (3.21b)$$

where the number of quasi-particles changes by two. The upper sign is used for magnetic multipoles and the lower sign for electric multipoles. Consequently, for transitions between single quasi-particle states near the Fermi surface, the electric transition rate may be reduced by two or three orders of magnitude below the Nilsson model estimates (Vergnes and Rasmussen 1965), whereas the magnetic transition rates are only slightly affected. For transitions between 2 quasi-particle states and the ground state the reverse may be true.

As previously mentioned there is also a long range component of the residual interaction. This is usually represented as a multipole-multipole expansion, each term of which may be written in the form

$$H = - \sum_{\mu} \sum_{\alpha>\beta} \kappa_{\lambda\mu} (-)^{\mu} Q_{\lambda\mu}{}^{\alpha} Q_{\lambda\mu}{}^{\beta} \qquad (3.22)$$

where

$$Q^{\alpha}_{\lambda\mu} = r_\alpha{}^{\lambda} Y_{\lambda\mu}(\theta_\alpha, \phi_\alpha). \qquad (3.23)$$

The single particles are represented by α and β; $\kappa_{\lambda\mu}$ represents the strength of the force. Whereas the pairing force connects only pairs of nucleons in time-reversed orbitals, the multipole-multipole force affects all pair combinations, with the nucleon-pairs all acting coherently. The inclusion of the multipole-multipole

force is, therefore, essential for a description of collective phenomena (see the next section).

3.5 Excited States in Even-Even Nuclei

In the ground state of an even-even nucleus, the nucleons occupy the orbitals pairwise with $+\Omega$ and $-\Omega$ to form total angular momentum 0. A rotational band with spin sequence 0, 2, 4, etc. is formed and is usually referred to as the ground state band (g.s.b.). The lowest excited states are formed by breaking a nucleon pair, resulting in one quasi-particle in each of the orbitals ν_1 and ν_2 with projections Ω_1 and Ω_2 on the symmetry axis. These projections can couple either parallel or antiparallel to form resultant projections

$$K = \Omega_1 + \Omega_2$$

or

$$K = |\Omega_1 - \Omega_2|.$$

These states are, to a first approximation, degenerate with energy given by

$$\begin{aligned} E &= E_{\nu_1} + E_{\nu_2} \\ &= \sqrt{(\varepsilon_{\nu_1} - \lambda)^2 + \Delta^2} + \sqrt{(\varepsilon_{\nu_2} - \lambda)^2 + \Delta^2} \qquad (3.24) \\ &\gtrsim 2\Delta. \end{aligned}$$

Since $2\Delta \sim 1$ MeV, these states occur at energies above ~ 1 MeV in the mass region $150 \leq A \leq 190$. Gallagher and Soloviev (1962) have calculated the energies of the low lying two quasi-particle

states of the doubly-even nuclei in this mass region, using the BCS model mentioned in section 3.4.

In actual fact, the degeneracy of the two states formed is removed by a spin-spin interaction. For like particles Gallagher (1962) has formulated the rule that the lower lying state is the one in which the intrinsic spins are coupled antiparallel, i.e. $\Sigma_1 + \Sigma_2 = 0$. In other words, the K of the lower-lying state is

$$\begin{aligned} K &= |\Omega_1 - \Omega_2| \text{ if } \Omega_1 = \Lambda_1 \pm \tfrac{1}{2}\,, \ \Omega_2 = \Lambda_2 \pm \tfrac{1}{2} \\ K &= \Omega_1 + \Omega_2 \qquad \Omega_1 = \Lambda_1 \pm \tfrac{1}{2} \quad \Omega_2 = \Lambda_2 \mp \tfrac{1}{2} \end{aligned} \tag{3.25}$$

This is a consequence of the fact that the singlet interaction is stronger than the triplet interaction in the case of like particles.† For example, the two protons in the orbitals 7/2+[404↓] and 5/2+[402↑]* may be expected to form states of K = 6 and K = 1, with the K = 6 state having the lower energy.

The available Nilsson orbitals in ^{176}Hf are shown

---

†The reverse is true for proton-neutron coupling in odd-odd nuclei so that the lower state in this case has $\Sigma_1 + \Sigma_2 = 1$ (Gallagher and Moszkowski 1958) .

*This notation is equivalent to the Nilsson notation $[Nn_z\Lambda\Sigma]$ where we indicate that Σ is $+\frac{1}{2}$ by an upward arrow and that $\Sigma = -\frac{1}{2}$ by a downward arrow.

in Fig. 3.4 and 3.5 for neutrons and protons, respectively. The Nilsson energies, shown on the left in each figure, are calculated using the programme GREAT (written by O'Neil and Price, based on a programme oroginally due to Chi 1966) with the parameters $\delta = 0.28$, $\kappa = 0.0637$ and $\mu = 0.42$ (neutrons) and $\mu = 0.60$ (protons). The quasi-particle energies, plotted on the right in each figure, are obtained using eq. 3.16, with the Fermi energy λ set, somewhat arbitrarily, as indicated in the figures and with $\Delta_n = 736$ keV and $\Delta_p = 863$ keV. Hole states are plotted below the Fermi surface. The quantity E_ν, given by eq. 3.15, is given beside each quasi-particle level.

The lower-lying (< 2.5 MeV) two quasi-particle states that can be formed from the orbitals shown in Figs. 3.4 and 3.5 are listed in Tables 3.1 and 3.2.The K quantum number of the lower energy members of each pair (formed from two given quasi-particles) is given first (see eq. 3.25). The indicated energy is obtained from eq. 3.24, using the values of E_ν given in Figs. 3.4 and 3.5. For this purpose, each pair is considered degenerate and no account is taken of the expected splitting (100-400 keV) due to the spin-spin interaction.

Besides the quasi-particle excitation, there occur collective vibrational excitations. In the microscopic picture, these are viewed as coherent superpositions of many two quasi-particle states, each such state occurring with a small amplitude. These collective states are depressed in energy and can occur below the pairing gap energy, 2Δ. They are

Figure 3.4

Neutron Nilsson orbitals near the Fermi surface in ^{176}Hf. The Fermi surface has been set 200 keV above the orbital that would be last-filled in the absence of pairing. ε_ν is the Nilsson energy calculated with the parameters in the insert. The horizontal lines indicate the single-particle and quasi-particle energies, $\varepsilon_\nu - \lambda$ and $\sqrt{(\varepsilon_\nu - \lambda)^2 + \Delta^2} - \Delta$, respectively; although the latter are always positive, the hole states are drawn below the Fermi surface. The quasi-particle energy E_{qp} (E_ν in the text) is given beside each quasi-particle level to facilitate the calculation of two quasi-particle energies using eq. 3.24.

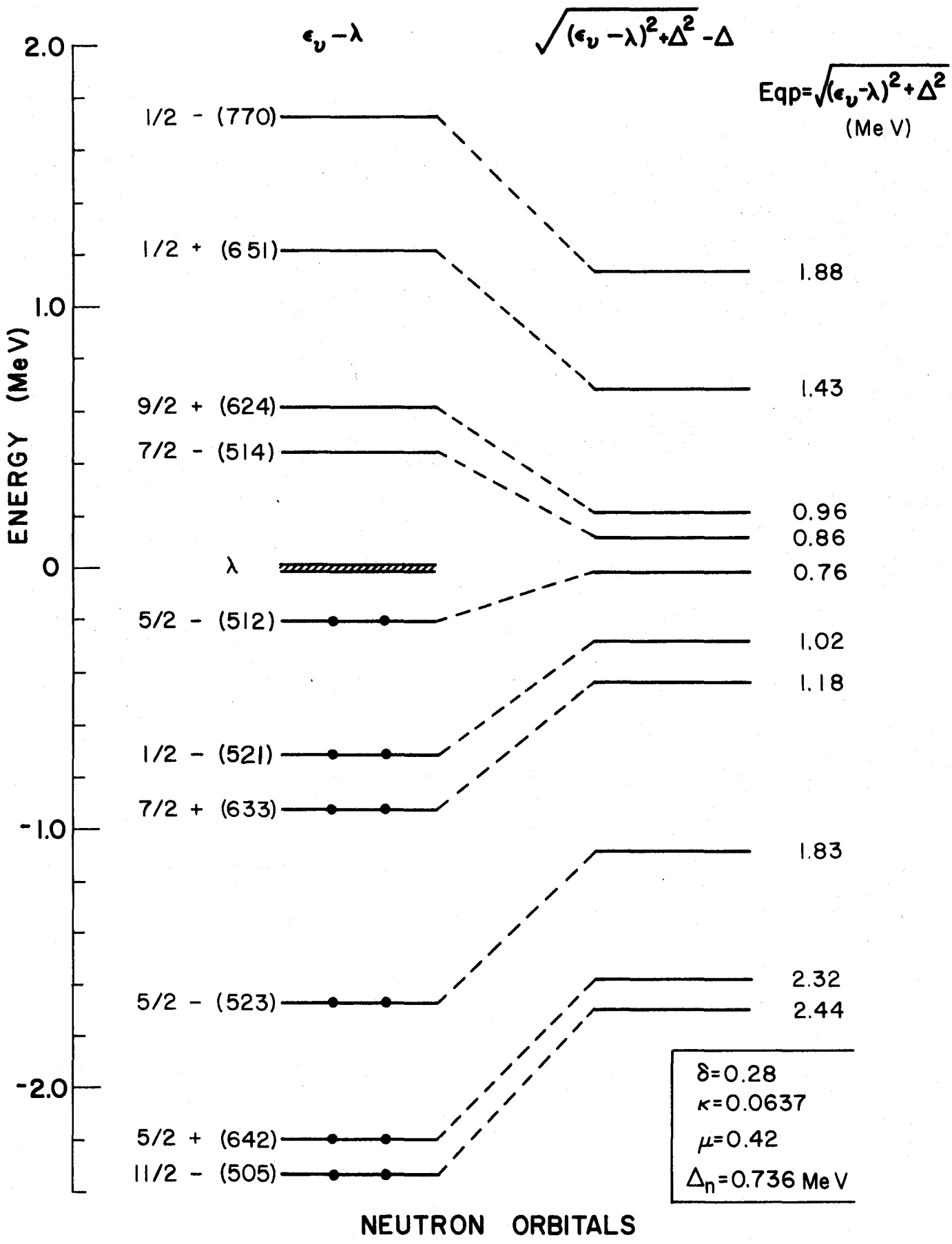
$\epsilon_\upsilon - \lambda$
$\sqrt{(\epsilon_\upsilon - \lambda)^2 + \Delta^2} - \Delta$
$Eqp = \sqrt{(\epsilon_\upsilon - \lambda)^2 + \Delta^2}$
(Me V)
2.0
1.0
0
-1.0
-2.0
ENERGY (Me V)
1/2 - (770)
1/2 + (651)
9/2 + (624)
7/2 - (514)
λ
5/2 - (512)
1/2 - (521)
7/2 + (633)
5/2 - (523)
5/2 + (642)
11/2 - (505)
1.88
1.43
0.96
0.86
0.76
1.02
1.18
1.83
2.32
2.44
δ=0.28
κ=0.0637
μ=0.42
Δ_n=0.736 Me V
NEUTRON ORBITALS

Figure 3.5

Proton Nilsson orbitals near the Fermi surface in ^{176}Hf. (see caption of Figure 3.4).

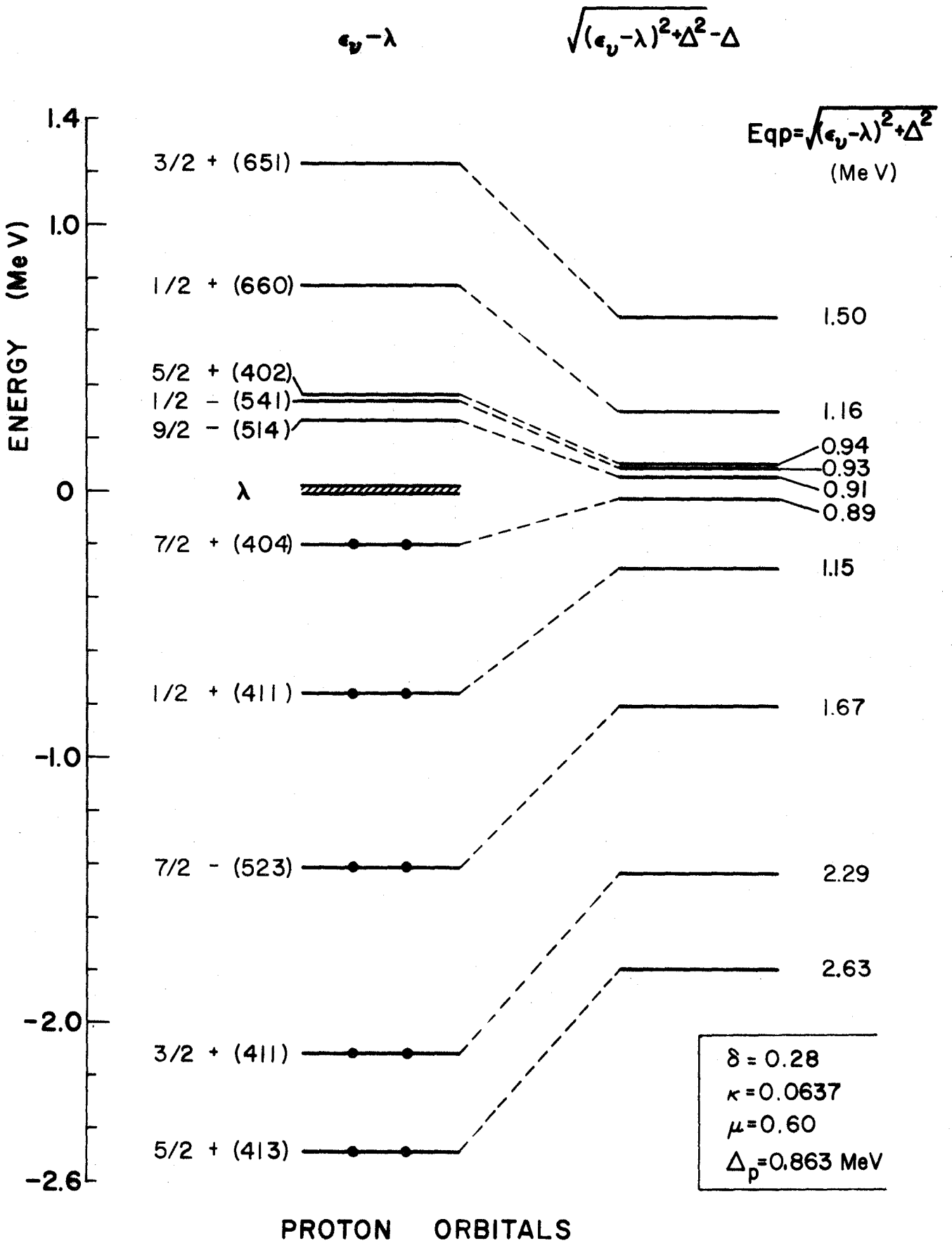
$\epsilon_\nu - \lambda$
$\sqrt{(\epsilon_\nu-\lambda)^2+\Delta^2}-\Delta$
$E_{qp}=\sqrt{(\epsilon_\nu-\lambda)^2+\Delta^2}$
(Me V)
ENERGY (Me V)
1.4
1.0
0
-1.0
-2.0
-2.6
3/2 + (651)
1/2 + (660)
5/2 + (402)
1/2 − (541)
9/2 − (514)
λ
7/2 + (404)
1/2 + (411)
7/2 − (523)
3/2 + (411)
5/2 + (413)
1.50
1.16
0.94
0.93
0.91
0.89
1.15
1.67
2.29
2.63
δ = 0.28
κ = 0.0637
μ = 0.60
Δ_p = 0.863 MeV
PROTON ORBITALS

TABLE 3.1

TWO QUASI-NEUTRON STATES

K	Orbitals		E MeV	K	Orbitals		E MeV
	ν	ν'			ν	ν'	
$6^+,1^+$	7/2-[514↓]	5/2-[512↑]	1.6	$5^+,4^+$	1/2+[651↓]	9/2+[624↑]	2.4
$2^-,7^-$	9/2+[624↑]		1.7	$4^-,5^-$	1/2-[770↑]		2.8
$3^-,2^-$	1/2+[651↓]		2.2	$5^-,4^-$	1/2-[521↓]		2.0
$2^+,3^+$	1/2-[770↑]		2.6	$1^+,8^+$	7/2+[633↑]		2.1
$3^+,2^+$	1/2-[521↓]		1.8	$7^-,2^-$	5/2-[523↓]		2.8
$1^-,6^-$	7/2+[633↑]		1.9	$1^-,0^-$	1/2-[770↑]	1/2+[651↓]	3.3
$5^+,0^+$	5/2-[523↓]		2.6	$0^-,1^-$	1/2-[521↓]		2.4
$8^-,1^-$	9/2+[624↑]	7/2-[514↓]	1.8	$3^+,4^+$	7/2+[633↑]		2.6
$3^-,4^-$	1/2+[651↓]		2.3	$2^-,3^-$	5/2-[523↓]		2.3
$4^+,3^+$	1/2-[770↑]		2.7	$1^+,0^+$	1/2-[521↓]	1/2-[770↑]	2.9
$3^+,4^+$	1/2-[521↓]		1.9	$3^-,4^-$	7/2+[633↑]		3.1
$7^-,0^-$	7/2+[633↑]		2.0	$3^+,2^+$	5/2-[523↓]		3.7
$1^+,6^+$	5/2-[523↓]		2.7	$4^-,3^-$	7/2+[633↑]	1/2-[521↓]	2.2
				$2^+,3^+$	5/2-[523↓]		2.8
				$6^-,1^-$	5/2-[523↓]	7/2+[633↑]	3.0

STATES IN ^{176}Hf POPULATED BY THE (α,2n) REACTION

TABLE 3.2

TWO QUASI-PROTON STATES

K	Orbitals		E (MeV)	K	Orbitals		E (MeV)
	ν	ν'			ν	ν'	
$8^-,1^-$	9/2-[514↑]	7/2+[404↓]	1.8	$3^-,2^-$	5/2+[402↑]	1/2-[541↓]	1.9
$3^-,4^-$	1/2-[541↓]		1.8	$1^-,0^-$	1/2+[660↑]		2.1
$6^+,1^+$	5/2+[402↑]		1.8	$2^-,1^-$	3/2+[651↑]		2.4
$4^+,3^+$	1/2 [660↑]		2.0	$0^-,1^-$	1/2+[411↓]		2.1
$5^+,2^+$	3/2+[651↑]		2.4	$4^+,3^+$	7/2-[523↑]		2.6
$3^+,4^+$	1/2+[411↓]		2.0				
$7^-,0^-$	7/2-[523↑]		2.6	$2^+,3^+$	1/2+[660↑]	5/2+[402↑]	2.1
				$1^+,4^+$	3/2+[651↑]		2.4
$5^+,4^+$	1/2-[541↓]	9/2-[514↑]	1.8	$3^+,2^+$	1/2+[411↓]		2.1
$2^-,7^-$	5/2+[402↑]		1.8	$1^-,6^-$	7/2-[523↑]		2.6
$4^-,5^-$	1/2+[660↑]		2.1				
$3^-,6^-$	3/2+[651↑]		2.4	$1^+,2^+$	3/2+[651↑]	1/2+[660↑]	2.7
$5^-,4^-$	1/2+[411↓]		2.1	$1^+,0^+$	1/2+[411↓]		2.3
$1^+,8^+$	7/2-[523↑]		2.6	$3^-,4^-$	7/2-[523↑]		2.8
				$2^+,1^+$	1/2+[411↓]	3/2+[651↑]	2.6
				$2^-,5^-$	7/2-[523↑]		3.2
				$4^-,3^-$	7/2-[523↑]	1/2+[411↓]	2.8

characterized by large transition probabilities of the electric multipole type to the ground state and by large Coulomb excitation probabilities. Calculations of the structure of such states show that the distinction between "two-quasi-particle" and "collective" states is not a sharp one. It is often found that one or a few two quasi-particle components constitute a large fraction of the total state.

The vibrational states are characterised by the multipole order λ of the long range residual interaction used in the calculation. Such collective states may be viewed, in terms of a classical picture, as surface vibrations of the spheroidal nucleus. β-vibrations arise from the Y_{20} term ($K=0^+$), γ-vibrations from the Y_{22} term ($K=2^+$), and octupole vibrations from the $Y_{3\mu}$ term ($K = \mu = 0^-, 1^-, 2^-, 3^-$). From symmetry arguments, the positive parity 0^+ rotational band has spin sequence 0, 2, 4, etc, while the negative parity 0-band has spin 1, 3, 5 etc. Bands based on other K-values have the usual K, K+1, K+2, ... sequence.

Microscopic treatments of the collective states are usually based on the BCS and RPA (random phase approximation) theories. Detailed discussions of these methods may be found in review papers by Nathan and Nilsson (1965) or Bes and Sorensen (1969). Here, we shall only sketch the method in order to get some physical insight into the problem. The multipole-multipole force (eq. 3.19) introduced in the last section is represented, in the framework of the BCS theory, by its

matrix element

$$\langle\alpha\beta^{-1}|H_\lambda|\gamma\delta^{-1}\rangle = - \sum_\mu \kappa_{\lambda\mu} \langle\alpha|Q_{\lambda\mu}|\beta\rangle\langle\gamma|Q_{\lambda\mu}|\delta\rangle \qquad (3.26)$$

Here, $\alpha,\beta,\delta,\gamma$ denote single particle states. The two quasi-particle states, $\alpha\beta^{-1}$, $\gamma\delta^{-1}$ .., with angular momentum projection $K = \mu$, are created by the multipole field operator $H_\lambda \equiv \sum_\mu Q_{\lambda\mu}\cdot Q_{\lambda\mu}$. States of a given K are affected only by that part of the interaction with $\mu = K$. The force is, therefore, seen to mix several two quasi-particle components (both neutrons and protons), thus providing a mechanism for collectivity. The energies, E_i, of the resultant states are obtained from the RPA calculations from the so-called secular equation

$$\frac{1}{\kappa_{\lambda\mu}} = \sum_{\alpha>\beta} \frac{|\langle\alpha|Q_{\lambda\mu}|\beta\rangle|^2 U^+_{\alpha\beta}\, E_{\alpha\beta}}{E^2_{\alpha\beta} - E_i^2} \qquad (3.27)$$

where $\kappa_{\lambda\mu}$ is the strength of the multipole-multipole force in eq. (3.32),

$E_{\alpha\beta}$ is the two quasi-particle energy (eq. 3.24) and

$U^+_{\alpha\beta}$ is the pairing factor given by

$$U^+_{\alpha\beta} = (U_\alpha V_\beta + U_\beta V_\alpha) . \qquad (3.28)$$

The character of the solutions is illustrated in Fig. 3.6, which shows a plot of the right hand side of eq. 3.27 against positive values of E_i. For a given strength of the interaction, there are many roots of this equation, with one lying between each successive pair of $E_{\alpha\beta}$ values.

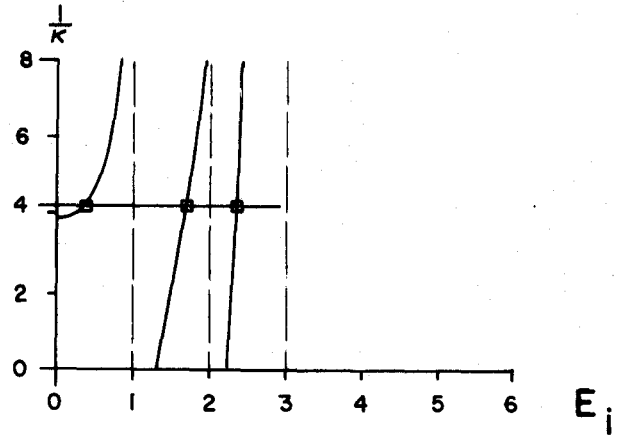

Figure 3.6

The RPA equation (3.27) plotted as a function of E_i for a system of three levels at E = 1, 2 and 2.5 MeV. The curves represent the right side of eq. (3.27) and the intersections with the horizontal line $1/\kappa$ indicated by □ are roots of E_i satisfying the RPA equation. (Reproduced from Bès and Sorensen 1969).

When the interaction is very weak, the roots lie close to the single particle energies. However, as it grows stronger, one solution is depressed in energy below the lowest single particle state. This low lying state is collective in character and can be shown to have a large λ-electric transition strength to the ground state.

A comprehensive calculation for the octupole states has been performed by Neergård and Vogel (1970) with results that are in good agreement with experimental data (see e.g. Chapter 7 or O'Neil and Burke 1972)). In particular, the distortion of the rotational bounds built on the octupole states and the distribution of the B(E3 g.s. → 3-) strengths are generally well reproduced. The key to the success of Neergård and Vogel's calculations lies in the inclusion of Coriolis coupling between states with K and K+1. In the Coriolis mixing procedure, the unperturbed wave functions and band-head energies were obtained from their RPA calculations for states up to 2.5 MeV.

Numerous calculations on the quadrupole vibrational states have been undertaken, e.g. by Bes et al. (1965) and Malov et al. (1968). It has recently been evident that there are more K = 0 states than can be explained on the basis of quadrupole (β) vibrations. For instance, five such bands are thought to exist in ^{178}Hf.

However, the theorists, seemingly not wishing to be

outdone by nature, have generated a generous number of 0+ states of varying description. A discussion of the various models may be found in Bernthal (1969) and Dzhelepov and Shestopalova (1968). Here, we shall merely mention the various types of states that have been proposed. The quadrupole (β) vibration, which arises from fluctuations of the average nuclear field, has already been discussed above. Pairing vibrations associated with the coherent transfer of pairs of particles across the Fermi level are also expected. These may be thought of as fluctuations in the diffuseness of the Fermi surface. Bes and Broglia (1966) have formulated a description of these states, which has been extended by Mikoshiba et al. (1967). Several pairing vibrational states may occur in a given nucleus. Experimentally, these states may be identified in reactions transferring pairs of like particles, e.g. (p,t) and (t,p) reactions.

Another class of 0+ (and also 2+) states may arise from the use of residual spin-quadrupole interactions (Pyatov 1967). For nuclei within the deformed region, states of this type are predicted to have smaller electric quadrupole transition probabilities than for quadrupole vibrational states and therefore may be relatively long lived. Such states are expected to occur at an excitation of $\sim$ 1 MeV. The experimental evidence for spin-quadrupole vibrations is very scanty; Bernthal (1969) has speculated that such a state may occur in ^{176}Hf at 1293 keV.

3.6 Electromagnetic Transition Rates

The general theory of photon radiation may be found in standard texts such as Preston (1962) or Moszkowski (1965). In this section we present only the selection rules that govern photon emission.

For a system proceeding via radiation of a photon of multipolarity λ, from an initial state $|I_i \pi_i>$ to the final state $|I_f \pi_f>$,

$$|I_i - I_f| \leq \lambda \leq I_i + I_f$$

and

$$\pi_i \pi_f = \begin{cases} (-)^{\lambda} & \text{for an electric radiation} \\ (-)^{\lambda+1} & \text{for a magnetic radiation.} \end{cases}$$

I_i and I_f are the initial and final spins of the system; π is the corresponding parity.

The transition probability for emission of a photon of energy $\hbar\omega$, angular momentum λ is given by

$$T(\lambda, I_i \to I_f) = \frac{8\pi(\lambda+1)}{\lambda[(2\lambda+1)!!]^2} \frac{1}{\hbar} \left(\frac{\omega}{c}\right)^{2\lambda+1} B(\lambda, I_i \to I_f) \text{ sec.}^{-1} \qquad (3.29)$$

where $B(\lambda, I_i \to I_f)$, the reduced transition probability, is given by

$$B(\lambda, I_i \to I_f) = \sum_{\mu M_f} |<I_f M_f | O(\lambda, \mu) | I_i M_i>|^2 \qquad (3.30)$$

$O(\lambda, \mu)$ is the μ-component of the electric or magnetic multipole transition operator of multipole order λ.

For the first few values of λ, equation (3.29) gives,

for the decay rate per second

$$\left.\begin{aligned} T(E1) &= 1.59 \times 10^{15}\ (E)^3\ B(E1) \\ T(E2) &= 1.22 \times 10^{9}\ \ (E)^5\ B(E2) \\ T(E3) &= 5.67 \times 10^{2}\ \ (E)^7\ B(E3) \\ T(M1) &= 1.76 \times 10^{13}\ (E)^3\ B(M1) \\ T(M2) &= 1.35 \times 10^{7}\ \ (E)^5\ B(M2) \end{aligned}\right\} \qquad (3.31)$$

where E is in MeV, $B(E\lambda)$ in units of $e^2(fm)^{2\lambda}$, and $B(M\lambda)$ in units of $(e\hbar/2Mc)^2(fm)^{2\lambda-2}$; $(e\hbar/2Mc$ is the nuclear magneton, $\mu_N)$.

A crude estimate of the ratio of the magnetic and electric transition rates of the same order, λ, made from equation (3.31) gives $\sim 10^{-2}$. Similarly, the ratio of successive multipole order λ and $\lambda+1$ (of the same type) is ~ 10 . Thus, it is usually only the lowest multipole which contributes to a given transition. One common exception to this rule occurs in cascade transitions within rotational bands in deformed nuclei, where enhanced E2 transitions compete with the otherwise faster M1 transitions.

The reduced transition probability, defined in eqn. 3.30, can be evaluated explicitly in the unified model and may be written as a product of a geometrical factor, governed by angular momentum coupling rules, and a factor depending only on the intrinsic wave functions of the initial and final states:

$$B(\lambda) = \langle I_i\ \lambda\ K_i\ K_i\text{-}K_f | I_f\ K_f\rangle^2 \langle K_f | O(\lambda) | K_i\rangle^2 \qquad (3.32)$$

where I_iK_i and I_fK_f are the quantum numbers of the initial and final states. For transitions from the same initial state to two different final states in the same rotational band, the ratio of the reduced transition probabilities is given by Alaga's rules (Alaga et al 1955):

$$\frac{B(\lambda\ I_iK_i \rightarrow I_fK_f)}{B(\lambda\ I_iK_i \rightarrow I_f,K_f)} = \frac{\langle I_i\ \lambda\ K_i\ K_f\text{-}K_i | I_fK_f\rangle^2}{\langle I_i\ \lambda\ K_i\ K_f\text{-}K_i | I_f,K_f\rangle^2} \qquad (3.33)$$

Equations 3.32 and 3.33 are strictly applicable for transitions between states for which K is a good quantum number. The equations do not apply in those rare cases where $\lambda \geq K_i + K_f$ (with neither K_i nor K_f equal to zero).

The Clebsch-Gordan coefficients in the expression for the reduced transition probability (eq.3.32) give rise to a K-selection rule

$$\Delta K^\circ = K_i^\circ - K_f^\circ \leq \lambda\ . \qquad (3.34)$$

This rule is not strictly obeyed since transitions of reduced intensity can still occur because of small admixtures of other K values to the main components of the wave functions. (the superscript "°" in eq. 3.34 indicates the main components). To first order, transitions proceed through admixtures of the type $|K_i\text{-}K_f| = \lambda$ and branching ratios (for transitions from the same initial state) will, in this case, follow the Bohr-Mottelson (1963) rule. Higher order corrections, taking into account admixtures of the type $|K_i\text{-}K_f| = \lambda\text{-}1$ and, possibly

$|K_i - K_f| = \lambda - 2$, have been incorporated into a formula derived by Mikhailov (1966). For the case $K_i^\circ > K_f^\circ$ and neither K_i° or K_f° equal to 1/2, the expression reads

$$B(\lambda\ I_i \to I_f) = \langle I_i \lambda (K_i^\circ - \nu)(K_f^\circ - K_i^\circ + \nu) | I_f K_f^\circ \rangle^2 \times \frac{(I_i + K_i^\circ)!\,(I_i - K_i^\circ + \nu)!}{(I_i - K_i^\circ)!\,(I_i + K_i^\circ - \nu)!}\ M^2(1+\delta^2) \qquad (3.35)$$

where

$$\delta = [I_f(I_f+1) - I_i(I_i+1)]a \qquad (3.36)$$

and

$$\nu = |K_i^\circ - K_f^\circ| - \lambda. \qquad (3.37)$$

Here, M and a are constants, the latter being a measure of the higher order K-admixtures in the transition. The Bohr-Mottelson rule corresponds to a = 0, the Alaga rule to a = 0 and $\nu = 0$.

The quantity ν defined in eq. 3.37 is usually referred to as the degree of K-forbiddenness. It is customary to define a retardation factor as the ratio of the observed half-life to that predicted according to the Weisskopf (1952) single particle estimate, i.e.,

$$F_W = T_{1/2}(\text{expt.})/T_{1/2}(\text{SP}) \qquad (3.38)$$

Retardation factors are also commonly defined with respect to the Moskowski (1965) or Nilsson estimates. Furthermore, the retardation factor may be expressed in the form

$$F_W = (f_W)^\nu\ , \qquad (3.39)$$

where f_W is the degree of forbiddenness per unit of ν. f_W is usually of the order of 100 (Rusinov 1961; Löbner 1968).

For the deformed nuclei, expressions for the reduced transition probabilities have been given by Nilsson (1955) and Kerman (1956). The following expressions are quoted in Hjorth et al. (1970) who consider the transition proceeding between mixed (as opposed to pure single particle) states given by

$$\psi^I = \sum_{i=1}^{N} C^I_{K_i} \psi_o^{I,K_i} \quad \text{and} \quad \psi^{I'} = \sum_{j=1}^{N} C^{I'}_{K_j} \psi_o^{I'K_j} . \qquad (3.40)$$

Here, the quantity C_{K_i} is the amplitude of the admixture of the single quasi-particle wave function ψ_o^{I,K_i} in the state with spin-I, and N is the number of mixed states. (The mixing of states will be discussed later). For E2 and M1 transitions,

$$B(E2,\ I\to I') = \frac{5}{16\pi} e^2 Q_o^2 \left[\sum_{K_i=K_j} C^I_{K_i} C^{I'}_{K_j} \langle I2K_i 0 | I'K_j\rangle \right]^2 \qquad (3.41)$$

and

$$B(M1,I\to I') = \left(\frac{e\hbar}{2Mc}\right)^2 \frac{3}{4\pi}\frac{1}{4} \left[\sum_{K_i=K_j,K_j\pm1} C^I_{K_i} C^{I'}_{K_j} \{\langle I1\ K_iK_j-K_i | I'K_j\rangle \right.$$

$$\left. + b_{M1}\, \delta_{K_i,\frac{1}{2}}\, \delta_{K_j,\frac{1}{2}} (-)^{I'+\frac{1}{2}} \langle I1\ \tfrac{1}{2}\ -1 | I'-\tfrac{1}{2}\rangle \} G_{M_1}^{K_iK_j} \right]^2 . \qquad (3.42)$$

Because of the large intrinsic quadrupole moments, Q_o, in the deformed region, the single particle contribution is usually negligible in the B(E2) values, and only diagonal elements are included in eq. (3.41).

The quantity b_{M1} in equation (3.42) vanishes except between $K = \frac{1}{2}$ bands where it is given by

$$b_{M_1} G_{M_1}^{\frac{1}{2}\frac{1}{2}} = \sqrt{2}(-1)^{\ell+1} \sum_{\ell} [a_{\ell o}^2 (g_s - g_R) + 2a_{\ell o} a_{\ell 1} \sqrt{\ell(\ell+1)}\ (g_\ell - g_R)] \quad (3.42a)$$

The diagonal elements $G_{M_1}^{K_i K_j}$ $(K_i = K_j = K)$ are given by

$$G_{M_1}^{KK} = \sum_{\ell\Lambda} a_{\ell\Lambda}^2 [(-)^{\Sigma-\frac{1}{2}}(g_s - g_R) + 2\Lambda(g_\ell - g_R)] \quad (3.42b)$$

or

$$G_{M_1}^{KK} = 2K(g_K - g_R). \quad (3.42c)$$

The off-diagonal elements $(K_i = K+1, K_j = K)$ are given by

$$G_{M_1}^{K+1,K} = -G_{M_1}^{K,K+1} = -\sqrt{2} \sum_{\ell\Lambda} [a_{\ell\Lambda}^{K_j} a_{\ell\Lambda}^{K_i} (g_s - g_R)$$

$$+ a_{\ell\Lambda+1}^{K_j} a_{\ell\Lambda}^{K_i} \sqrt{(\ell+\Lambda+1)(\ell-\Lambda)}\ (g_\ell - g_R)] \quad (3.42d)$$

The coefficients $a_{\ell\Lambda}^{K}$ are the normalized Nilsson amplitudes, while g_s, g_ℓ, g_K, g_R are the g-factors for the spin, orbital, intrinsic and collective motion, respectively.

The reduced E1 rates are given by

$$B(E1, I \to I') = e^2 (1 - \frac{Z}{A})^2 (\frac{\hbar}{M\omega_o})\ \frac{3}{4\pi} [\sum_{K_i = K_j, K_j \pm 1} C_{K_i}^{I} C_{K_j}^{I'}$$

$$\times \{\langle I 1 K_i K_j - K_i | I' K_j \rangle + b_{E1}^{K_i K_j} (-)^{I'+K_j'} \langle I 1 K_i - K_j - K_i | I' - K_j \rangle\}$$

$$\times G_{E1}^{K_i K_j}]^2 \quad (3.43)$$

where

$$b_{El}^{K_iK_j} G_{El} = (-)^{K_j+\frac{1}{2}+\ell'} \{ \sum_{\ell'\ell} \langle N'\ell'|r|N\ell\rangle \sqrt{\frac{2\ell+1}{2\ell'+1}} \langle \ell 1 o o|\ell' o\rangle$$

$$\times \sum_{\Lambda'\Lambda\Sigma'\Sigma} \delta_{-\Sigma',\Sigma} \; a_{\ell'\Lambda'}^{K_j} \; a_{\ell\Lambda}^{K_i} \langle \ell 1 \Lambda - K_j - K_i | \ell' - \Lambda' \rangle \} \quad (3.43a)$$

($b_{El}^{K_iK_j}$ vanishes unless $|K_j+K_i| \leq 1$)

and

$$G_{El}^{K_iK_j} = \sum_{\ell'\ell} \langle N'\ell'|r|N\ell\rangle \sqrt{\frac{2\ell+1}{2\ell'+1}} \langle \ell 1 o o|\ell' o\rangle$$

$$\times \sum_{\Lambda'\Lambda\Sigma'\Sigma} \delta_{\Sigma'\Sigma} \; a_{\ell'\Lambda}^{K_j} \; a_{\ell\Lambda}^{K_i} \langle \ell 1 \Lambda K_j - K_i | \ell' \Lambda' \rangle \quad (3.43b)$$

Expressions for the radial integrals $\langle N'\ell'|r|N\ell\rangle$ may be found in Nilsson's (1955) paper. When B(El) is to be used in eq. 3.31, the units are such that $(\frac{\hbar}{M\omega_o})$ = 1 fm.

In the case where only unmixed single-particle states are involved, the expressions are simplified by setting $C_{K_i}^{I} = C_{K_j}^{I'}$ = 1 in eq. 3.41 - 3.43.

A comparison of crossover-to-cascade branching ratios in a rotational band yields the mixing ratio, δ^2, in a cascade transition. With the use of eq.(3.31), (3.41), (3.42) and (3.42c), one can write the expression (Alexander, Boehm and Kankeleit 1964) (for an unmixed band)

$$\frac{1}{\delta^2} = \frac{T_\gamma'(M1)}{T_\gamma'(E2)} = [\frac{1}{\lambda} (\frac{E_\gamma}{E_\gamma'})^5 \frac{(I+1)(I-1+K)(I-1-K)}{2K^2(2I-1)}] - 1 \quad (3.44)$$

where

$$\lambda = \frac{T_\gamma(E2)}{[T\gamma'(E2) + T\gamma'(M1)]} \; ; \qquad (3.45)$$

and γ and γ' denote the crossover I→I-2 and cascade I→I-1 transitions, respectively. The appropriate Clebsch-Gordan coefficients have been replaced by their closed form expressions. According to the rotational model, (g_K-g_R) is a constant for all the rotational states of an unperturbed band and is given by

$$[(g_K-g_R)/Q_o]^2 = \frac{8.71\times10^{-1}\ E_\gamma'^2}{(I+1)(I-1)} \frac{1}{\delta^2} \qquad (3.46)$$

where Q_o is the intrinsic quadrupole moment in barns, and E_γ' is in MeV. The sign of (g_K-g_R) is the same as that of δ, which may be found from angular distribution measurements.

3.7 Internal Conversion

A transition between nuclear states corresponds to a change in the nuclear multipole field. The atomic electrons orbiting the nucleus are affected by this change in field and one of them may be given sufficient energy to leave the atom. Such a process is referred to as internal conversion. The energy of the conversion electron is

$$E_e = E_\gamma - E_{B.E.} \qquad (3.47)$$

where E_γ is the transition energy between two states, $E_{B.E.}$ the electron binding energy and E_e the electron energy. Several discrete electron lines appear corresponding to electrons ejected from the K, L_I, L_{II}, L_{III}, etc. shells.

The rate of gamma emission (given in the previous section) is essentially unaffected by this process. Therefore, if the decay rate via gamma emission is $T_\gamma(sec^{-1})$ and for electron emission T_e (sec^{-1}), the total rate is given by $(T_e + T_\gamma)$ sec^{-1}. The ratio of the number of electrons to the number of photons emitted is given by $\alpha = \frac{T_e}{T_\gamma}$, and is defined as the internal conversion coefficient. α is almost independent of nuclear structure but depends strongly on the energy of the transition, the charge number Z (which determines the electronic wave function) and the multipolarity of the transition.

Tables of conversion coefficients have been compiled by a number of authors; the most recent compilation is that of Hager and Seltzer (1968). Fig. 3.7 shows a plot of α_K versus transition energy for E1, E2, M1 and M2 for Z = 72 (hafnium), drawn by interpolating between the values given in this reference. (In the rare earth region, transitions of higher multipolarity are normally not expected, mainly because a given state, when it decays, usually has a large number of spins to choose from in the rotational bands below it.) It is evident from these graphs that a measurement of the conversion coefficient may identify the multipolarity of the transition.

Since one unit of angular momentum is carried away by the photon in an electromagnetic transition, a 0+→0+ transition can proceed only via the emission of a monopole conversion electron. Classically this corresponds to a simple change in radius

Figure 3.7

Theoretical K-conversion coefficients for Hf (Z=72). From Hager and Seltzer (1968). A number of experimentally measured coefficients are also indicated.

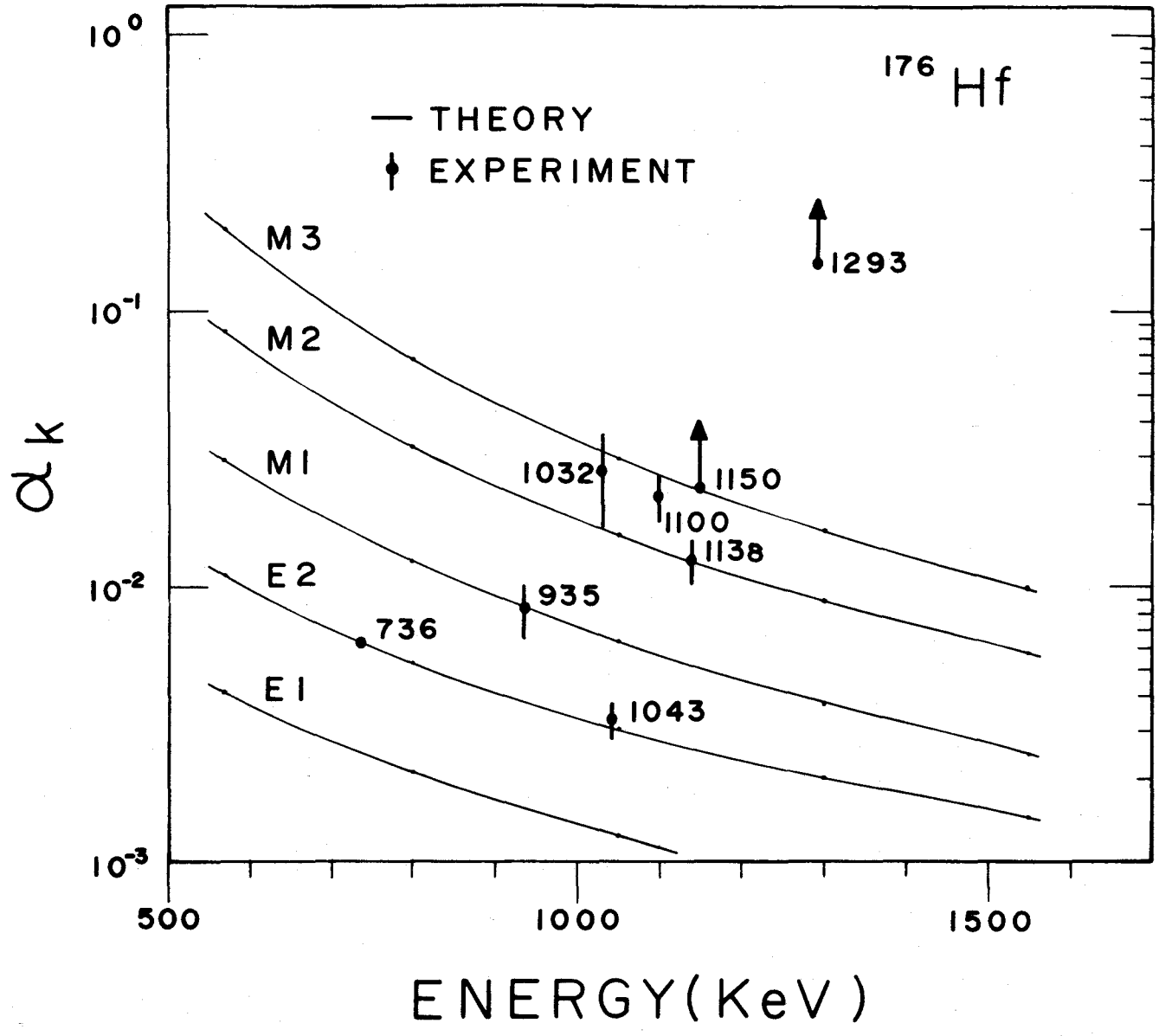
10^0
10^{-1}
10^{-2}
10^{-3}
α_K
^{176}Hf
— THEORY
EXPERIMENT
M3
M2
M1
E2
E1
1293
1032
1150
1100
1138
935
736
1043
500
1000
1500
ENERGY(KeV)

of a spherical charge distribution, a process that produces no alteration in the field outside the charge. Internal conversion is possible in such a case only because of the overlap of the wave functions of the nucleus and atomic electrons.

The theory of electric monopole transitions has been developed by Church and Weneser (1956). The monopole electron emission rate, T(EO), may be written as the product of an electronic factor, Ω, and the square of the nuclear "strength parameter", ρ, which contains the nuclear matrix elements:

$$I(EO) = \Omega\rho^2 \ . \qquad (3.48)$$

Values of Ω computed for various atomic shells have been given by Church and Weneser, who used for the electron wave functions the relativistic Dirac solutions for a uniformly changed sphere of radius $R = 1.20 \times 10^{-13} A^{1/3}$ cm.

In general, a 0'+ vibrational state decays to the 0+ ground state via a monopole transition and to the first 2+ member of the g.s.b. via an E2 transition. The type of vibrational state involved (see section 3.5) may be characterized by the branching ratio through the two paths. The ratio of the reduced EO and E2 strengths is usually defined as the parameter X:

$$X = \left(\frac{B(EO,0'+\rightarrow 0+)}{B(E2,0'+\rightarrow 2+)}\right) .$$

This may be written in the dimensionless form:

$$X = \frac{\rho^2 e^2 R_o^4}{B(E2,0'+\rightarrow 2+)} \ . \qquad (3.49)$$

By combining eq. (3.31), (3.48) and (3.49), and using $R_o = 1.2\ A^{1/3}$ fm, X may be rewritten as

$$X = 2.56 \times 10^9\ A^{4/3}\ E_\gamma^{\ 5}\ \Omega_k^{-1}\ [I_{e_k}(EO)/I_\gamma(E2)], \qquad (3.50)$$

where E_γ, the gamma transition energy, is given in MeV. In general, the $\Delta I = 0$ transitions from the rotational band members of an excited $K = 0$ state to the ground state $K = 0$ band contain EO admixtures. In this case, the general form for X, obtained by using eq. (3.32) is

$$X = 2.56 \times 10^9\ A^{4/3}\ E^5\ \Omega_k^{-1} |\langle I'200|IO\rangle|^2 [I_{e_k}(EO)/I_\gamma(E2)] \qquad (3.51a)$$

where I', the spin of the initial state, is equal to I, the spin of the final state. For ^{176}Hf, A = 176 and we obtain

$$X_{^{176}Hf} = 2.53 \times 10^{12}\ E_\gamma^5\ \Omega_k^{-1} |\langle I'200|IO\rangle|^2\ [I_e(EO)/I_\gamma(E2)]. \qquad (3.51b)$$

3.8 Intrinsic g factors of Nuclear States

It has previously been pointed out that a measurement of cross-over cascade branching ratios in a rotational band can yield (see eq. (3.45) and (3.46)) the quantity $[\frac{g_K - g_R}{Q_o}]$ which, in the rotational model, is a constant for the band. To first order, g_R and Q_o may be assumed to be the same for all bands in the nucleus; thus, the quantity g_K is a characteristic of the band. In this section we shall outline the formulas

necessary for the determination of g_K factors both from empirical magnetic moments and from calculations using the Nilsson model. The extension from one to two quasiparticle states will also be presented. In Chapter 7 these ideas will be used to characterise some of the observed states in ^{176}Hf.

The magnetic moment operator for a single particle is

$$\mu^{op} = g_s \underline{s} + g_\ell \underline{\ell} + g_R \underline{R} \qquad (3.52)$$

and the magnetic moment is defined as

$$\mu = \frac{<\underline{\mu}^{op} \cdot I>}{I+1} \quad (M = I) \qquad (3.53)$$

where $\underline{s}$, $\underline{\ell}$ and $\underline{R}$ represent the intrinsic spin, orbital, and core rotational angular momenta, respectively; the g's represent the respective g factors. For the case $I = \Omega = K$, μ may be written in the form

$$\mu = \frac{I}{I+1} \{g_s <s_z> + g_\ell <\ell_z> + g_R\} , \qquad (3.54)$$

where z refers to the nuclear symmetry axis. For any I, μ may also be formally written in the simple form

$$\mu = (g_\Omega - g_R) \frac{\Omega K}{I+1} + g_R I , \qquad (3.55)$$

or, if $I = K = \Omega$

$$\mu = \frac{I}{I+1} [\Omega g_\Omega + g_R] . \qquad (3.55a)$$

Eq. (3.54) and (3.55a) define g_Ω :

$$g_\Omega = \frac{1}{\Omega} [g_s <s_z> + g_\ell <\ell_z>] . \qquad (3.56)$$

This intrinsic g-factor may also be written in terms

of the Nilsson amplitudes as

$$g_\Omega = g_\ell + \frac{1}{2\Omega}(g_s - g_\ell) \sum_\ell (a^2_{\ell,\Omega-\frac{1}{2}} - a^2_{\ell,\Omega+\frac{1}{2}}). \qquad (3.57)$$

The g-factors for a free nucleon are

$$\left.\begin{aligned} g_\ell &= 1 \\ g_s &= 5.587 \end{aligned}\right\} \text{ for protons}$$

and (3.58)

$$\left.\begin{aligned} g_\ell &= 0 \\ g_s &= -3.826 \end{aligned}\right\} \text{ for neutrons}$$

It has been found that the use of an effective spin g-factor

$$g_{s\ \text{effective}} = 0.6\ g_{s\ \text{free}}$$

produces better agreement with experiment. By using eq. (3.55a) the quantity, g_Ω may also be determined from the measured moments of single particle states in odd A nuclei, with values of g_R obtained from neighboring even-even nuclei ($g_R \sim 0.3$)

The formalism may be extended to two quasiparticle states by writing the appropriate magnetic moment operator as

$$\underline{\mu}^{op} = g_s\underline{s}_1 + g_\ell\underline{\ell}_1 + g_s\underline{s}_2 + g_\ell\underline{\ell}_2 + g_R\underline{R}\ . \qquad (3.59)$$

In the strong-coupling model, in which the two particles 1 and 2 do not interact with each other,

$$\mu = \frac{I}{I+1}[g_s\langle s_{z_1}\rangle + g_\ell\langle \ell_{z_1}\rangle] \pm [g_s\langle s_{z_2}\rangle + g_\ell\langle \ell_{z_2}\rangle] + g_R\} \qquad (3.60)$$

for I = K (Hooke 1959). The sign is the same as that which is used in defining the K value (see section 3.5) of the two quasi-

particle states $K = |\Omega_1 \pm \Omega_2|$. Using eq. (3.56), eq. (3.60) may be rewritten in the form

$$\mu = \frac{I}{I+1} \{\Omega_1 g_\Omega \pm \Omega_2 g_{\Omega_2} + g_R\} . \qquad (3.61a)$$

By analogy with eq. (3.55a), this may be written as

$$\mu = \frac{I}{I+1} \{K g_K - g_R\}, \qquad (3.61b)$$

where

$$K g_K = \Omega_1 g_{\Omega_1} \pm \Omega_2 g_{\Omega_2} . \qquad (3.61c)$$

In the asymptotic limit, $\langle s_z \rangle$ and $\langle \ell_z \rangle$ may be replaced by Σ and Λ respectively; in that case eq. (3.60) may be rewritten as

$$\mu = \frac{I}{I+1} \{g_s(\Sigma_1 \pm \Sigma_2) + g_\ell(\Lambda_1 \pm \Lambda_2) + g_R\} . \qquad (3.62)$$

In this form it is obvious that the spin contribution vanishes in the singlet spin state since in this case $\Sigma_1 \pm \Sigma_2 = 0$. Eq. (3.62) thus becomes

$$\mu = \frac{I}{I+1} \{g_\ell(\Lambda_1 \pm \Lambda_2) + g_R\} \qquad (3.63a)$$

$$= \frac{I}{I+1} \{g_\ell K + g_R\} . \qquad (3.63b)$$

By comparison with eq. (3.61b), we readily obtain

$$g_K = g_\ell \ ; \qquad (3.64a)$$

thus

$$g_K = 1 \qquad (3.64b)$$

for two quasi-proton states

$$= 0 \qquad (3.64c)$$

for two quasi-neutron states .

Although equations (3.64) are only strictly correct for singlet states in the asymptotic limit, they apply to a good approximation for highly deformed nuclei such as ^{176}Hf for which $\eta \simeq 6$ ($\delta \sim 0.3$). For such cases, the magnetic moment and g_K are quite insensitive to the effective value chosen for g_s. For the Nilsson orbitals with which we shall be concerned in Chapter 7, the largest component corresponds to the asymptotic Nilsson state. In general, the amplitude squared of this component is greater than 90%.

When equation (3.62) is applied to the triplet spin state, for which $\Sigma_1 \pm \Sigma_2 = 1$, it yields the relation

$$\mu = \frac{I}{I+1} \{g_s + g_\ell(\Lambda_1 \pm \Lambda_2) + g_R\} . \qquad (3.65)$$

Since $(\Sigma_1+\Lambda_1) \pm (\Sigma_2+\Lambda_2) = K$,

$$\Lambda_1 \pm \Lambda_2 = K - (\Sigma_1 \pm \Sigma_2) = K-1 \qquad (3.66)$$

and one can rewrite 3.65 as

$$\mu = \frac{I}{I+1} \{g_s + g_\ell(K-1) + g_R\}. \qquad (3.67)$$

A comparison of this equation with eq. (3.61b) shows that

$$g_K = \frac{1}{K} \{g_s + g_\ell(K-1)\} . \qquad (3.68)$$

This result is also a good approximation for large but non-infinite deformation, and provides an easy method of obtaining g_K for the triplet two quasi particle states. Since the spin contributions no longer tend to cancel, as they did in the singlet state, the result is more sensitive to the value of

TABLE 3.3

SINGLE PARTICLE INTRINSIC GYROMAGNETIC RATIOS - g_Ω

	Orbital	g_Ω-calculated [a] ($g_s=g_{s\ free}$)	g_Ω-calculated [a] ($g_s=0.6\,g_{s\ free}$)	g_Ω-empirical	Ref.
Protons	5/2+[402]	1.89	1.46	1.68	1,2 μ)
				1.41	3 γ)
	7/2+[404]	0.40	0.69	0.75	1,4 μ)
				0.65	5 γ)
	9/2-[514]	1.47	1.24	1.31	6 μ)
				1.21	7 γ)
Neutrons					
	5/2-[512]	-0.62	-0.37	-0.48	8 μ)
	7/2-[514]	+0.43	+0.26	+0.15	1,2 μ)
	9/2+[624]	-0.36	-0.21	-0.26	1,9 μ)
				-0.23	9 γ)

References

1 Shirley (1971)
2 Lindgren et al. (1965)
3 Skånberg et al. (1970)
4 Reddoch and Ritter(1962)
5 Boehm et al. (1968)
6 Sauer et al. (1968)
7 Hübel et. al. (1971)
8 Olschewski and Otten (1967)
9 Hübel et al. (1969)

μ) From measurements of magnetic moments

γ) From gamma ray data

a) Calculated using eq. (3.57); the Nilsson amplitudes used correspond to a deformation of $\eta = 6$.

TABLE 3.4

g_K's FOR SOME TWO QUASI-PARTICLE STATES

Particles	K^π	g_K (Calculated) (a)		g_K Calc.
		$g_s = g_{s\ free}$	$g_{s\ eff} = 0.6\ g_{s\ free}$	(asymptotic limit)
$5/2+[402\uparrow]_p$	6^+	1.02	1.01	1.0
$7/2+[404\downarrow]_p$				
$5/2+[402\uparrow]_p$	2^-	0.95	0.97	1.0
$9/2-[514\uparrow]_p$	7^-	1.62	1.32	1.3 (b)
$7/2+[404\downarrow]_p$	8^-	1.00	1.00	1.0
$9/2-[514\uparrow]_p$				
$5/2-[512\uparrow]_n$	6^+	-0.007	-0.004	0
$7/2-[514\downarrow]_n$				
$5/2-[512\uparrow]_n$	2^-	-0.03	-0.01	0
$9/2+[624\downarrow]_n$	7^-	-0.45	-0.27	-0.33 (b)
$7/2-[514\downarrow]_n$	8^-	-0.013	-0.008	0
$9/2+[624\uparrow]_n$				

(a) Calculated using eq. (3.61c), with theoretical values of g_{Ω_1} and g_{Ω_2} obtained from table 3.3.

(b) $g_{s\ eff} = 0.6\ g_{s\ free}$ used in eq. 3.68.

g_s chosen.

The g_K factors of the two quasi particle states of interest are now calculated. The intrinsic gyromagnetic ratios, g_Ω, of the single particle states are first determined using eq. 3.57. Values of $g_{s\ effective} = g_{s\ free}$ and $0.6\ g_{s\ free}$ have been used in the calculations. The results are given in table 3.3. For comparison empirical values of g_Ω are also shown; these have been obtained from measured magnetic moments (labelled μ) and from measured values of $[(g_K - g_R)/Q_o]$ (labelled γ, see section 3.6). The g_K values of the two quasi-particle states are obtained from the calculated g_Ω values in Table 3.3, using eq. (3.61c). Values of g_K obtained in this manner are given in Table 3.4 (columns 3 and 4, corresponding to the use of $g_{s\ eff} = g_{s\ free}$ and $0.60_{s\ free}$, respectively). We note that the values for the singlet spin states are insensitive to the value of g_s used. The g_K-factors have also been calculated in the asymptotic limit, using eq. (3.64) and (3.68) for the singlet triplet spin states, respectively; the results are given in column 5 of Table 3.4.

The above discussion has concerned "pure" states. When mixed states are involved, the matrix elements of s_z and ℓ_z in eq. (3.54) and (3.60) are given by $\langle\psi|s_z|\psi\rangle$ and $\langle\psi|\ell_z|\psi\rangle$ where

$$\psi = \sum_{i=1}^{N} C_{K_i}\ \psi_o^{K_i} \quad . \qquad \text{(cf. eq.3.40)}$$

In some of the cases encountered in Chapter 7, all the K_i's are equal*, and the non-diagonal elements vanish. Under these circumstances, g_K is simply given by

$$g_K = \sum_{i=1}^{N} C_{K_i}^2 \, g_{K_i}, \tag{3.69}$$

i.e. the contribution of a component i is proportional to its admixture $C_{K_i}^2$.

3.9 Band-Mixing

In this section we shall discuss some of the effects of band-mixing without regard for the particular interaction responsible for the mixing. For simplicity we shall consider the case in which only two intrinsic (and orthogonal) states, with wave functions ψ_a and ψ_b mix.

The wave function of the mixed state may be written as

$$\psi = C_1\psi_a + C_2\psi_b \tag{3.70}$$

---

*If all the K_i's are not all the same, it becomes meaningless to define a K and g_K value for the mixed state. In such a case, however, the magnetic moment may be written as:

$$\mu = \sum_{i=1}^{N} \left[C_{K_i}^2 (g_{K_i} - g_R) \frac{K_i^2}{I+1}\right] + g_R I$$

where C_1 and C_2 are the mixing amplitudes, assumed to be normalised, i.e.

$$C_1^2 + C_2^2 = 1. \tag{3.71}$$

The appropriate Schrödinger equation may then be written as

$$H(C_1\psi_a+C_2\psi_b) = E(C_1\psi_a+C_2\psi_b). \tag{3.72}$$

This yields the secular equations

$$\begin{aligned} C_1(E_a-E) + C_2H_{ab} &= 0 \\ C_1H_{ba} + (E_b-E)C_2 &= 0 \ , \end{aligned} \tag{3.73}$$

where H_{ab} is the matrix element $\langle\psi_a|H|\psi_b\rangle$, and E_a and E_b are the unperturbed energies. For non-trivial solutions of C to exist, the determinant

$$\begin{vmatrix} (E_a-E) & H_{ab} \\ H_{ba} & (E_b-E) \end{vmatrix} = 0 \tag{3.74a}$$

or

$$E^2 - E(E_a+E_b) + E_aE_b - H_{ab}^2 = 0 \tag{3.74b}$$

where it has been assumed that $H_{ab} = H_{ba}$.

The solutions to eq. (3.74) are:

$$E \pm= \frac{1}{2}\left\{(E_a+E_b) \pm (E_a-E_b)\left[1 +\left(\frac{2H_{ab}}{E_a-E_b}\right)^2\right]^{1/2}\right\} . \tag{3.75}$$

If the notation is chosen such that $E_a>E_b$, then the + and - sign signify the higher and lower perturbed energies, respectively. The ratio of the differences of the perturbed

and unperturbed energies may be given by

$$\frac{E_+ - E_-}{E_a - E_b} = [1 + (\frac{2H_{ab}}{E_a - E_b})^2]^{1/2} . \qquad (3.76)$$

By substituting E into eq. (3.73) the amplitudes C may be obtained

$$C_{1\pm} = [1 + (\frac{E_a - E_\pm}{H_{ab}})^2]^{-1/2}$$

and (3.77)

$$C_{2\pm} = (\frac{E_\pm - E_a}{H_{ab}}) C_{1\pm}$$

and the corresponding eigenfunctions may be written as

$$\psi_\pm = C_{1\pm}\,\psi_a + C_{2\pm}\,\psi_b \quad . \qquad (3.78)$$

It may be simply shown that

$$C_{1+} = C_{2-}$$

and (3.79)

$$C_{1-} = -C_{2+}$$

so that the eigenfunctions may be written as

$$\begin{aligned} \psi_+ &= C_{2-}\psi_a - C_{1-}\psi_b \\ \psi_- &= C_{1-}\psi_a + C_{2-}\psi_b \; . \end{aligned} \qquad (3.80)$$

The ratio of the amplitudes may be defined as α_I, i.e.

$$\alpha_I = \frac{C_{1-}}{C_{2-}} = -\frac{2H_{ab}}{E_a - E_b} \Big/ \{1 + \sqrt{1 + (\frac{2H_{ab}}{E_a - E_b})^2}\} \qquad (3.81)$$

where any possible spin dependence is implicitly included.

The wavefunction may be written in the form

$$\psi_u(I) = \psi_+ = \frac{1}{(1+\alpha_I^2)^{1/2}} [\psi_a - \alpha_I \psi_b]$$
$$\psi_\ell(I) = \psi_- = \frac{1}{(1+\alpha_I^2)^{1/2}} [\psi_b + \alpha_I \psi_a], \qquad (3.82)$$

where $\psi_u(I)$ and $\psi_\ell(I)$ have been introduced to denote the upper and lower states, respectively. With this notation the E2 and M1 transition matrix elements may be written as

$$Q_{u\ell}(I'I) = \langle \psi_u(I) | O(E2) | \psi_\ell(I) \rangle$$

$$= \{\alpha_I Q_{aa} - \alpha_{I'} Q_{bb} + Q_{ab}(1-\alpha_I \alpha_{I'})\} / \sqrt{(1+\alpha_I^2)(1+\alpha_{I'}^2)} \qquad (3.83)$$

and

$$M_{u\ell}(I'I) = \langle \psi_n(I') | O(M1) | \psi_\ell(J) \rangle$$

$$= \{\alpha_I M_{aa} - \alpha_{I'} M_{bb} + M_{ab}(1-\alpha_I \alpha_{I'})\} / \sqrt{(1+\alpha_I^2)(1+\alpha_{I'}^2)} \qquad (3.84)$$

where Q and M are the E2 and M1 matrix elements respectively. When considering mixing between the ground and β-vibrational band it is convenient to rearrange (3.83) in the form :

$$Q_{u\ell}(I') = \frac{Q_{ab}\{1+(\alpha_I - \alpha_{I'})\frac{Q_{aa}}{Q_{ab}} + \alpha_{I'}[\frac{Q_{aa}-Q_{bb}}{Q_{ab}}] - \alpha_I \alpha_{I'}\}}{\sqrt{(1+\alpha_I^2)(1+\alpha_{I'}^2)}} \qquad (3.83a)$$

3.10 Coriolis interaction between "two quasi-particle states"

In the case of "single-quasi-particles", only states of K differing by unity can Coriolis couple. A similar requirement holds for "2 quasi-particle" states. In this case there are two additional conditions: (i) the two interacting states must each contain a common quasi-particle (ii) the Ω of the other two quasi-particles must differ by unity.

This may be understood by writing the Coriolis matrix element explicitly (Jones 1969):

$$\langle IK\Omega_1\Omega_2|H_{Cor}|IK'\Omega_1'\Omega_2'\rangle = -\frac{\hbar^2}{2\mathcal{J}}\sqrt{(I-K)(I+K+1)}\times$$

$$\delta_{K+1,K'}\ \langle\Omega_1\Omega_2|j_{1-}+j_{2-}|\Omega_1'\Omega_2'\rangle \qquad (3.85)$$

where Ω is the spin projection of the individual quasi-particle on the nuclear symmetry axis and j_- is defined as usual (cf. eq. 3.7) for the quasi-particle . Since each j_- is a single-particle operator, it can only connect states differing by only one particle; hence

$$\langle\Omega_1\Omega_2|j_{1-}|\Omega_1'\Omega_2'\rangle = \delta_{\Omega_2\Omega_2'}\delta_{\Omega_1+1,\Omega_1'}\ \langle\Omega_1|j_{1-}|\Omega_1'\rangle$$

$$= \delta_{\Omega_2\Omega_2'}\ \langle\Omega_1|j_{1-}|\Omega_1+1\rangle\ . \qquad (3.86)$$

To account for the occupational probabilities of the quasi-particles, the $\langle j_-\rangle$ matrix element must be multiplied by an appropriate factor. The complete Coriolis matrix element between two "2 quasi-particle states" is then given by

$$\langle IK\Omega_1\Omega_2 | H_{Cor} | IK+1\ \Omega_1+1\Omega_2 \rangle = -\frac{\hbar^2}{2\mathcal{J}} \sqrt{(I-K)(I+K+1)} \times$$

$$\langle \Omega_1 | j_{1-} | \Omega_1+1 \rangle \ (U_{\Omega_1} U_{\Omega_1+1} + V_{\Omega_1} V_{\Omega_1+1}) \qquad (3.87)$$

CHAPTER 4

EXPERIMENTAL TECHNIQUES - CONTINUOUS BEAM METHODS

4.1 Introduction

This thesis deals with a study of the levels of ^{176}Hf populated in the $^{174}Yb(\alpha,2n)^{176}Hf$ reaction. It is,therefore, concerned with the experimental techniques necessary to focus the beam on the target, to minimize the background from unwanted radiation, and to study the radiations emitted from ^{176}Hf.

Section 4.2 outlines the techniques used to focus the alpha beam, and section 4.3 deals with the experimental facilities available on the 33° beam line. The following two sections describe the techniques used in obtaining in beam spectra of gamma rays, and conversion electrons. Finally section 4.6 describes the 2 parameter γ-γ coincidence measurements. The special techniques used for studying the gamma ray spectra associated with the isomeric states will be discussed in Chapter 5.

4.2 The beam transport system

The high energy beam was provided by the McMaster Tandem van de Graaff accelerator. The negative He^- ions produced at the ion source are accelerated to the high voltage terminal,

where the electrons are stripped off by a carbon foil through which the beam passes. The resultant positive He^{++} ions are then repelled from the positive terminal voltage. If this voltage is $V \times 10^6$ volts, the final beam energy is then 3V MeV.

The beam emerging from the high energy tank of the machine is focussed by a triplet set of magnetic quadrupole "lenses". It is then defined by a set of object slits. The size and shape of the object aperture influences the size and shape of the beam spot at the target.

After passing through the object slits, the beam is analysed by a 90° magnet to select the desired beam energy, and then directed into the 33° line by the switching magnet. Two sets of quadrupole lenses are used for further focussing. In addition to the focussing elements, there are a number of magnetic steerers strategically located along the beam line in order to guide the beam along the axis of the system and to direct it on to the target. Fig. 4.1 shows the complete beam transport system.

4.3 Experimental facilities in the target area

The experimental arrangements used for electron and gamma ray measurements are schematically indicated in Fig. 4.2. For the former the beam was focussed by means of quadrupole magnets on a target located at the source position (e) of the orange beta-ray spectrometer; for the latter, the quadrupoles were adjusted to focus the beam at the point indicated (γ) beyond

Figure 4.1

Schematic plan (not to scale) of the McMaster FN Tandem Accelerator Laboratory showing the location of beam-handling elements and shielding walls (from Robertson, 1971).

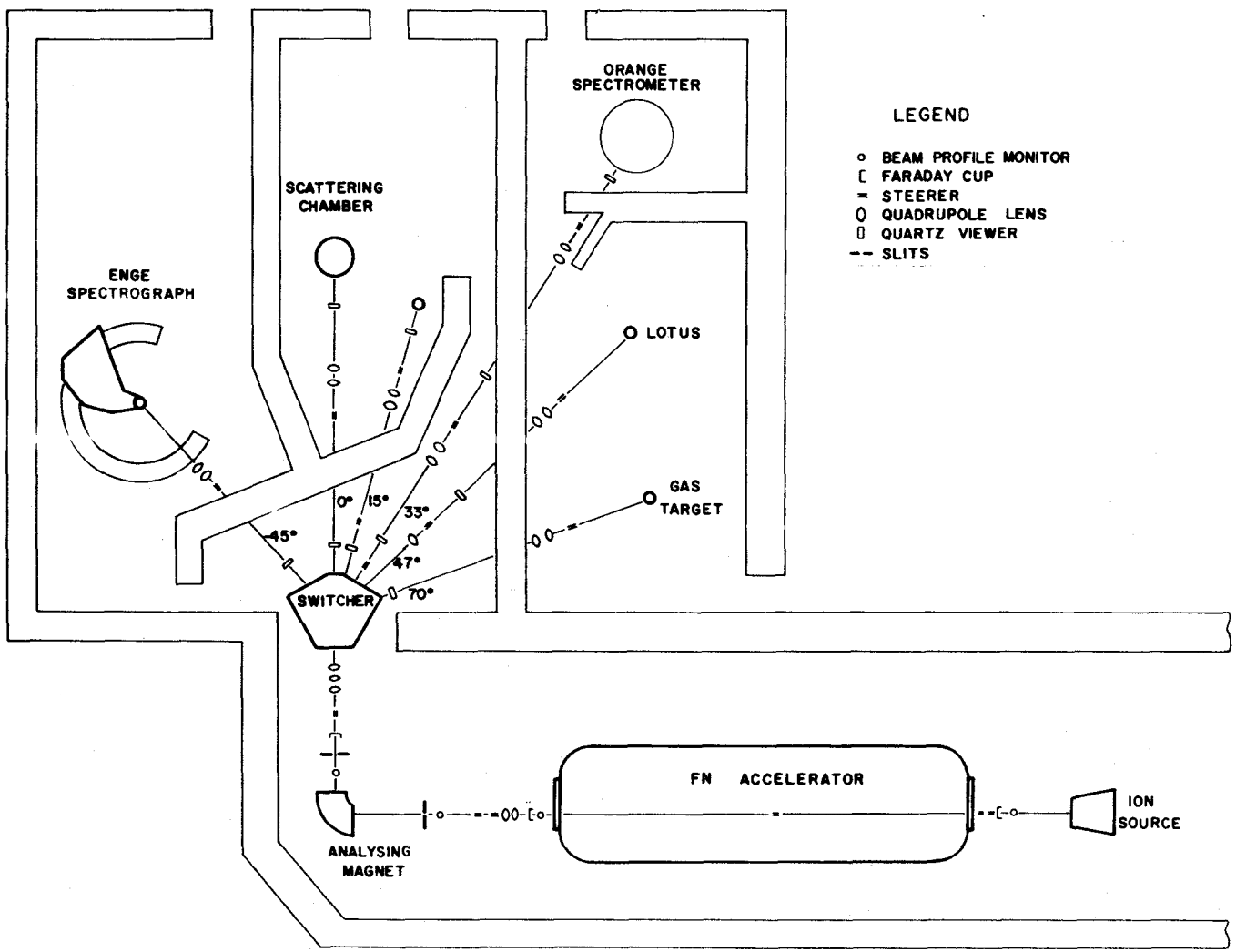
ORANGE
SPECTROMETER
LEGEND
BEAM PROFILE MONITOR
FARADAY CUP
STEERER
QUADRUPOLE LENS
QUARTZ VIEWER
SLITS
SCATTERING
CHAMBER
ENGE
SPECTROGRAPH
LOTUS
GAS
TARGET
0°
15°
33°
45°
47°
70°
SWITCHER
FN ACCELERATOR
ION
SOURCE
ANALYSING
MAGNET

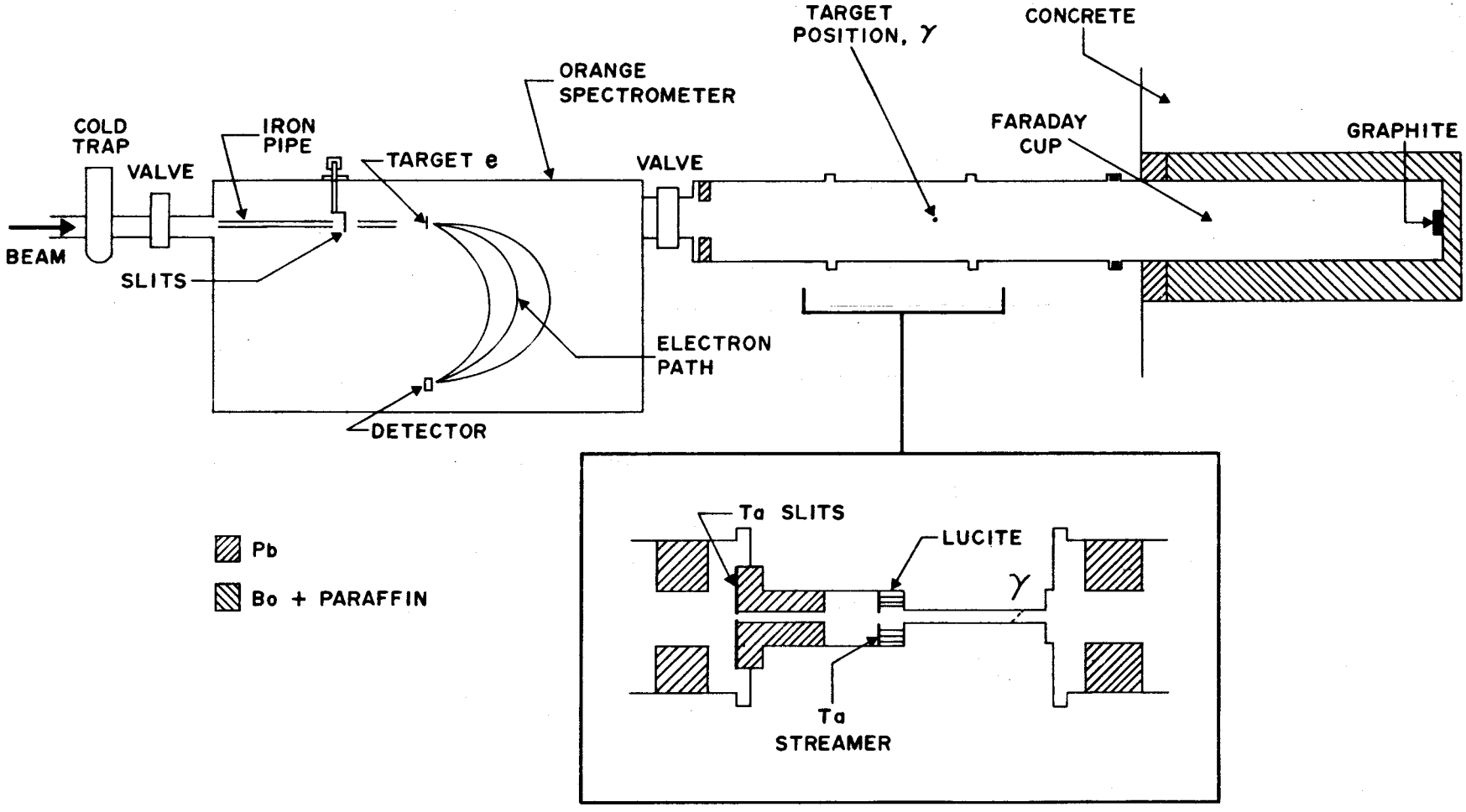

Figure 4.2

Target area of the 33° beam line. The target positions for electron and gamma ray measurements are indicated by e and γ, respectively

the orange spectrometer. In either case most of the beam passed through the thin target and was stopped in an insulated Faraday cup. The charge collected in this cup was measured by an electrometer.

Shielding against the intense gamma ray and neutron background created by the stopping of the beam on the graphite plug in the Faraday cup was provided by embedding the cup in a concrete cave and surrounding it with a layer of borax and paraffin. In addition the mouth of the cave was blocked by lead.

The special shielding problems in the Orange Spectrometer will be discussed in section E. For the moment, it will be pointed out that it was necessary to enlarge the exit aperture and to use an 8" diameter beam pipe between the spectrometer and the Faraday cup to prevent particles which had experienced multiple small angle scattering in the target from reaching the walls of the beam line before entering the shielded region. Valves were provided to isolate various sections of the assembly and a cold trap to prevent oil vapour (from the diffusion pump used in this area) from entering the rest of the beam line system.

For the gamma ray measurements, the section of the beam pipe in front of the Faraday cup was replaced by the section shown in the insert in Fig. 4.2. Before the beam reached the target in this position, it was collimated by two pairs of tantalum slits which defined a 3 × 3 mm. aperture. Each of the

four jaws was separately insulated so that the current on each could be measured. This simplified the problem of steering and focussing the beam to maximize the current passing through the aperture. Under proper conditions, less than 1% of the total current hit the jaws and the current to each jaw could be continuously monitored throughout an experiment to maintain this condition.

The detector was shielded from the gamma rays originating from these slits by means of a lead plug on which the slits were mounted. The particles scattered from these slits were prevented from hitting the target frame and the walls of the target chamber by means of a streamer consisting of a tantalum plate with a 7 mm. hole.

Details of the target chamber and holder are shown in Fig. 4.3. The target of self-supporting metal foil was mounted on a lead frame which was then held at an angle of 45° to the beam axis. With this arrangement the gamma rays from the target passed through a minimum of material in reaching the gamma ray detectors. Two typical arrangements are illustrated in Fig. 4.4

In singles runs where the detection solid angle was not of prime importance, a paraffin block was placed between the detector and the target to reduce the deleterious fast neutron flux through the detector. Additional shielding in the form of a lead doughnut around the detector was used

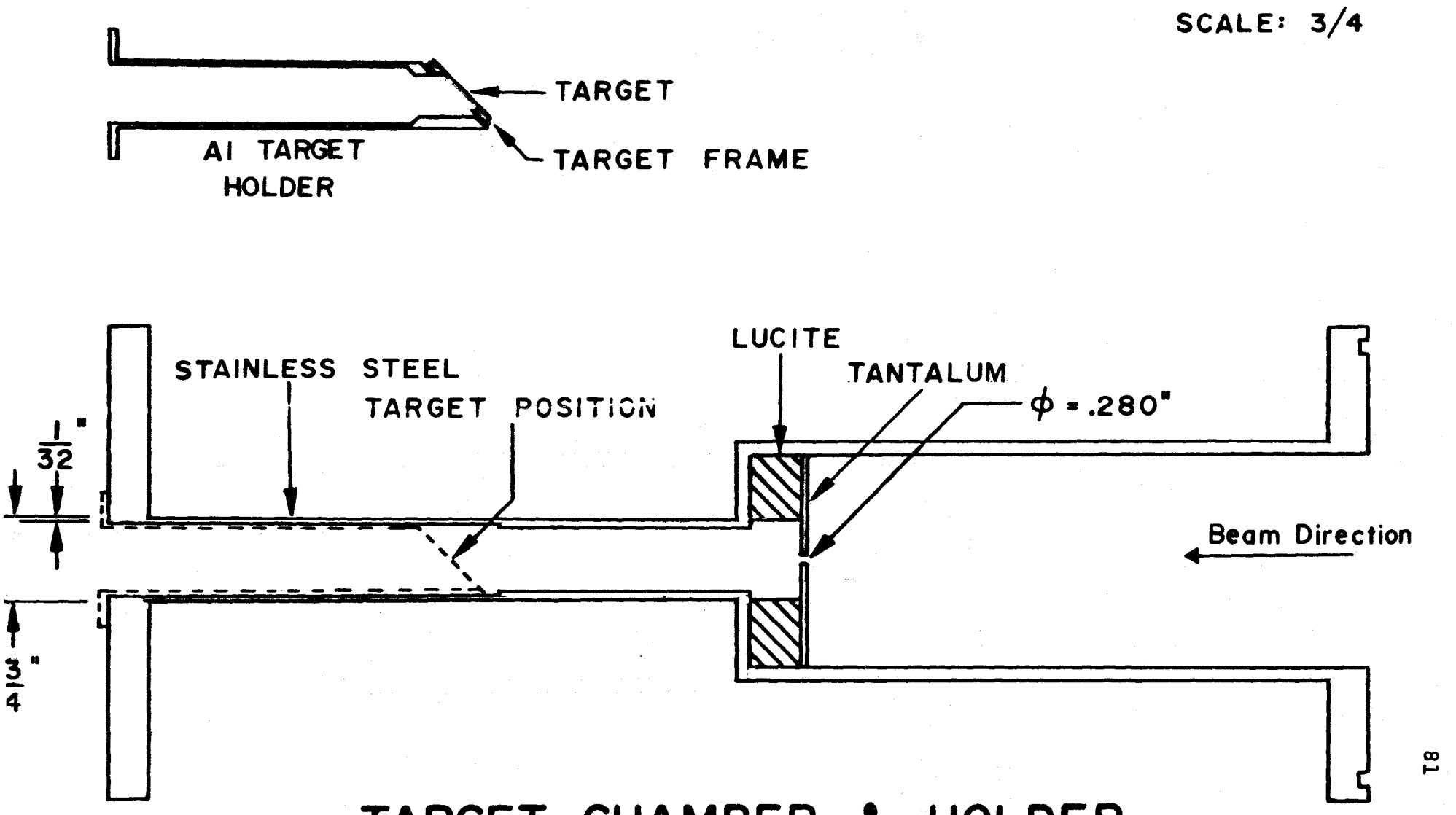

TARGET CHAMBER & HOLDER

Figure 4-3

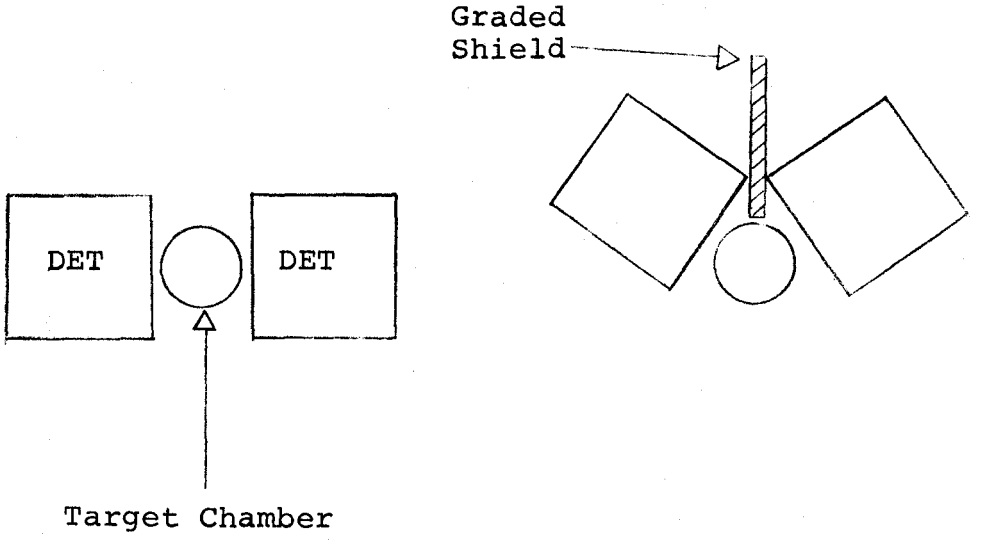

Two typical detector arrangements

Fig. 4.4

against background gamma rays. Furthermore, in order to attenuate the lead x-rays,a graded shield of copper and cadmium was wrapped around the detector. With these arrangements it was possible to record the spectrum of gamma rays originating in the target without undue interference from the background.

The targets of isotopically enriched ^{174}Yb were self-supporting metal foils of thicknesses varying from approximately 1 to 6 mgm. cm^{-2}. These were prepared by evaporating the metal from a mixture composed of equal parts by weight of Yb_2O_3 and La metal on to a tantalum plate, the lanthanum being used as a reducing agent. The Yb was then removed from the plate and cold-rolled to the desired thickness. The optimum thickness varied with the experiment. Typical values were:

$\lesssim 0.5$ mgm. cm^{-2}	low energy (< 600 keV) electron spectroscopy
~ 2-4 mgm. cm^{-2}	high energy (> 600 keV) electron spectroscopy and γ-spectroscopy
~ 5-6 mgm. cm^{-2}	γ-spectroscopy

For the gamma ray experiments it was necessary to limit the intensity of the gamma rays from the target to avoid overloading the Ge(Li) detectors. Because the ratio of the intensity of the gamma rays from the target to the intensity of the beam-induced background was proportional to the target thickness, it was generally preferable to increase the target thickness and reduce the beam current correspondingly to maintain reasonable counting rates. This trade off was limited on the one hand by the necessity of using a beam large enough to stabilize the accelerator and on the other, by the necessity of avoiding undue degradation of beam energy in the target.

The ytterbium used in making the targets had the following isotopic constitution (figures supplied by ORNL):

Yb Isotope	Atomic %
168	<0.01
170	0.05
171	0.41
172	0.99
173	2.2
174	95.8
176	0.57

4.4 Gamma ray measurements

Gamma ray measurements were performed with the following Ge(Li) detectors:

(a) 40 cc coaxial (Ortec) - 4.4 keV fwhm at 1.33 MeV

(b) 12 cc trapezoidal (Nuclear Diodes) - 3.3 keV fwhm at 1.33 MeV

(c) 38 cc coaxial (Ortec) - 3.2 keV fwhm at 1.33 MeV

(d) 50 cc coaxial (Ortec) - 3.0 keV fwhm at 1.33 MeV

(d) 0.9 cc planar (Ortec) - 0.65 keV fwhm at 122 keV.

The larger detectors are listed in the order in which they were acquired by the laboratory and accordingly show a steady improvement in quality.

The pulses from the detectors were processed by commercial preamplifiers (Ortec) and linear amplifiers (Tennelec TC 203 BLR or Ortec 452). Although these electronic units were fairly easy to use, care was taken to properly adjust the pole-zero compensation in the linear amplifiers. In addition, a baseline restorer was used to couple the signal to the analog-to-digital converter (ADC). With a shaping time of 2 μsec in the linear amplifiers, it was found that rates of up to 10^4 counts/sec. did not cause any significant deterioration in energy resolution or peak shape. Although in principle the baseline restorer need only be used with high rates, it was found to be beneficial at all times since it acted as a filter for low frequency noise (hum and microphonics). This feature was

particularly important because the long cables required to conduct the signals from the target area to the analyzing system in the control room rendered the system susceptibile to 60 cycle pick-up. It was also found that ground loop problems could be minimized by connecting all the electronics used, including preamp power and detector bias, to the same power outlet.

Two systems were available in the laboratory for data collection: (a) a Nuclear Data 3300 Analyser and (b) a PDP-9 computer with interfaced ADC's. The PDP-9 system was designed to share all or part of the 16 K memory of the 3300 analyser.

In order to conserve beam time, it was often desirable to collect data from two detectors (normally one large one and one small one) simultaneously. In these cases, the large detector was used with a graded shield (1.0 mm. Pb, 1.0 mm. Cd, 0.5 mm. Cu) to attenuate the large number of low energy transitions and X-rays. In all the singles measurements, the detectors were placed at 90° to the beam axis.

The data were analysed with the use of a CDC 6400 computer and the program 'Jagspot' written originally at Chalk River, and developed by various members of the McMaster β- and γ-ray spectroscopy group. (A detailed account of this program has been written by Brian Cook). Briefly, the programme performed a least squares fitting routine to a peak shape which is the convolution of an exponential (decreasing towards lower energy)

and a Gaussian, and which can be mathematically expressed as follows:

$$I(x) = \alpha + \beta x + \sum_{y=1}^{N} \gamma_i \int_{-\infty}^{x_{pj}} e^{\varepsilon(y-x_{pj})} e^{-\delta(x_{pj}-y)^2} dy$$

where

x = channel number

$I(x)$ = counts in channel x

N = number of peaks in window ($N \leq 6$)

$\alpha+\beta x$ = linear background term

γ_j = intensity of the Gaussian located at x_{pj}

ε = constant determining the exponential fall-off of Gaussian intensities

x_{pj} = peak position of Gaussian in peak j.

For certain detectors, e.g. the 0.9 cc. detector described above, the peak shapes are almost pure Gaussians, and the programme may be made to fit peaks of such a form. The variation of the shape parameters as a function of energy may be determined from the fits to strong isolated single peaks. The fitting of weaker peaks may then be facilitated by fixing these parameters.

The energies and intensities of the lower energy ($\lesssim$ 500 keV) lines were determined by using the 0.9 cc. detector, whose excellent resolution made it possible to resolve many closely spaced multiplets. For higher energies, the larger detectors were used.

The energies of the stronger lines were first determined by comparing them with gamma rays from standard sources (see Table 4.1). This was done by accumulating a singles in-beam spectrum in the presence of the radiation from a number of radioactive sources, emitting gamma rays of known energy. The energies determined in this way were free from the effects of any possible baseline drift or gain change and were then used as internal standards against which the weaker lines could be measured.

The energies and peak positions of the standard lines were used to establish a third order polynomial relating energy to channel number, which could then be used to determine the energies of unknown lines.

To measure the relative intensities of the gamma rays it was necessary to determine the relative efficiency of each detector as a function of energy. This was performed by using a set of absolutely calibrated IEAE sources. In order to obtain additional calibration points, a number of other sources (^{182}Ta, ^{152}Eu, ^{160}Tb) with lines of well known relative intensities were used.

It was important that all the calibration sources be placed at the same location as the beam spot on the target. Since it was not possible to place these sources in the regular target chamber, a dummy target chamber was constructed with a milled slot in the stainless steel tubing to permit the

Table 4.1

Energy Calibration Standards

Energy	Source	Reference
100.104±0.002	^{182}Ta	a
122.03 ± .03	^{57}Co	c
152.435±0.003	^{182}Ta	a
179.393±0.004	^{182}Ta	a
222.109±0.005	^{182}Ta	a
279.191±0.008	^{203}Hg	b
320.080±0.013	^{51}Cr	b
411.795±0.009	^{198}Au	b
511.006±0.002	$m_o c^2$	
661.615±0.076	^{137}Cs	b
834.81 ±0.03	^{54}Mn	b
898.04 ±0.04	^{88}Y	b
1173.23 ±0.04	^{60}Co	b
1274.55 ±0.04	^{22}Na	b
1332.505±0.04	^{60}Co	c
1836.13 ±0.04	^{88}Y	b
2753.92 ±0.12	^{24}Na	b

a. Lederer, et al. Table of Isotopes (1968)

b. Marion (1968)

c. Bernthal (1969)

calibration sources to be properly located.

The excitation functions of individual lines were determined by recording the entire spectra at alpha beam energies of 18.0, 19.5, 21.0, 22.5 and 24.0 MeV. The detector geometry was kept fixed so that a plot of the area of a particular line, relative to that of the 2 → 0 ground state transition, would yield a relative excitation curve, without any corrections for detector efficiency. In a separate experiment, a beam energy of 16.3 MeV was used to identify gamma rays excited by the other reactions at beam energies below the $(\alpha,2n)$ threshold of 16.34 MeV.

4.5 Conversion electron measurements

The following section outlines the principle of measuring particle momenta with magnetic spectrometers, the procedures used for measuring electron spectra with the orange β-ray spectrometer, and a brief description of the spectrometer itself. A more detailed discussion on the spectrometer and its magnet control system is in a separate manual written by the author.

A charged particle moving in a magnetic field is deflected in a circular path according to the relation

$$B\rho = p/q$$

where p = momentum of the particle

q = charge of the particle

B = component of magnetic induction perpendicular to the path

ρ = radius of curvature.

The product $B\rho$ is called the magnetic rigidity of the particle. The measurement of charged particle momenta with magnetic spectrometers is based on this simple equation. In many instruments, e.g. the orange spectrometer, ρ is effectively fixed, so that particles of different momenta are focussed by changing the magnetic field B.

The orange spectrometer, as first developed by O. B. Nielsen et al. (1955), consisted of six 1/r sector type spectrometers of the Kofoed-Hansen (1950) design arranged symmetrically around a common source-focus axis (see fig. 4.5). The McMaster instrument was patterned after the 7-gap version built at Chalk River by Jim Geiger (1965). In this instrument electrons from the common target, or radioactive source, are focussed by the seven gaps onto a common cylindrical plastic detector of 1 cm. diameter. In practice, the Rawson probe occupies one of the gaps, leaving six for data collection. The focussed electrons enter the detector through an annular ring whose width may be varied from 1 to 5 mm. The momentum resolution of the spectrometer depends on the width of this ring, being about 1% with a 3 mm. annulus and 0.5% with a 1 mm. annulus.

The magnetic field for focussing the electrons is held constant (within 5 parts in 10^5) by continuously measu-

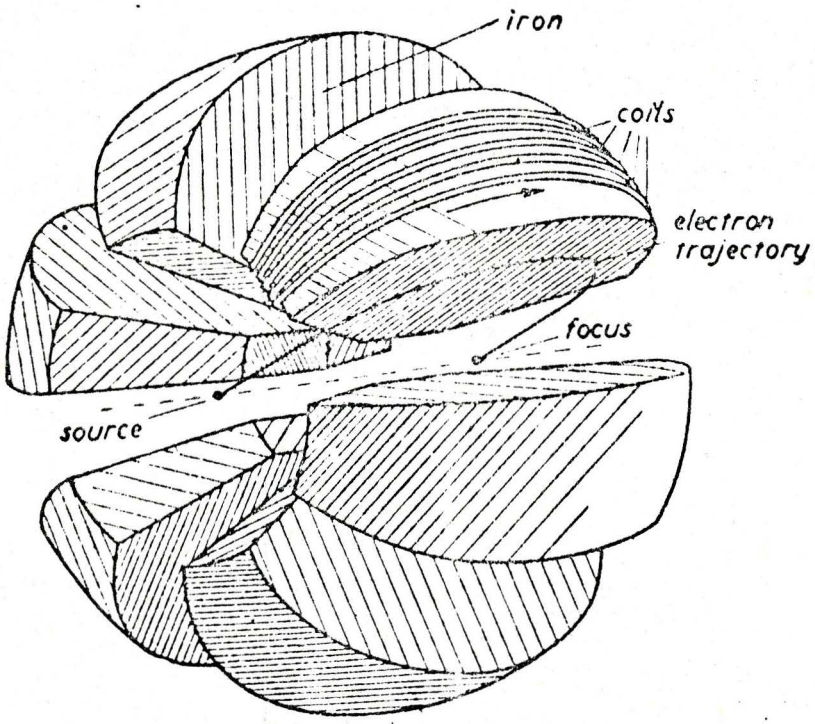

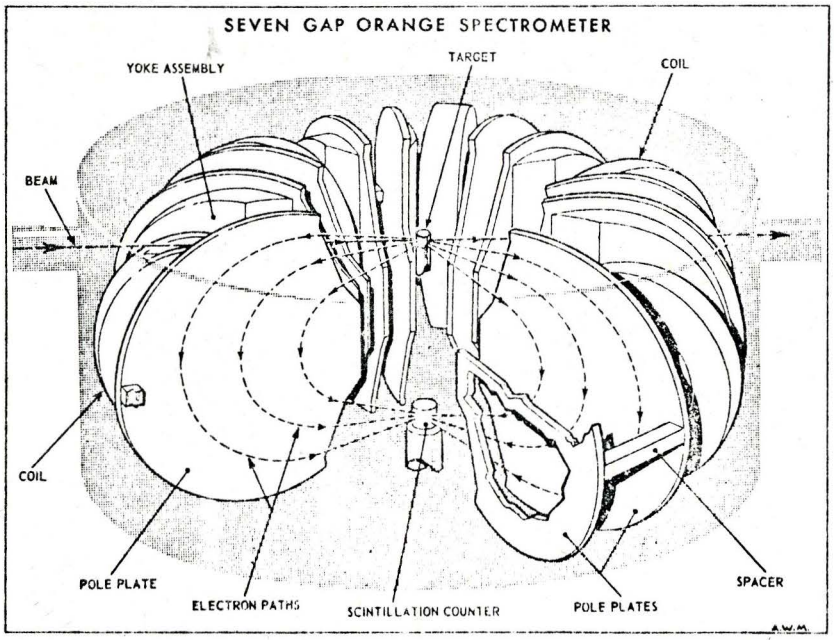

Figure 4.5

Schematic illustration of the "Orange" beta ray spectrometer. (From Geiger 1965).

suring it with a Rawson probe and by controlling the magnet current through a feed-back network.

A number of problems arose in attempting to use this instrument for in-beam measurements. The most recalcitrant of these was the background of gammas and, to some extent, neutrons detected by the plastic scintillator. This undesired radiation originated, as has been mentioned before, from small angle scattering of the incident beam by the target onto the beam line at the exit side of the spectrometer. To reduce this effect, the beam exit aperture of the spectrometer was enlarged to 4" (from 2") and the exit beam pipe diameter increased to 8" (from the normal 2"). In addition, to attenuate the gamma ray flux reaching the electron detector a lead shield was arranged around the detector and another, with an appropriate aperture for electron transmission, placed in the equatorial plane of each gap. These were covered with aluminum to prevent electrons from being scattered by the lead and to attenuate the lead x-rays excited by stray gamma radiation. Anti-scattering baffles were also arranged in each gap to prevent low energy electrons from spiralling (in loops of small diameter) onto the detector. A cross-section of the spectrometer (fig. 4.6) shows the arrangement of these various shields.

As a further means of reducing the background, the size of the plastic detector was reduced to a cylinder 1 cm. in

Figure 4.6

Cross-section of the McMaster "orange" β-ray spectrometer, showing the location of shielding material.

ORANGE SPECTROMETER

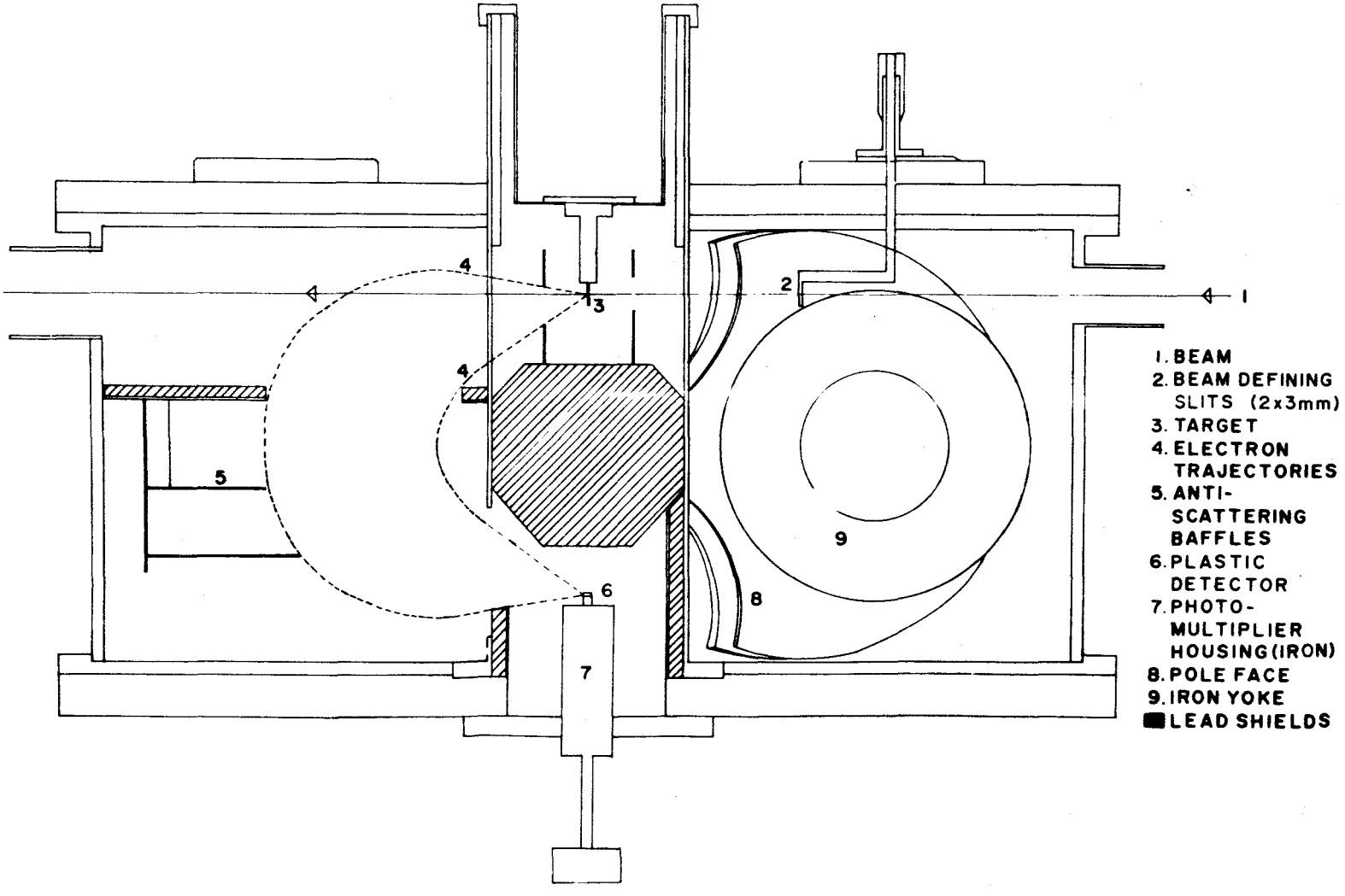

1. BEAM
2. BEAM DEFINING SLITS (2x3mm)
3. TARGET
4. ELECTRON TRAJECTORIES
5. ANTI-SCATTERING BAFFLES
6. PLASTIC DETECTOR
7. PHOTO-MULTIPLIER HOUSING (IRON)
8. POLE FACE
9. IRON YOKE

■ LEAD SHIELDS

diameter and 0.5 cm in height, which gave the minimum possible volume consistent with good electron detection efficiency. A typical spectrum obtained with this detector is shown in fig. 4.7, where one can distinguish the monoenergetic electron peak, the relatively flat background below this peak which arises from electrons backscattered from the detector, and a sharply rising low energy tail created by low energy background radiation. For 100% detection efficiency the whole of the flat background should be accepted; this means that the low energy tail can only be rejected at the expense of losing some detection efficiency. The continuous beta spectrum from a ^{212}Pb source (ThB and daughter) was used to produce an electron spectrum free from undesired background, in order to determine the fraction of the monoenergetic electron group that was actually detected. Since in this work we were interested only in conversion lines of energy greater than 700 keV, it was possible to choose a fixed discriminator* setting of 370 keV and determine this fraction at various electron energies. The resulting efficiency curve is shown in Fig. 4.8.

---

*If we had been interested in focussing low energy electrons, it would have been advantageous, for a good true/background ratio, to set the discriminator at a point where the low energy background was mostly removed, even though this meant a serious loss in detection efficiency. As the energy of the focussed electrons is increased during a momentum scan, this discriminator setting can be varied, thus eliminating the low energy background without seriously reducing the efficiency.

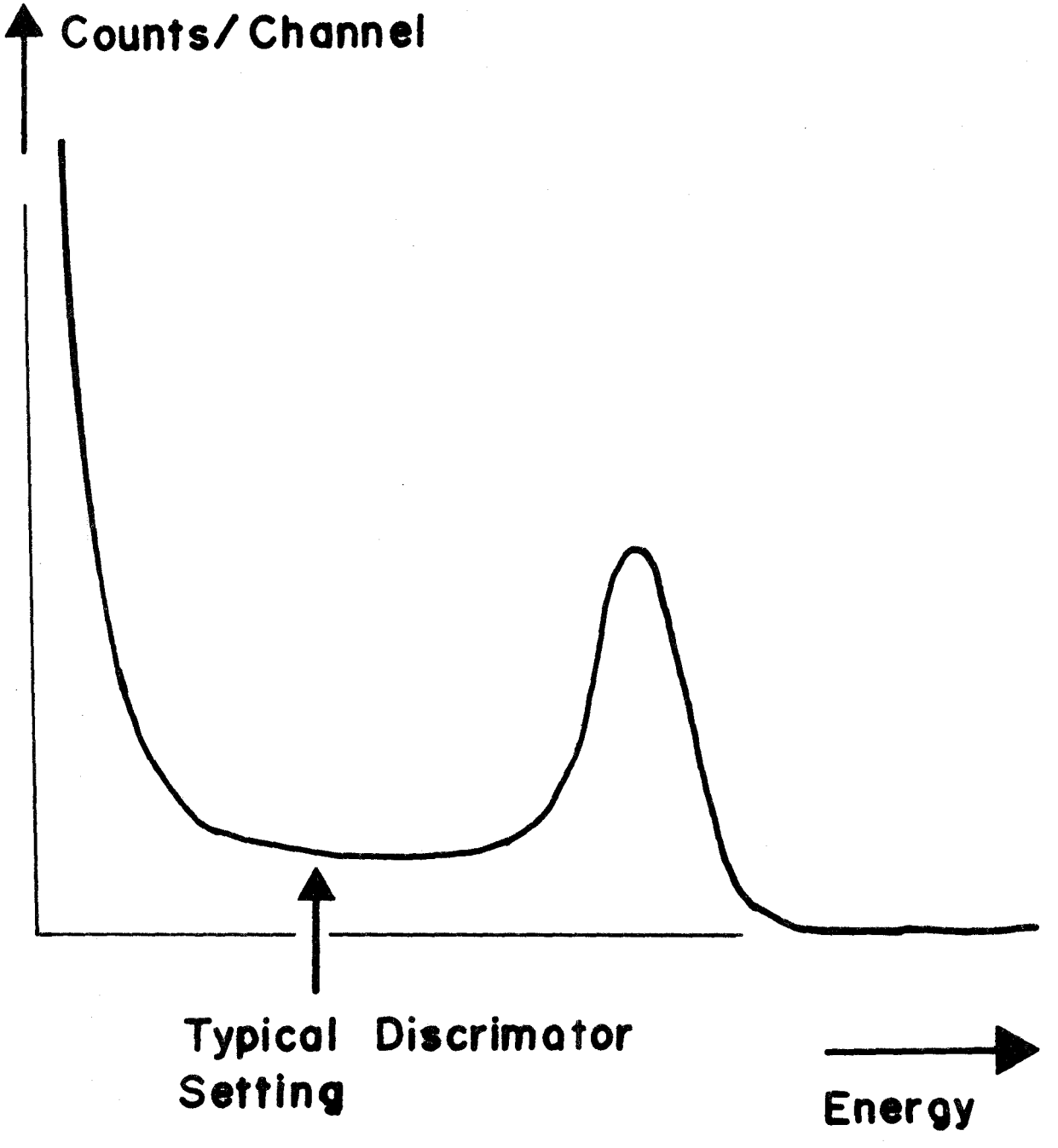

Figure 4.7

Typical spectrum obtained with the plastic scintillation detector of the "orange" electron spectrometer

Figure 4.8

Electron detection relative efficiency curve. The discriminator was set to accept all pulses of energy greater than 370 keV.

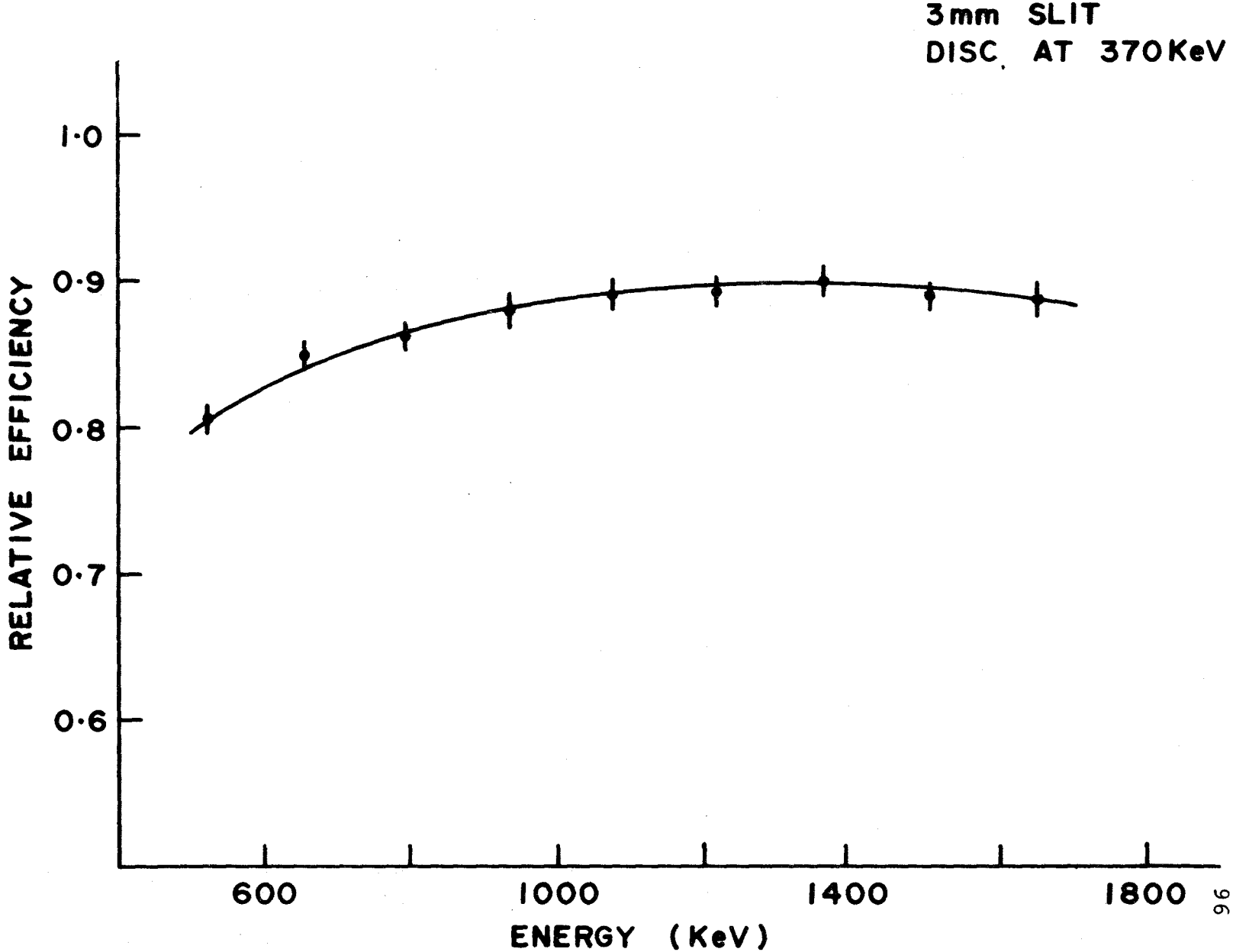
3mm SLIT
DISC. AT 370KeV
RELATIVE EFFICIENCY
1·0
0·9
0·8
0·7
0·6
600
1000
1400
1800
ENERGY (KeV)
96

Because a small detector was used, it was necessary to limit the source (or target) dimensions. This was done by installing a set of 2 mm. × 3 mm. slits 24 cm. upstream from the target. The defining slits also served the important function of monitoring the position of the beam spot on the target during the course of the experiment.

To obtain the spectrum of electrons from the target, it was necessary to record the number of electrons for a fixed number of nuclear reactions in the target as a function of electron momentum. If the target had been absolutely uniform in thickness and its condition constant in time, one could have used the charge collected in the Faraday cup as a good measure of the number of nuclear reactions. Because neither of these target conditions was satisfied, a more reliable measure of the number of reactions was provided by the number of alpha particles elastically scattered at a fixed angle to the beam. The number of such scattered particles should be strictly proportional to the number of α particles interacting with the target. To make this measurement, a disc-shaped plastic scintillator, 1 cm. in diameter, was mounted on the surface of a 7764 RCA photomultiplier and located on a flange at the spectrometer wall, at an angle of 52° to the beam axis. The number of α particles recorded in the full energy peak of the spectrum during

the experiment is proportional to the number of nuclear reactions. Although a solid state detector would have had better resolution, these plastic detectors were adequate for our purpose and had the great advantage that they were insensitive to continued exposure to a high neutron field.

In practice both the elastically scattered alpha particles and the charge collected in the Faraday cup were recorded at each momentum setting. It was found that the ratio of these two quantities was a good indicator of the target condition.

If the beam was intermittent, the electron count contained an abnormally high background contribution. Since in these conditions the time required to record the preset number of elastically scattered alpha particles was also abnormally high, it was found useful to record the counting time to provide a criterion for rejecting untrustworthy data.

The instrument was fully automated to record at each momentum setting ($B\rho$) the number of elastically scattered alphas, the number of micro-coulombs collected in the Faraday cup, the elapsed counting time, and the number of focussed electrons. The arrangement whereby this was done is schematically indicated in fig. 4.9 and 4.10. After a preset number of alphas had been collected in the master scalar, counting was stopped, and the $B\rho$ value and the contents of the scalers were printed out on the teletype. When the printing was finished, the magnetic field was increased, a four second pause was

Figure 4.9

Schematic of the electronics used for an automatic scan of an electron spectrum with the "orange" spectrometer.

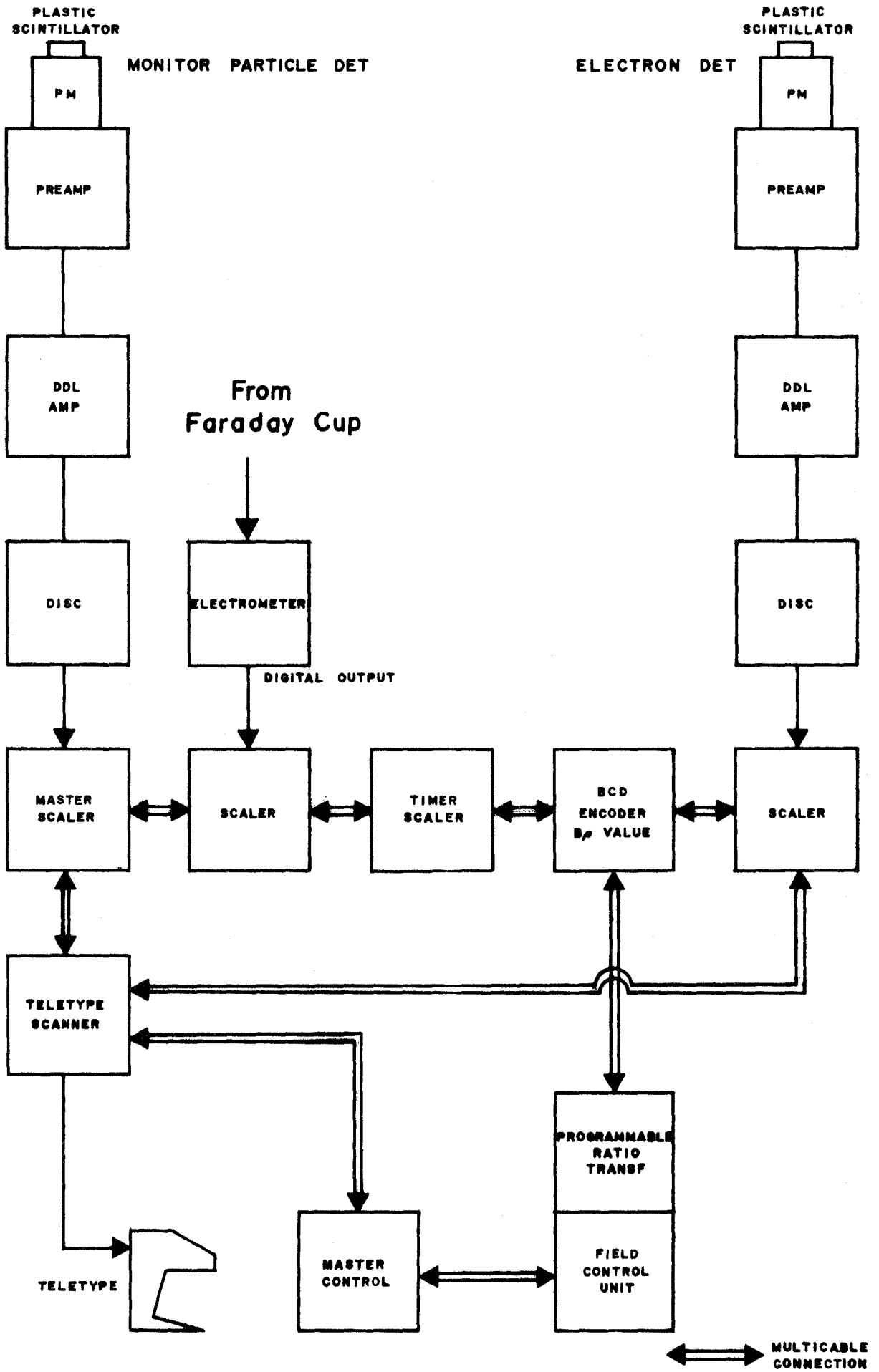
PLASTIC SCINTILLATOR
MONITOR PARTICLE DET
PM
PREAMP
DDL AMP
DISC
From Faraday Cup
ELECTROMETER
DIGITAL OUTPUT
PLASTIC SCINTILLATOR
ELECTRON DET
PM
PREAMP
DDL AMP
DISC
MASTER SCALER
SCALER
TIMER SCALER
BCD ENCODER Bρ VALUE
SCALER
TELETYPE SCANNER
PROGRAMMABLE RATIO TRANSF
TELETYPE
MASTER CONTROL
FIELD CONTROL UNIT
MULTICABLE CONNECTION

Figure 4.10

Block diagram illustrating the automatic control of the magnetic field in the "orange" spectrometer. The field is altered by using the stepping switches to change the setting of a programmable ratio transformer (see fig. 4.9). After the field is changed, there is a $\sim$ 4 sec. pause (for stabilization) before counting is resumed.

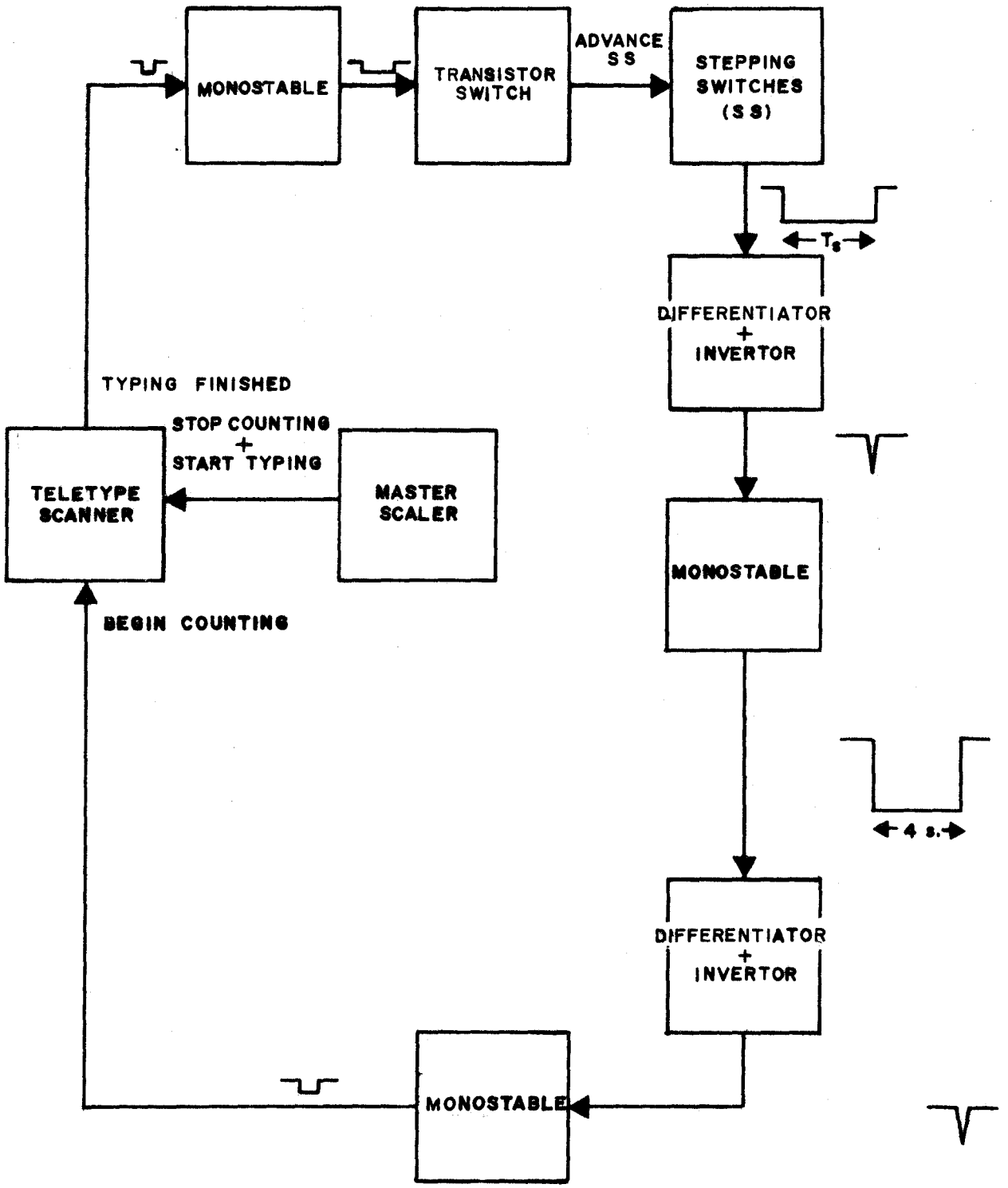
MONOSTABLE
TRANSISTOR SWITCH
ADVANCE S S
STEPPING SWITCHES (S S)
T_s
DIFFERENTIATOR + INVERTOR
MONOSTABLE
4 s.
DIFFERENTIATOR + INVERTOR
MONOSTABLE
TYPING FINISHED
STOP COUNTING + START TYPING
TELETYPE SCANNER
MASTER SCALER
BEGIN COUNTING

allowed for field stabilization, the scalers were reset and the counting cycle resumed. There was also provision for repeated scans of the spectrum across a predetermined range. Further details are given in a report prepared by the author.

A preliminary calibration of the spectrometer was performed by scanning the spectrum of a ^{198}Au source to determine the field required to focus the K-conversion line of the 411.8 keV transition. The digital readout corresponding to this field was then adjusted to read 2222.5 to correspond to the accepted $B\rho$ value for this line. With this adjustment, the magnetic field readout gave $B\rho$ values directly, to a good approximation. Small corrections to this linear calibration were applied by using internal standards whose energies were determined from gamma ray measurements.

The intensity of a conversion line was obtained either by simply measuring its height (on a linear plot) or by determining the area of the entire peak and then dividing this area by its $B\rho$ value, to correct for the fact that the line width of the spectrometer is proportional to $B\rho$. The areas were found by using the computer programme JAGSPOT referred to in section 4.4. The two methods were found to agree satisfactorily. A small correction for detection efficiency (fig. 4.8) was then applied to obtain relative conversion line intensities.

4.6 γ-γ coincidences with Ge(Li) detectors

For complicated spectra, such as those obtained with the (α,2n) reactions in medium or heavy targets, γ-γ coincidence measurements employing Ge(Li) detectors are essential to reduce the complexity of the spectra and to make possible an understanding of the level scheme. The performance of a γ-γ coincidence spectrometer depends ultimately on the timing properties of Ge(Li) detectors, which are discussed in the next section.

(i) Timing with a Ge(Li) detector

Whereas in a scintillation counter all the pulses have approximately the same rise time, in a germanium detector the rise time is a complicated function of the position in the crystal at which the gamma ray is detected. This means that the usual cross-over technique, which produces a cross-over point independent of the pulse height for pulses of identical shape, does not provide a good time marker for Ge(Li) detectors. For these detectors leading-edge timing has been found to be preferable (Graham et al. 1966; Ewan et al. 1966); however, it is subject to the usual problem of "walk", i.e. the variation with pulse amplitude of the time at which the leading edge discriminator fires, which is a characteristic of this method. An ingeneous combination of the two methods has been developed by Chase (1968) which compensates for variations in both pulse amplitude and rise-time and is referred to, quite appropriately,

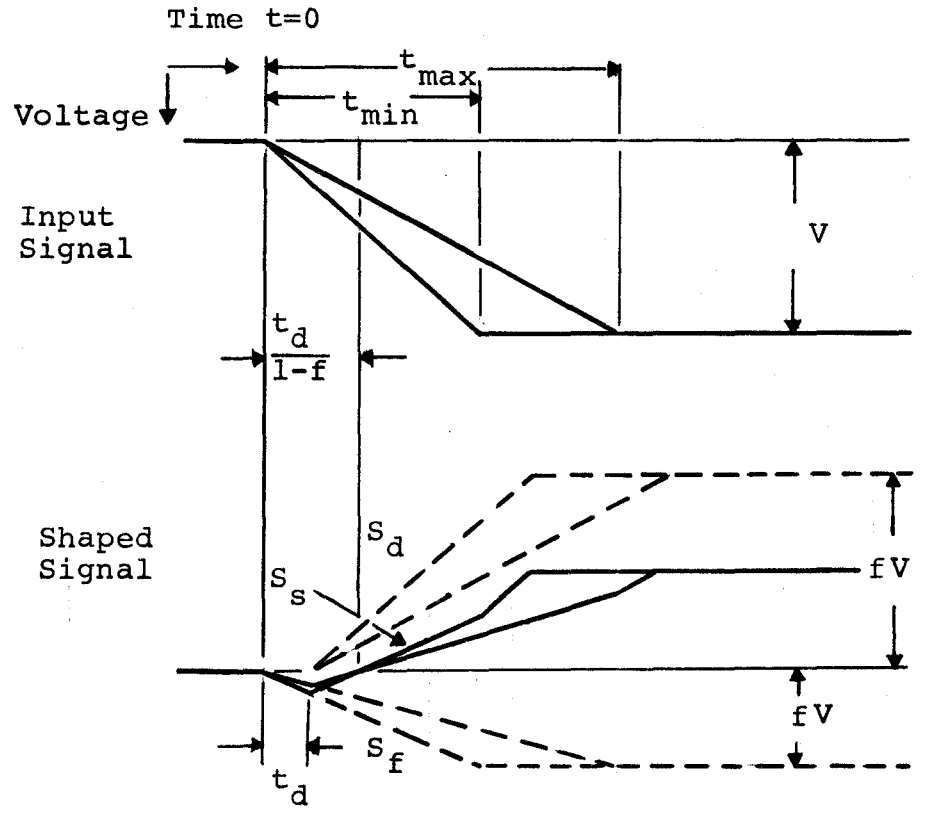

(Diagram reproduced from Ortec Application Note AN 31)

Definitions: f = attenuation fraction of input signal

r = rise-time (slope) of signal

t_d = delay time

$S_f = -frt$ attenuated signal

$S_d = r(t-t_d)$ delayed signal

$S_s = S_f + S_d$ shaped signal

$= r[t(1-f)-t_d]$

$= 0$ when $t = \frac{t_d}{1-f}$; independent of r and V.

Figure 4.11

as the amplitude and rise time compensation method (ARC). In this method, which is actually a variation of the constant fraction technique (Gedke and McDonald, 1967), a fraction of the pulse, s_f, is added to an inverted, appropriately delayed and unattenuated signal, s_d, so that a cross-over point is produced which is independent of both rise-time and amplitude. This is illustrated in Fig. 4.11. In the γ-γ coincidence experiments described below, this method of timing was used.

(ii) Description of γ-γ coincidence measurements

A block diagram of the γ-γ coincidence system employed is shown in Fig. 4.12. Timing pulses from each detector were produced by the ARC method described above, with the use of a timing amplifier (Ortec 454) and a constant fraction timing discriminator (Ortec 453), and fed to the TAC. The time distribution obtained from the latter in the course of the experiment is shown in Fig. 4.13; the width of the peak in this figure provides a direct measure of the system resolution. It is seen that most of the true coincidence events are within an interval defined by the points at 1/15 of the maximum height in the TAC spectrum. The tails in the distribution are due mainly to low energy gamma rays, which were not in the region of interest. 72 ns time gates were set on the peak and the flat portion of the distribution respectively. These defined

Figure 4.12

Schematic arrangement for a γ-γ coincidence experiment.

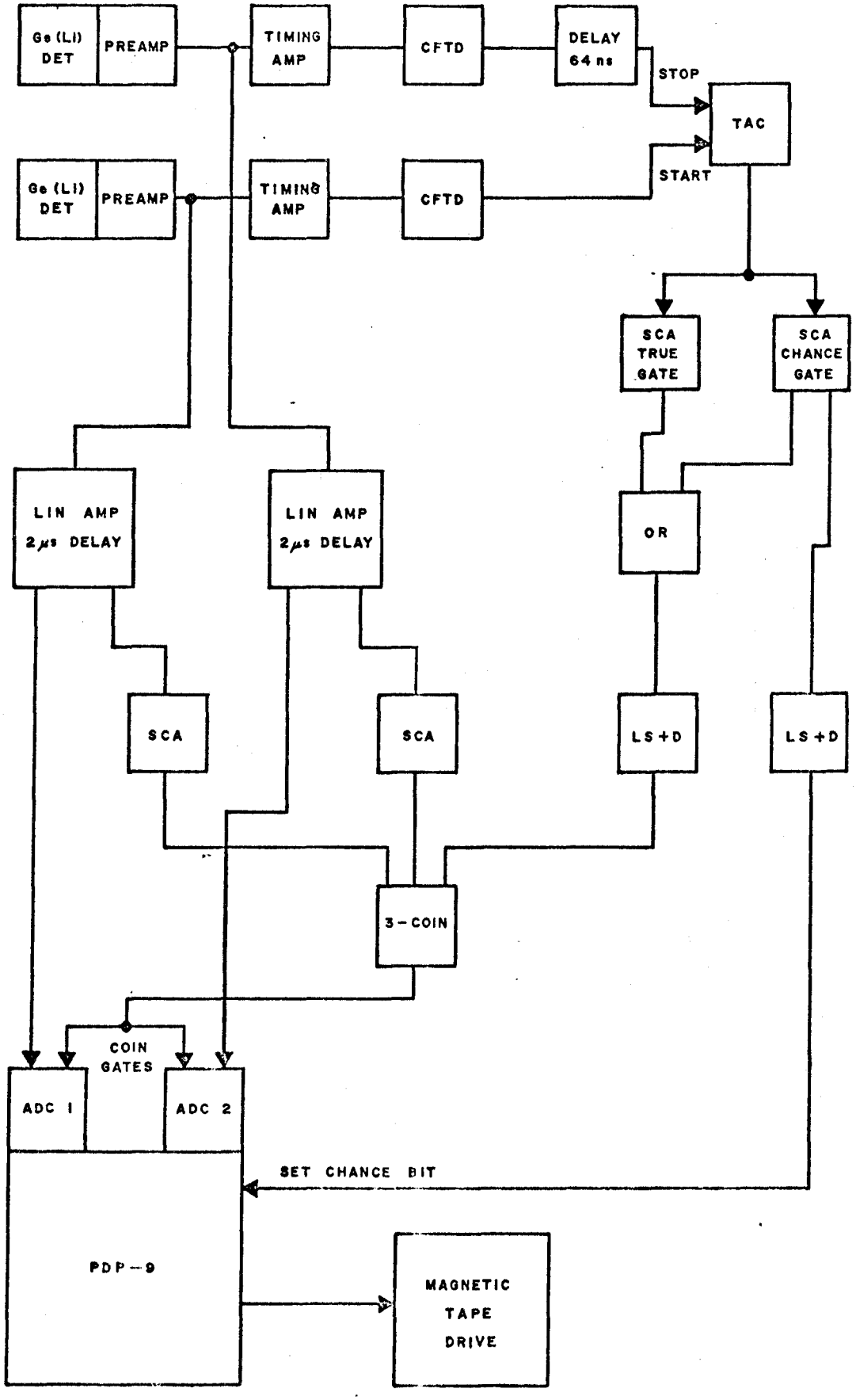
Ge (Li) DET
PREAMP
TIMING AMP
CFTD
DELAY 64 ns
STOP
TAC
START
Ge (Li) DET
PREAMP
TIMING AMP
CFTD
SCA TRUE GATE
SCA CHANCE GATE
LIN AMP 2μs DELAY
LIN AMP 2μs DELAY
OR
SCA
SCA
LS+D
LS+D
3-COIN
COIN GATES
ADC 1
ADC 2
SET CHANCE BIT
PDP-9
MAGNETIC TAPE DRIVE

Figure 4.13

Time distribution for γ-γ coincidence experiment. Taken with a 38 cc and a 50 cc. coaxial Ge(Li) detector.

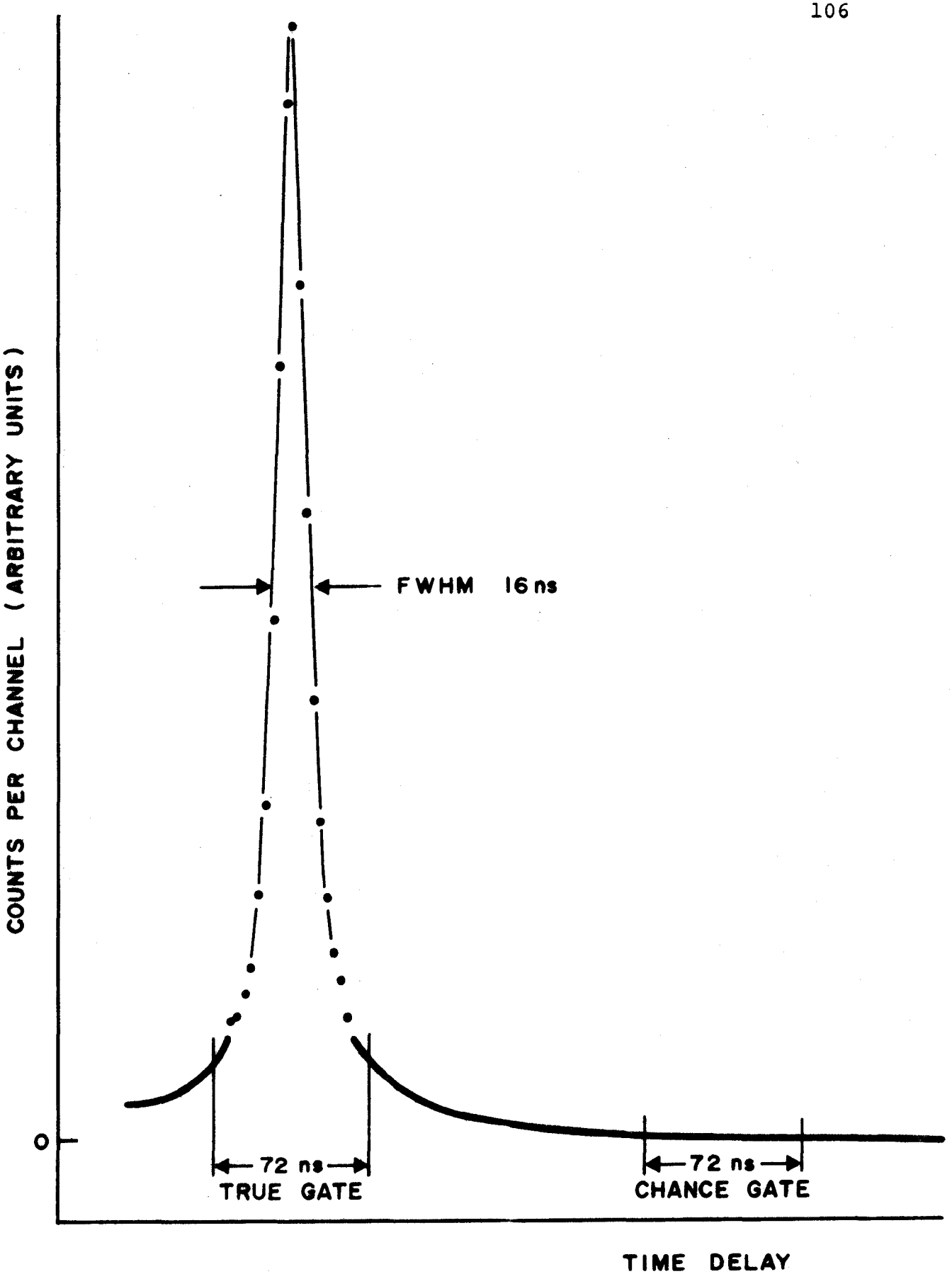
COUNTS PER CHANNEL (ARBITRARY UNITS)
FWHM 16 ns
0
72 ns
TRUE GATE
72 ns
CHANCE GATE
TIME DELAY

the system resolution and made it possible to record both true and chance events simultaneously. By scaling the outputs of the two SCA's used for the gates, both the true and change rates were directly measured.

The linear pulses from the detector were shaped in the usual manner and digitized by two ADC's (conversion gain (2048) interfaced to the PDP-9 computer. The digital output was then stored as pairs of 18 bit words in two alternating buffers, each 1000 words long, and dumped on tape when a buffer was full. The structure of a word pair is indicated in fig. 4.14.

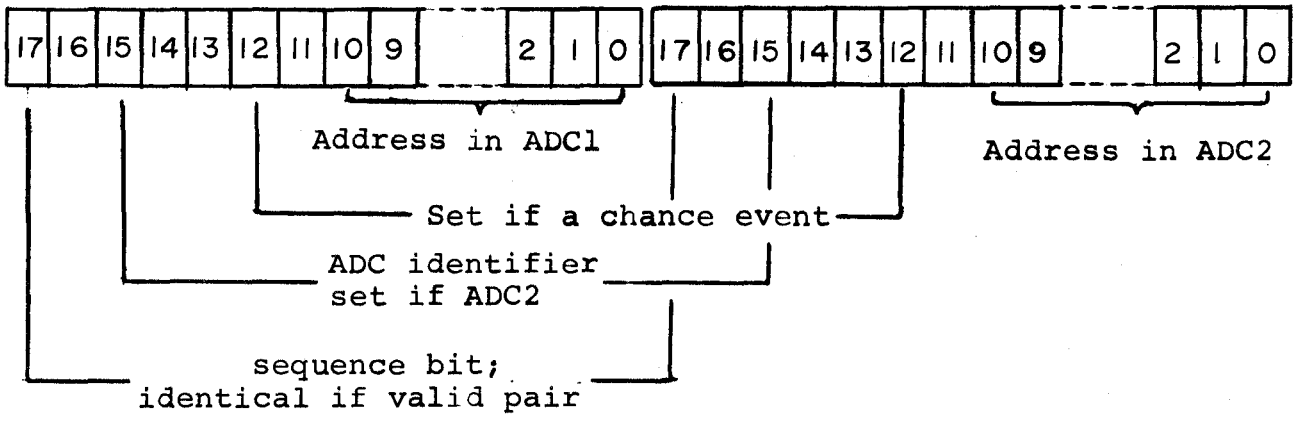

Fig. 4.14

Since the data in each record block on magnetic tape consisted of contigious words, it was important to ensure that the proper pair of words for a coincident pair was selected in the analysis. The sequence bits (#17) and the ADC identifier

bits (#15) were used for this purpose. In a proper pair, bits #17 read the same while bits #15 read 0 for the first word and 1 for the second. Bits #17 also alternated between 0 and 1 on successive pairs of words. This coding made it possible to reject a word if the other member of the pair had not been recorded, as might happen if the height of the analog signal to one ADC was either below its lower threshold or above its upper threshold. To minimize the number of such events, the windows of the two SCA's in the linear channels were set to correspond to the lower and upper thresholds of their respective ADC's and a triple coincidence was required between the analog pulses and the time pulse before the linear gates of the ADC's were opened.

The events on tape, consisting of pairs of words, formed the elements of two 2048-2048 element matrices, one of which included true coincidence events (plus some chance events) and the other of which was composed only of chance events. The tapes were first sorted on the CDC 6400 computer to obtain a gross "true" coincidence spectrum (projection) for each detector. The projection for the 38 cc detector, which had a slightly superior resolution at low energies, was used to select the channels appropriate to the coincidence gates of interest. Gates were chosen to include all the peaks in the projection spectrum. In addition, suitable background gates were chosen

below and/or above each peak gate, to make it possible to subtract off the events associated with the underlying Compton background. The tapes were then sorted to yield both the "true" and chance spectra associated with all these gates. For each gate, the chance spectrum was subtracted from the true spectrum. Finally, the chance corrected "background spectra" were subtracted from the corresponding chance corrected "peak spectra" to yield a set of coincidence spectra. Each member of this set was the spectrum of the true events in one detector in coincidence with a photopeak in the spectrum of the other detector.

The statistical error, e, in the number of counts in a given channel of the spectrum is given by the expression

$$e = [(T+C)_p + C_p + (T+C)_b + C_b]^{1/2}$$

where $(T+C)_p$ and C_p are the number of events at this channel in the "true and chance" and "chance" spectra derived from the peak gates and $(T+C)_b$ and C_b represent the corresponding quantities for the background gates.

The size of the memory in the CDC 6400 made it more practical to compress the spectra into 1024 channels so that more windows could be sorted at one time. This compression of course reduced the number of channels in a photopeak by a factor of two with some loss of resolution.

The two detectors, of volumes 38 and 50 cc respectively,

were mounted as shown in Fig. 4.4 at an angle of 90° to the beam axis and at an angle of approximately 120° to each other. A graded shield between the detectors eliminated coincidences caused by inter-detector scattering.

Two separate γ-γ coincidence experiments were carried out. Since the data from the first experiment were of rather poor quality, they were used only to obtain an idea of the scope of the problem and to test out our analysis techniques. The results presented in chapter 6 were all obtained from the second experiment. In actual fact, the second experiment was carried out with a pulsed beam so that the events associated with the decay of the low lying isomers could be simultaneously studied. Pulsing the beam had a negligible effect on the quality of the prompt γ-γ data. The conditions of the pulsed beam experiment will be discussed in Chapter 5.

CHAPTER 5

EXPERIMENTAL TECHNIQUES II - PULSED BEAM METHODS

5.1 Introduction

Two known isomeric states exist in ^{176}Hf, a 6+ level at 1333 keV and an 8- level at 1559 keV (Borggreen et al. 1967). The upper isomer decays to the lower one, as shown in Fig. 5.1, the latter then deexciting to the ground state band by the emission of either a 736 or a 1043 keV gamma ray. In our initial in-beam studies on this nucleus, these two transitions were among the strongest observed, indicating a surprisingly large population of the isomeric states in the ^{174}Yb(α,2n)^{176}Hf reaction. In an attempt to understand this phenomenon a number of experiments were planned, some of which employed novel techniques, to study the isomeric states and the levels which feed them. These experiments constitute the subject matter of this chapter.

Since it was necessary to use a pulsed beam in these studies, there is first a brief discussion, in section 5.2, of the beam pulsing system. This section is followed in turn by sections dealing with the methods used to study the decay of the isomer (5.3) and to determine the half lives of the isomers (5.4). Finally section 5.5 describes the delayed coincidence

techniques used to study the gamma rays feeding the isomeric states and section (5.6) describes the $(\gamma\text{-}\gamma)\text{-}\gamma_{delayed}$ coincidence experiment.

5.2 The Beam Pulsing System

The pulsed beam was obtained by electrostatically deflecting the continuous beam from the ion source through the application of a 600 volt potential difference to a pair of steerers at the low energy end of the accelerator. This voltage deflected the beam sufficiently to prevent it from passing through the defining slits at the high energy end of the machine. The deflection voltage was controlled by a modulator which was fed instructions in the form of ordinary logic pulses of approximately 5 volt amplitude.

The transit time of the beam from these deflection plates to the target position was approximately 4 μs. Consequently there was a 4 μs lag between the instructions to the modulator and the actual response at the target location. It was necessary to take this time lag into account in designing the experiments.

5.3 The Decay of the Isomeric States

Fig. 5.1 presents the information concerning the isomers of ^{176}Hf which was available at the time these measurements were begun. The 1333.3 keV state was observed by Brandi et al

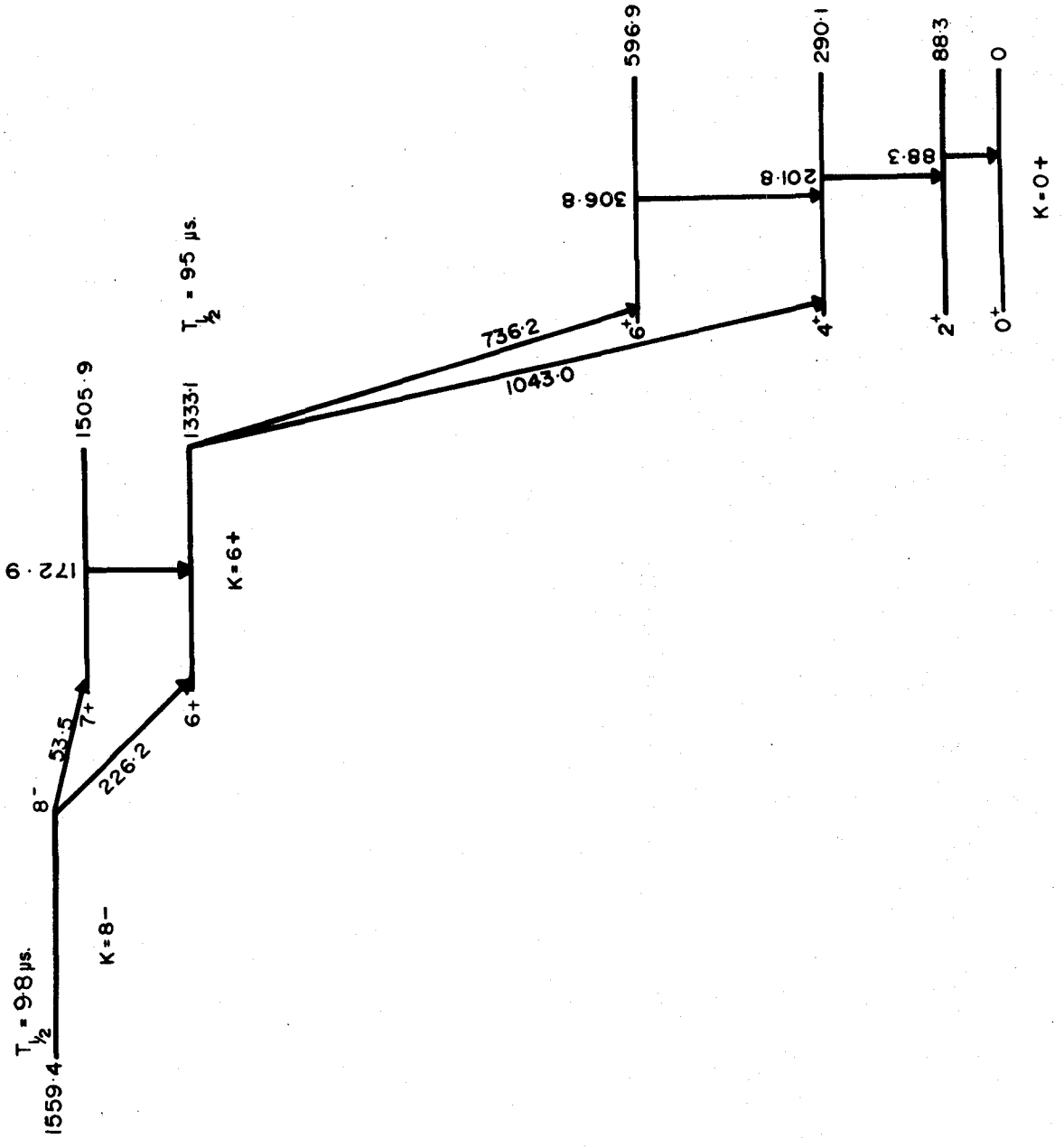

Figure 5.1

The decay of the two isomers in ^{176}Hf. The half-lives and energies are those measured in this work.

(1964) via the $^{177}Hf(\gamma,n)^{176}Hf$ reaction and its half life de-determined as 10.5±0.7 μs.

Borggreen et al (1967) used the $^{176}Lu(p,n)^{176}Hf$ reaction to populate both isomers and to obtain half lives of 10.3±0.3 and 13.0±0.5 μsec for the 1559 and 1333 keV states respectively. These authors observed both the 173 and 226 keV transitions and postulated the 53 keV transition.

The present experiments were conducted to (i) confirm the decay mechanism of Fig. 5.1, (ii) to make a direct observation of the 53 keV transition, (iii) to resolve the disagreement in the published half lives, (iv) to establish the energy difference between the 8- and 6+ states precisely, (v) to obtain a more detailed knowledge of the transitions deexciting the isomers and (vi) to search for other isomeric states in this nucleus. The techniques required for the third item in the list will be discussed in section 5.4, those for the others follow in succeeding paragraphs. Item 4 in the list rests on precise energy determinations of the 53, 173 and 226 keV transitions. The 53 keV transition was masked by x rays, and the 226 keV transition was one member of an unresolved triplet in the in-beam singles spectrum.

In order to collect the gamma spectrum resulting from the decay of the isomers, the target was periodically irradiated with alpha particles for periods of 20 μsec and the gamma spectrum observed for an 80 μsec period after the beam was

turned off. The time of arrival of the gamma-ray after the beam was turned off was also recorded. The time and energy information for an event were processed by two ADC's, and the data stored in the two parameter mode. The circuit used is shown in Fig. 5.2.

The experiment was performed twice, the data being collected differently in each case. In the first experiment the two ADC's were interfaced to the Nuclear Data 3300 analyser system with the memory arranged so that 1024 channel energy spectra were stored in 16 consecutive time groups spaced 5 μsec apart in time. In the second experiment, the two ADC's were interfaced to a PDP-9 computer. The data were then address-recorded in the manner used in the γ-γ coincidence experiment already described in section (4.6); in the present measurement the conversion gain of the "energy ADC" was 4096 channels while the "time ADC" was set at 1024 channels. The data could then be sorted in a variety of ways appropriate to the purpose of the experiment.

In the first experiment, a 38 cc Ge(Li) detector was used to record the delayed spectrum up to ∿ 1.4 MeV; in the second experiment, an 0.9 cc detector was used with the emphasis being placed on the low energy portion of the spectrum. In these experiments, the beam rate was limited by the in-beam counting rate, which had to be kept below counter break-down. It was also limited by the necessity of keeping the rate during the early time groups below the values where line shape

Figure 5.2

Block diagram of a typical system for measuring the energy and time distribution of delayed γ-rays from the decay of isomers.

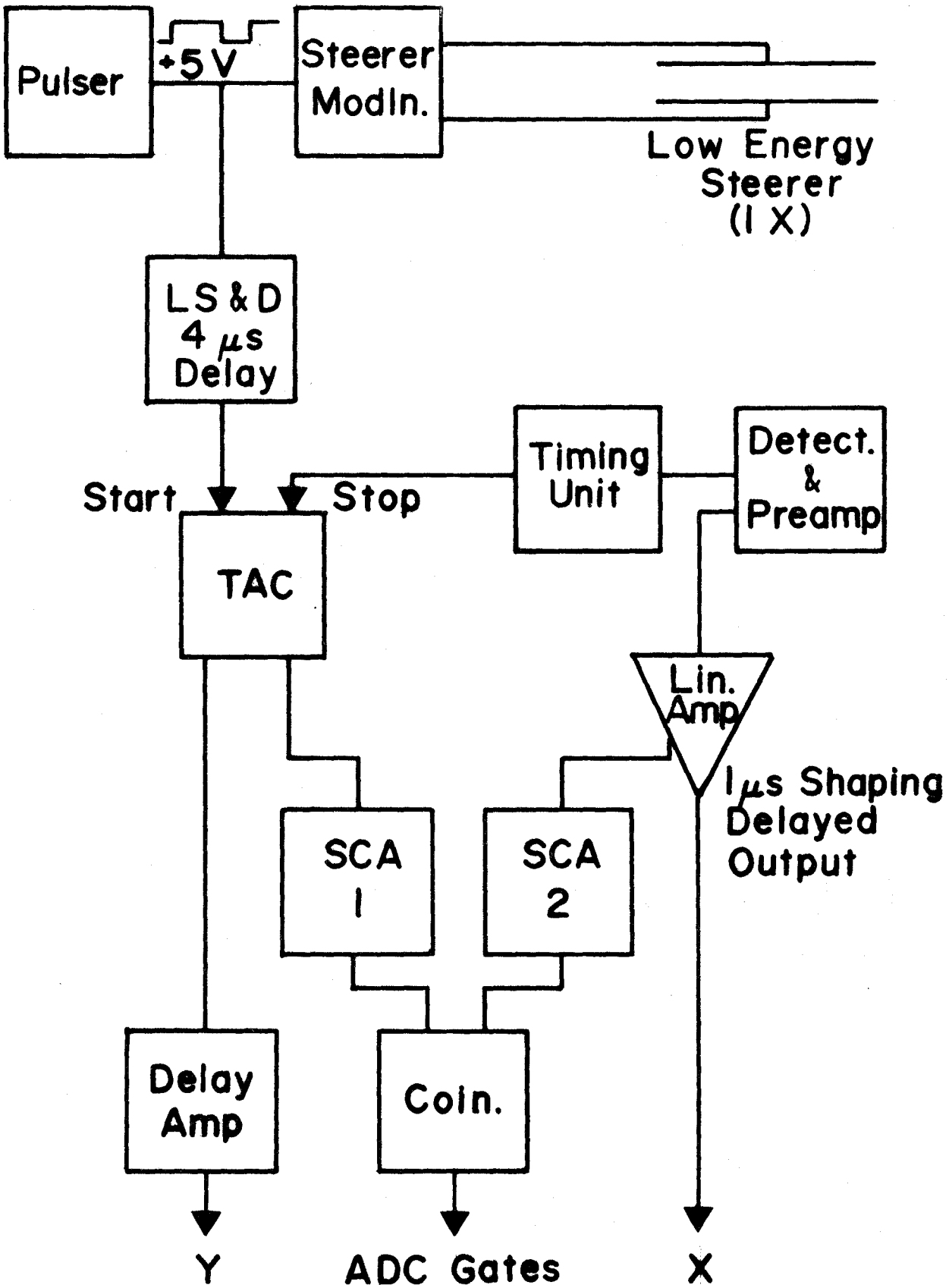
Pulser
+5V
Steerer
Modln.
Low Energy
Steerer
(1 X)
LS & D
4 μs
Delay
Timing
Unit
Detect.
&
Preamp
Start
Stop
TAC
Lin.
Amp
1μs Shaping
Delayed
Output
SCA
1
SCA
2
Delay
Amp
Coin.
Y
ADC Gates
X

distortion occurred. It was not possible to use pile-up rejection as this introduced a dead time ($\sim$ 10 μsec) which seriously affected the counting rate in the early time periods.

5.4 The Half-Lifes of the 6+ and 8- Isomeric States

It is clear from Fig. 5.1 that the 1559 keV isomer in ^{176}Hf decays to the 1333 keV isomer and thence to the ground state band. Presumably both isomeric states are fed directly in the (α,2n) reaction from higher lying states of ^{176}Hf. Borggreen et al (1967) determined the half-life of this 1333 keV state by following the decay of the 202 keV transition and noted that it decayed in a manner characteristic of an activity undergoing simultaneous growth and decay. They then fitted a straight line to the apparently linear portion of the decay curve to get the half life of the 1333 keV state. This procedure leads to an incorrect result in the case when both the parent and daughter activities have almost equal half lives.

Under the conditions existing in ^{176}Hf (see accompanying figure), the decay of γ_2 will have the form

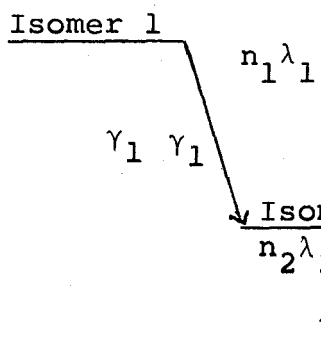

$$N_{\gamma_2}(t) = \lambda_2 n_2(t)$$

$$= \lambda_2 n_{20} \left[e^{-\lambda_2 t} + \left(\frac{\lambda_1 n_{10}}{\lambda_2 n_{20}}\right) \frac{\lambda_2}{\lambda_2 - \lambda_1} \left(e^{-\lambda_1 t} - e^{-\lambda_2 t} \right) \right] \qquad (5.4(i))$$

where λ_1 and λ_2 are the appropriate decay constants; $\lambda_2 n_t(t)$ is the decay rate of the lower isomer 2; and n_{10} and n_{20} are the populations of the isomers at time zero. When λ_1 and λ_2 are approximately equal, $N_{\gamma_2}(t)$ will decay in an approximately exponential manner with a decay constant less than either λ_1 or λ_2.

(i) Determination of half life of the 1559 keV isomer

The half life of the 1559 keV state was determined by measuring the intensities of the 173 and 226 keV transitions as a function of the time after the beam was pulsed off (see section 5.3). In the experiment where the spectra were stored in sixteen time groups within the ND3300 analyser memory, this was done very simply by determining the areas of the two peaks of interest in each of the sixteen spectra, plotting these as a function of time and analysing the decay curve. In the experiment where the PDP 9 was used to store the data as elements of an energy-time matrix, digital gates were set on the peaks and adjacent backgrounds along the energy axis to give the decay spectra of the counts in each peak as a function of time. These data were therefore treated in the same way as were the γ-γ coincidence data described in section 4.6.

The decay curves from both experiments were analysed by subtracting a flat background to obtain a linear decay curve when plotted on a semilogarithmic scale. The first experiment was carried out with the 38 cc Ge(Li) detector whose resolution

was not good enough to separate the 173 and 226 keV transitions from the weak 174 and 228 keV transitions originating in the 1.1 sec isomer of ^{177}Hf which was also created in the target. Thus, in this experiment, the background was primarily due to this 1.1 sec activity. In the second experiment, the high resolution 0.9 cc detector was used and it was therefore possible to separate the ^{177}Hf lines from those in ^{176}Hf. Unfortunately, due to poor adjustment of the beam-pulsing system in this one experiment, a small fraction of the beam leaked through to the target during the beam-off portion of the cycle to give rise to an undesired background. Despite these limitations, both experiments gave consistent results.

(ii) Half life of the 1333 keV isomer

The decay curves of the transitions depopulating the 1333 keV isomer could also be similarly obtained. However, as has been previously explained, a half-life determined from the decay curve will appear to be too long because of feeding from the 8- isomer. Although equation (5.4(i)) may be used to obtain an estimate of the half-life of the 1333 keV isomer (by a least squares fitting procedure, for instance) a direct measurement is preferable. The following experiment employing the delayed coincidence lifetime measurement technique was therefore designed for this purpose.

This experiment used a time to amplitude converter (TAC) to measure the elapsed interval between the detection of a

transition (of energy 54, 173 or 226 keV) feeding the 1333 keV isomer and the detection of a gamma ray deexciting this state (88, 202, 307, 736, or 1043 keV). These two instants of time were marked by logic pulses which we shall label as "start" and "stop" pulses respectively. While any pulse from the detector could create a "start",only those associated with the full energy peaks of the three special gamma rays provided proper start pulses for the half life measurement. It was therefore necessary to record both the size of the pulse responsible for each "start" and the time interval between it and its associated "stop" event, in order to be able to select the proper results for analysis.

Since the effective "source strength" of the target was decreasing with the decay of the isomer, the chance rate was also a decaying function of time during the beam-off period. It was therefore necessary to determine it both at the beginning and end of the off-period. In order to get a measure of its value at the beginning of the off-period, the stop pulses were artificially delayed for 5 μsec to make coincident start-stop pairs appear at 5 μsec on the TAC output. Events falling in the first 5 μsec of this output were then due to chance events in which the "stop" pulse preceded the "start" pulse. The TAC input was also prevented from receiving any "start" pulses until 5 μsec after the beam came off target. This ensured that the "stop" initiated chance events in the first 5 μsec of the TAC

spectrum did not arise from the target while it was exposed to the beam.

The electronic arrangement for the experiment is shown in Fig. 5.3 while the timing sequence is illustrated in Fig. 5.4. The timing cycle was controlled by a pulser [see Fig. 5.3 and first line of Fig. 5.4] which drove a beam modulator at the low energy end of the machine. This cycle produced a target irradiation of 21 μsec followed by a 144 μsec off period. The actual irradiation cycle was delayed by 4 μsec with respect to the pulser cycle because of the transit time of the beam in the machine (see line 2 of Fig. 5.4). The pulser also turned on a 15 μsec monostable which activated the AND #1 circuit so that any "start" pulse generated in the 15 μsec "enable" period could start the TAC. The 9 μsec delay introduced ensured that the beam had been off target for 5 μsec before the start pulse could be accepted (see lines 3 and 4 of Fig. 5.4). The "start" pulse passed by the AND #1 unit,triggered the sweep (linear ramp) of the oscilloscope, which, in conjunction with the linear gate and the AND #2 unit, acted as a time-to-amplitude converter with a 120 μsec range. The buffered sweep gate output also applied a signal to the AND #2 gate, enabling it to accept "stop pulses" during the period when the sweep voltage was rising and blocking it at all other times (see lines 5, 6, 7 of Fig. 5.4).

The start events were derived from the 38 cm^3 Ge(Li) detector. These events, after processing by the timing filter amplifier (TFA) and the constant fraction discriminator (CFTD),

Figure 5.3

Block diagram of the electronics for measuring the half-life of the 1333 keV isomer.

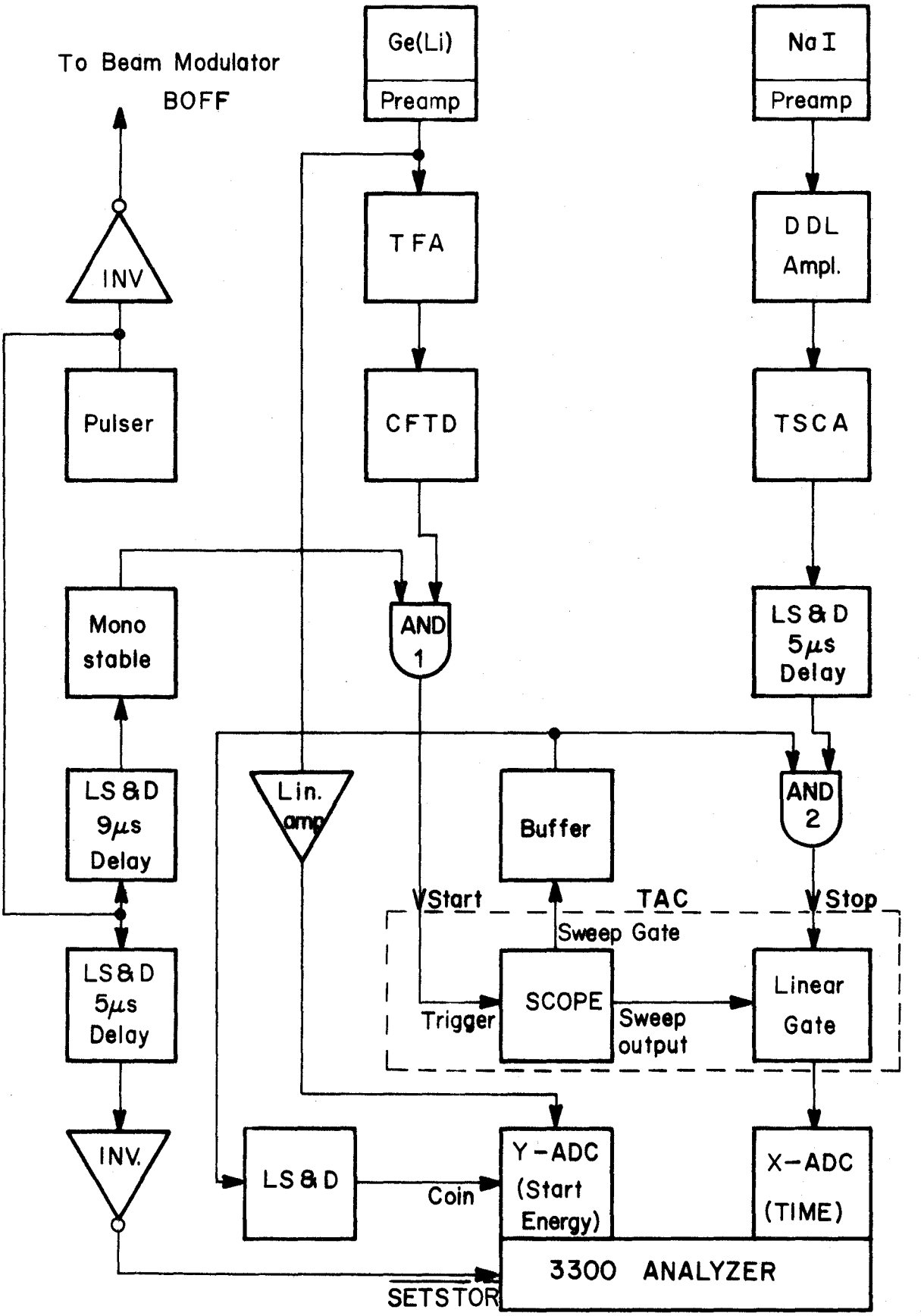
To Beam Modulator
BOFF
Ge(Li)
Preamp
NaI
Preamp
INV
TFA
DDL
Ampl.
Pulser
CFTD
TSCA
Mono
stable
AND
1
LS&D
5μs
Delay
LS&D
9μs
Delay
Lin.
amp
Buffer
AND
2
Start
TAC
Stop
Sweep Gate
LS&D
5μs
Delay
SCOPE
Linear
Gate
Trigger
Sweep
output
INV.
LS&D
Coin
Y-ADC
(Start
Energy)
X-ADC
(TIME)
3300 ANALYZER
SETSTOR

Figure 5.4

Timing sequence in the measurement of the 1333 keV isomer half-life.

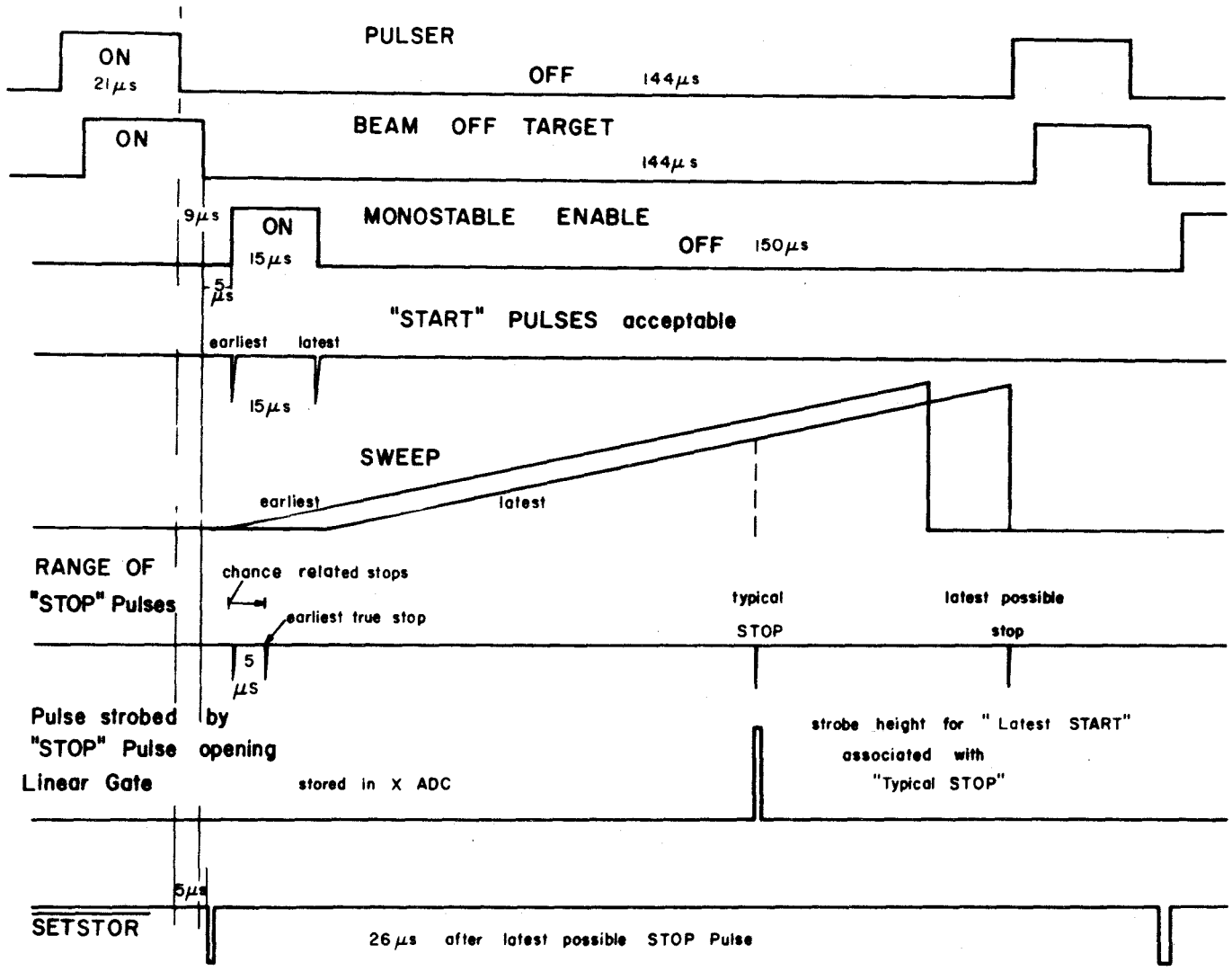
PULSER
ON
21μs
OFF
144μs
BEAM OFF TARGET
ON
144μs
9μs
ON
15μs
MONOSTABLE ENABLE
OFF
150μs
5
μs
"START" PULSES acceptable
earliest
latest
15μs
SWEEP
earliest
latest
RANGE OF
"STOP" Pulses
chance related stops
earliest true stop
typical
STOP
latest possible
stop
5
μs
Pulse strobed by
"STOP" Pulse opening
Linear Gate
stored in X ADC
strobe height for " Latest START"
associated with
"Typical STOP"
5μs
SETSTOR
26μs after latest possible STOP Pulse

produced the required timing signal. The "stop" events were derived from an NaI(Tl) detector, pulses from which were processed by a DDL amplifier and a timing single channel analyzer (TSCA) set to accept all pulses corresponding to gamma ray energies up to 1100 keV. These pulses, after the 5 μsec delay which shifted time zero of the TAC spectrum (line 6 of Fig. 5.4) were passed by the AND #2 gate to strobe the TAC output and allow it to be registered in the X-ADC. The energy of the gamma ray which provided the "start" pulse was measured in the usual fashion by processing the linear signal from the Ge(Li) detector and storing it in the Y-ADC. The linear gate to this ADC was opened by a timing signal from the buffer sweep gate output which corresponded in time with the arrival of the "start" pulse. Thus at the end of each cycle, the energy of the "start" event and the time interval between the "start" and "stop" events had been recorded in the two ADC's. Since the events in these two ADC's were stored at points of time which were up to 120 μsec apart, it was necessary to generate an external signal $\overline{\text{SETSTOR}}$ to instruct the ND3300 system to store the ADC addresses in the memory. Pulses for this purpose were generated by the inverter 5 μsec after the pulser turned off, ie 4 μsec before the beginning of the next "monostable period" (see line 8 of Fig. 5.4). This allowed sufficient time for the X ADC to complete conversion of the time delay pulse (maximum time required $\sim$ 21 μsec) before the next cycle.

5.5 Gamma Rays Feeding the Isomeric States

^{176}Hf is a deformed nucleus so that one would expect to have a rotational band built on each of the two isomeric states at 1333 and 1559 keV,with transitions cascading down each band to these two levels. In addition, there are other states that decay preferentially to the isomers and to the members of the bands built on them. This rather large group of transitions may be isolated from the totality of ^{176}Hf transitions by means of the delayed coincidence experiment outlined below. The resulting spectrum is, of course, much simpler than that obtained in an ordinary in-beam experiment. The delayed coincidence technique complements the prompt γ-γ coincidence method. The latter can establish the existence of cascades but it cannot distinguish those that feed the isomer from those that feed the ground state. Finally, a double delayed coincidence experiment permits one to establish which of the two isomers is being fed. The technique to be described was suggested by Hamish Robertson and developed jointly by Hamish and the author. The counting rates which can be achieved in these delayed experiments are somewhat larger than those in a prompt γ-γ coincidence measurement. This is due to the fact that the energies of the stop pulses need not be determined, with the consequence that the detection efficiency for "stop" pulses can be made very large.

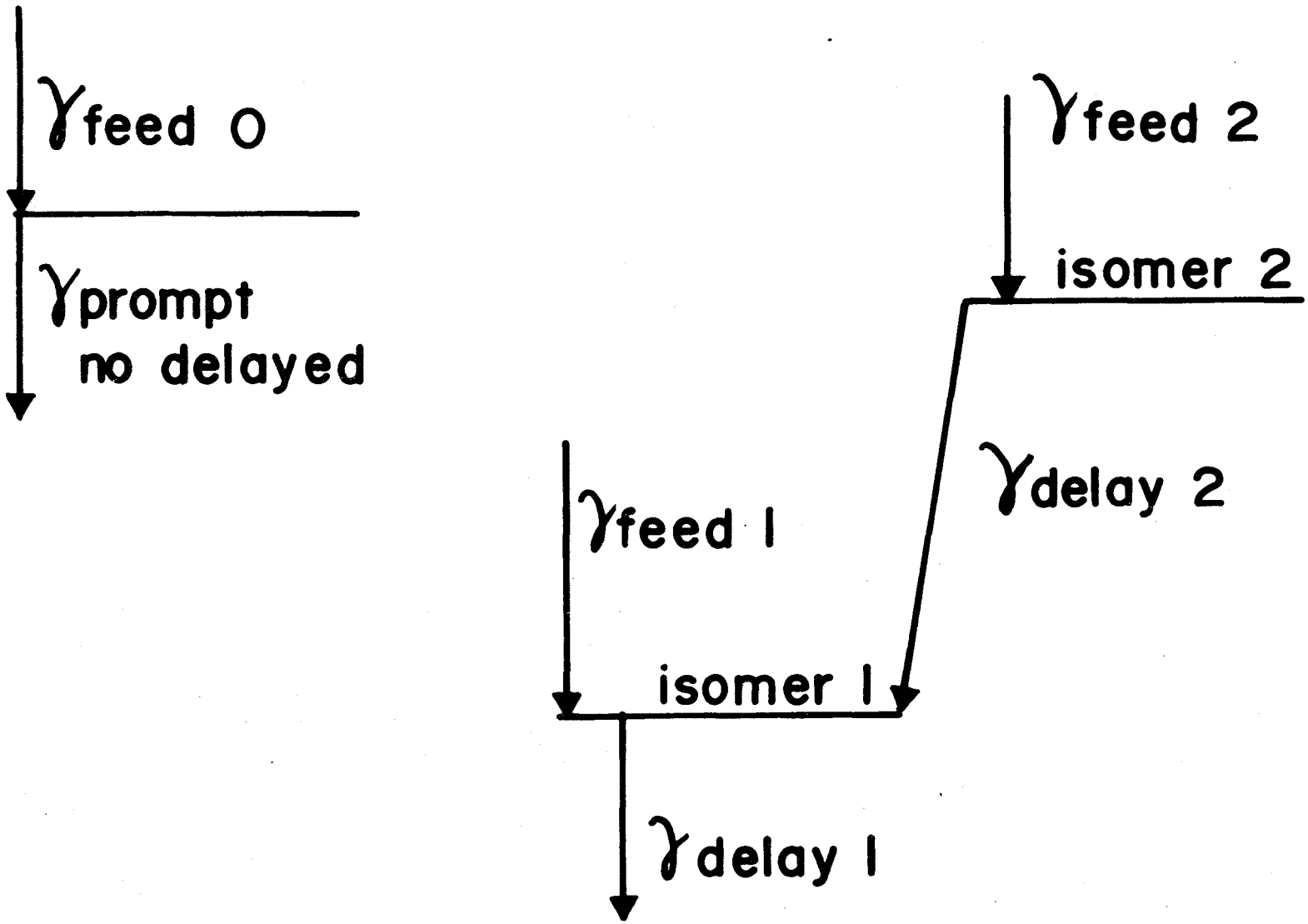

Figure 5.5

Illustration of 3 possible coincidence relationships

(i) Principle of the delayed coincidence experiment

The highly excited ^{176}Hf nucleus decays by γ ray emission according to one of the three possibilities presented schematically in Fig. 5.5. $\gamma_{feed\ 0}$ produces no delayed events; $\gamma_{feed\ 1}$ produces one delayed gamma ray; while $\gamma_{feed\ 2}$ produces two delayed gamma rays, one from the decay of isomer 2 followed later by another from isomer 1.

To distinguish between these three processes, the following sequence was follows:

a) The beam was turned on until a gamma ray, γ_{feed}, was detected.

b) γ_{feed} was used to turn off the beam in the manner described in section 5.4 and its energy was determined.

c) Delayed events were searched for the in beam-off period.

d) The ADC address of γ_{feed} was tagged according to the result of the search and stored in the appropriate section of the analyser memory.

The coding was achieved by setting either or both of the most significant bits (#12 and 13) of the 14 bit address in the ADC, as indicated in the sketch.

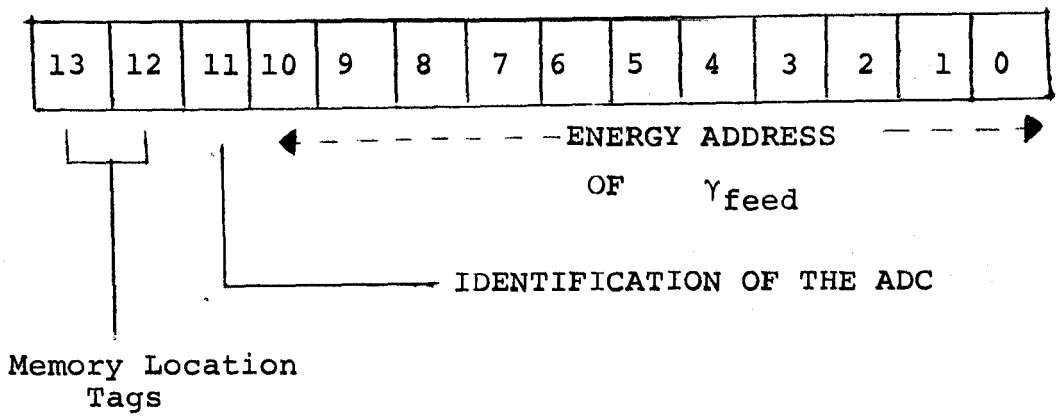

0 0 indicated that no delayed gamma ray was detected, corresponding to $\gamma_{feed\ 0}$

0 1 indicated that <u>one</u> delayed event was detected corresponding to the process $\gamma_{feed\ 1}$

1 0 also indicated that one delayed event was detected but that, in addition, the pulse height of the delayed γ ray had a pulse corresponding to the photopeak of one of the gamma rays in the cascade deexciting isomer 1.

1 1 indicated that two delayed events were detected, corresponding to $\gamma_{feed\ 2}$.

It was originally felt that Tag 10 might provide a better signal to chance ratio in the recorded spectra than Tag 01, because it would eliminate most of the chance events created by room background. In fact, the improvement was not significant and Tags 01 and 10 were combined to give better statistics.

By using two Ge(II) detectors arranged so that either detector could detect γ_{feed} or provide a stop pulse, a four fold improvement in counting rate was obtained. When two detectors were used, bit 11 of the ADC address was used to identify the detector.

(ii) The circuit

The circuit employed with two Ge(Li) detectors is shown schematically in Fig. 5.6. A gamma ray, γ_{feed}, from either direction, after appropriate processing, initiated the memory cycle, which was controlled by the unit labelled "logic control". The beam was turned off, scaling of the 2MHz clock was started, and the ADC linear gates were opened. These gates were held open for $\sim$ 5 μsec so that the linear pulse associated with the gamma ray could be processed in either ADC1 or ADC2. At the end of the cycle, typically 100 clock pulses or 50 μsec later, the control unit turned the beam back on and generated a pulse $\overline{\text{SETSTOR}}$ which caused the ADC's to be interrogated and their addresses to be stored in the memory. At the end of the storage period, the pulse ENDSTOR reset the memory cycle and flip flops (FF) in anticipation of another pulse from the detectors.

The logic pulse from γ_{feed}, which started the memory cycle, also started (after a 4.5 μsec delay provided by the LS & D unit) TAC #1 and set the flip flop (FF) which prevented the TAC from being restarted by any subsequent pulse

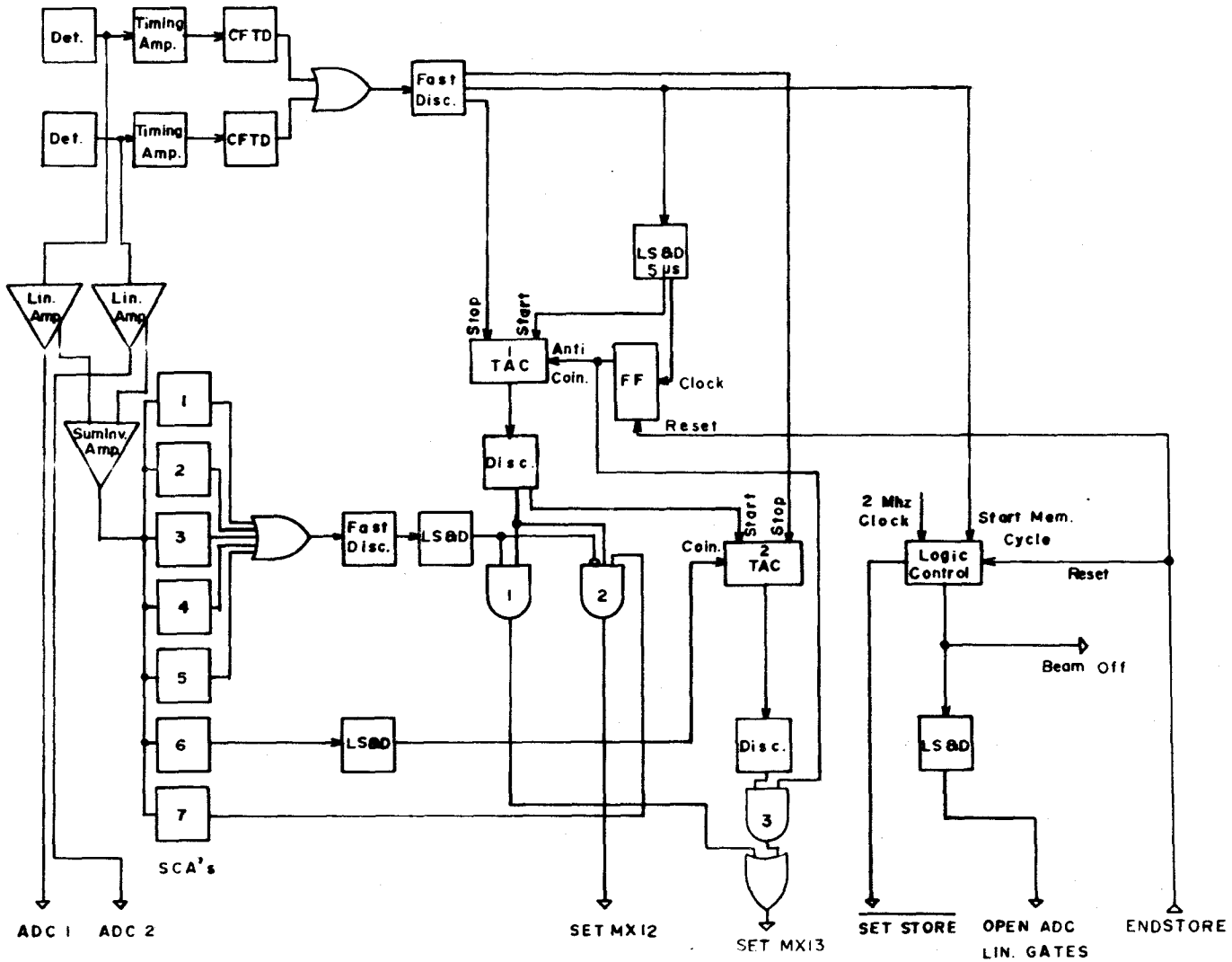

Figure 5.6

Block diagram of the system used in the delayed coincidence experiments

until the FF had been reset at the end of the cycle. The 4.5 μsec delay was necessary to ensure that the search for a stop-pulse began after the beam was off the target. Pulses arriving in this 4.5 μsec interval could neither be processed by the ADC's nor affect either TAC unit.

The first pulse to be detected in either detector after the 4.5 μsec delay stopped TAC 1 and caused it to start TAC 2 and send logic pulses to AND 1 and AND 2. The next pulse to be detected in either detector stopped TAC 2 and caused it to send a logic pulse to AND 3. These logic pulses were used to distinguish the four groups of γ_{feed} events described in section (i) in the manner described below.

The linear pulses from the two Ge(Li) detectors were mixed in the summing amplifier and fed to the array of seven single channel analysers (SCA's). Analysers 1 to 5 were set up with narrow windows covering the photopeaks of the gamma rays which followed the decay of the 1333 keV isomer. Wide windows were set on analysers #6 and #7, the window for #6 covering the range 40 to 230 keV (the energy separation of the two isomers is 226 keV) and the window for #7 extending from 40 to 1050 keV to cover the full range of energies emitted in the decay of the lower isomer. Pulses from analysers #1 to 5 opened AND 1 and at the same time disabled AND 2, while pulses from analyser #7 opened AND 2 (unless it was simultaneously disabled). Thus it can readily be seen that the

output from TAC 1 set MX 13 (tag 10) if the energy of the first event corresponded to one of the gamma rays following the decay of the 1333 keV isomer ; or set MX 12 (tag 01) if the energy of the first event fell anywhere else in the range 40 to 1050 keV. In the same way the pulses from SCA #6 allowed TAC 2 to start its search for a second delayed pulse only when the first delayed event had an energy from 40-60 230 keV. This restriction on the operation of TAC 2 had the effect of reducing the number of accidental events which could start TAC 2. Finally, if a second delayed event was found, TAC 2 was stopped and a logic pulse set MX 13 via the AND 3 gate.(It should be noted that this gate was enabled only during the beam-off period.) MX 12 would have been previously set, so that both routing bits were set (tag 11).

The routing arrangements described above achieved the coding of the γ_{feed} events described in section (i) above. In order to avoid the incorrect routing of events, it was essential that the primary event occur in the beam-on period, that the first and second delayed events occur only in the beam-off cycle and the TAC 1 and TAC 2 be allowed to operate only once in each memory cycle. These conditions were met by delaying the logic event for the first event by 4.5 μsec, by employing a flip flop (FF) to prevent TAC 1 from being restarted, and by enabling AND 3 only during the beam-off period.

The 50 μsec duration of the memory cycle was imposed by the necessity of allowing the ADC's to complete their conversion process (∿ 41 μsec maximum for a conversion gain of 2048) and of allowing time for the two TAC's to go through their 20 (maximum) μsec cycles sequentially.

(iii) Experimental Details

The Ge(Li) detectors (volumes 39 cm^3 and 50 cm^3 respectively were placed 1.8 cm apart, on the opposite sides of a 6 mg/cm^2 target and at 90° to the beam line. The beam current was reduced to 0.5 na to keep the chance rate low. Under these conditions the beam was turned off every 120 μsec on the average and remained off for ∿ 57 μsec each time. The data were accumulated in about 36 hours of running time.

5.6 The $(\gamma-\gamma)-\gamma_{delayed}$ coincidence experiment

While the delayed coincidence experiment described in 5.5 above was able to select those γ rays which fed the 1333 or 1559 keV isomeric states, it did nothing to establish the cascade relationships between these transitions. By means of a simple modification of the technique, it was possible to isolate the prompt γ-γ coincidence events associated with decays to the isomers from the totality of γ-γ coincidence events and thus to establish a large number of rotational bands related to these isomeric states. This modification, which

we have christened the $(\gamma\text{-}\gamma)\text{-}\gamma_{delayed}$ coincidence method, is briefly described below.

A block diagram of the circuit for the $(\gamma\text{-}\gamma)\text{-}\gamma_{delayed}$ experiment is shown in Fig. 5.7. It consists of the circuit used in the prompt $(\gamma\text{-}\gamma)$ coincidence experiment (see Fig. 4.12) coupled to the circuit shown within the dotted lines. This additional section served to (i) turn the beam on and off, (ii) register the detection of delayed γ rays, (iii) set appropriate bits in the ADC's to label the prompt coincidence pairs which were followed by a delayed event, and (iv) control the memory cycle in a manner analogous to that in the delayed coincidence experiment described in section 5.5 (ii).

When a prompt $\gamma\text{-}\gamma$ coincidence was detected, TAC 2 was started (after a delay of 4.5 μsec. to ensure the beam was off the target). The first pulse from either detector arriving within the next 40 μsec stopped TAC 2. SCA's were used to sort the arrival time of the delayed event into two groups: 0-20 μsec or 0-40 μsec. It was thus possible to distinguish prompt $\gamma\text{-}\gamma$ coincidences which were followed by an event delayed by 0-20 μsec., from those followed by an event delayed by 0-40 μsec. In fact, because of the need for improved statistics, only the latter group was used in the analysis.

The $(\gamma\text{-}\gamma)\text{-}\gamma_{delayed}$ and the prompt $(\gamma\text{-}\gamma)$ experiments were performed simultaneously. The distinction between the

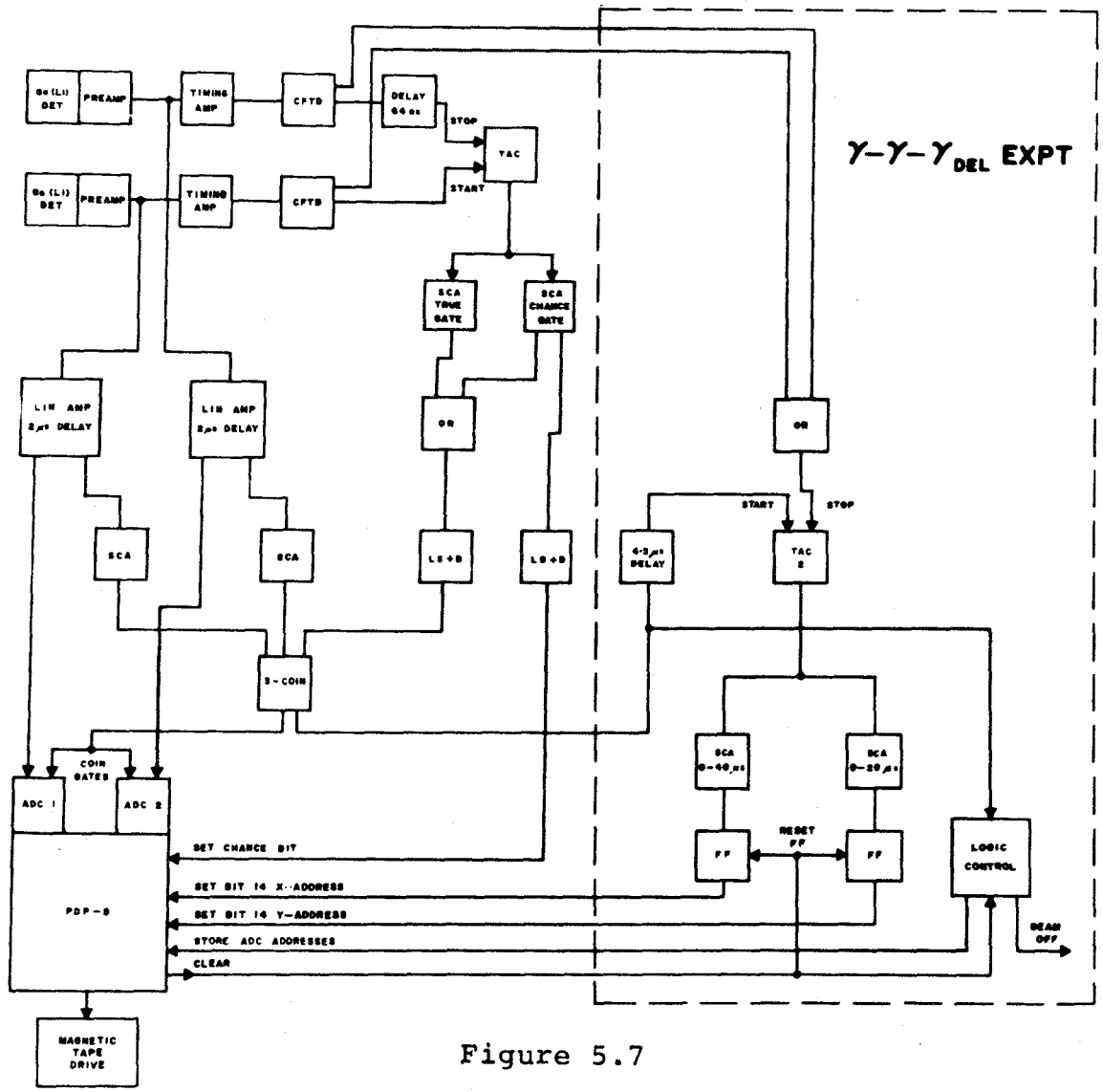

Figure 5.7

Block diagram of the system used for the prompt (γ-γ) and (γ-γ)-$\gamma_{delayed}$ coincidence experiments

two experiments was made only when the data was sorted. For the $(\gamma\text{-}\gamma)\text{-}\gamma_{delayed}$ experiment, only appropriately coded events (bit 14 of X-address set) were considered, whereas all valid coincidences were accepted for the prompt $\gamma\text{-}\gamma$ experiment. Since the prompt coincidence rate was sufficiently low ($\lesssim$ 150 per sec.), pulsing the beam off for 50 μsec after the arrival of each coincident event did not significantly affect the data accumulation rate.

CHAPTER 6

EXPERIMENTAL RESULTS AND CONSTRUCTION OF ^{176}Hf LEVEL SCHEME

6.1 Introduction

The results of the experiments, described in detail in Chapters 4 and 5 are now presented in turn. The results of the in-beam singles gamma measurements are presented in section 6.2, together with the excitation functions of a number of transitions. The in-beam conversion electron spectra are presented in section 6.3. In the next section, the γ-γ coincidence data for transitions that feed the g.s.b. promptly are discussed, together with some details concerning the construction of the level scheme. There is also a discussion of the methods used in evaluating the data in this section. In subsequent sections the results of the measurements associated with the isomeric states are presented. Section 6.6 deals with the decay of the isomeric states, section 6.7 with the half-life measurements, while section 6.8 discusses the results of the experiments which isolated the gamma rays feeding the isomer. The procedures involved in developing the level scheme based on the two isomeric states are discussed in section 6.9 and, finally, the data from the γ-γ and $(\gamma$-$\gamma)$-$\gamma_{delayed}$ coincidence experiments, are presented in section 6.10.

6.2 In-Beam Singles Gamma Spectra

a) Energies and intensities

A gamma spectrum accumulated in-beam (E_α = 22.5 MeV), using a 0.9 cc Ge(Li) detector, of resolution ~ 650 eV at 122 keV, is shown in fig. 6.1. A similar spectrum, extending to higher energy, and accumulated with a 38 cc. detector of resolution 3.2 keV at 1.3 MeV is shown in fig. 6.2. Many real but weak peaks in these spectra cannot be seen because of the high background which is typical of (particle,xn) reactions. In order to present the experimental data more clearly, Figs. 6.3 and 6.4 present the same spectra after a background, with an exponential fall-off that roughly matched the continuum, was removed. These spectra show the weak peaks much more clearly and were used to set the windows for the Jagspot peak fitting program.

A considerable number of lines in these spectra are due to impurities or competing reactions. Whenever possible, such lines have been labelled in Figs. 6.1 to 6.4. There will of course be other impurity lines which we have been unable to distinguish from those originating in ^{176}Hf. Therefore, we have taken the position that a line is not proven to belong to ^{176}Hf unless it is seen in a coincidence experiment.

The energies and intensities of the lines in these spectra were determined in the manner described in section 4.4.

Figure 6.1

In-beam γ-ray spectrum from 22.5 MeV α-particles on ^{174}Yb target. Recorded with a 0.9 cc Ge(Li) detector (resolution 650 eV at 122 keV).

Notation for figures 6.1 to 6.4.

- * From ^{175}Hf
- ** From ^{178}Hf
- † From ^{174}Hf
- c From contaminant
- ▲ Line in ^{176}Hf containing a contaminant component.

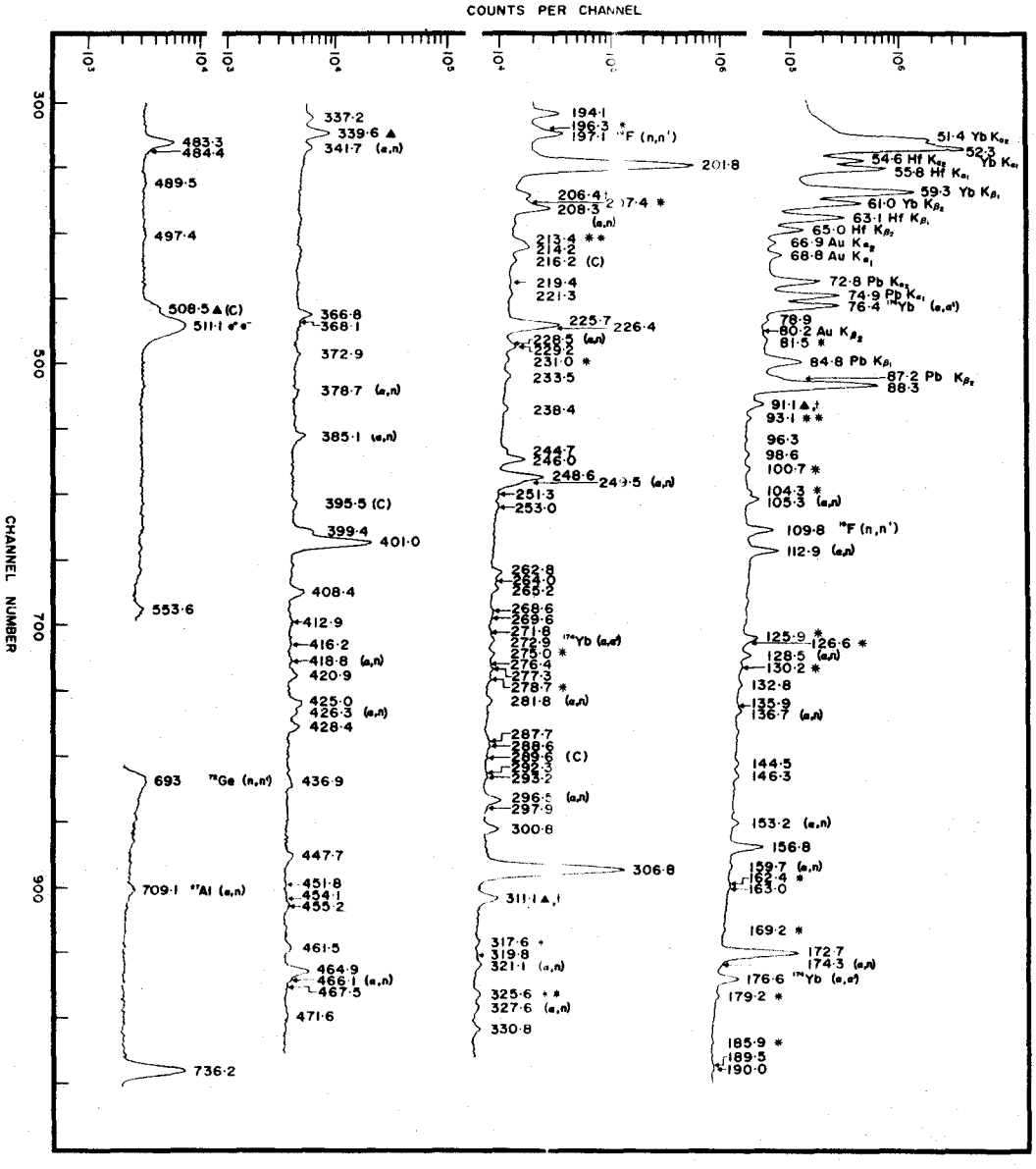
COUNTS PER CHANNEL
CHANNEL NUMBER
300
500
700
900
483·3
484·4
489·5
497·4
508·5 ▲ (C)
511·1 e⁺e⁻
553·6
693 ⁷³Ge (n,n')
709·1 ²⁷Al (n,n)
736·2
337·2
339·6 ▲
341·7 (n,n)
366·8
368·1
372·9
378·7 (n,n)
385·1 (n,n)
395·5 (C)
399·4
401·0
408·4
412·9
416·2
418·8 (n,n)
420·9
425·0
426·3 (n,n)
428·4
436·9
447·7
451·8
454·1
455·2
461·5
464·9
466·1 (n,n)
467·5
471·6
194·1
196·3 *
197·1 ¹⁹F (n,n')
201·8
206·4
208·3
207·4 *
(n,n)
213·4 **
214·2
216·2 (C)
219·4
221·3
225·7
226·4
228·5 (n,n)
229·2
231·0 *
233·5
238·4
244·7
246·0
248·6
249·5 (n,n)
251·3
253·0
262·8
264·0
265·2
268·6
269·6
271·8
272·9 ¹⁷⁴Yb (n,n')
275·0 *
276·4
277·3
278·7 *
281·8 (n,n)
287·7
288·6
289·6 (C)
292·3
293·2
296·5 (n,n)
297·9
300·8
306·8
311·1 ▲,†
317·6 *
319·8
321·1 (n,n)
325·6 * *
327·6 (n,n)
330·8
51·4 Yb Kα₂
52·3 Yb Kα₁
54·6 Hf Kα₂
55·8 Hf Kα₁
59·3 Yb Kβ₁
61·0 Yb Kβ₂
63·1 Hf Kβ₁
65·0 Hf Kβ₂
66·9 Au Kα₂
68·8 Au Kα₁
72·8 Pb Kα₂
74·9 Pb Kα₁
76·4 ¹⁷⁴Yb (n,n')
78·9
80·2 Au Kβ₂
81·5 *
84·8 Pb Kβ₁
87·2 Pb Kβ₂
88·3
91·1 ▲,†
93·1 * *
96·3
98·6
100·7 *
104·3 *
105·3 (n,n)
109·8 ¹⁹F (n,n')
112·9 (n,n)
125·9 *
126·6 *
128·5 (n,n)
130·2 *
132·8
135·9
136·7 (n,n)
144·5
146·3
153·2 (n,n)
156·8
159·7 (n,n)
162·4 *
163·0
169·2 *
172·7
174·3 (n,n)
176·6 ¹⁷⁴Yb (n,n')
179·2 *
185·9 *
189·5
190·0

Figure 6.2

In-beam γ-ray spectrum from 22.5 MeV α-particles on ^{174}Yb target. Recorded with a 38 cc Ge(Li) detector (resolution 3.2 keV at 1.3 MeV). (See figure 6.1 for notation).

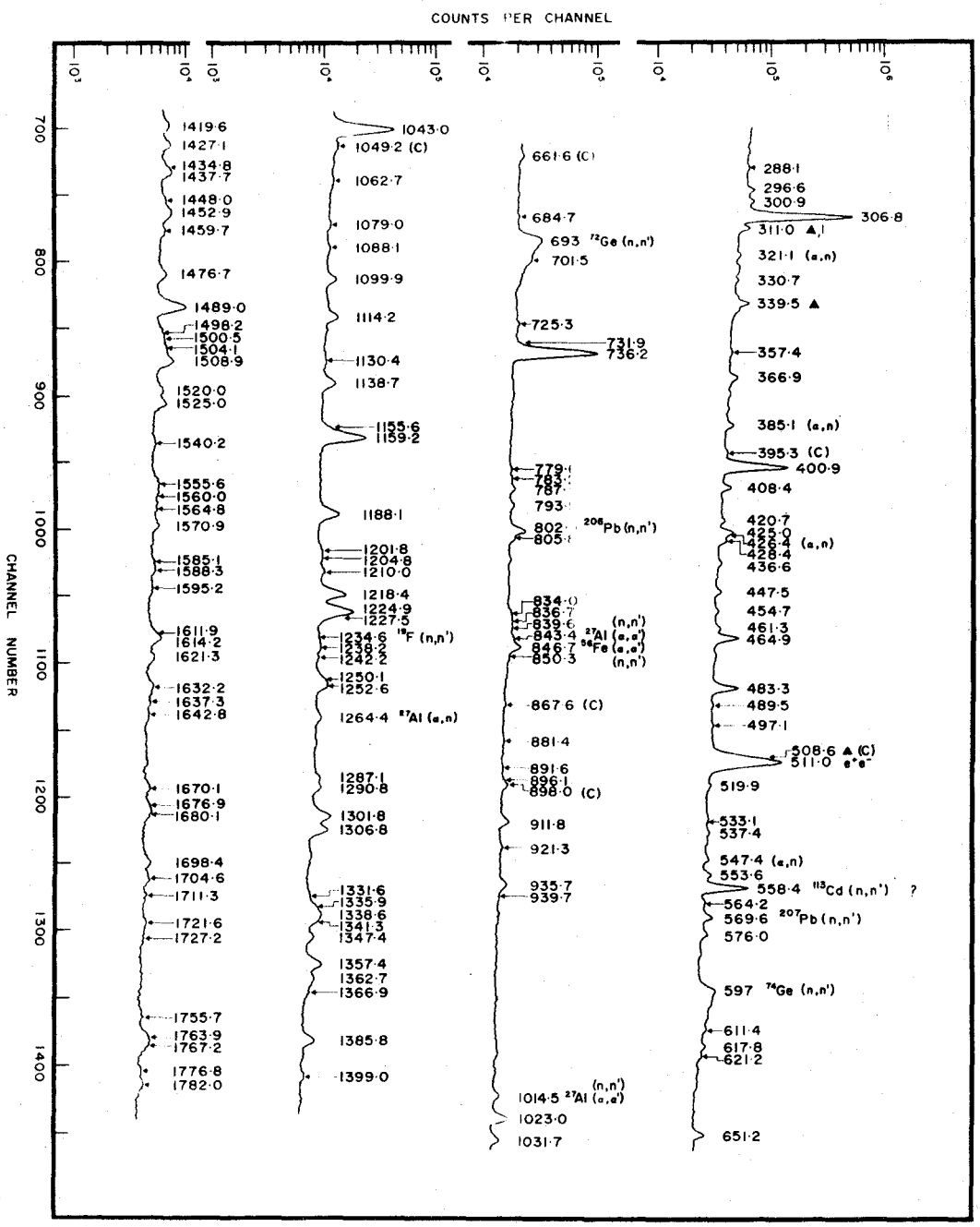
COUNTS PER CHANNEL
CHANNEL NUMBER
1419·6
1427·1
1434·8
1437·7
1448·0
1452·9
1459·7
1476·7
1489·0
1498·2
1500·5
1504·1
1508·9
1520·0
1525·0
1540·2
1555·6
1560·0
1564·8
1570·9
1585·1
1588·3
1595·2
1611·9
1614·2
1621·3
1632·2
1637·3
1642·8
1670·1
1676·9
1680·1
1698·4
1704·6
1711·3
1721·6
1727·2
1755·7
1763·9
1767·2
1776·8
1782·0
1043·0
1049·2 (C)
1062·7
1079·0
1088·1
1099·9
1114·2
1130·4
1138·7
1155·6
1159·2
1188·1
1201·8
1204·8
1210·0
1218·4
1224·9
1227·5
1234·6 19F (n,n')
1238·2
1242·2
1250·1
1252·6
1264·4 27Al (α,n)
1287·1
1290·8
1301·8
1306·8
1331·6
1335·9
1338·6
1341·3
1347·4
1357·4
1362·7
1366·9
1385·8
1399·0
661·6 (C)
684·7
693 72Ge (n,n')
701·5
725·3
731·9
736·2
779·1
783·
787·
793·
802· 206Pb (n,n')
805·
834·0
836·7
839·6 (n,n')
843·4 27Al (α,α')
846·7 56Fe (α,α')
850·3 (n,n')
867·6 (C)
881·4
891·6
896·1
898·0 (C)
911·8
921·3
935·7
939·7
1014·5 27Al (n,n') (α,α')
1023·0
1031·7
288·1
296·6
300·9
306·8
311·0 ▲,I
321·1 (α,n)
330·7
339·5 ▲
357·4
366·9
385·1 (α,n)
395·3 (C)
400·9
408·4
420·7
425·0
426·4 (α,n)
428·4
436·6
447·5
454·7
461·3
464·9
483·3
489·5
497·1
508·6 ▲ (C)
511·0 e⁺e⁻
519·9
533·1
537·4
547·4 (α,n)
553·6
558·4 113Cd (n,n') ?
564·2
569·6 207Pb (n,n')
576·0
597 74Ge (n,n')
611·4
617·8
621·2
651·2

Figure 6.3

See caption of figure 6.1. An exponentially sloping background has been subtracted to accentuate the peaks. Typical error bars are enclosed in circles at the beginning of each section.

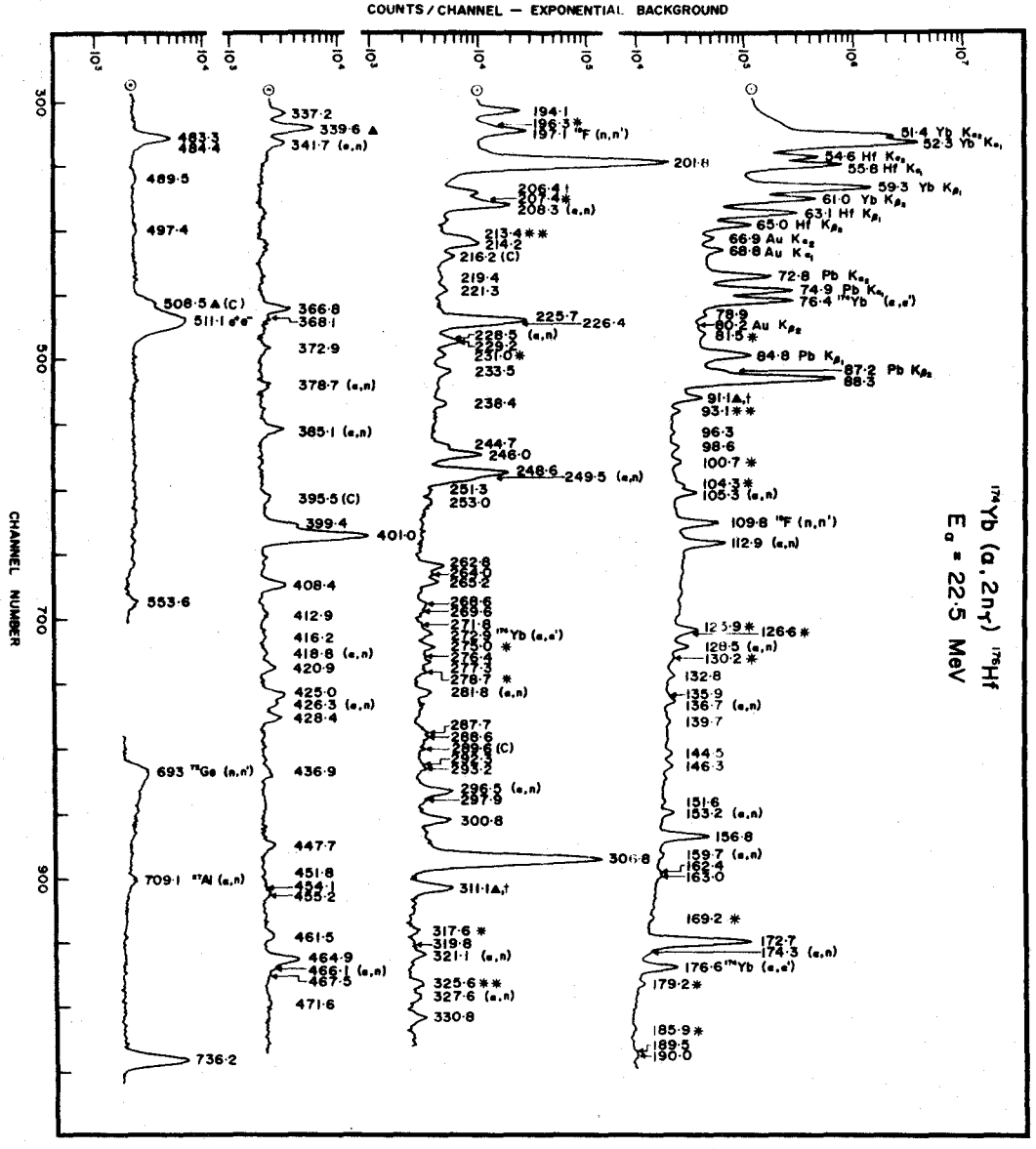
COUNTS / CHANNEL — EXPONENTIAL BACKGROUND
CHANNEL NUMBER
174Yb (α, 2nγ) 175Hf
Eα = 22·5 MeV

Figure 6.4

See caption of figure 6.2. An exponentially sloping background has been subtracted to accentuate the peaks. Typical error bars are enclosed in circles at the beginning of each section.

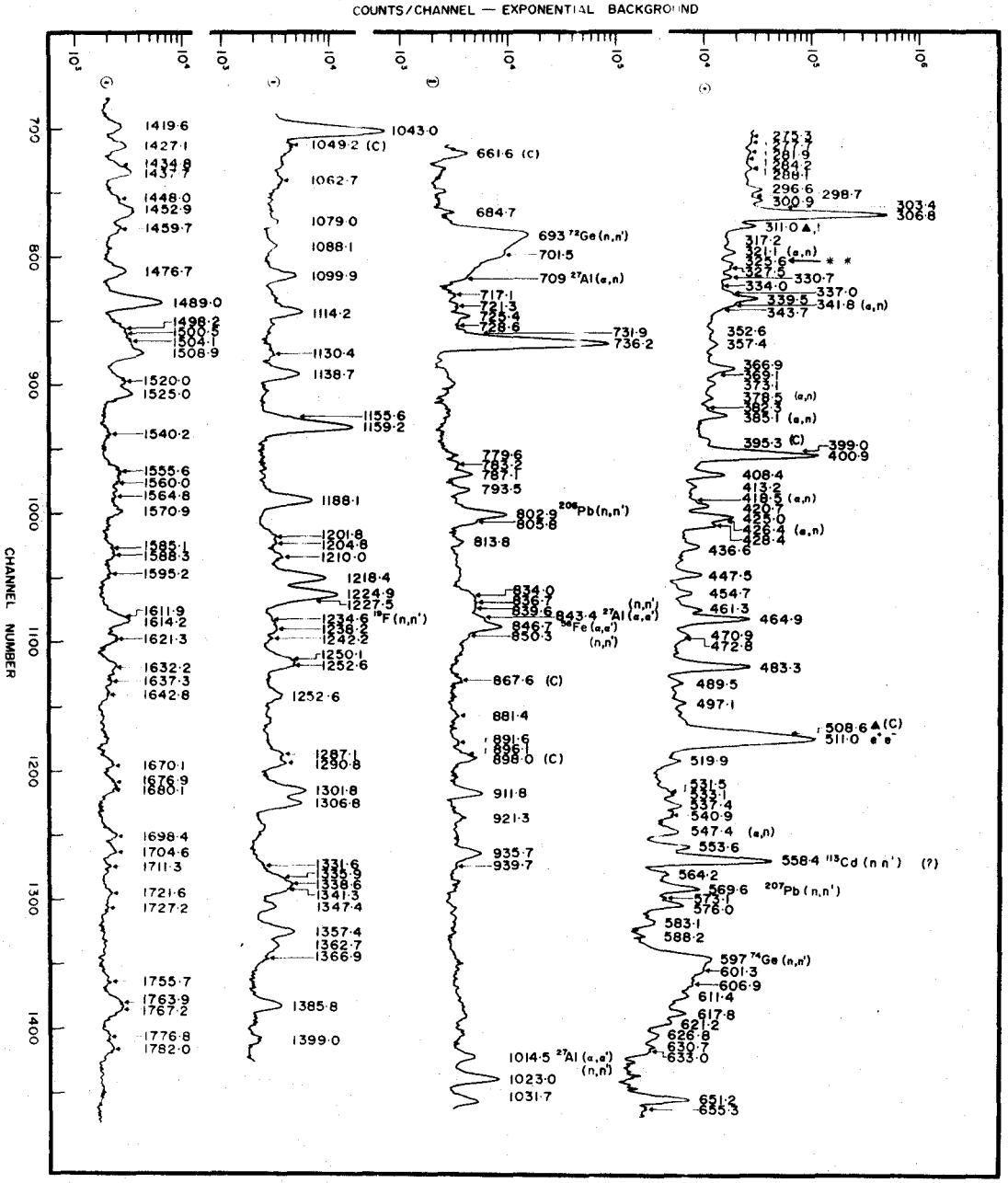
COUNTS/CHANNEL — EXPONENTIAL BACKGROUND
CHANNEL NUMBER
700
800
900
1000
1100
1200
1300
1400
1419·6
1427·1
1434·8
1437·7
1448·0
1452·9
1459·7
1476·7
1489·0
1498·2
1500·5
1504·1
1508·9
1520·0
1525·0
1540·2
1555·6
1560·0
1564·8
1570·9
1585·1
1588·3
1595·2
1611·9
1614·2
1621·3
1632·2
1637·3
1642·8
1670·1
1676·9
1680·1
1698·4
1704·6
1711·3
1721·6
1727·2
1755·7
1763·9
1767·2
1776·8
1782·0
1043·0
1049·2 (C)
1062·7
1079·0
1088·1
1099·9
1114·2
1130·4
1138·7
1155·6
1159·2
1188·1
1201·8
1204·8
1210·0
1218·4
1224·9
1227·5
1234·6 19F (n,n')
1239·2
1242·2
1250·1
1252·6
1252·6
1287·1
1290·8
1301·8
1306·8
1331·6
1335·9
1338·6
1341·3
1347·4
1357·4
1362·7
1366·9
1385·8
1399·0
661·6 (C)
684·7
693 72Ge (n,n')
701·5
709 27Al (α,n)
717·1
721·3
725·4
728·6
731·9
736·2
779·6
784·2
787·1
793·5
802·9 206Pb (n,n')
805·8
813·8
834·0
836·7
839·6
843·4 27Al (α,α') (n,n')
846·7 56Fe (α,α') (n,n')
850·3
867·6 (C)
881·4
891·6
896·1
898·0 (C)
911·8
921·3
935·7
939·7
1014·5 27Al (α,α') (n,n')
1023·0
1031·7
275·3
284·2
288·1
296·6
300·9
298·7
303·4
306·8
311·0 ▲,!
317·2
321·1 (α,n)
325·6
327·5
330·7
334·0
337·0
339·5
341·8 (α,n)
343·7
352·6
357·4
366·9
369·1
373·1
378·5 (α,n)
382·3
385·1 (α,n)
395·3 (C)
399·0
400·9
408·4
413·2
418·5 (α,n)
420·7
425·0
426·4 (α,n)
428·4
436·6
447·5
454·7
461·3
464·9
470·9
472·8
483·3
489·5
497·1
508·6 ▲(C)
511·0 e+e-
519·9
531·5
535·1
537·4
540·9
547·4 (α,n)
553·6
558·4 113Cd (n,n') (?)
564·2
569·6 207Pb (n,n')
573·1
576·0
583·1
588·2
597 74Ge (n,n')
601·3
606·9
611·4
617·8
621·2
626·8
630·7
633·0
651·2
655·3

The agreement between the results from different spectra has been very gratifying since often the program JAGSPOT was required to unravel several partially resolved peaks. For example, the computer fits for the same energy region of the spectrum as recorded by the large and small detectors have been in excellent agreement, even though many complexes in the large detector were not resolved. Furthermore, when complexes were resolved through the γ-γ coincidence experiment, the results were generally in good agreement with those obtained from the computer fits to the singles spectra. In the relatively few cases where the coincidence and singles data disagreed, the former showed that there were several completely unresolved lines in the singles spectra. The tabulated errors in the gamma ray energies are those obtained from the JAGSPOT program or 0.04 keV, whichever is larger. In the case of some peaks, the program gave errors smaller than 0.04 keV which we felt were unrealistic for the conditions of these experiments.

The errors in the measured relative intensities are approximately 15% for well resolved strong transitions; for weaker and partially resolved lines the errors may be much larger. The estimated errors include an allowance for uncertainties in the relative efficiency calibration of the detectors ($\sim$ 10%) and possible angular distribution effects. The latter are expected to contribute $\lesssim$ 10% error since the solid angle subtended by the detector at the target was large

Table 6.1

Transitions in ^{176}Hf Feeding the Ground State Band

Energy keV	Relative* Intensity in Singles	Assignment[e]	I_{88}^{C}[a]	I_{202}^{C}	I_{307}^{C}	I_{401}^{C}	Other Coincident γ's
54.59±0.05		Hf K_{α_2}					
55.77±0.05		Hf K_{α_1}					
63.13±0.05		Hf $K_{\beta_1'}$					
64.96±0.08		Hf $K_{\beta_2'}$					
88.32±0.05	26.5	88.32→ 0	-	100	67	14[b]	583, 554, etc.
91.12±0.05	0.40[c]	1404.4→1313.3					249, 1225
144.45±0.07	0.19	1652.9→1508.5		0.37	≈0.15		912, 1218
146.28±0.05	0.24	2050.2→1903.7					
156.83±0.04	2.7	1404.4→1247.5	2.6				249, 311, 339, 462, 1159
196 ±0.5	≈0.2[c]	(1508.6→1313.2)					1225
196.3 ±0.5	0.15[c]	2160.3→1964.0					249, 311
201.82±0.04	100	290.14→88.3	106	-	70	12[b]	483, 554, etc.
238.36±0.07	0.33	(1628.6→1390.2)					

(continued next page)

Table 6.1 (continued)

Energy keV	Relative* Intensity in Singles	Assignment[e]	I^C_{88} [a]	I^C_{202}	I^C_{307}	I^C_{401}	Other Coincident γ's
248.58±0.04	4.2	1652.9→1404.3	5.2	3.9			91,157,196,311,340, 1023,1114,1159,1225
263.95±0.10	0.30	1577.3→1313.2	0.95	∿0.40	∿0.30	∿0.08	1023, 1225
265.15±0.07	0.40	2050.2→1785.0					1188
268.61±0.12	0.18	(1944.3→1675.8)					
271.8 ±0.3	0.09	(1675.8→1404.3)					
276.4 ±0.3	0.14	(1785.0→1508.6)		∿0.2[d]	∿0.1[d]		1218[d]
306.78±0.04	69.5	596.9→ 290.1	65	71	-	10	483, 554, etc.
311.1 ±0.3	1.1[c]	1964.0→1652.9	1.4	∿1.6	-	-	91,157,196,249,1159, 1225
339.59±0.08	1.3[c]	1992.5→1652.9	2.5	0.63	-	-	157,249,1023,1056[d] 1114, 1159, 1225
352.4 ±0.3	∿0.2	(2137.3→1785.0)					
361.9 ±0.8[c]	0.1[c]	2295.0→1932.7	-	-	0.14	0.10	
400.99±0.04	19.2	997.9→596.9	12[b]	12[b]	10[b]	-	483, 554, etc.

(continued next page)

Table 6.1 (continued)

Energy keV	Relative* Intensity in Singles	Assignment[e]	I^C_{88} [a]	I^C_{202}	I^C_{307}	I^C_{401}	Other Coincident γ's
462.0 ±0.5	0.3[c]	1866.3→1404.3	0.37	∿0.4	-	-	157, 1159[d]
483.33±0.05	5.1	1481.2→ 997.9	3.0[b]	2.9[b]	3.0[b]	2.7[b]	554, 601[d], 814
553.6 ±0.10	1.0	2034.8→1481.2	0.68[b]	0.63[b]	0.5[b]	0.4[b]	
601.3 ±0.6	0.2	([2082.5]→1481.2)	-	-	0.18	.13	483
611.4 ±0.4	0.33	([1609.3]→997.9)	0.6	0.3	0.16	.21	1225
611.4 ±0.6	0.2[c]	([1924.6]→1313.2)					
630.7 ±0.3	0.2[c]	1628.6 →997.9	-	-	0.16	.21	
655.3 ±0.5	∿0.15	(2137.3→1481.2)	-	-	0.13	.15[d]	(483[d]
736.2 ±0.07	28.9	1333.1 →596.9	30	32	32	-	
787.14±0.15	1.0	1785.0 →997.9	.86	.61	0.64	.52	
793.5 ±0.25	0.57	1390.2 →596.9	-	.47	0.53	-	
813.8 ±0.3	0.30	2295.0→1481.2	-	-	0.23	.16	483
857.1 ±0.10	0.33	([1454] →596.9)	-	0.19[b]	0.28	-	

(continued next page)

Table 6.1 (continued)

Energy keV	Relative* Intensity in Singles	Assignment[e]	I^C_{88} [a]	I^C_{202}	I^C_{307}	I^C_{401}	Other Coincident γ's
908 ±1.0	0.2[c]	([1906]→997.9)	-	0.17[d]	0.12[d]	0.21	
911.8 ±0.3	1.8	1508.6 →596.9	.95	1.2	1.4	-	
934.8[c] ±0.5	0.6[c]	1932.7 →997.9	1.5	1.0	0.9	.40	
935.8[c] ±0.5	0.8[c]	1532.7 →596.9					
1023.0 ±0.1	3.2	1313.1 →290.1	3.1	2.5	-	-	
1031.7 ±0.3	1.4	1628.6 →596.9	1.6	1.2	0.95	-	
1043.0 ±0.1	18.5	1333.1 →290.1	18	19	-	-	
1055.8 ±0.5	0.34[c]	1652.9 →596.9	-	-	0.26	-	
1078.9 ±0.3	0.40	(1675.8 →596.9)	-	0.49	0.38	0.21[d]	
1088.1 ±0.2	0.45	2086.0 →997.9	-	0.47	0.30	0.27	
1099.9 ±0.3	1.6	1390.2 →290.1	2.1	1.6	-	-	
1100 ±1.0	0.3[c]	2096.7 →997.9	-	-	0.25	0.26	
1108.7 ±0.5	0.5	(2106.8 →997.9)	-	0.39	0.39	0.30[d]	
1114.2 ±0.1	2.3	1404.3 →290.1	1.8	1.6	-	-	

(continued next page)

Table 6.1 (continued)

Energy keV	Relative* Intensity in Singles	Assignment[e]	I^{C}_{88} [a]	I^{C}_{202}	I^{C}_{307}	I^{C}_{401}	Other Coincident γ's
1130.4 ±0.5	0.50	1727.7 →596.9	-	0.63	0.6	-	
1138.1[c] ±0.5	1.1[c]	1226.3 → 88.3	3.1				
1139.4[c] ±0.5	1.1[c]	2137.3 →997.9		1.5	1.2	1.0	
1150 ±0.1	-	1150 →0 (EO)					
1155.6 ±0.4	0.7	1445.7 →290.1	10.6	1.2	-	-	
1159.2 ±0.2	10.6	1247.5 → 88.3		-			
1160.1[c] ±0.8	0.7	([1450] →290.1)	-	0.68	-	-	
1166.8[c] ±0.8	0.4[c]	([1457] →290.1)	0.4	0.36			
1177.7[c] ±0.8	0.3[c]	([1775] →596.9)	0.6	0.25	0.24	-	
1188.1 ±0.2	4.0	1785.0 →596.9	3.3	3.8	3.3	-	
1201.8 ±0.7	0.4	(1798.4 →596.9)	-	0.32	0.2[d]	-	
1204.8 ±0.6	0.6	(1292.9 → 88.3)					
1218.4 ±0.1	5.0[c]	1508.6 →290.1	4.8	5.6	-	-	
1218.4 ±0.8	0.5[c]	1815.2 →596.9	-	-	0.44	-	
1224.9 ±0.1	7.3	1313.2 → 88.3	7.0	-	-	-	508, 611
1227.5 ±0.2[g]	<1.3	1226.4 →0					
1250.1 ±0.4	1.0	1540.2 →290.1	-	1.2	-	-	

(continued next page)

Table 6.1 (continued)

Energy keV	Relative* Intensity in Singles	Assignment[e]	I^{C}_{88} [a]	I^{C}_{202}	I^{C}_{307}	I^{C}_{401}	Other Coincident γ's
1252.6 ±0.3	2.1	1341.0 → 88.3	2.1	-	-	-	
1265.2 ±0.5	0.9[c]	1861.9 →596.9	-	0.45	0.95		
1281 ±1[c]	0.45[c]	1878 →596.9	-	0.50	0.43	-	
1287.1 ±0.5	0.4[c]	1577.3 →290.1	∿0.5	1.2			
1287.1 ±0.5	0.4[c]	2285.0 →997.9			0.54	0.41	
1290.8 ±0.2	1.2	1379.1 → 88.3	∿0.7		-	-	
1292.9 ±0.3	-	1292.9 → 0 (EO)	-	-	-	-	
1297.2 ±0.8	0.5[c]	2295 →997.9	0.66	0.44	0.16	-	
1301.8 ±0.3	1.3[c]	1390.1 → 88.3	2.6		-	-	
1301.8 ±0.3	1.9[c]	1591.9 →290.1		1.9			
1306.8 ±0.2	2.6[c]	1903.7 →596.9	2.3	2.6	2.9		
1307.0 ±0.8	0.4[c]	2305 →997.9				0.34	
1335.9 ±0.4	1.1	1932.8 →596.9	-	1.0	0.69	-	
1338.6 ±0.4	1.8	1628.7 →290.1	-	1.5	-	-	
1341.3 ±0.3	1.8	1341.0 →0	-	-	-	-	

(continued next page)

Table 6.1 (continued)

Energy keV	Relative* Intensity in Singles	Assignment[e]	I^C_{88} [a]	I^C_{202}	I^C_{307}	I^C_{401}	Other Coincident γ's
1347.4 ±0.2	1.2	1944.3 →596.9	0.64	1.1	0.88	-	
1357.4 ±0.15	2.8	1445.7 → 88.3					
1362.7 ±0.2	0.9[c]	([1959.6]→596.9)+	4.2	1.2	0.88		
1362.7 ±0.2	0.4[c]	(2360.1 →997.9)				0.40	
1385.7 ±0.3	2.1	1675.9 →290.1	1.4	2.0	-	-	
1419.6 ±0.2	1.0	1709.7 →290.1	0.71	1.1	-	-	
1427.1 ±0.2	1.0	2024.0 →596.9	0.85	0.56	0.50	-	
1437.7 ±0.2	1.6	1727.7 →290.1	1.3	1.9	-	-	
1448.0 ±0.6	0.8	([2446.9]→997.9)	-	0.76	0.62	0.35[d]	
1460.2 ±0.7	0.8	([2458.1]→997.9)	-	0.75	0.62	0.32[d]	
1476.7 ±0.2	1.2	1766.8 →290.1	0.43	1.0			
1489.0 ±0.3	4.2[c]	1577.3 → 88.3	4.5	-	-	-	
1489.0[c] ±0.5	1.0[c]	2086.0 →596.9	-	1.2	0.79	-	
1499.8 ±0.5	1.0	2096.7 →596.9	-	1.0	1.0	-	
1508[c] ±1.0	2.0[c]	1798.4 →290.1	1.9	3.4	-	-	

(continued next page)

Table 6.1 (continued)

Energy keV	Relative* Intensity in Singles	Assignment[e]	I_{88}^{C}[a]	I_{202}^{C}	I_{307}^{C}	I_{401}^{C}	Other Coincident γ's
1509.7[c] ±0.8	1.2[c]	2106.8 →596.9	-	-	1.3	-	
1520.0 ±0.3	1.2	2116.9 →596.9	1.4	0.81	0.85	-	
1525.0[c] ±0.5	0.4[c]	1815.2 →290.1	-	0.43	-	-	
1540.2 ±0.5	0.4	1830.3 →290.1	-	0.37	-	-	
1559.5 ±0.8	0.3	2557 →997.9	-	∿0.7	0.39	0.35	
1563 ±1.0	0.9	1853.4 →290.1	-	∿1.2	-	-	
1567 ±1.0	0.2	2565 →997.9	-	∿0.5	0.26	0.27	
1571.6 ±0.8	1.2	1861.9 →290.1	-	1.7	-	-	
1577.0 ±0.8	0.3	2174 →596.9	-	0.25	0.32	-	
1588.3 ±0.5	0.58	(1675.8 → 88.3)					
1614.2 ±0.3	2.0	(1903.7 →290.1)	f)	f)	f)	f)	
1621.3 ±0.3	0.8	(1709.7 → 88.3)	f)	f)	f)	f)	
1670.1 ±0.4	0.70	([1959.6]→290.1)					
1704.6 ±0.3	0.93	([1704.6]→ 0)	f)	f)	f)	f)	

(continued next page)

Table 6.1 (continued)

*Relative intensities observed in the $^{174}Yb(\alpha,2n)^{176}Hf$ reaction with an alpha beam energy of 22.5 MeV

a) I_E^C is the intensity of the upper member of the coincident pair deduced from the spectrum in coincidence with a gate set on the member of the ground state band of energy E.

b) For a stretched E2 cascade, the values of I_E^C are lower than expected because of angular correlation effects.

c) Energy or intensity deduced from γ-γ measurements.

d) At limit of detection.

e) a square bracket indicates a tentative level assignment; a curved bracket indicates a tentative transition assignment.

f) Coincidence spectra recorded only up to 1600 keV.

g) Complex peak.

TABLE 6.2

Gamma Rays Feeding the Isomeric States

Energy (keV)	Relative* Intensity in Singles	Relative Intensity in Delayed Coincidence	Relative Intensity in Double Delayed Coincidence	Assignment[a]
53.49±0.07	3.9[b]			1559.4→1505.8
55.5 ±0.1				Hf K_α's
63.2 ±0.1				Hf K_β's
74.8 ±0.1				Pb K_α's
84.7 ±0.1				Pb K_β's
88.4 ±0.1		0.35[i]		
109.84±0.04[g]	1.7	0.25		^{19}F(n,n')
132.80±0.07	0.16	0.15		1930.8→1798.0
155 ±1		0.09[d]		(2014.4→1860.3)
163.0 ±0.2	0.09	0.24		2194.2→2031.1
169.6 ±0.5		0.34[d]		
172.73±0.04	11.4	11.4[e]		505.8→1333.1
180 ±1		0.06[d]		
192 ±1		0.05[d]		([1977]→1785.1)
194.09±0.04	2.2	2.4		1699.9→1505.8
197.10±0.05[g]	3.0	0.32		^{19}F(n,n')
214.22±0.04	1.0	0.88		1914.1→1699.9
225.74±0.1	5.0		5.1	1785.1→1559.4
226.25±0.06 (6.5)	1.2[b]	7.6		1559.4→1333.1
226.9 ±0.5	0.3[c]			1732.5→1505.8

(continued next Page)

TABLE 6.2 (continued)

Energy (keV)	Relative Intensity in Singles	Relative Intensity in Delayed Coincidence	Relative Intensity in Double Delayed Coincidence	Assignment[a]
229.15±0.07	0.7	0.8	0.8	2014.2→1785.1
233.54±0.1	0.40[f]	0.18		2147.7→1914.1
245.97±0.04	1.91	2.5	1.9[e]	2031.1→1785.1
251.36±0.10	0.10	0.08		2399.0→2147.7
262.78±0.06	0.62	0.7	0.7	2293.9→2031.1
269.64±0.18	0.11	0.11		2563.5→2293.9
272.88±0.1	0.28[f]	0.08		([2304.0]→2031.1)
287.69±0.2	0.20	0.16		(2085.7→1798.0)
288.60±0.2	0.23			
300.78±0.06	1.1	1.8	1.2	1860.2→1559.4
301.5 ±0.8	0.2[c]			([2332.6]→2031.1) or (2085.7→1785.1)
330.77±0.08	0.46	0.34		2261.7→1930.9
334.3 ±0.5		0.10		(2194.2→1860.3)
337.23±0.08	0.62	0.48		2069.7→1732.5
344.3 ±0.5		0.06[d]		([2638.1]→2293.9)
366.87±0.05	1.1	1.4		1699.9→1333.1
368.1 ±0.2	0.16		0.17	2399.0→2031.1
386.3 ±0.6		0.11[d]		2085.7→1699.9
399.38±0.07	2.3	1.8		1732.5→1333.1
404.7 ±0.6		0.16[d]		(2318.4→1914.2)
408.3 ±0.2	1.2[c]	1.2	<0.3	1914.1→1505.4
408.7 ±0.3	0.5[c]			2194.2→1785.1

(continued next page)

TABLE 6.2 (continued)

Energy (keV)	Relative Intensity	Relative Intensity in Delayed Coincidence	Relative Intensity in Double Delayed Coincidence	Assignment[a]
412.9 ±0.2	0.23[f]	0.24		2112.8→1699.9
420.86±0.08	0.91	0.52		1926.7→1505.8
424.96±0.06	1.4	1.2		1930.8→1505.8
428.40±0.07	1.1	1.2		1761.5→1333.1
436.85±0.15	0.61[f]	0.14		
447.66±0.09	0.96	0.52		2147.7→1699.9
455.1 ±0.2	0.42	0.48	∿0.3	2014.4→1559.4
460.7 ±0.5	0.2[c]	0.16		2258.7→1798.0
464.92±0.07	3.3	2.7		1798.0→1333.1
467.4 ±0.3	0.2			2265.4→1798.0
471.6 ±0.2	0.24	0.24	∿0.2	2031.1→1559.4
484.8 ±0.2		0.19[d]		2399.0→1914.1
497.4 ±0.2	0.34	0.24		
508.9[c] ±0.5	0.24[c]			2293.9→1785.1
533.1 ±0.7	0.26	0.30	<0.08	(2564 →2031.1)
			.18 to .26	(2827 →2294)
537.4 ±0.2	0.54[f]	0.34		(2568.5→2031.1)
554.3 ±0.5	∿0.16[c]	0.31		(2568.5→2014.4)
576.0 ±0.5	0.8[f]	0.1		(2361.1→1785.1)
594 ±1	(h)	0.15		(1926.7→1333.1)
598[g]				^{74}Ge(n,n')

(continued next page)

TABLE 6.2 (continued)

Energy (keV)	Relative Intensity in Singles	Relative Intensity in Delayed Coincidence	Relative Intensity in Double Delayed Coincidence	Assignment[a]
607 ±1	0.13	0.22		2112.8→1505.8
618.5 ±0.8	0.2[c]	0.42		2318.4→1699.9
621 ±1	0.2[c]			
626.8 ±0.5	0.31[f]	0.08		([2326.7]→1700.0)
647.0 ±0.8	0.13[c]			([2432] →1785.1)
667.1 ±0.5		0.05		([2173] →1505.9)
694[g]				^{72}Ge(n,n')
701.5 ±0.2	0.51	0.52		
750.2 ±0.5		0.25[d]		
754.5 ±0.5		0.26[d]		
767.6 ±0.5		0.26[d]		([2680.8]→1914.1)
783 ±1	0.15[c]			[2568 →2031.1)
802 ±1	(h)	0.29		([2502] →1700.0)

(a) a square bracket [ ] indicates a tentative level assignment
a curved bracket ( ) indicates a tentative transition assignment

(b) determined from delayed gamma spectrum (see Table 6.7)

(c) intensity determined from γ-γ coincidence measurement

(d) observed in delayed coincidence spectrum only

(e) normalization

(f) complex

(g) emission of neutron coincident with formation of isomeric states

(h) masked

(i) insufficient background subtracted

* relative intensity scale same as in table 6.1

Table 6.3

Unassigned Transitions

Energy (keV)	Relative Intensity[a]	Energy (keV)	Relative Intensity[a]
94.9 ±0.3	0.02	293.15±0.13	0.19
96.3 ±0.1	0.06	297.9 ±0.3	0.18
98.58±0.05	0.15	319.76±0.2	0.12
135.87±0.06	0.09	321.10±0.07	0.41
189.5 ±0.3	0.07		
190.0 ±0.3	0.13	327.57±0.11	0.33
196.3 ±0.2[b]	0.25[c]	372.92±0.12	0.29
219.4 ±0.2	0.07	416.2 ±0.3	0.17
221.26±0.08	0.18	451.8 ±0.5	0.08
244.74±0.09	0.43	454.1 ±0.3	0.20
253.0 ±0.2	0.15	467.4 ±0.3	0.21
268.61±0.12	0.18	497.4 ±0.2	0.22
271.8 ±0.3	0.09	519.9 ±0.2	0.31
277.27±0.15	0.26	531.5 ±1.0	0.11
281.79±0.08	0.34	540.9 ±0.3	0.36
288.6 ±0.2	0.23	564.2 ±0.3	0.36
292.3 ±0.3	0.08		

(continued next page)

TABLE 6.3 (continued)

Energy (keV)	Relative Intensity[a]	Energy (keV)	Relative Intensity[a]
573.0 ±0.6	0.15	891.6 ±0.9	0.23
583.1 ±0.3	0.28	921.2 ±0.6	
588.2 ±1.0	0.07	939.7 ±1.0	0.3
617.8 ±0.1	0.78	1062.7 ±0.4	0.4
633.0 ±0.4	0.3	1201.8 ±0.7	0.4
684.7 ±0.7	0.23	1204.8 ±0.6	0.6
717 ±0.5[b]	∿ 0.2	1210.0 ±0.3	0.9
721.3 ±0.6[b]	∿ 0.2	1227.5 ±0.2	1.4
725.3 ±0.5[b]	∿ 0.45	1238.2 ±0.5	0.8
728.6 ±1.0[b]	∿ 0.1	1242.2 ±1.0	0.3
731.9 ±0.5[b]	∿ 0.2	1331.6 ±0.8	0.3
748.7 ±0.7[b]	∿ 0.2	1366.9 ±0.5	1.5
752.0 ±0.5[b]	∿ 0.4	1399.0 ±0.4	0.5
762 ±1 [b]	∿ 0.3	1434.8 ±1.0	0.5
764 ±1 [b]	∿ 0.2	1504 ±1.0	1.4
779.6 ±0.5	0.25	1555.6 ±0.4	0.9
783.2 ±0.2	0.39	1585.1 ±0.9	0.33
805.8 ±0.2	0.82	1588.3 ±0.5	0.58
836.7 ±0.4	0.6	1595.2 ±0.4	0.44
839.6 ±0.4	0.7	1611.9 ±1.6	0.34
850.3 ±0.5	0.3	1632.2 ±0.4	0.82
881.4 ±0.4	0.26	1637.3 ±0.5	0.56

(continued next page)

TABLE 6.3 (continued)

Energy (keV)	Relative Intensity (a)	Energy (keV)	Relative Intensity (a)
1642.8±0.6	0.54	1727.6±0.5	0.37
1676.9±0.6	0.60	1755.7±0.7	0.37
1680.1±0.5	0.83	1763.9±0.4	1.2
1698.4±0.3	1.0	1767.2±0.4	1.4
1711.3±0.6	0.37	1776.8±0.9	0.38
1721.6±0.4	0.55	1782.0±0.4	0.86

a) The relative intensity scale is the same as that in Table 6.1

b) complex

c) intensity determined from γ-γ coincidence data

TABLE 6.4

Transitions Identified as Impurities

Energy (keV)	Relative Intensity (a)	Origin	Energy (keV)	Relative Intensity (a)	Origin
51.38±0.05		Yb K_{α_2}	136.69±0.04	0.27	^{177}Hf
52.30±0.1		Yb K_{α_1}	153.23±0.05	0.41	^{177}Hf
59.29±0.1		Yb $K_{\beta_2'}$	159.70±0.09	0.12	^{177}Hf
61.0 ±0.2		Yb $K_{\beta_2'}$	162.37±0.15	0.12	
66.94±0.04	0.37	Au K_{α_2}	169.2 ±0.2	0.06	^{175}Hf
68.79±0.04	0.68	Au K_{α_1}	174.3 ±0.14	0.61	^{177}Hf
72.76±0.04	4.4	Pb K_{α_2}	176.61±0.04	1.6	^{174}Yb(α,α')
74.93±0.03	8.1	Pb K_{α_1}	179.15±0.09	0.15	^{175}Hf
76.42±0.04	7.9	^{174}Yb(α,α')	185.9 ±0.2	0.07	^{175}Hf
80.2 ±0.4	0.03	Au K_{β_2}	197.10±0.04	3.0	^{19}F(n,n')
81.53±0.06 (b)	0.20	^{175}Hf	206.39±0.05	0.93	^{174}Hf
84.75±0.1	3.9	Pb $K_{\beta_1'}$	207.40±0.05	0.78	^{175}Hf
87.19±0.1	9.9	Pb $K_{\beta_2'}$	208.33±0.04	2.9	^{177}Hf
93.13±0.05	0.16	^{178}Hf	213.41±0.05 (b)	0.7	^{178}Hf
100.74±0.04	0.19	^{175}Hf	214.4 ±0.1	0.1(c)	^{177}Hf
104.31±0.07	0.26	^{175}Hf	216.15±0.05	0.36	
105.31±0.04	0.57	^{177}Hf	228.52±0.16	0.18	^{177}Hf
109.84±0.04	1.7	^{19}F(n,n')	231.04±0.10	0.30	^{175}Hf
112.90±0.04	2.0	^{177}Hf	238.36±0.07	0.33	^{16}O(α,n)^{19}Ne(?)
125.90±0.04	0.78	^{175}Hf	249.53±0.05	1.4	^{177}Hf
126.57±0.06	0.22	^{175}Hf	274.96±0.07	0.37	^{175}Hf
128.46±0.04	0.48	^{177}Hf	278.68±0.15	0.17	^{175}Hf
130.23±0.06	0.09	^{175}Hf	289.6 ±0.4	0.11	

(continued next page)

TABLE 6.4 (continued)

Energy (keV)	Relative Intensity (a)	Origin	Energy (keV)	Relative Intensity (a)	Origin
296.51±0.04 (b)	1.4	^{177}Hf	597		^{74}Ge(n,n')
311.1 ±0.3	1.0(c)	^{174}Hf	569.6 ±0.1	1.3	^{207}Pb(n,n')
317.58±0.13	0.21	^{175}Hf	651.2 ±0.1	1.7	^{139}La(α,p)
325.63±0.08 (b)	0.42	^{178}Hf	661.6 ±0.2	0.6	^{137}Cs (?)
339.6 ±0.1	1.3(c)		693		^{72}Ge(n,n')
341.73±0.07	0.70	^{177}Hf	802.92±0.12	2.8	^{206}Pb(n,n')
378.6 ±0.2	0.28	^{177}Hf	834.0 ±0.4	0.5	
385.11±0.06	1.0	^{177}Hf	843.4 ±0.2	1.2	^{27}Al(n,n') (α,α')
395.50±0.10	0.26		846.7 ±0.1	2.5	^{56}Fe(n,n') (α,α')
418.76±0.19	0.30	^{177}Hf			
426.31±0.09	0.89	^{178}Hf + ^{177}Hf	867.6 ±0.4	0.37	
			898.0 ±0.5	1.3	
466.10±0.11 (b)	0.67	^{177}Hf(?)	1014.46±0.13	2.1	^{27}Al(n,n') (α,α')
508.5 ±0.3	4.3(c)				
511.0 ±0.1	26.5	e^+e^-	1049.2±0.4	0.7	
547.4 ±0.2	0.6	^{177}Hf	1234.6±0.7	0.4	^{19}F(n,n')
558.4 ±0.1	8.9	^{113}Cd(n,γ)	1453.8±0.3	2.4	^{27}Al(α,n) (?)

(a) The relative intensity scale is the same as that in Table 6.1.

(b) complex

(c) intensity of component belonging to ^{176}Hf (determined from γ-γ coincidence data) subtracted.

enough to smear out the anisotropy.

The energies and intensities resulting from these analyses are presented in Tables 6.1 to 6.4. Table 6.1 lists the transitions that feed members of the ground state band and includes both the assignments and the coincidence information on which these were made. Table 6.2 lists the transitions that feed the isomeric states while 6.3 and 6.4 respectively list the unclassified transitions and those that have been identified in other reactions. The assignments will be discussed later.

b) Excitation functions

Singles spectra were recorded at beam energies of 16.5, 18.0, 19.5, 21.0, 22.5, and 24 MeV in order to determine the excitation functions for individual gamma ray transitions. These spectra were analysed in the fashion described above and the ratio $\frac{(I_\gamma/I_{88})E_\alpha}{(I_\gamma/I_{88})E_{\alpha=24\ MeV}}$ was plotted as a function of beam energy to obtain relative excitation curves for individual transitions. (The 88 keV line is the 2→0 transition of the g.s.b.) This procedure made it possible to distinguish transitions associated with the (α,2n) reactions from others and also to give a rough indication of the spin of the state deexcited by the transition.

Fig. 6.5 shows the relative excitation function of a few transitions originating from the $^{174}Yb(\alpha,n)^{177}Hf$ and $^{174}Yb(\alpha,a')^{174}Yb$ reactions; the spins of the states which

Figure 6.5

Relative excitation functions of some gamma rays originating from contaminant reactions.

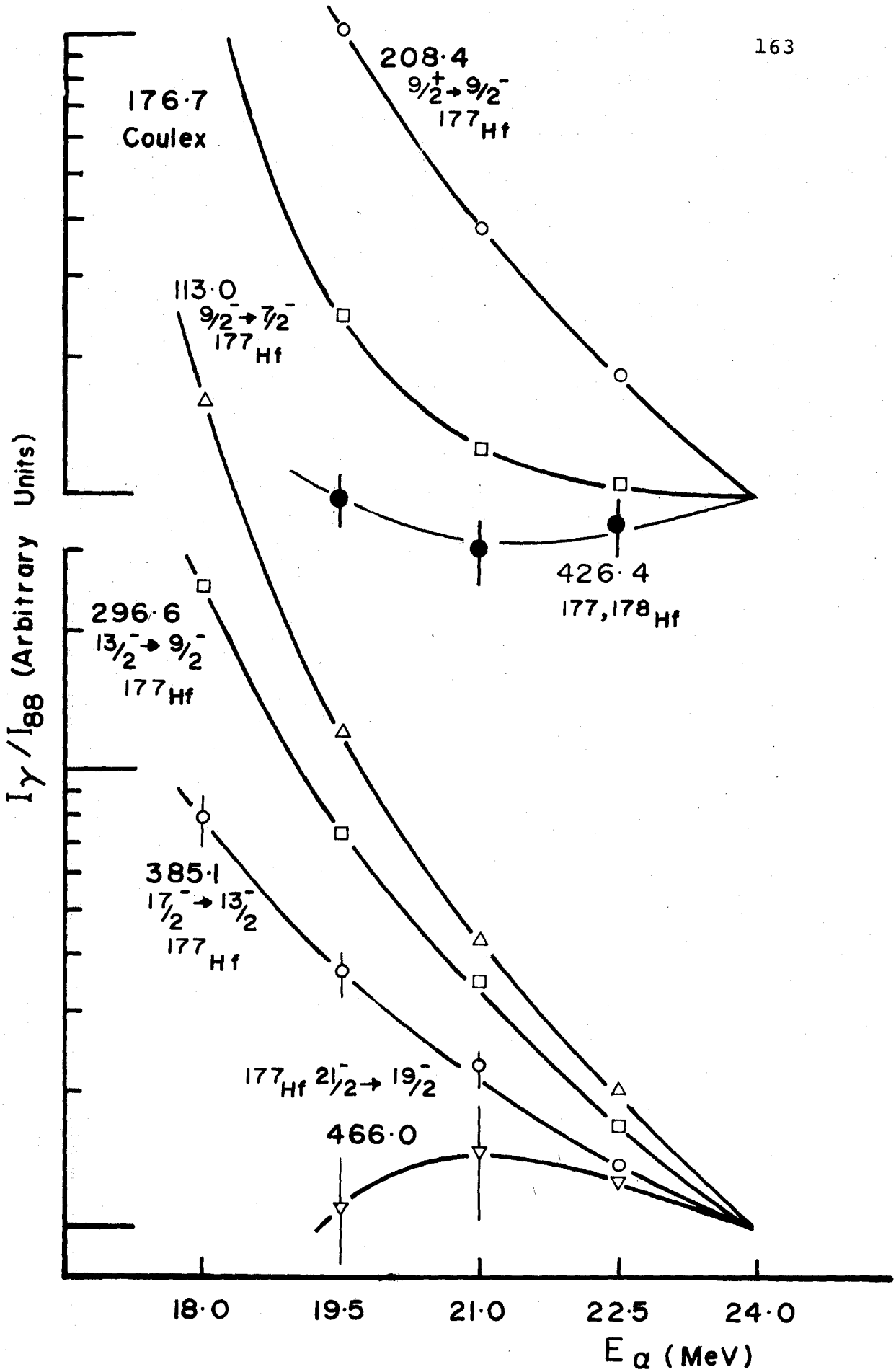
208·4
9/2+ → 9/2−
177Hf
176·7
Coulex
113·0
9/2− → 7/2−
177Hf
426·4
177,178Hf
296·6
13/2− → 9/2−
177Hf
385·1
17/2− → 13/2−
177Hf
177Hf 21/2− → 19/2−
466·0
Iγ / I88 (Arbitrary Units)
18·0
19·5
21·0
22·5
24·0
Eα (MeV)

these transitions connect are also given. It may be seen that, as the bombarding alpha energy increases, the yields of these gamma rays decreases relative to that of the 88 keV line, the decrease being less rapid for lines originating from higher spin states. The shape of the curve for the 466 (21/2 → 17/2) transition indicates that,with an alpha energy of 18 MeV, insufficient angular momentum is brought into the system to significantly populate states with spins $\gtrsim$ 21/2. The form of the curve for the 426 line clearly indicates that it consists of two components, one from the (α,n) reaction, and another from the (α,2n) reaction (resulting in this case in ^{178}Hf).

The relative excitation functions of the g.s.b. transition in ^{176}Hf, are shown in fig. 6.6. It is observed that the higher the spin of a state, the more rapidly its yield increases with alpha energy, in accord with the expectation from the statistical theory. If the gamma deexcitation from the product nucleus were completely statistical, the excitation functions for all states with the same spin should be identical and one could use them to assign spins uniquely. In fact, as pointed out in Chapter 2, this is not the case and therefore the shape of the excitation curve can only be used as a rough guide to the spin. Within a rotational band, however, the excitation curves may be used more confidently to

Figure 6.6

Relative excitation functions of transitions from the ground state band (upper set) and the $K=2^-$ octupole band (lower set).

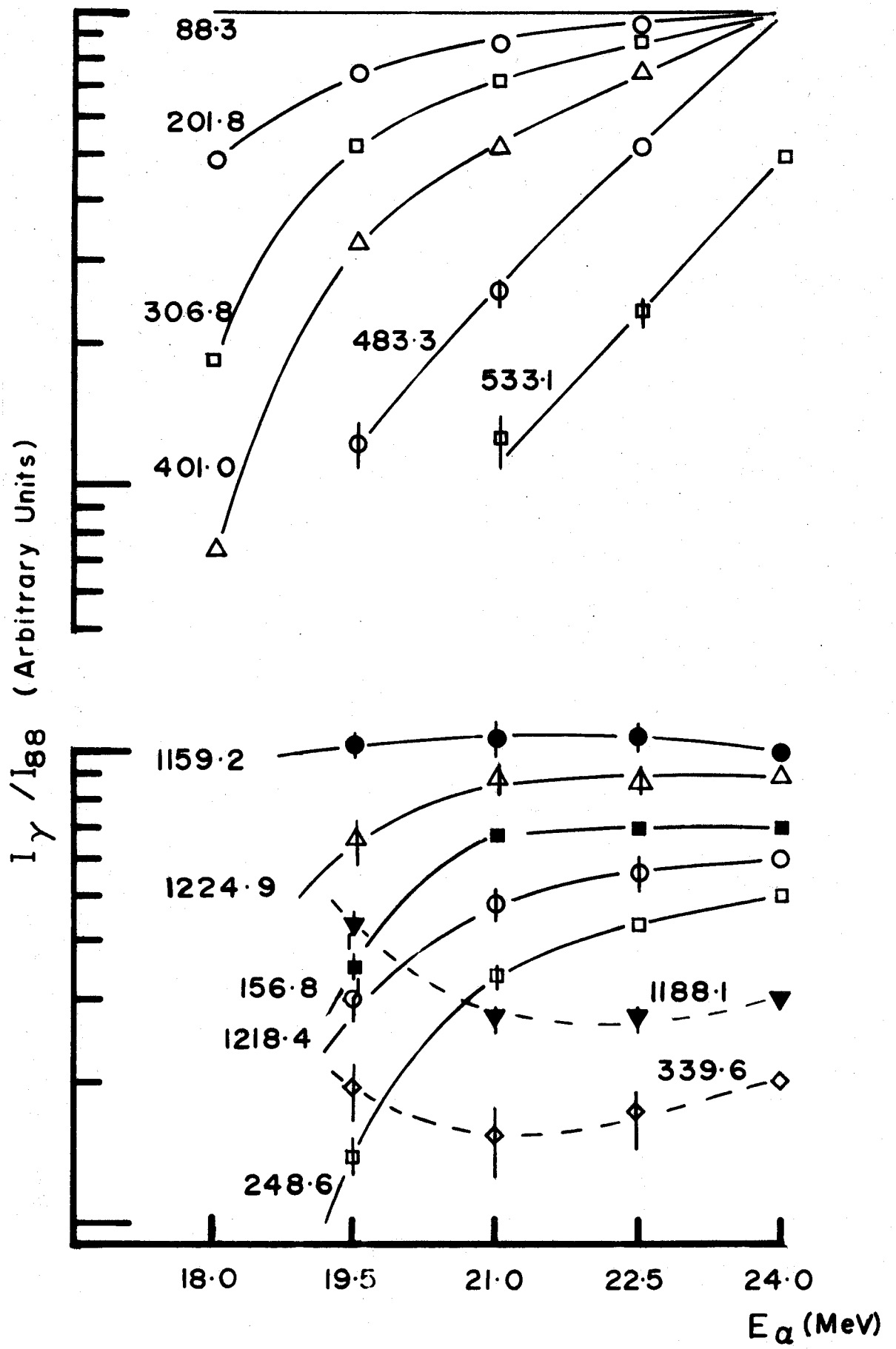
88·3
201·8
306·8
401·0
483·3
533·1
1159·2
1224·9
156·8
1218·4
248·6
1188·1
339·6
I_γ / I_{88} (Arbitrary Units)
18·0
19·5
21·0
22·5
24·0
E_α (MeV)

check the ordering of the members. For example, the lower section of Fig. 6.6 shows the relative excitation functions of a number of transitions within the 2- octupole band. The changes in slope exhibited by the 339.6 and 1188.1 keV excitation functions clearly indicate the presence of unresolved components which do not arise from the (α,2n) reaction. Fig. 6.7 shows the excitation functions associated with the transitions within the $K = 6^+$ and $K = 8^-$ bands based on the 1333 and 1559 keV states. The figure also includes the excitation function for the 736 keV transition deexciting the 1333 keV level. The 194.0 and 233.5 keV excitation functions are obviously due to doublets.

6.3 In-Beam Conversion Electron Spectra

Conversion electron spectra from 700 to 1400 keV were measured with the orange spectrometer at alpha beam energies of 18.5, 19.5, 20.5 and 22.5 MeV. The resultant spectra are shown in Fig. 6.8. The momentum resolution in these measurements was 0.9% corresponding to a line width of $\sim$ 15 keV for electron peaks at 1300 keV. With this resolution it was impossible to resolve many of the transitions.

The situation is clearly revealed in Fig. 6.9 which

Figure 6.7

Relative excitation functions for transitions from the $K = 6^+$ band at 1333 keV (upper set) and from the $K = 8^-$ band at 1559 keV (lower set).

*Complex peak.

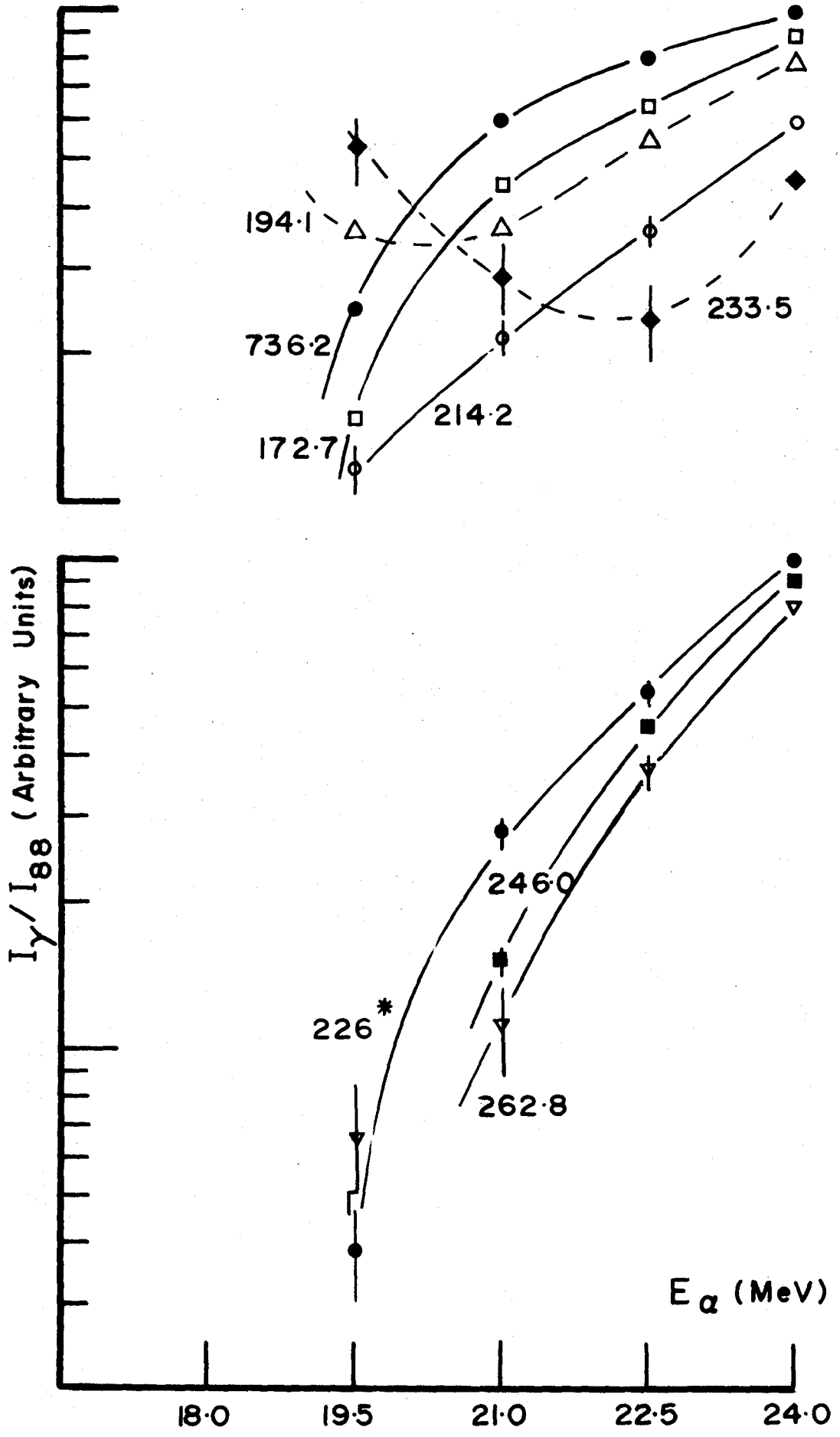
194·1
736·2
172·7
214·2
233·5
246·0
226*
262·8
I_γ / I_{88} (Arbitrary Units)
E_α (MeV)
18·0
19·5
21·0
22·5
24·0

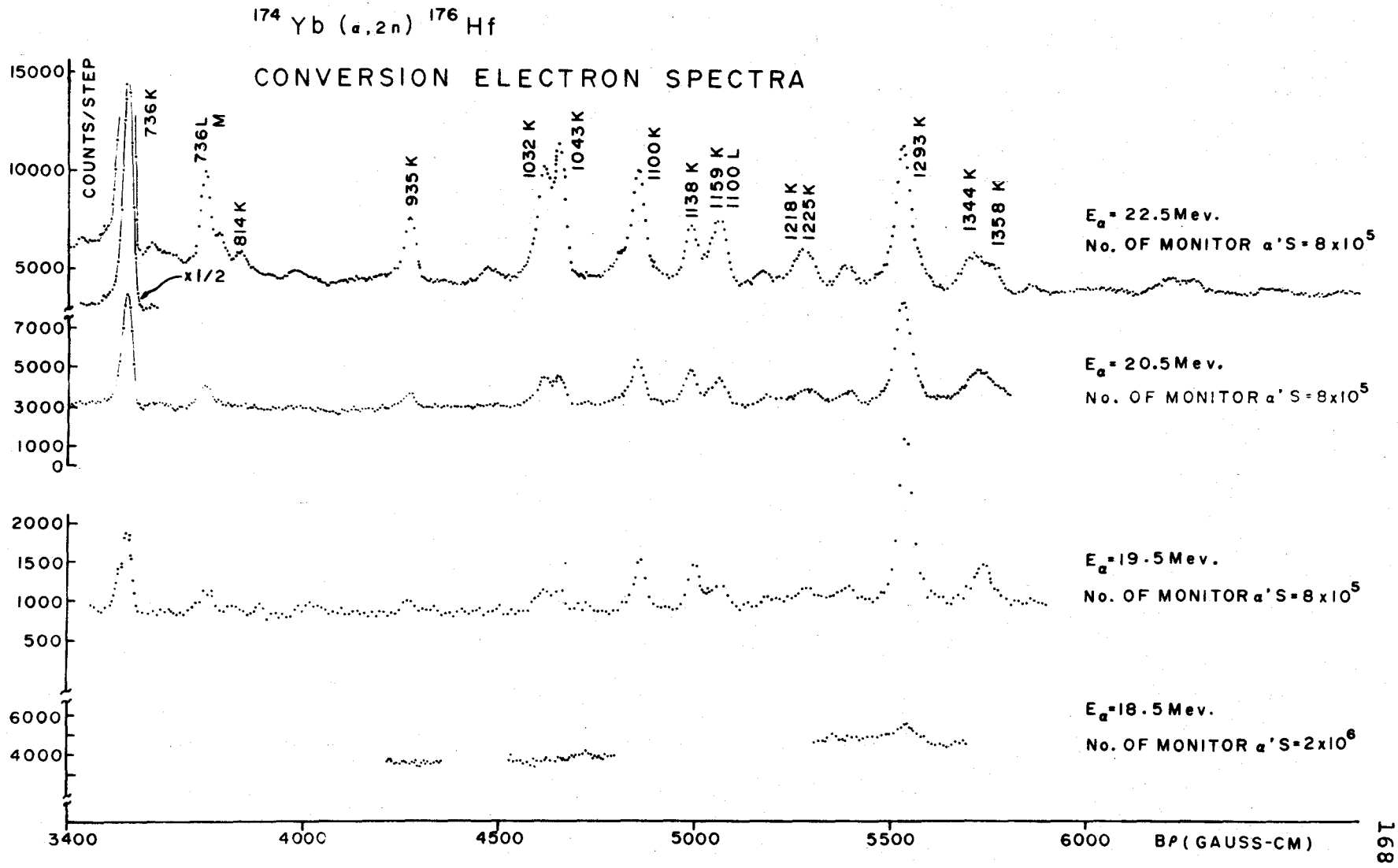

Figure 6.8

In-beam conversion electron spectra. Recorded with the "orange" spectrometer at a resolution of 1%

presents a portion of fig. 6.8 together with the corresponding gamma ray spectrum. In the energy region presented, the electron energy is almost proportional to the momentum and it was therefore possible to adjust the energy scale of the gamma spectrum to match the momentum scale of the electron spectrum over the 400 keV range of fig. 6.9. When one considers that the transition at 1043 keV in pure E2, it is clear that strong peaks at 935, 1032, 1100 and 1293 keV contain large EO admixtures.

In an attempt to resolve some of the multiplets in fig. 6.8, the spectrum was recorded again with better resolution (0.5% in momentum) at a beam energy of 22.5 keV.

The resulting spectrum, shown in fig. 6.10, is considerably better than the corresponding spectrum of fig. 6.8, but it is still not good enough to resolve all the conversion lines. It was not practicable to reduce the resolution much below 0.5% because of the severe loss in transmission which would have resulted.

The electron lines observed are listed in table 6.5, together with the deduced K conversion coefficients (α_k), the assigned multipolarity (where possible), and the theoretical conversion coefficients which have been taken from the tabulation of Hager and Seltzer (1968). The electron intensities have been normalised to correspond to the gamma intensity

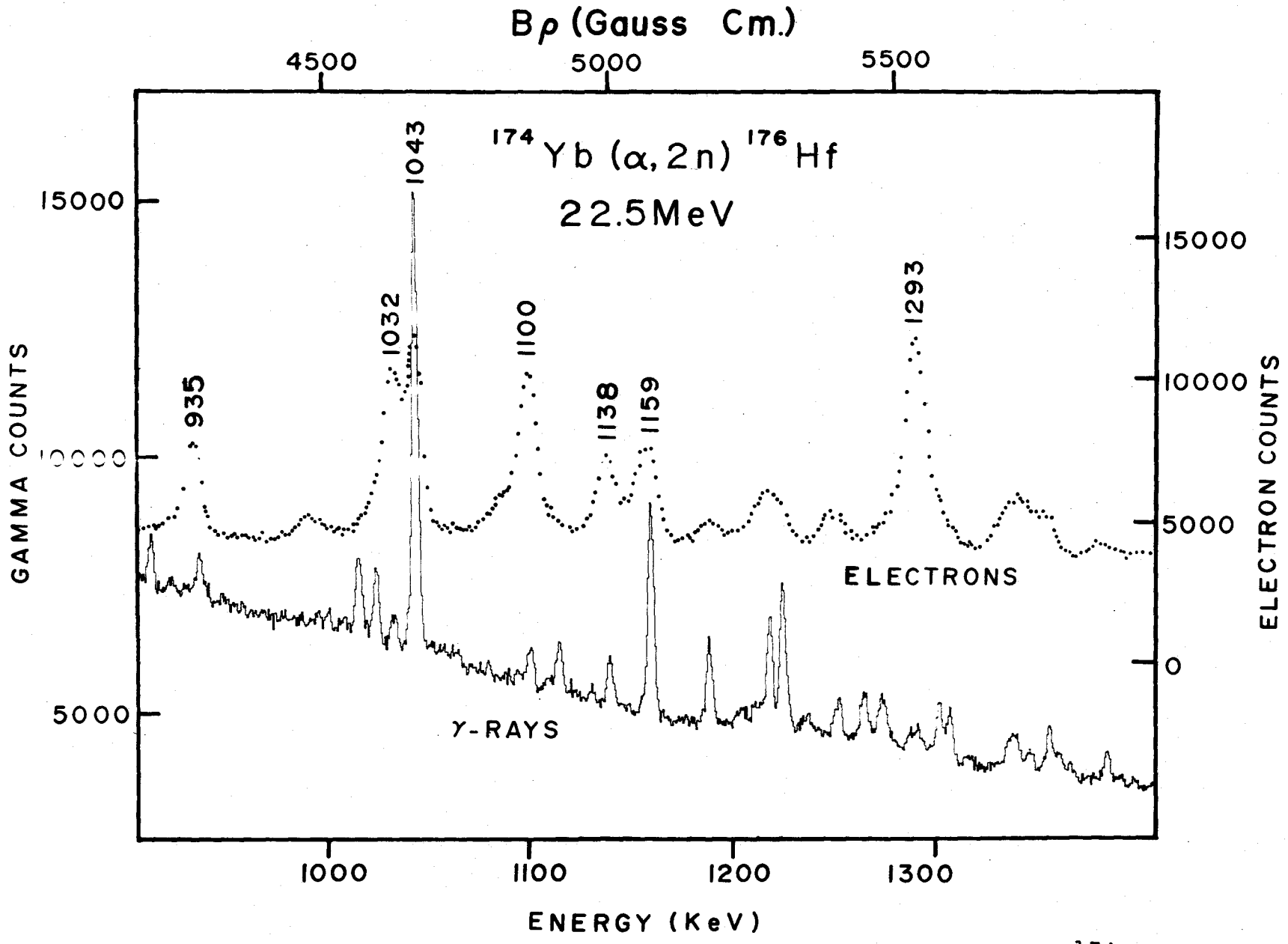

Figure 6.9: Comparison of γ-ray and conversion electron spectra from the ^{174}Yb (α,2n) ^{176}Hf reaction

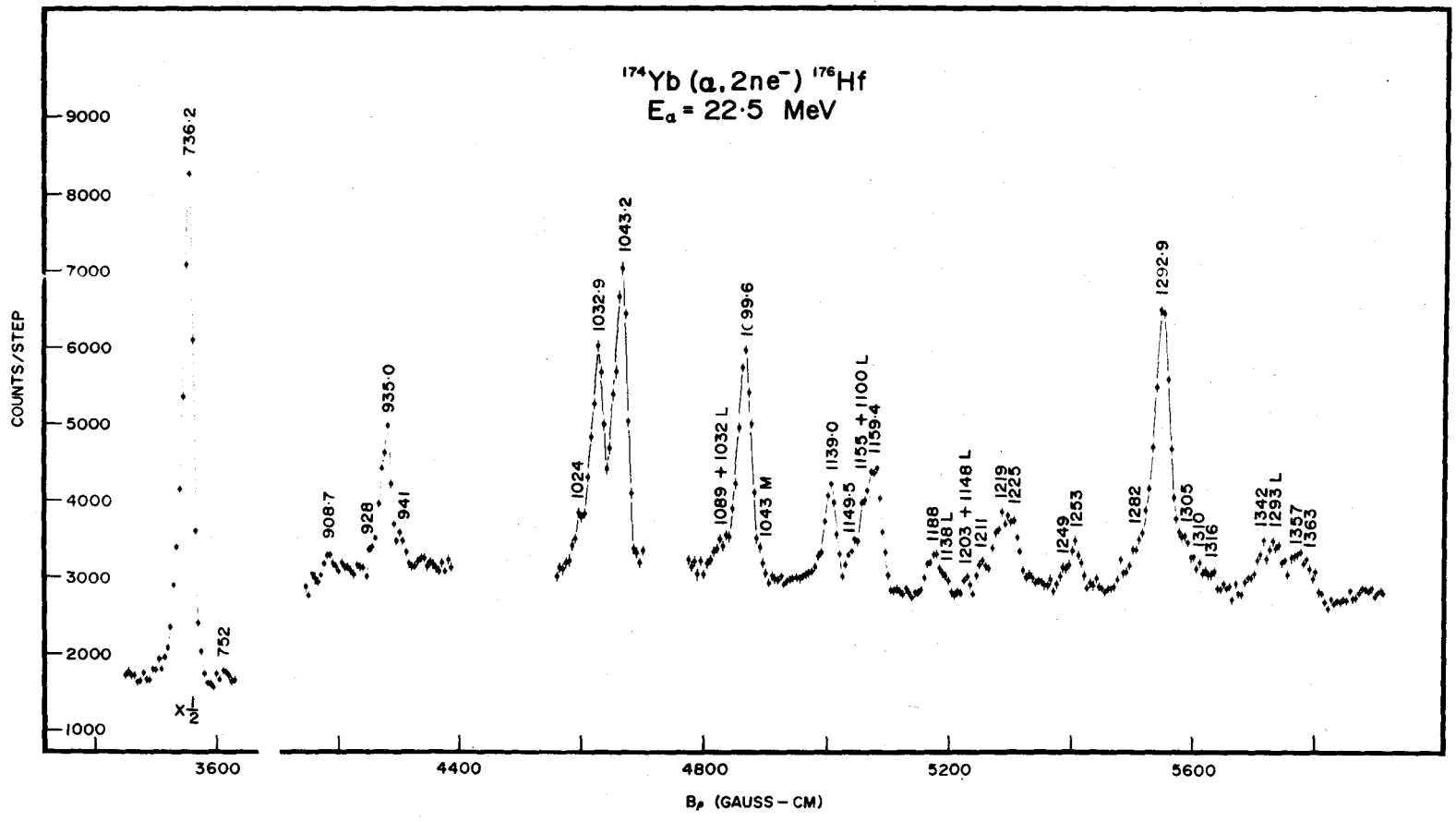

Figure 6.10

Conversion electron spectrum. Recorded with the "orange" spectrometer at a resolution of 0.5%

Table 6.5

Conversion Electron Intensities and Coefficients in ^{176}Hf

E_γ keV	I_γ	$I_e \times 10^3$	$\alpha_K \times 10^3$	Theoretical $\alpha_K \times 10^3$			Assigned[a] Multipolarity	Origin[b]
				E1	E2	M1		
736.21 ± 0.05	28.9	179 ± 3[d]	6.2	2.5	6.2	15.5	E2 (assumed)	
752 ± 0.5	0.4	7.3 ± 1.5	18 ± 5	2.3	6.0	14.0	(M1)	
764 ± 1	0.2	4.2 ± 1.5	21 ± 8	2.3	5.8	13.5	(M1)	
783.2 ± 0.3	0.39	5.3 ± 2.3	13.5 ± 6	2.2	5.5	13.3	(M1)	
787.1 ± 0.2	1.0	4.5 ± 2.3	4.5 ± 2.4	2.2	5.5	13.3		
805.8 ± 0.2	0.8	2.2 ± 1.5	2.7 ± 1.9	2.0	5.1	12.0	E1	
813.8 ± 0.3	0.30	9.0 ± 1.5	30 ± 5	2.0	5.1	12.0	E0 + E2 + M1	2295.0
850.3 ± 0.5	0.3	3.9 ± 1.5	13 ± 5	1.9	4.6	10.6	(M1)	
857.1 ± 1.0	0.33	2.2 ± 1.5	6.8 ± 3	1.9	4.6	10.6	(M1+E2)	
908 ± 1	0.2	1.7 ± 0.8	8.5 ± 3	1.6	4.0	9.3	(M1 + E2)	(1906)
911.8 ± 0.3	1.8	1.3 ± 0.6	0.7 ± 0.3	1.6	4.0	9.3	E1	1508.6
934.8 ± 0.5	0.6	24.0 ± 1.3	17.1 ± 2.6	1.5	3.8	8.4	E0 + E2 + M1	1932.7
935.8 ± 0.5	0.8							
940 ± 1	0.3	5.1 ± 1.6	17.1 ± 6	1.5	3.7	8.3	(E0+E2+M1)	
1023.0 ± 0.1	3.2	5.8 ± 1.2	1.8 ± 0.5	1.3	3.2	6.9	E1	1313.2

Table 6.5 (continued)

E_γ keV	I_γ	I_e x 10^3	α_K x 10^3	Theoretical α_K x 10^3			Assigned[a] Multipolarity	Origin[b]
				E1	E2	M1		
1031.7 ± 0.3	1.4	36.7 ± 2.6	25.6 ± 4.4	1.3	3.1	6.8	E0 + E2 + M1	1628.6
1043.0 ± 0.1	18.5	51.4 ± 2.6	2.7 ± 0.5	1.3	3.0	6.6	E2	1333.1
1078.9 ± 0.3	0.4	1.3 ± 1.0	3.3 ± 2.3	1.2	2.9	6.0		
1088.1 ± 0.5	0.5	< 2.6	< 5.2	1.2	2.8	5.8		
1099.9 ± 0.3	1.6	34.0 ± 2.6	21.2 ± 3.8	1.1	2.8	5.8	E0 + E2 + M1	1390.2
1100 ± 1	~0.3							
1108.7 ± 0.5	0.5	< 1.3	< 2.6	1.1	2.7	5.7		
1114.2 ± 0.1	2.2	< 1.3	< 0.6	1.1	2.6	5.6	E1	1404.3
1138.1 ± 0.5[c]	1.1	17.2 ± 1.3	7.8 ± 1.3	1.1	2.6	5.3	E0 + E2 + M1	1226.4
1139.4 ± 0.5[c]	1.1							
1149.5 ± 1.0	<0.1	4.0 ± 1.9	> 40	1.1	2.6	5.2	E0	1149.5
1155.6 ± 0.7	0.7	6.0 ± 1.9	8.6 ± 3.4	1.1	2.5	5.2	(M1)	1445.7
1159.2 ± 0.2	10.6	20.1 ± 1.3	1.9 ± 0.5	1.1	2.5	5.2	E1 + (M2+E3)[e]	
1160.1 ± 0.8								
1188.1 ± 0.2	4.0	5.7 ± 1.3	1.4 ± 0.4	1.0	2.4	5.0	E1	1785.0
1201.8 ± 0.7	0.4	1.7 ± 0.7	1.7 ± 0.7	0.98	2.3	4.7		
1204.8 ± 0.6	0.6							

Table 6.5 (continued)

E_γ keV	I_γ	I_e x 10^3	α_K x 10^3	Theoretical α_K x 10^3			Assigned[a] Multipolarity	Origin[b]
				E1	E2	M1		
1210.0 ± 0.3	0.9	2.2 ± 0.6	2.5 ± 0.8	0.97	2.3	4.6	(M1 + E2)	
1218.4 ± 0.1[c]	5.0	13.0 ± 2.6	2.6 ± 0.5	0.95	2.2	4.5		
1218.4 ± 0.8[c]	0.5							
1224.9 ± 0.1	7.3	11.0 ± 1.9	1.3 ± 0.3	0.94	2.2	4.5	E1	1313.2
1227.5 ± 0.2	1.4							
1250.1 ± 0.4	1.0	2.6 ± 1.3	2.6 ± 1.3	0.90	2.2	4.3	(M1+E2)	
1252.6 ± 0.3	2.1	6.5 ± 1.9	3.1 ± 1.0	0.90	2.2	4.3	(M1 + E2)	1341.0
1281 ± 1[c]	0.4	1.9 ± 1.3	4.8 ± 3	0.87	2.1	4.2		
1290.8 ± 0.2	1.2	10.4 ± 2.6[f]	8.7 ± 2.9	0.86	2.0	4.0	E0 + E2 + M1	1379.2
1293.2 ± 0.5	<0.38	38.7 ± 6.5[f]	>100	0.86	2.0	4.0	E0	1293.2
1301.8 ± 0.3[c]	1.3	6.5 ± 1.9	2.0 ± 0.7	0.85	2.0	3.8		
1301.8 ± 0.3[c]	1.9							
1306.8 ± 0.1	2.6	4.5 ± 1.9	1.5 ± 0.7	0.85	2.0	3.8		
1307.0 ± 0.8	0.4							
1331.6 ± 0.8	0.3	1.3 ± 0.8	4.3 ± 3	0.82	1.9	3.6		
1335.9 ± 0.4	1.1	6.5 ± 1.9		0.82	1.9	3.6		
1338.6 ± 0.4	1.8							
1341.3 ± 0.3	1.8							

Table 6.5 (continued)

E_γ keV	I_γ	I_e x 10^3	α_K x 10^3	Theoretical α_K x 10^3			Assigned[a] Multipolarity	Origin[b]
				E1	E2	M1		
1347.4 ± 0.2	1.2	3.2 ± 1.9	2.6 ± 1.6	0.80	1.9	3.6		
1357.4 ± 0.1	2.8	6.5 ± 1.3	2.3 ± 0.5	0.79	1.8	3.5	(M1 + E2)	1445.7
1362.7 ± 0.5[c]	0.9	5.8 ± 1.3	4.5 ± 1.0	0.78	1.8	3.5		
1362.7 ± 0.5[c]	0.4							
1366.9 ± 0.5	1.5	1.9 ± 1.0	1.2 ± 0.7	0.77	1.8	3.4		
1385.7 ± 0.3	2.1	2.6 ± 1.0	1.3 ± 0.5	0.76	1.8	3.4	E1 or E2	1675.8
1399.0 ± 0.4	0.5	< 0.7	< 1.4	0.75	1.7	3.2		
1419.6 ± 0.2	1.0	0.9 ± 0.5	0.9 ± 0.5	0.73	1.7	3.2	(E1)	1709.7
1427.1 ± 0.2	0.8	2.2 ± 0.7	2.7 ± 0.9	0.73	1.7	3.1	(M1 + E2)	2024.0
1434.8 ± 1.2	0.5	< 0.7	< 1.4	0.70	1.6	3.1		
1437.7 ± 0.2	1.6	2.0 ± 0.7	1.2 ± 0.5	0.70	1.6	3.1		
1448.4 ± 0.6	0.8	1.1 ± 0.7	1.4 ± 0.9	0.70	1.6	3.0		
1453.8 ± 0.3	2.4[f]	1.2 ± 0.4	0.5 ± 0.2	0.70	1.6	3.0		
1460.2 ± 0.7	0.8	< 0.7	< 0.9	0.69	1.6	2.9	E1	2457.6
1476.7 ± 0.2	1.2	2.5 ± 0.7	2.1 ± 0.7	0.68	1.6	2.9	(M1 + E2)	1766.8
1489.0 ± 0.3[c]	4.2	6.5 ± 0.7	1.2 ± 0.3	0.67	1.5	2.8		
1489.0 ± 0.5[c]	1.0							
1499.8 ± 0.5	1.0	4.3 ± 0.4	4.3 ± 0.8	0.66	1.5	2.8	(M1)	2096.7

Tabled 6.5 (continued)

E_γ keV	I_γ	I_e x 10^3	α_K x 10^3	Theoretical α_K x 10^3			Assigned[a] Multipolarity	Origin[b]
				E1	E2	M1		
1504.0 ± 1.0	1.4							
1508.0 ± 0.8	2.0	5.0 ± 1.1	1.1 ± 0.3	0.66	1.5	2.7		
1510.2 ± 0.8	1.2							
1520.0 ± 0.3	1.2	1.1 ± 0.5	0.9 ± 0.4	0.65	1.5	2.6	(E1)	2116.9
1525.0 ± 0.2	0.4	0.7 ± 0.4	1.7 ± 1.0	0.65	1.5	2.6		
1540.2 ± 0.5	0.4	0.4 ± 0.4	1.0 ± 1.0	0.64	1.4	2.6		
1555.6 ± 0.4	0.9	2.5 ± 0.4	2.7 ± 0.5	0.63	1.4	2.5	(M1 + E2)	
1559.5 ± 1.0[c]	0.3							
1559.5 ± 1.0[c]	0.3	2.0 ± 0.5	1.7 ± 0.5	0.62	1.4	2.5		
1563.0 ± 0.8	0.9							
1571.6 ± 0.8	1.2	2.1 ± 0.7	1.8 ± 0.7	0.62	1.4	2.4	(M1 + E2)	1860.7
1585.1 ± 0.9	0.33	1.0 ± 0.4	1.1 ± 0.4	0.61	1.4	2.4		
1588.3 ± 0.5	0.58							
1595.2 ± 0.4	0.44	< 0.5	< 1.1	0.60	1.4	2.3		
1612 ± 1	0.34	1.8 ± 0.7	0.8 ± 0.3	0.58	1.4	2.3		
1614.2 ± 0.3	2.0						(E1)	1903.7
1621.3 ± 0.3	0.7	0.9 ± 0.5	1.3 ± 0.8	0.57	1.3	2.3		

Table 6.5 (continued)

E_γ keV	I_γ	I_e x 10^3	α_K x 10^3	Theoretical α_K x 10^3			Assigned[a] Multipolarity	Origin[b]
				E1	E2	M1		
1632.2 ± 0.4	0.82	1.1 ± 0.5	0.8 ± 0.3	0.56	1.3	2.3		
1637.3 ± 0.5	0.56							

(a) A bracket indicates a tentative assignment. A (M1+E2) assignment is considered to be M1 and/or E2.

(b) The level from which a transition originates; this is given only when the multipolarity is known.

(c) Resolved by coincidence measurement.

(d) Normalization.

(e) E1 - M2 - E3 admixture deduced from branching ratios (see Table 7.6), consistent with coversion coefficient.

(f) Separation of the electron complex at 1293 keV based on the intensities given by Bernthal et al (1971).

(g) Might contain an impurity line.

scale, using the fact that the strong 736 keV transition is pure E2 in character (Borggreen et al. 1967). The K-conversion coefficient is then simply defined as

$$\alpha_k = \frac{I_e}{I_\gamma} \quad .$$

A check on the normalisation procedure is provided by the agreement between the experimental and theoretical values of α_k for the 1043 keV E2 transition. The energies quoted in Table 6.5 were taken from the gamma ray measurements. The superior precision and resolution in these measurements made it possible to determine the positions of the corresponding conversion electron lines within an unresolved peak. These peaks were then decomposed into components using the line shape of the strong 736 keV K-line appropriately modified to allow for the change in line width with momentum. The difficulties inherent in this process led to large uncertainties in many of the conversion line intensities and the resulting conversion coefficients. Nevertheless, the results are adequate to identify those transitions which are either pure E0 or contain a large E0 admixture. In some cases it has also been possible to distinguish between E1 and (M1+E2) transitions. In making this analysis, it has been tacitly assumed that the transitions of higher multipolarity (M2, E3 etc) do not occur with measurable intensity.

At the time when this thesis was being prepared, the

conversion electron data were extended to include the range of electron energies from 150 to 800 keV. These measurements were made at a beam energy of 24 MeV and a resolution of 0.5%. Although the data obtained in this experiment is not included in the thesis, the measured conversion coefficients for a few of the crucial transitions have been used in the interpretation.

6.4 The γ-γ Coincidence Data

The γ-γ coincidence experiment was performed and analysed in the manner described in section 4.6. A total of 34×10^6 events were collected on fifteen 2400 ft. magnetic tapes over a period of three days. In the analysis, gates were set on and around 122 peaks, in the manner previously explained and an equal number of coincidence spectra were generated. A selection of the coincidence spectra associated with these gates is shown in Fig. 6.11 to 6.24. Fig. 6.11 to 6.13 show the spectra in coincidence with successive members of the ground state band. The relative intensities of many of the lines in this sequence of spectra uniquely defined their positions in the level scheme. Fig. 6.14 presents the spectra in coincidence with the two gamma rays de-exciting the 1333 keV isomer. These spectra show only the members of the ground state band and are free of the background caused by the prompt high energy gamma rays which accompany the decay of the highly excited nucleus.

Figures 6.11-6.18

A selection of γ-γ coincidence spectra, recorded with 38 cc and 50 cc Ge(Li) detectors. In these figures, a symbol beside a peak label indicates that it is coincidence with a component in the gate labelled with the like symbol.

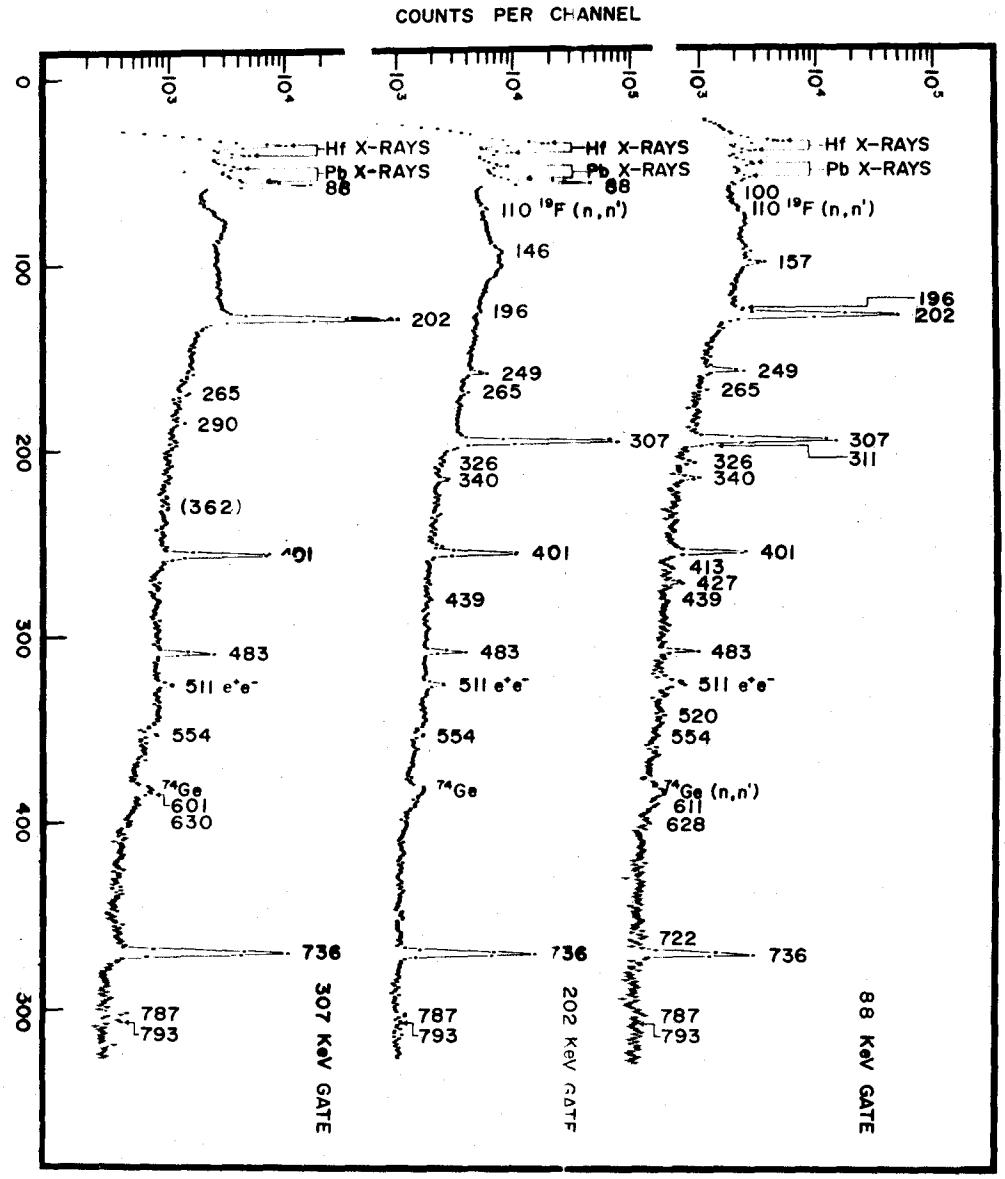
COUNTS PER CHANNEL
CHANNEL NUMBER
Hf X-RAYS
Pb X-RAYS
88
202
265
290
(362)
401
483
511 e⁺e⁻
554
74Ge
601
630
736
787
793
307 KeV GATE
110 19F (n,n')
146
196
249
265
307
326
340
401
439
483
511 e⁺e⁻
554
74Ge
736
787
793
202 KeV GATE
100
110 19F (n,n')
157
196
202
249
265
307
311
326
340
401
413
427
439
483
511 e⁺e⁻
520
554
74Ge (n,n')
611
628
722
736
787
793
88 KeV GATE

Figure 6.11

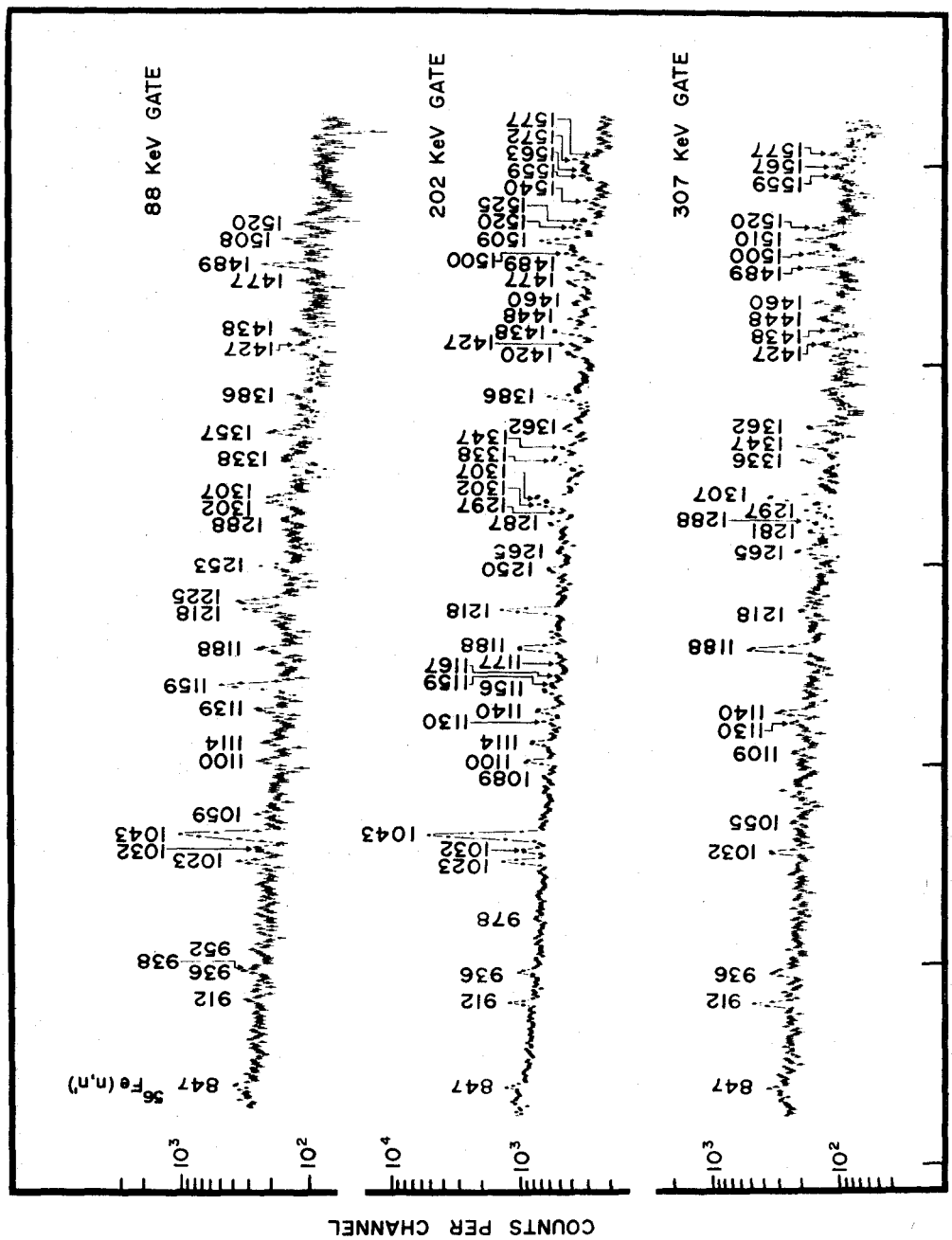

Figure 6.12

(see p.180 for caption)

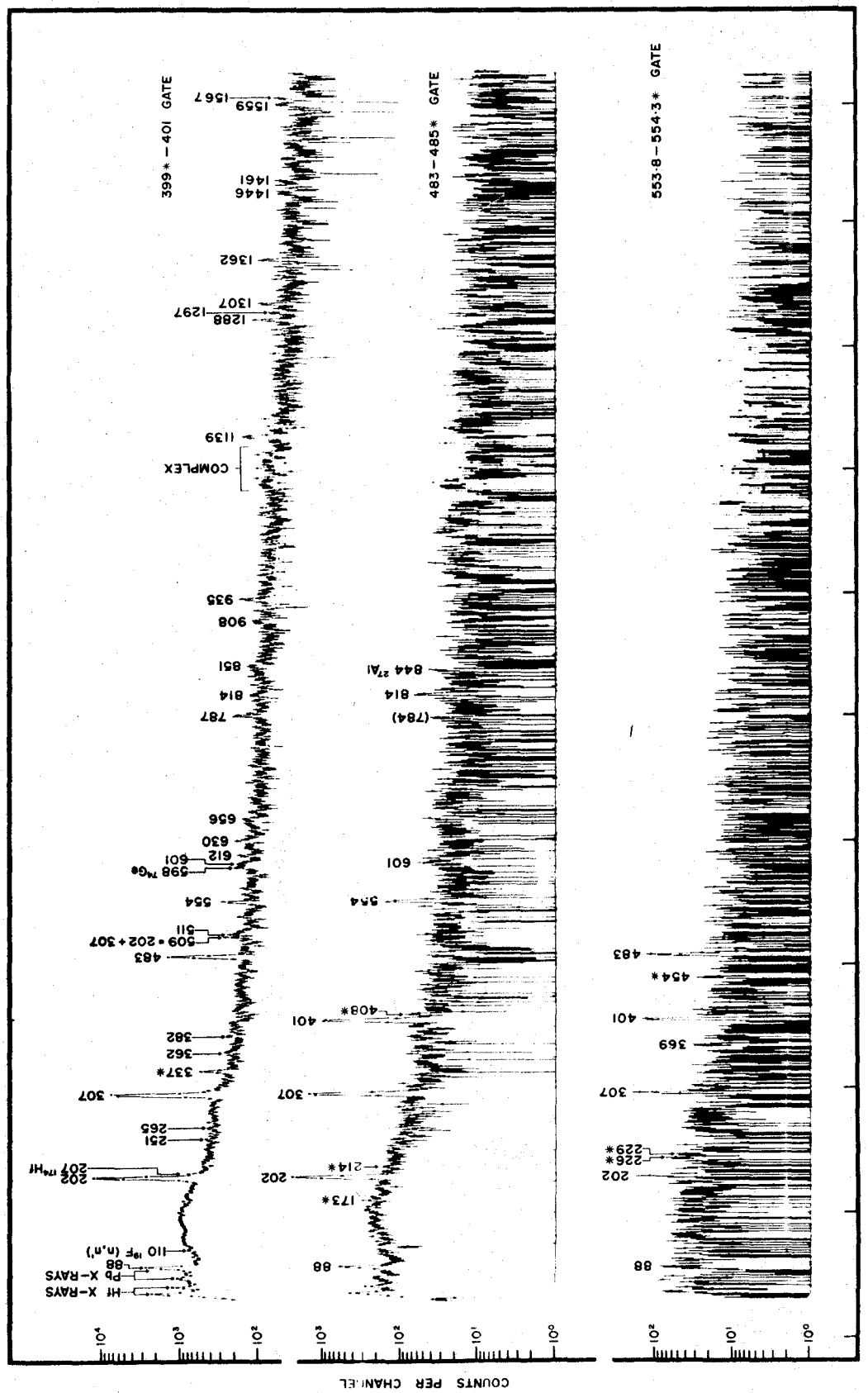

Figure 6.13
(see p.180 for caption)

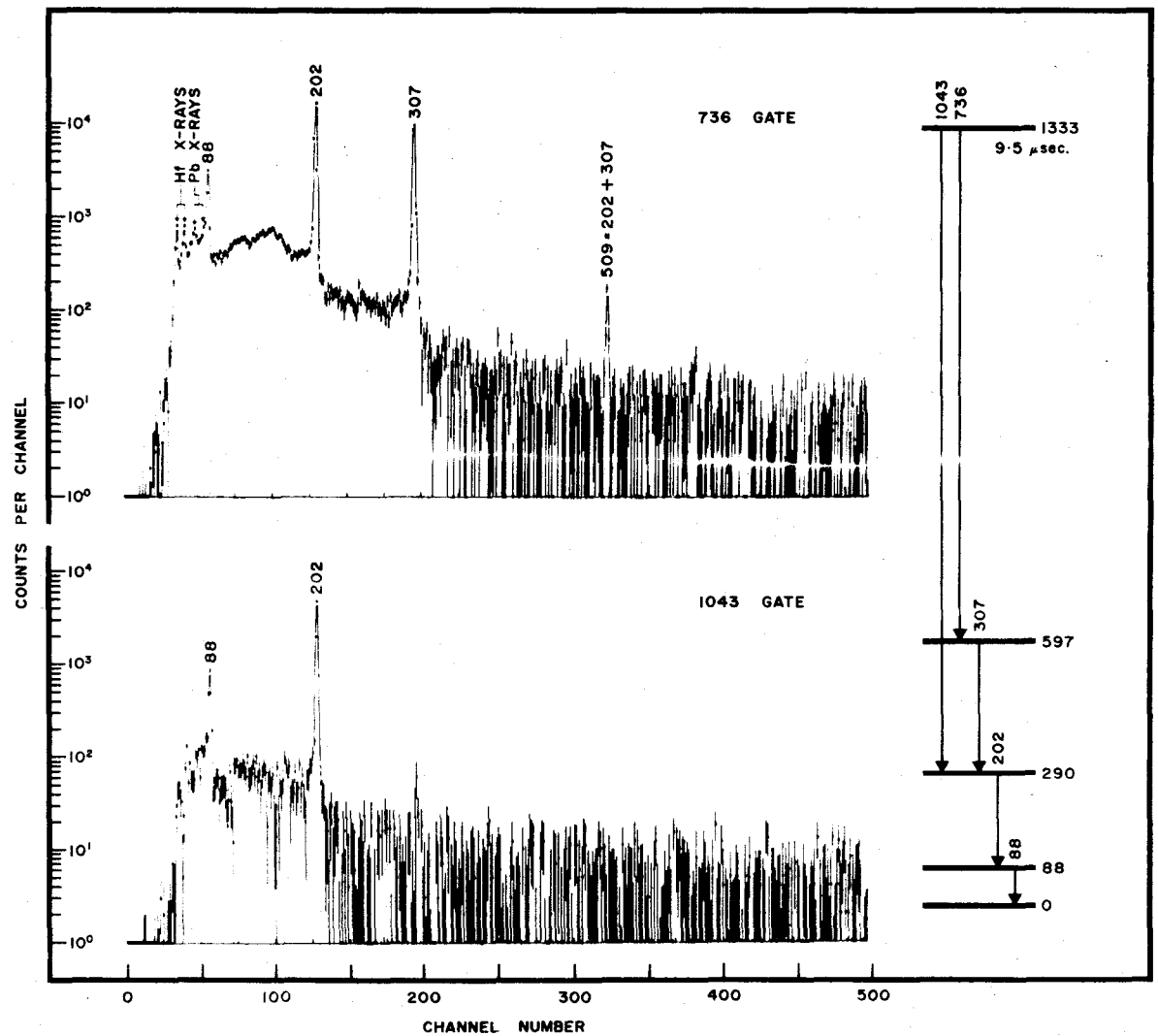

Figure 6.14

(see p. 180 for caption)

Fig. 6.15 presents the coincidence spectra associated with transitions between the beta band, whose band head falls at 1150 keV, and the ground state band. Most of the peaks appearing can be associated with the transitions shown in the partial decay scheme. The 1138 and 1139 keV gates were obtained by setting windows on the upper and lower portions of the unresolved 1138 keV doublet. The 1139 keV component deexcites a level at 2137 keV. Similarly, the 935 and 1100 keV gates contain components which define levels at 1533 and 2098 keV respectively. The weak 362 keV transition, which appears in fig. 6.11 and 6.13, connects the 10+ and 8+ members of the beta band. The 10+ member is more firmly established by the 814 peak in fig. 6.12 and 6.13.

The next three figures (6.16, 6.17 and 6.18) present evidence for the 2- octupole band, whose states are shown in the partial decay scheme of fig. 6.16. This figure presents the spectra in coincidence with five of the interband transitions. Most of the peaks appearing can be interpreted in terms of the level scheme: the 264 keV peak in the 1225 keV gate connects the level at 1577 (not shown) to the 1313 keV state. The levels at 1964 and 2050 keV are not members of the 2- band. Fig. 6.17 shows the spectra in coincidence with the 157 and 249 keV cross-over transitions within the 2- band. The presence of 202-157 keV coincidences suggests that the 157 keV

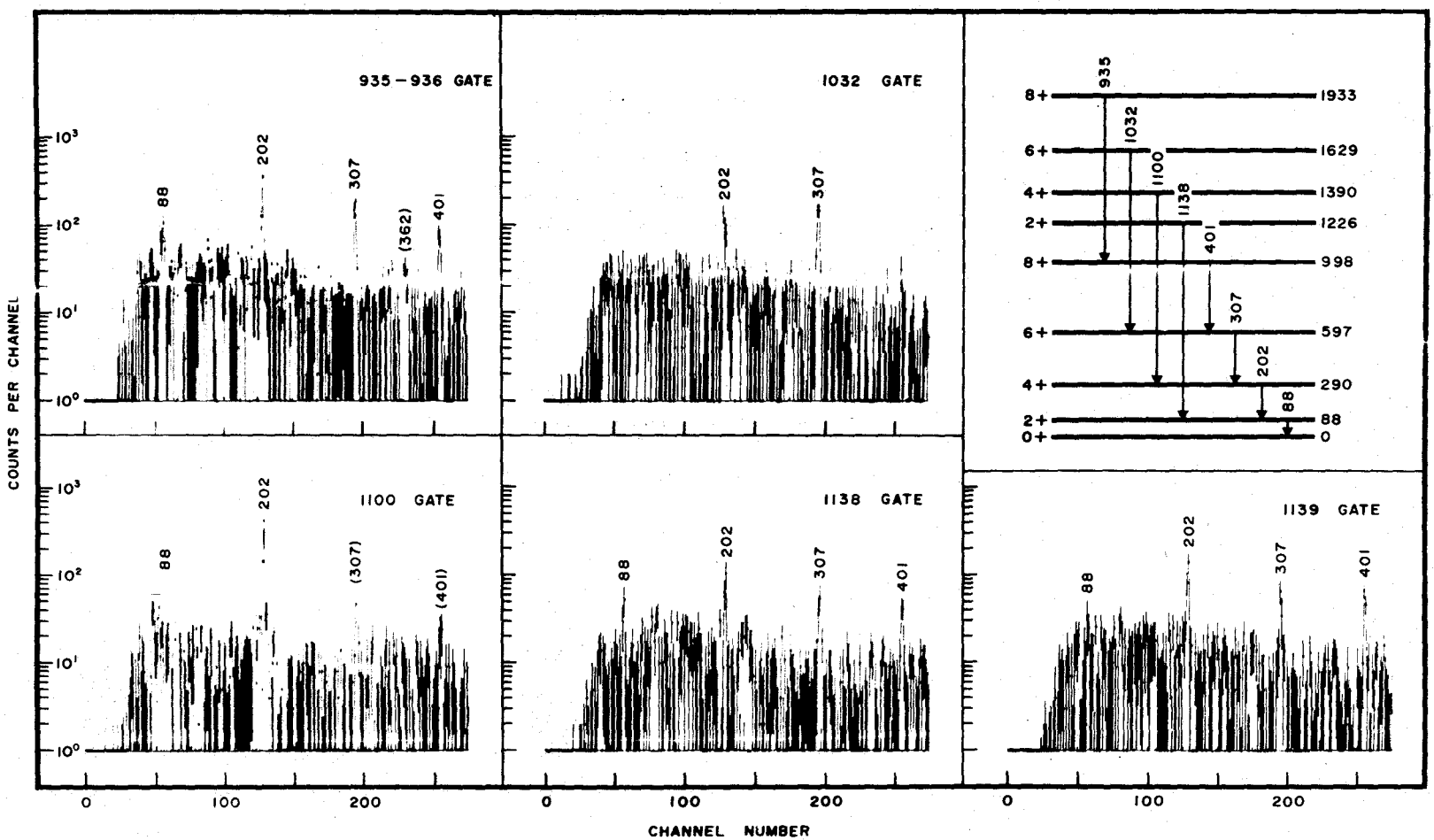

Figure 6.15

(see p. 180 for caption)

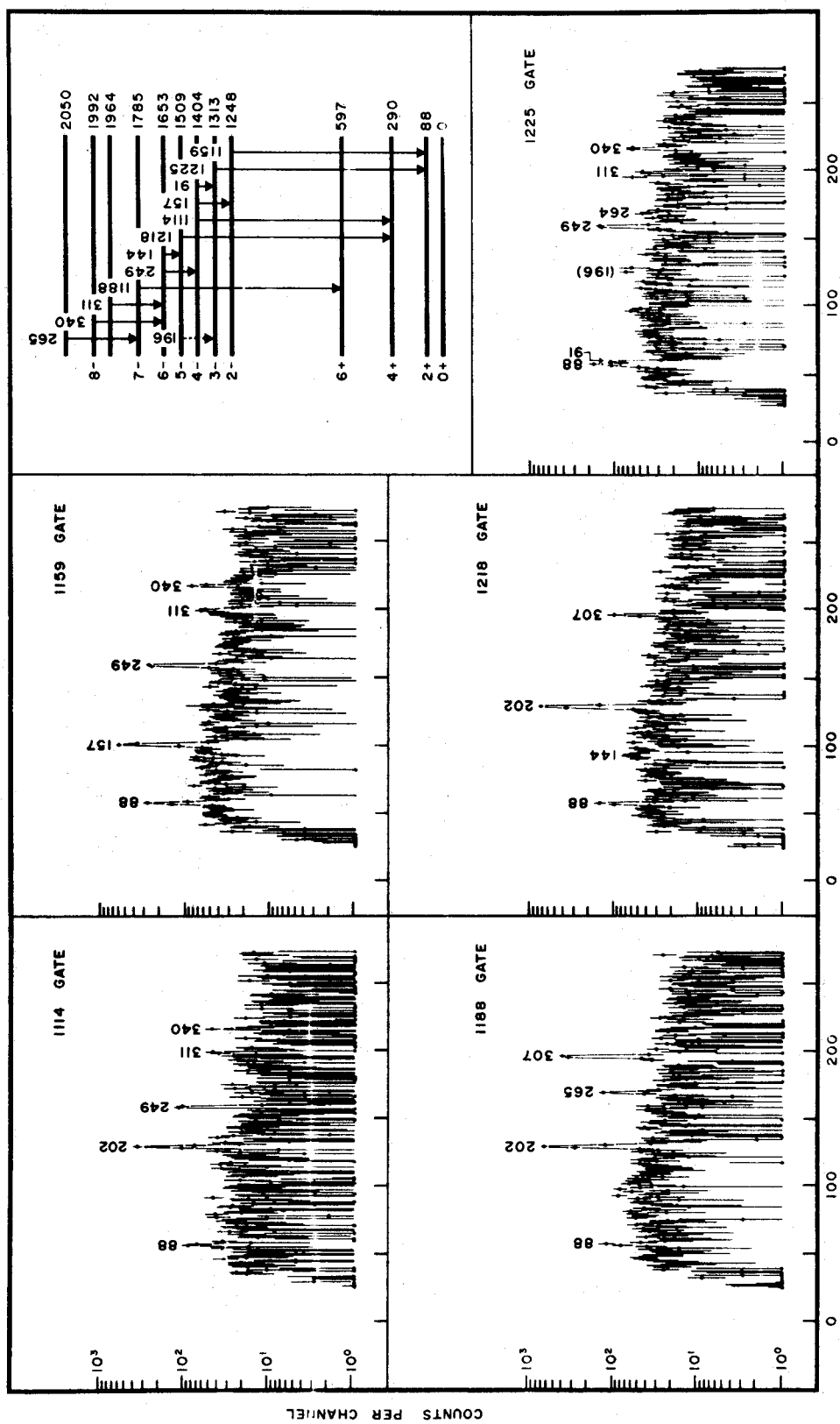

Figure 6.16

(see p. 180 for caption)

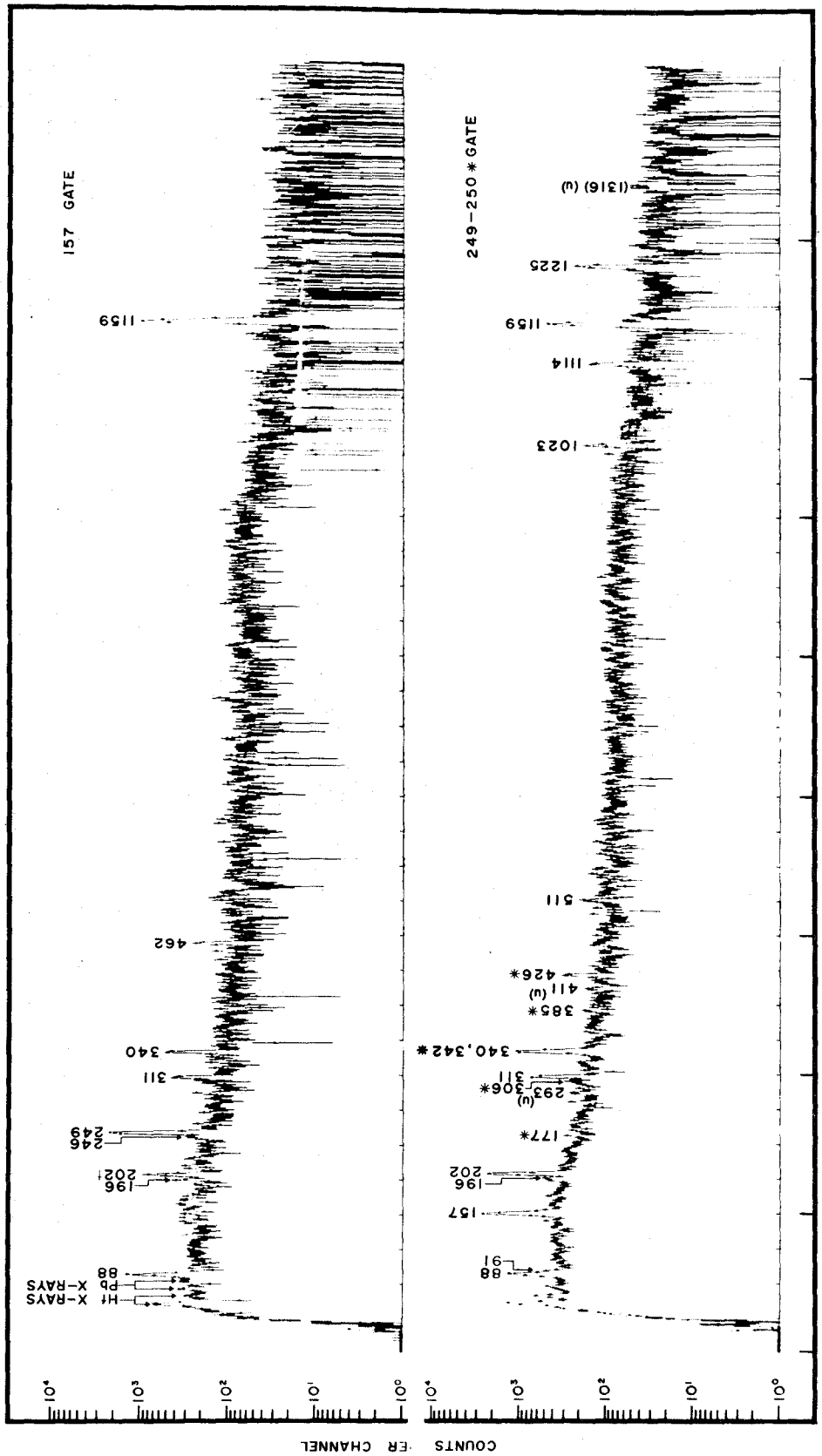

Figure 6.17

(see p. 180 for caption)

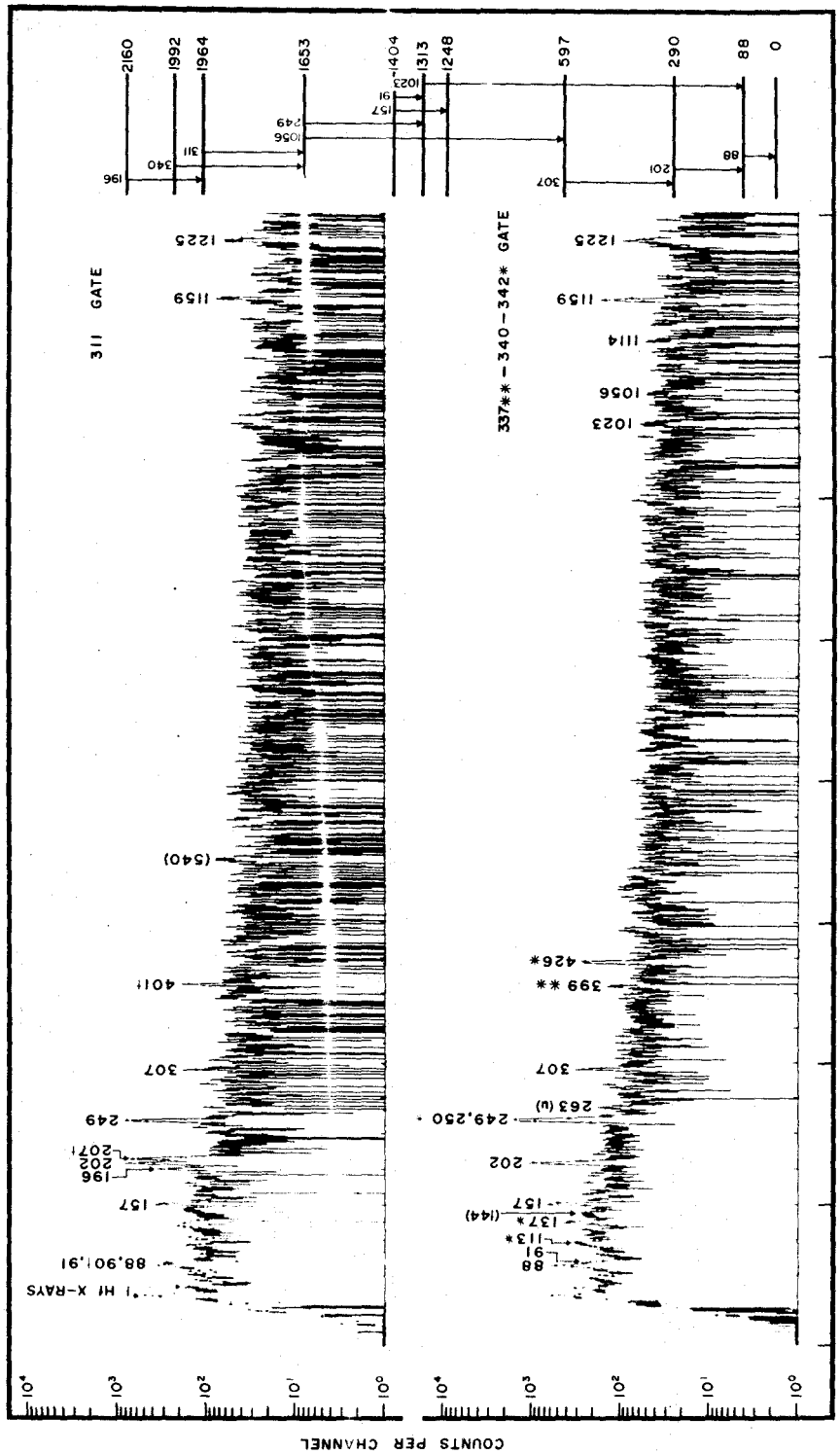

Figure 6.18

(see p. 180 for caption)

gamma ray is a doublet but we have been unable to explain the second component. The 462-157 and weak 462-1159 keV (not shown) coincidences tentatively define a level at 1866 keV. The 249 keV gate includes two transitions, one of which is in ^{177}Hf. The problem of separating these is complicated by the fact that both components are in coincidence with transitions of $\sim$ 341 keV. The lines at 293, 411 and 1316 keV are unexplained. Fig. 6.18 shows the spectra in coincidence with the 311 and 340 keV gamma rays which feed the 1653 keV state. The two spectra are very similar except for intensity. The 311 gate contains a line in ^{174}Hf which brings up several members (indicated by †) of its g.s.b. Similarly the 340-2 gate contains a line in ^{177}Hf which brings up other impurity lines (indicated by *); all the rest of the transitions are explicable in terms of the level scheme except for the 540 and 399 keV peaks.

This selection of coincidence spectra will serve to illustrate the quality of the data and to support many of the levels which have been defined in this work. All of the data were used in the analysis, and the level structure tested by means of coincidence probabilities derived in the manner described below.

Each coincidence spectrum was analyzed to obtain the coincidence probability between the gating transition and each transition appearing in coincidence with it, using the ex-

pression

$$C_{ij} = \frac{N_{ij}}{N_o w_g (\varepsilon\omega)_i (\varepsilon\omega)_j}$$

where C_{ij} (= C_{ji}) is the coincidence probability between γ_i and γ_j;

N_{ij} is the number of coincident events occurring between the gate and the full energy peak of the gamma ray in the spectrum;

w_g is the fraction of the full energy peak of the gating transition that is included in the gate;

$(\varepsilon\omega)_i$ and $(\varepsilon\omega)_j$ are the appropriate coincidence detection efficiencies; and

N_o is the total number of gamma rays from the target.

N_o was determined by normalizing to the well-known 307-202 keV (6+ → 4+) cascade of the ground state band (g.s.b.) Relative efficiency curves were determined for each detector, using the 736→307→202→88 and 1043→202→88 keV cascades following the decay of the 1333 keV isomers. Interpolated points on the curve were obtained using standard sources in a similar but not precisely identical geometry (see section 3.5).

In order to use these cascades for the purpose of efficiency calibration, it was necessary to use the theoretical E2 conversion coefficients and to ignore angular correlation effects. Since the 10 μsec isomer has lost its initial alignment before it decays, correlation effects in its

deexciting gamma rays are small (∿ 10 to 15%) and negligible compared to other uncertainties in the coincidence measurements.

The experimentally determined C_{ij}'s may be compared with the values expected from the level scheme. For two directly coincident gamma rays, γ_i and γ_j, as shown in fig. 5, the coincidence probability is defined by $C_{ij} = I_i f_j$,

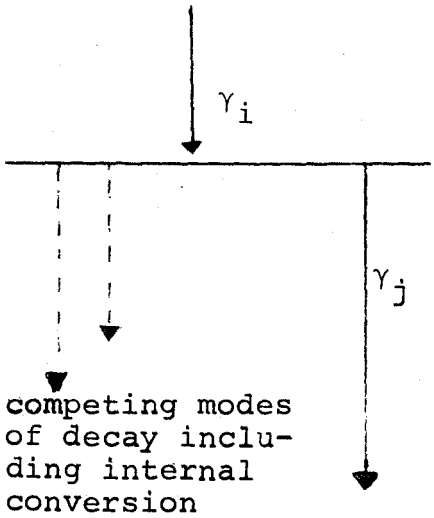

where I_i = the intensity of the upper number of the cascade and

f_j = the fraction of the decay proceeding through γ_j.

For indirect cascades, the coincidence probabilities may be derived when the appropriate branching ratios are known.

Alternatively, one may divide the experimental C_{ij} by the factor f_j to obtain the intensity of the upper member of the gamma-gamma cascade. This intensity, I_E^C, can then be compared with the intensity obtained from the singles measurement. This approach is particularly suited for transitions feeding members of the g.s.b. since in these cases the value of f_j is constant for all the transitions feeding a given level.

Table 6.1 presents values of I_E^C for all of the transitions which are in prompt coincidence with transitions within the g.s.b. In this case E takes the values 88, 202, 307 and 401 keV corresponding to the four lowest transitions in the bands and the values of f_j required to compute I_E^C are simply $(\frac{1}{1+\alpha_{jT}})$, where α_{jT} is the total conversion coefficient of the j^{th} in-band transition.

It is clear that for a transition feeding a given level of the g.s.b., the values of I_E^C should remain constant as one proceeds up the band and drop to zero when one passes that level (the 736 keV transition provides a good example). In many cases the value of I_E^C drops but does not go to zero, thus indicating that there are two (or more) unresolved gamma rays feeding the g.s.b. (the 1218 keV doublet is a good example of this situation). The members of the ground state band listed in table 6.1, show normal behaviour as long as the transition is the upper member of the cascade. When the transition energy is less than E, the value of I_E^C represents the intensity of the gamma ray of energy E (a good example is provided by the 201 keV transition). This behaviour provides a critical test for the ordering of the members of the g.s.b.

The values of I_E^C may be subject to rather large uncertainties due to errors in the efficiency curves ($\sim$ 15%) and in the determination of peak areas. The latter is dominant for weak peaks. Angular correlation effects from aligned nuclei,

which may be up to 40% for stretched E2 cascades, also contributes to the uncertainty. The 401 keV transition provides a good example of the effect of a stretched E2 cascade on the I_E^C values. Since in general, the angular effects are unknown, one cannot expect systematic agreement between the singles intensities and the I_E^C values to better than $\sim$ 30%.

For gamma rays which do not feed the ground state band directly, it proved simpler to compare the experimental C_{ij} values directly with those predicted from the level structure. These values are tabulated in Table 6.6. Some of the information in this table has already appeared in the alternate form in Table 6.1. Its main usefulness is in locating transitions within and between members of the high lying bands. Since the conversion coefficients were usually unknown, the values of f_j and therefore of $(C_{ij})_{expected}$ could not be predicted with much precision. In cases where the level structure suggested E2 transitions, E2 conversion coefficients were used; in cases of M1+E2 character, pure M1 conversion was assumed. It was particularly difficult to estimate C_{ij} values for pairs of gamma rays in an indirect cascade since the errors were cumulative. For many of these cases, no estimate of the expected C_{ij} has been included in Tables 6.6. In a few instances, it has been possible to use the conversion coefficients measured by Bernthal et al. (1971) and Borgreen et al. (1967). In general, agreement between expected and

Table 6.6

Coincidence probabilities of transitions associated with the $K=2^-$ octupole band

E_i	E_j	C_{ij}	C_{ji}	$C_{expected}$
144,146	88	∿0.03		0.06
	202	0.22	0.30	0.37
	307	0.05	∿0.03	0.05
	1218	0.22	0.21	0.14
	1307	0.08	0.12	0.13
157	88	0.31	0.44	0.38
	202	0.22	0.20	
	249	0.86	1.1	∿1.2
	311	0.17	0.21	0.26
	340	0.23		0.38
	426	<0.04	∿0.08	
	462	0.13	0.12	(a)
	1159	2.6	2.4	2.7
249	88	0.71	0.75	0.59
	91	∿0.10		∿0.2
	196	0.15		(a)
	202	1.0	1.2	1.6
	311	0.57	0.86	∿1.0[d]
	340	1.1 [d]		(a)
	410	0.086		

(continued next page)

Table 6.6 (continued)

E_i	E_j	C_{ij}	C_{ji}	$C_{expected}$
249 (cont'd)	426[b]	0.28		0.3[b]
	1023	0.44	0.33	0.4
	1114	0.54	0.4	1.0
	1159	2.1	2.1	1.9
	1225	1.3	1.1	0.9
	1316	0.15		
311	88	0.20		0.15
	92	0.15		
	196	0.20		(a)
	202	0.62		
	207[c]	0.58		
	307	0.09		
	401[c]	0.18		
	1023		∿0.1	
	1159	0.39	0.53	0.59
	1225	0.41	0.25	∿0.20
337,[f] 340	88	0.40		
	113[b]	∿0.1		
342[b]	137	0.16		
	202	0.72		
	249,250[b]	1.4	1.4	(a)
	307	0.19		
	399[f]	∿0.5[f]	0.75	0.6

(continued next page)

Table 6.6 (continued)

E_i	E_j	C_{ij}	C_{ji}	$C_{expected}$
	426[b]	0.39		
	461	∿0.08		
	1023	∿0.2	∿0.1	0.24
	1056	∿0.09		∿0.08
	1114	∿0.15	0.14	∿0.25
	1159	0.95	0.58	1.2
	1225	0.58	0.39	0.54
1023	88	0.21	0.44	0.46
	91	0.07		<0.19
	202	1.8	2.0	2.6
	264		0.11	0.09
1155,1159	88	1.2	1.3	1.5
	202	0.54[e]	0.47[e]	0.56
1225	88	0.70	0.84	1.0
	91	0.22		<0.44
	196	0.12		(a)
	264	0.15	0.19	0.21
	306	0.22	-	
	611	0.29	0.17	0.23

(a) I_j found from C_{ij}

(b) ^{177}Hf line from (α,n) reaction

(c) ^{174}Hf line

(continued next page)

Table 6.6 (continued)

(d) Complex; contribution of contaminant line subtracted

(e) Coincident with the 1155 keV line

(f) Only $\sim \frac{1}{5}$ of this peak in gate; C_{ij} given corrected for this.

measured C_{ij} values of 20 - 100% were considered acceptable, depending on the individual case.

6.5 Identification of Contaminant Lines

With an alpha beam of energy 22.5 MeV, the $^{174}Yb(\alpha,2n)^{176}Hf$ reaction is dominant but there is still a contribution from the $^{174}Yb(\alpha,n)^{177}Hf$ process. The strongest ^{177}Hf line (208.3 keV) observed was 3% of the strongest ^{176}Hf line (201.8 keV).

Since the cascades down two of the strongly populated rotational bands in ^{177}Hf are well known from studies on the decay of ^{177}Ta (Haverfield et al 1967) it was often possible to identify lines originating from ^{177}Hf in this reaction study by examining their energies and relative intensities. Moreover, the excitation functions for ^{177}Hf lines are in sharp contrast to those for ^{176}Hf (see fig. 6.5 and 6.6).

Isotopic impurities in the target (see page 83) led to the formation of hafnium isotopes of mass 174, 175 and 178. Fortunately, their decays were known from previous work (^{174}Hf, Ejiri and Hagerman (1971); ^{175}Hf, Rezanka (1971); ^{178}Hf, Helmer and Reich (1968) and Ryde et al (1971)). Although only the strongest transitions in the hafnium impurities appeared in our spectra, they were evident in both the singles and coincidence measurements and often created difficulties in interpretation because their energies were so close to those in ^{176}Hf.

Contaminants also appeared from the (α,n) and (α,α') reactions induced in the aluminum and iron of the beam line and

target chamber. The well known broad peaks at 597 and 693 keV arising from the (n,n') reaction in germanium were present in all the spectra. These owe their peculiar skewed shape to the ionization energy generated by the recoil of the germanium atoms in the detector.

A more subtle source of contaminants in the spectra arose from the (n,n') reaction in the material surrounding the detector. It was found that the relative intensities of such lines varied from run to run, depending on the detector environment and appeared at energies below the $^{174}Yb(\alpha,2n)^{176}Hf$ threshold. One of the strongest of these is the 803 keV line from the (n,n') reaction in the ^{206}Pb present in the shielding. The lines at 110, 197, and 1235 keV which appeared in our spectra arose from the $^{19}F(n,n')$ reaction in the material (presumably teflon) used in the Ge(Li) detector mounting. Other workers (Yamazaki and Ewan (1969) and Barnéoud et al (1970)) have attributed these lines to the (α,p) reaction in ^{16}O. While this may be one source of these lines, we believe that the (n,n') reaction on fluorine is mainly responsible for the ones appearing in the present experiment. This claim is based on the fact (i) that they have been seen in the gamma ray spectra arising from (p,xn), (α,xn) and $(^{7}Li,xn)$ reactions, and (ii) that they did not disappear when the detector was shielded from the target by sufficient lead to eliminate target induced gamma rays in the 100 keV region. Since the creation

of the ^{176}Hf nucleus is accompanied by neutron emission, these neutron induced gamma rays also appeared in both the γ-γ and γ-$\gamma_{delayed}$ coincidence spectra.

Table 6.4 presents the energies and intensities of the observed impurity lines. This list has proven useful in eliminating lines which might otherwise have been used in the construction of the ^{176}Hf level scheme.

6.6 The Decay of the Isomeric States

The delayed gamma spectra were recorded in the manner described in section 5.3. Fig. 6.19a shows a spectrum accumulated with the 38 cm^3 Ge(Li) detector over the full 80 μsec period following an irradiation. This spectrum was obtained by summing the sixteen spectra recorded at 5 μsec intervals in this period. For the stronger lines, it was of course possible to determine their half lives by following their decay in these sixteen spectra. For the weaker lines this was not possible; in order to separate those transitions that decayed appreciably in the 80 μsec observation period from the longer lived components, the sum of the last eight groups was subtracted from the sum of the first eight to obtain the spectrum of Fig. 6.19b. This spectrum identifies those lines with half lives less than $\sim$ 80 μsec. The negative peaks are associated with the build-up of activities during the observation period. The bombarding energy in this experiment was 22.5 MeV.

Figure 6.19 a, b

Delayed γ-ray spectra from the decay of the ^{176}Hf isomers.

(a) top: sum of spectra from 0-80 μsec.

(b) bottom: difference of the spectra from the first and second 40 μsec periods.

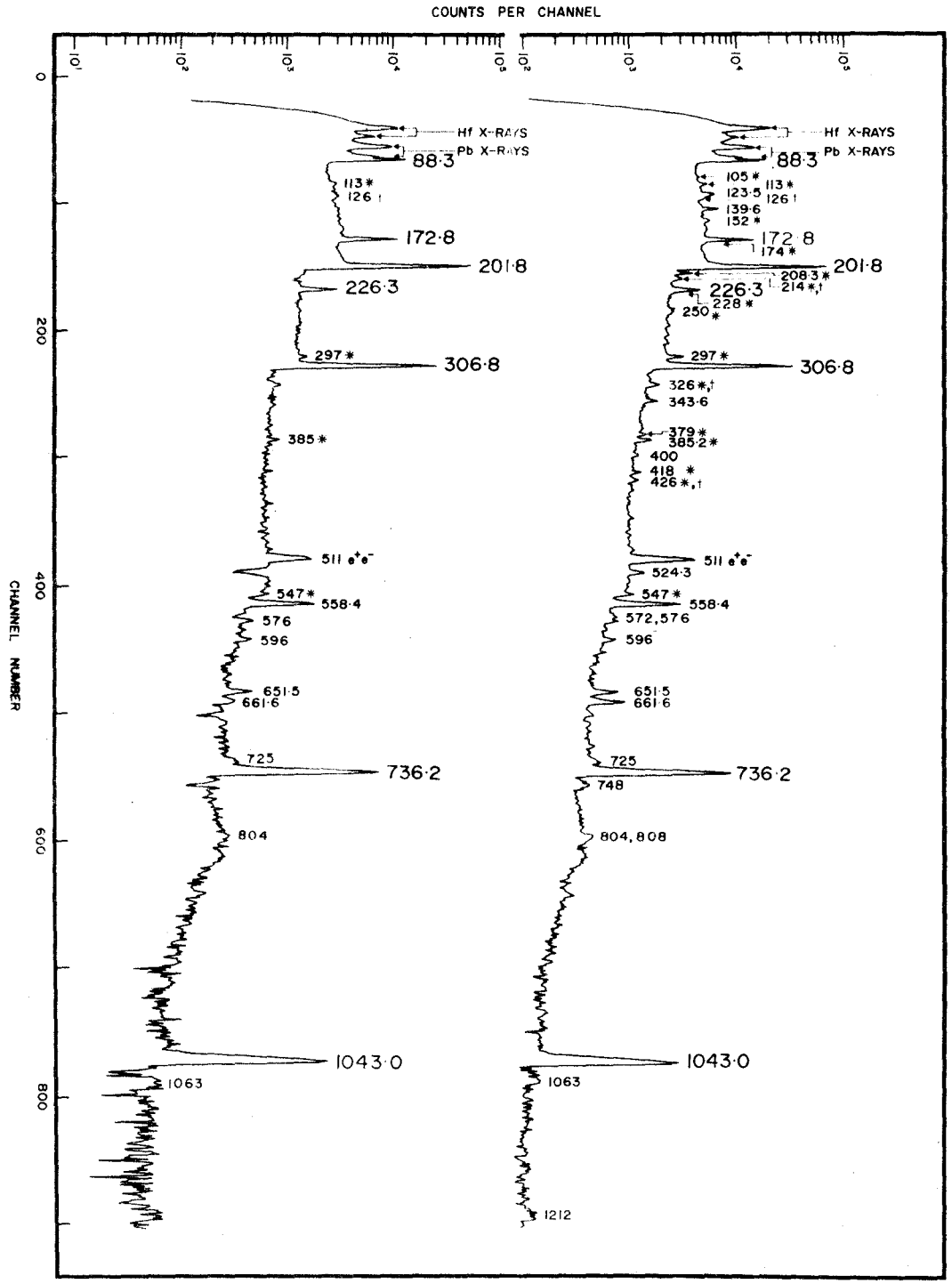
COUNTS PER CHANNEL
CHANNEL NUMBER
Hf X-RAYS
Pb X-RAYS
88·3
113*
126 †
172·8
201·8
226·3
297*
306·8
385*
511 e⁺e⁻
547*
558·4
576
596
651·5
661·6
725
736·2
804
1043·0
1063
1212
105*
123·5
139·6
152*
174*
208·3*
214*,†
228*
250*
326*,†
343·6
379*
385·2*
400
418*
426*,†
524·3
572,576
748
804, 808

The strong transitions at 88, 202, 307, 736, 1043, 173 and 226 keV in Fig. 6.19 are also prominent in the in-beam spectrum and belong in ^{176}Hf. This assignment is in agreement with that of Borggreen et al. (1967) who observed these lines by means of the ^{176}Lu(p,n)^{176}Hf reaction. The peaks in Fig. 6.19a marked with an asterisk arise from the well-known 23/2- isomeric state of half life 1.1 sec in ^{177}Hf (Haverfield et al., 1967 and Alexander et al., 1964). The fact that the 113, 297 and 385 keV members of this group also appear in Fig. 6.19b shows that they are fed from a much shorter-lived isomer in ^{177}Hf. Since the 547 keV gamma ray, which appears in Fig. 6.19a and very weakly in Fig. 6.19b, is in coincidence with these three lines and since both the 297 and 545 keV lines decay with a half life of 40 ± 10 μsec, these data appear to define a new isomeric state in ^{177}Hf at an excitation of 1341.8 keV. The lines marked with a dagger (†) in Fig. 6.19a are associated with the decay of isomers in ^{178}Hf (Ryde et al., 1971). The fact that 326 keV line still appears in the Fig. 6.19b is unexplained. The peak at 558.4 keV with a half life of $\sim$ 14 μsec appeared only in this one spectrum and is due to an impurity. The remaining weak transitions in the spectra are unexplained.

The low energy gamma rays following the decay of the isomers were also studied with a 0.9 cm^3 Ge(Li) detector at an α energy of 24.0 MeV. The detector was unshielded except for a 1 mm Cd foil. Unfortunately, in this experiment, the beam pulser was not operating properly and about 10% of the beam leaked through during the observation period. Despite this, it was possible to obtain "clean" delayed spectra from the data by subtracting the spectra recorded in the late time periods from those obtained in the early periods. The resulting "difference" spectrum is presented in Fig. 6.20. A measure of the effectiveness of the subtraction process is provided by the absence of the Yb X-rays which are very prominent in the in-beam spectra.

Fig. 6.20 clearly identifies the 53.5 keV transition which had been postulated but not observed in earlier studies (Borggreen et al,1967). It is completely masked in the in-beam experiments by the strong X-rays from Yb and Hf. The prominent 226.3 keV line forms about 20% of an unresolved triplet in the in-beam spectra but is isolated in the delayed spectrum of Fig. 6.30 . The origin of the weak low energy shoulder on this peak has not been identified.

The efficiency curve of the 0.9 cc detector in this one run was determined from the g.s.b. transitions, whose relative intensities were calculated from the known decay scheme of the 1333 keV isomer (fig.5.1),using the

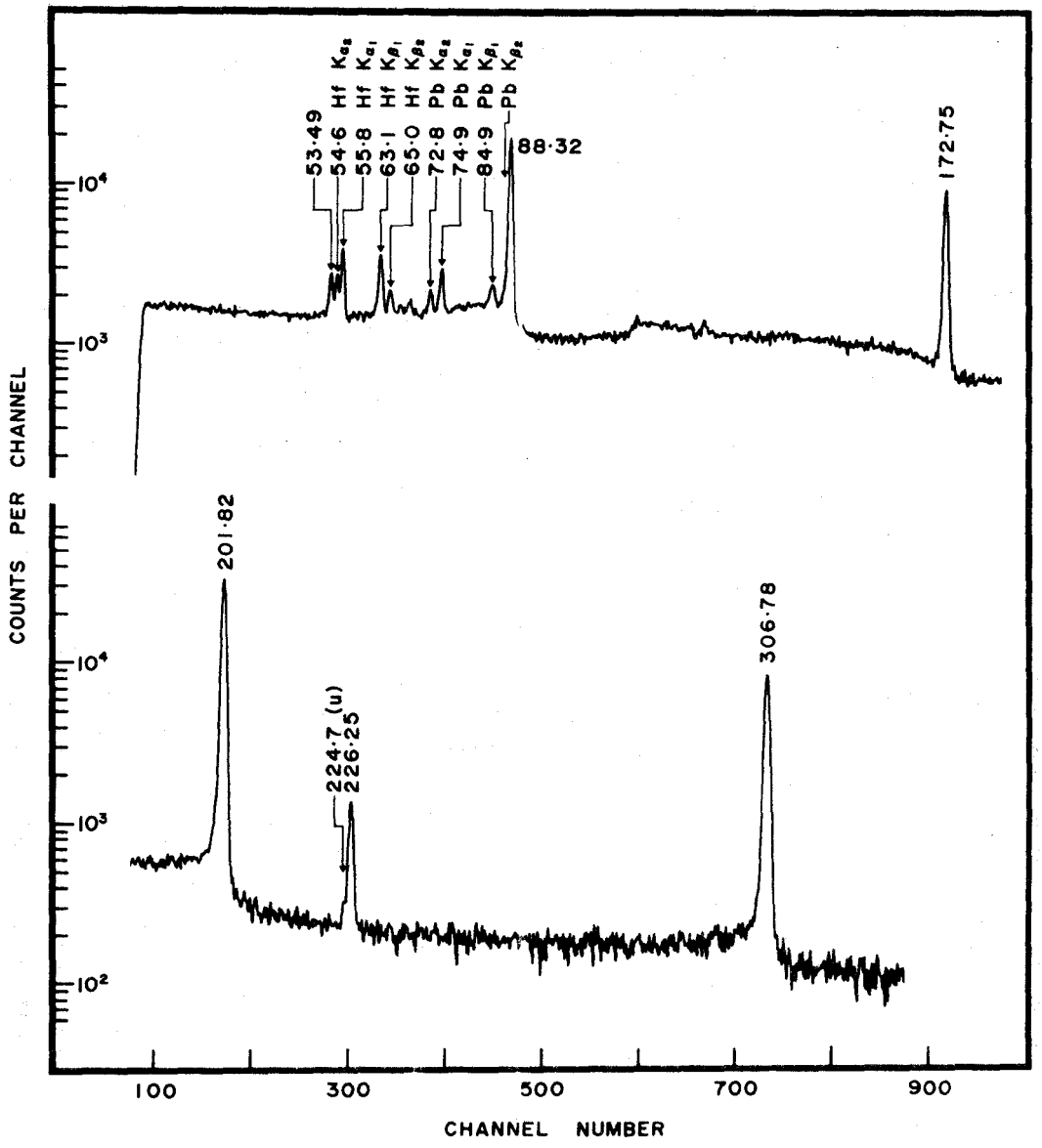

Figure 6.20

Delayed γ-ray spectrum. Recorded with 0.9 cc. Ge(Li) detector.

ratio $\frac{I_{736}}{I_{1043}} = \frac{28.9}{18.5}$ obtained from the in-beam experiments. The relative efficiency in the 50 keV region was determined by comparing the observed and expected K X-ray intensities. The expected intensities were calculated by first determining the total intensities of the K-conversion electrons, and then correcting for a fluorescent yield of 94% to obtain the total X-ray intensity; relative intensities of 100, 54, 33 and 8 were assumed for the K_{α_1}, K_{α_2}, K_{β_1}', K_{β_2}' X-rays respectively (Lederer et al 1968).

A summary of the transitions de-exciting the two isomers in ^{176}Hf is given in table 6.7. The gamma intensities, I_γ, obtained with alpha beam energies of 22.5 and 24.0 MeV, have been obtained from the difference spectra.

Table 6.7 shows unambiguously that the multipole character of the 53 keV transition is E1, since only in this case is its transition intensity equal, within experimental errors, to that of the 173 keV transition, with which it is in cascade coincidence. This assignment confirms that of Borgreen et al. (1967). The total transition intensities, T, [$T = I_\gamma(1+\alpha_T)$] obtained from the higher beam energy, are also tabulated, using the total internal conversion coefficient, α_T, shown.

TABLE 6.7

Transitions Following Decay of Isomers

Energy (keV)	I_γ E_α=22.5 MeV	I_γ E_α=24.0 MeV	α_T (Theor.)	Transition Intensity E_α=24.0 MeV
88.3	5.5±0.6	6.1 ±0.6[c]	6.1(E2)	43.5±4
201.8	35.2±3[b]	35.2±3[c]	0.24(E2)	43.6±3
306.8	26.9±3	25.0±2[c]	0.07(E2)	27.0±2
736.2	28.9±2[a]	-	0.006(E2)	29.1±2
1043.0	16.7±2	-	0.003(E2)	16.7±2
53.49	-	5.6±1.1	0.34(E1)	7.5±1.5
			4.1(M1)	28 ±6
			49(E2)	280 ±56
172.8	4.2±0.4	6.0±0.6	0.65±0.10[d]	9.9±1.2
226.25±0.06	1.3±0.15	1.65±0.15	1.9(M2)	4.8±0.5

(a) Normalized to the in-beam singles intensity

(b) Intensity to normalize the 24 MeV spectrum to the 22.5 MeV spectrum

(c) Intensities used to establish the detector efficiency curve.

(d) Value of α_T taken from Borgreen et al 1967.

The relative population of the 6+ and 8- isomers at 1333 and 1559 keV may be derived from the transition intensities. The population of the upper isomer is proportional to the sum of the intensities of the 173 (or 53) and 226 keV lines; the population of both isomers is proportional to the intensity of the 88 or 202 keV line. The results are tabulated below:

	E_α=22.5 MeV	E_α=240.0 MeV
Population of 8-Isomer	6.7+3.8=10.5±1.2	9.9+4.8=14.7±1.3
Population of 6+Isomer	35.2-10.5=24.5±3	35.2-14.7=20.5±3
$[\frac{\text{Pop. of 8- Isomer}}{\text{Pop. of 6+ Isomer}}]$	0.43±0.07	0.72±0.12

As might be expected, the higher spin isomer is more highly populated with a higher beam energy, since more angular momentum is brought into the system.

6.7 Lifetimes of the 1333 and 1559 keV States in ^{176}Hf

The decay curves of a number of gamma rays were determined in the manner described in section 5.4, and two typical spectra are shown in Fig. 6.21. The decay curves of the 173 (or 226) keV transition, which depopulates the 1559 keV isomer is a straight line on a semilogarithmic plot, while that of the 202 keV or any other gamma ray associated with the decay of the 1333 keV isomer, shows the shape characteristic of an activity undergoing simultaneous growth and decay.

Figure 6.21 a, b

Decay curves for the (a) 173 keV and (b) 202 keV γ-rays associated with the decay of the 1559 and 1333 keV isomers, respectively. The slope of the curve in figure 6.21b does not give the half life of the latter state. (see text)

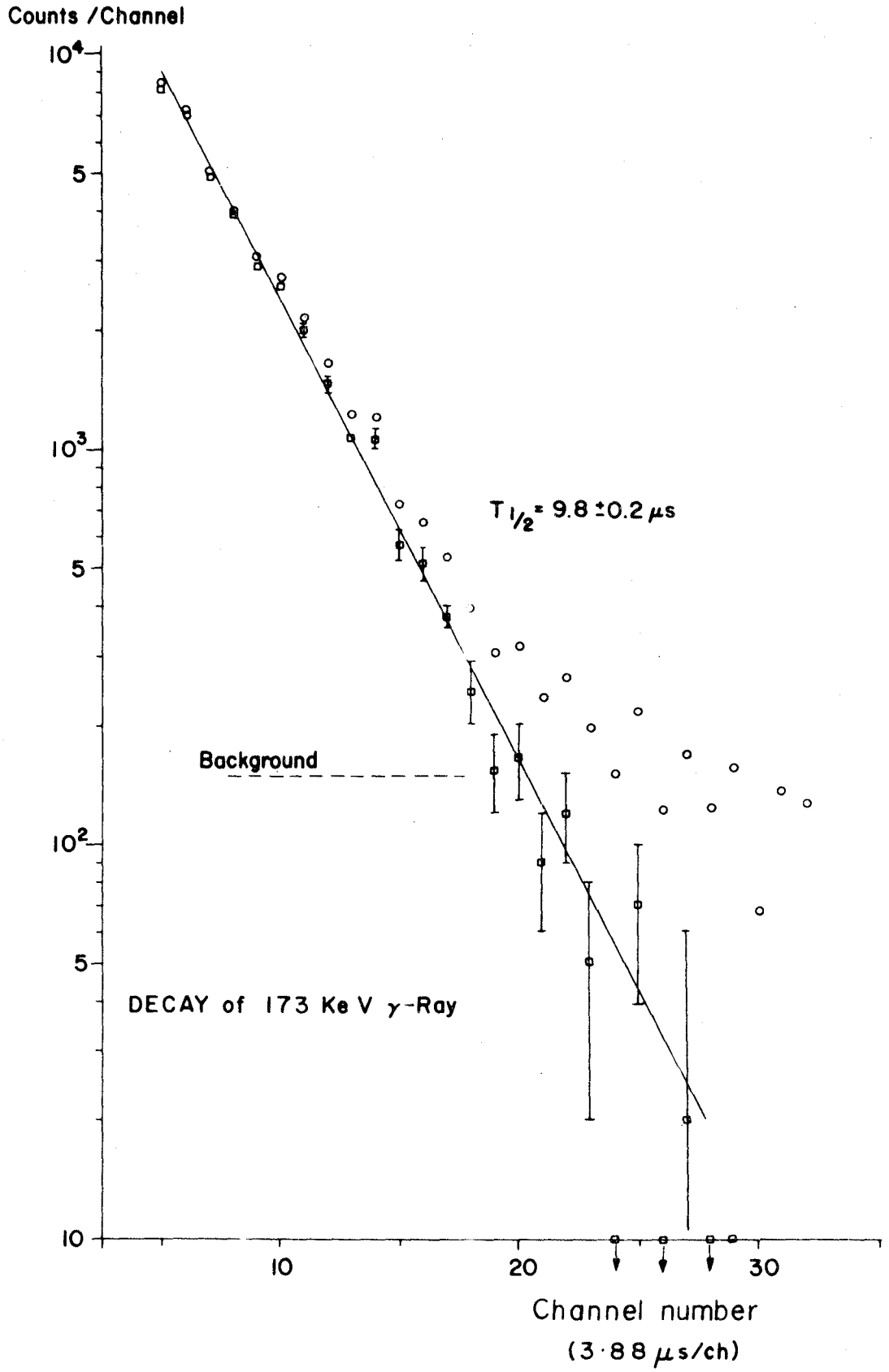
Counts /Channel
10⁴
5
10³
5
10²
5
10
T 1/2 = 9.8 ±0.2 μs
Background
DECAY of 173 Ke V γ-Ray
10
20
30
Channel number
(3·88 μs/ch)

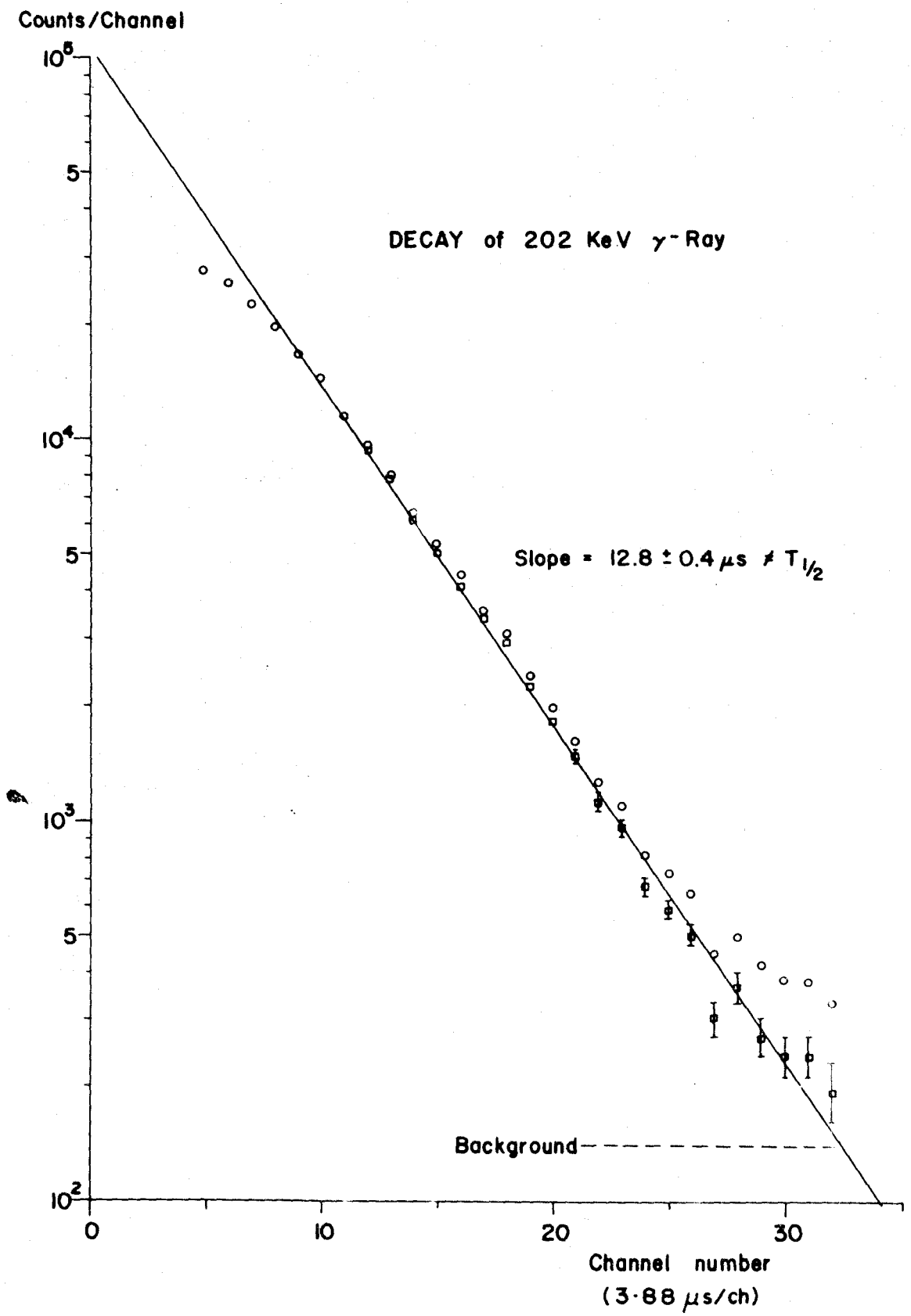
Counts/Channel
10^5
5
10^4
5
10^3
5
10^2
DECAY of 202 KeV γ-Ray
Slope = 12.8 ± 0.4 μs ≠ $T_{1/2}$
Background
0
10
20
30
Channel number
(3·88 μs/ch)

The half-life of the 1559 keV state was obtained from a least squares determination of the slope of the 173 keV decay curve and the weighted average from three separate experiments gave a value of 9.8±0.2 μsec.

As has already been indicated in section 5.4, a simple slope determination does not yield the correct half-life for the 1333 keV isomer and therefore the 12.8 μsec value derived in Fig.6.21b for the 202 keV transition has no physical meaning. The half-life of the 1333 keV state was measured in a separate delayed coincidence experiment (see section 5.4 (ii) for details) in which the TAC was started by a pulse of selected energy (in the 50 to 300 keV range) and stopped by any delayed event. In this experiment, 128 different time spectra were simultaneously recorded, each associated with "start" events of a given energy. The time spectrum associated with a particular "start" photopeak was obtained by summing the spectra associated with the channels in the peak and subtracting therefrom the spectra associated with an equal number of background channels. Fig. 6.22 presents a selection of six time spectra obtained in this manner.

Since the 202 and 240-300 keV "start" pulses are associated with gamma rays which decay promptly to the ground state of ^{176}Hf, the time spectra associated with these energies are due to chance , and provide the shape of the decay for

chance events,which is needed for analysis of the other time spectra. The spectrum associated with the K_α X-rays is likewise mainly due to chance* . On the other hand the time spectra associated with the 54+ X-ray, the 173 keV and the 226 keV "start" energies contain both a chance component and a stronger one determined by the decay of the 1333 keV isomer. The time spectra associated with these three gates provide striking evidence that these transitions feed the 1333 keV isomer; all of the other gates yielded time spectra similar to the upper three in Fig. 6.22.

The spikes in the upper three spectra are due to prompt γ-γ coincidences involving the g.s.b. The spikes in the three lower spectra are due to a combination of incorrect background subtraction and the prompt coincidences arising from the weak 174 and 228 keV transitions arising from the decay of the 1.1 sec isomer in ^{177}Hf. Events in the 5 μsec time interval to the left of the spike in the three lower spectra are due to chance. The shape of the chance spectrum should be a smooth curve connecting this section to the 120 μsec region. The points to the left of the spikes in the three upper curves are due to a combination of chance and true delayed coincidences between the gamma rays feeding and deexciting the 1333 keV state.

---

*This time spectrum contains a significant delayed coincidence component associated with the X-rays accompanying the internal conversion of the 53 and 226 keV transitions.

Figure 6.22

Delayed coincidence spectra associated with the 1333 keV isomer. The energy of the first "start" γ-ray is given; any second γ-ray provides the "stop" event.

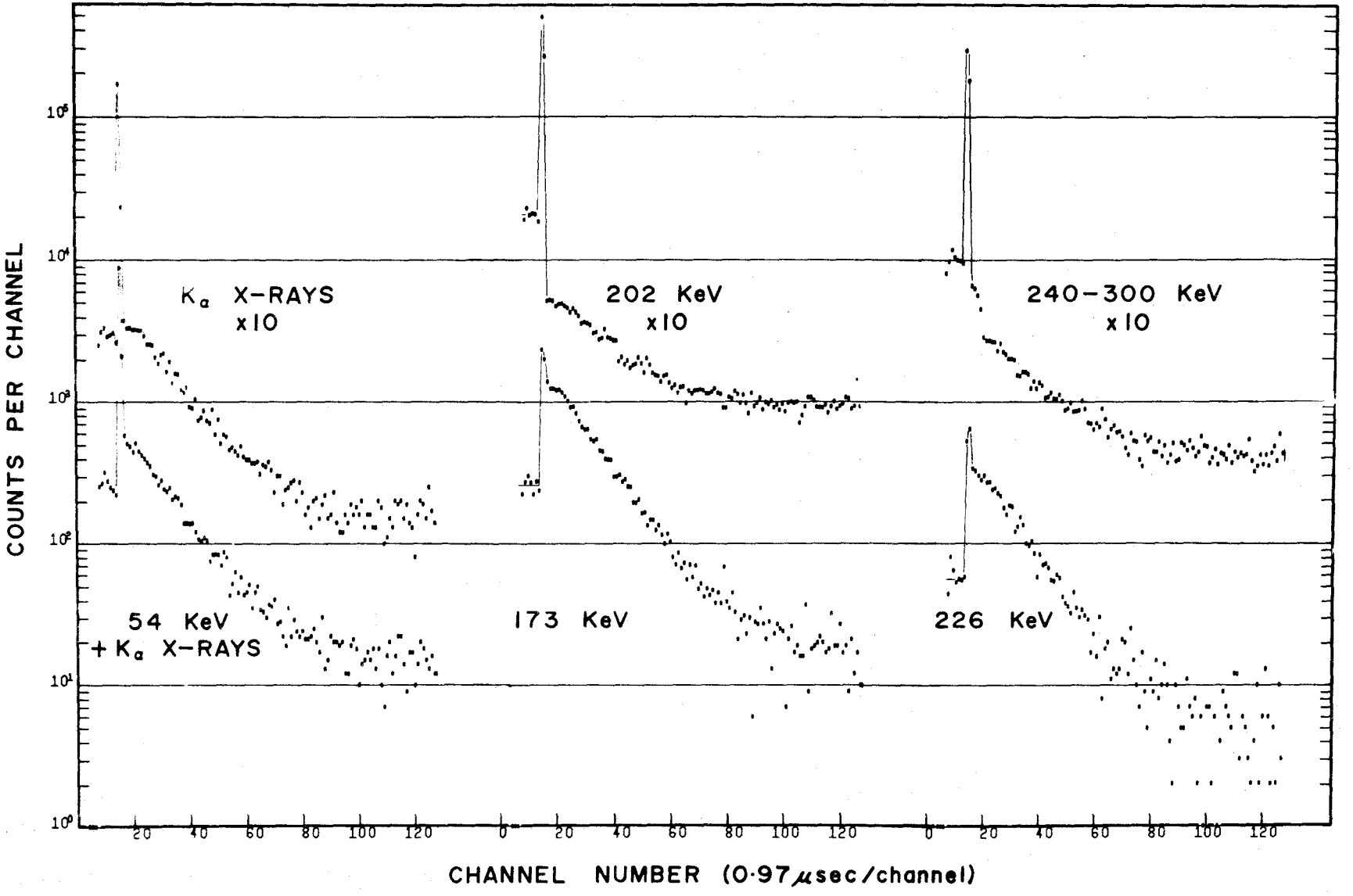
COUNTS PER CHANNEL
10^5
10^4
10^3
10^2
10^1
10^0
K_α X-RAYS
x10
202 KeV
x10
240-300 KeV
x10
54 KeV
+ K_α X-RAYS
173 KeV
226 KeV
20 40 60 80 100 120
0 20 40 60 80 100 120
0 20 40 60 80 100 120
CHANNEL NUMBER (0·97 μsec/channel)

Figure 6.23

1333 keV isomer delayed coincidence spectra (chance subtracted)

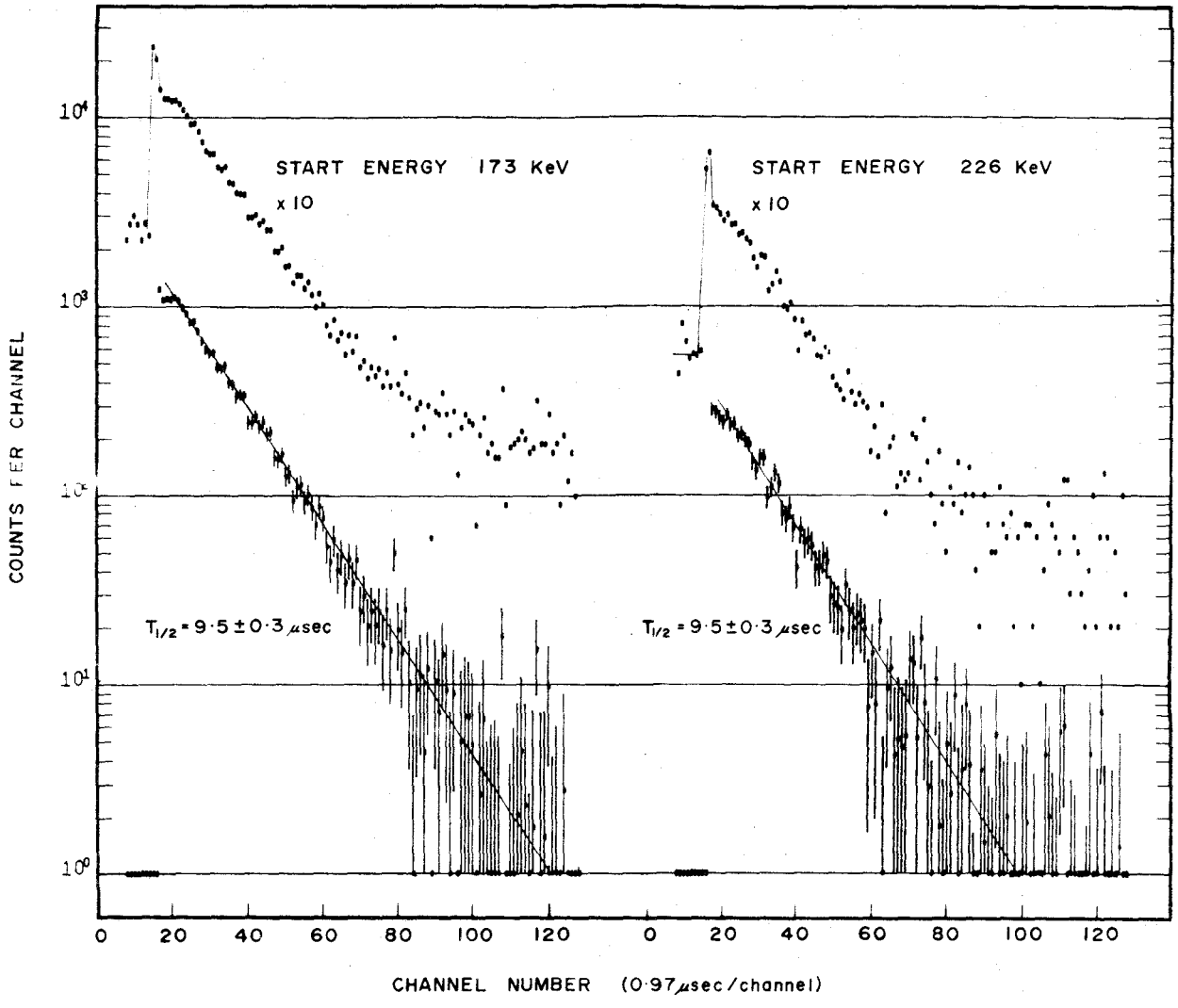
START ENERGY 173 KeV
x 10
START ENERGY 226 KeV
x 10
$T_{1/2}$ = 9·5 ± 0·3 μsec
$T_{1/2}$ = 9·5 ± 0·3 μsec
COUNTS PER CHANNEL
CHANNEL NUMBER (0·97 μsec/channel)
0
20
40
60
80
100
120

Fig. 6.23 shows the result of subtracting the chance component from the decay curves associated with the 173 and 226 keV transitions. This component was obtained by summing the time spectra for the 202 and 240-300 keV "start" energies and normalizing this sum spectrum to the 173 and 226 keV time spectra for delays greater than 100 μsec. The difference spectra follow an exponential decay over ∿ 2 decades and the half-lives obtained by the analyses of the two spectra are in gratifying agreement. The value of 9.5±0.3 μsec for the 1333 keV isomer is quite insensitive to the shape of the chance spectrum which was subtracted. The 9.5 μsec value is in marked disagreement with the value of 13.0±0.5 μsec obtained by Borgreen et al (1967) for the 1333 keV state. It is, however, in fair agreement with the value of 10.5±0.7 μsec by Brandi et al (1964).

6.8 Results of the Delayed Coincidence Experiments

The results of the γ-$\gamma_{delayed}$ and the γ-$\gamma_{delayed}$-$\gamma_{delayed}$ experiments described in section 5.5 are presented below. The lower energy half of the contents of the four sections of the memory, obtained with one detector, are presented in Fig. 6.24. (A severe gain shift in the response of the other detector used in the run made its data unusable). The singles spectrum A(Tag 00) is composed of events for which

Figure 6.24

γ-ray spectra from the delayed coincidence experiments

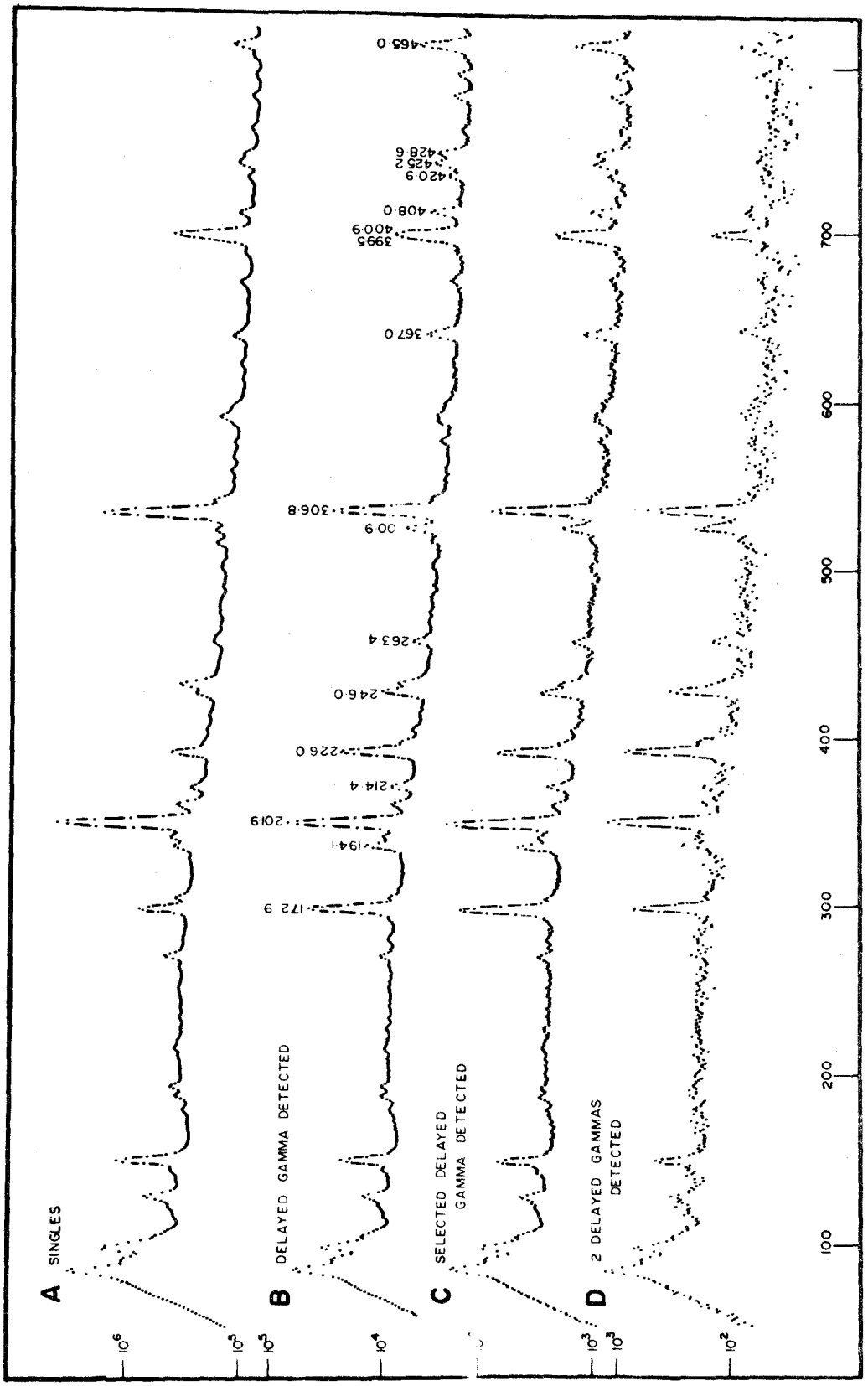
A SINGLES
B DELAYED GAMMA DETECTED
C SELECTED DELAYED GAMMA DETECTED
D 2 DELAYED GAMMAS DETECTED
172.9
194.1
201.9
214.4
226.0
246.0
263.4
300.9
306.8
367.0
399.5
400.9
408.0
420.9
425.2
428.6
465.0
CHANNEL

no delayed events were detected. Spectrum B (Tag 01) contains those events followed by any unspecified delayed event. Spectrum C (Tag 10) includes events where the pulse height of the delayed gamma ray corresponded to the photopeaks of one of the transitions following the decay of the 1333 keV state. Spectrum D (tag 11) emphasizes those gamma rays which feed the 1559 keV state. Spectra B and C were combined to identify all gamma rays feeding either isomer and corrected for chance as described below.

A comparison of the relative intensities of lines in the four spectra was often sufficient to determine which gamma ray fed which isomer. For example, the 226.0, 246.0, 300.9 keV lines clearly feed the upper isomer while the 172.9 and 194.1 keV gamma rays feed the lower. Since the 201.9 keV transition is a member of the g.s.b., its presence in spectra B, C or D of Fig. 6.24 must be due to chance and can be used to correct for chance events. The result of subtracting the appropriate fraction of the singles spectrum A from spectra B + C and spectrum D is shown in spectra E and F respectively of Fig. 6.25 and 6.26. Spectrum E now contains only transitions which feed either one of the two isomeric states. Spectrum F still includes chance events arising when one of the two delayed gamma rays was chance and the other was true. The spectrum of these chance events has the same shape as spectrum E and the latter was used for

Figure 6.25

γ-ray spectra (chance subtracted) from the delayed coincidence experiments. Spectrum E continued on figure 6.26

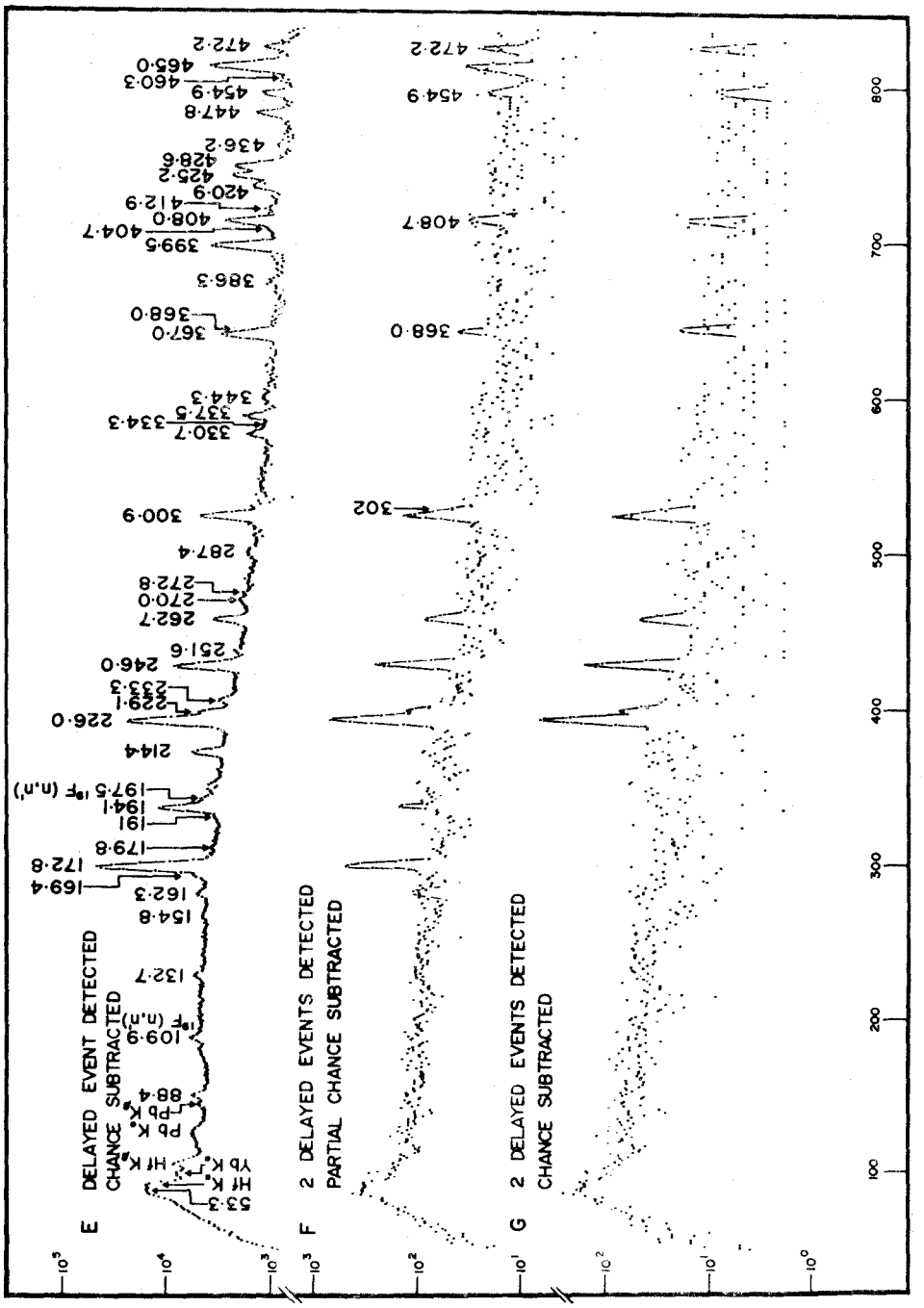
E DELAYED EVENT DETECTED
CHANCE SUBTRACTED
F 2 DELAYED EVENTS DETECTED
PARTIAL CHANCE SUBTRACTED
G 2 DELAYED EVENTS DETECTED
CHANCE SUBTRACTED
CHANNEL
53.3
Hf Kα
Yb Kα
Hf Kα
Pb Kα
Pb Kβ
88.4
109.9
132.7
154.8
162.3
169.4
172.8
179.8
191
194.1
197.5 19F (n,n')
214.4
226.0
229.1
233.3
246.0
251.6
262.7
270.0
272.8
287.4
300.9
330.7
337.5
334.3
344.3
367.0
368.0
386.3
399.5
404.7
408.0
412.9
420.9
425.2
428.6
436.2
447.8
454.9
460.3
465.0
472.2
302
368.0
408.7
454.9
472.2

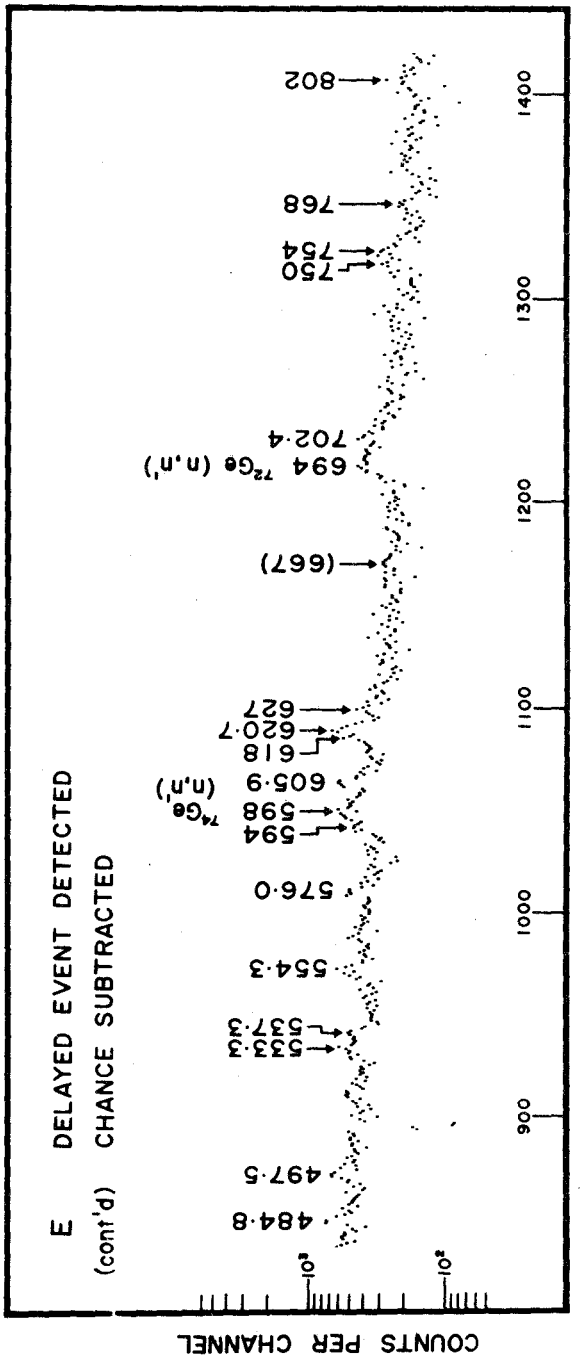
E DELAYED EVENT DETECTED
(cont'd) CHANCE SUBTRACTED
COUNTS PER CHANNEL
CHANNEL NUMBER
484.8
497.5
533.3
537.3
554.3
576.0
594
598
74Ge (n,n')
605.9
618
620.7
627
(667)
694 72Ge (n,n')
702.4
750
754
768
802

Figure 6.26

the chance correction. Since the 172.8 keV gamma ray feeds only the lower isomer, its presence in spectrum F is entirely due to chance and the fraction of E subtracted was adjusted to remove it. The true spectrum associated with two true delayed events is presented in spectrum G; all the gamma rays in this spectrum feed the upper isomer.

Table 6.2 presents the energies of the gamma rays associated with delayed events, together with their intensities in the singles spectrum, and the single and double delayed coincidence spectra. Finally, the table shows the classification for each transition.

6.9 Procedure for Determining the Levels Decaying to the Isomers

The details concerning the identification of the levels which feed the isomers are conveniently discussed together with the γ-γ and $(\gamma$-$\gamma)$-$\gamma_{delayed}$ coincidence data. However, the general procedure used in constructing the level scheme is first presented as an aid to the reader. The data will be presented in section 6.10.

In this section we are concerned only with gamma rays which decay to the isomers, i.e. those identified (section 6.8) in the delayed coincidence experiments and listed in table 6.2. The transitions which feed the 1559 keV isomer are further identified in the double delayed coincidence experiment.

The strong 173 and 225.7 gamma rays feed the 1333 and 1559 keV isomers directly and represent the lowest transitions within the bands built on these states. Other transitions which feed these bands are in prompt coincidence with these two radiations. Transitions which feed the isomers and are not in prompt coincidence with one of the pair must either feed one of the isomers directly or belong to some other cascade.

The relationships between the various transitions were established from the prompt γ-γ and $(\gamma$-$\gamma)$-$\gamma_{delayed}$ coincidence information. Their relative intensities (table 6.2) and the measured coincidence probabilities were sufficient to establish the ordering of the transitions. Cascade-crossover energy relationships provided a useful check.

Coincidences among contaminant lines caused some difficulty in the interpretation of the coincidence data. For the purposes of this section, these contaminants include not only products of other reactions, but also all gamma rays from the $^{174}Yb(\alpha,2n)^{176}Hf$ reaction which by-pass the two isomers. The spectra from the $(\gamma$-$\gamma)$-$\gamma_{delayed}$ experiment were very useful for identifying these extraneous transitions. These spectra represent prompt coincidences which are followed by delayed events (either true or accidental). Since no attempt has been made to remove the contribution caused by accidental delayed events, extraneous transitions still remain but with noticeably reduced intensities.

Table 6.8

Coincidence Probabilities for Gamma rays Associated with the 10μ sec. Isomers

E_i (KeV)	E_j (KeV)	C_{ij}	C_{ji}	$C_{expected}$
172.7	53.5	4.0 (g)		4.4 (g)
	64 (K_β)	0.18		
	90	0.045		
	160	0.041		
	194	0.95	1.2	1.4
	214	0.28	0.35	<0.46
	227	0.25	0.16	(a)
	234	0.17		0.11
	252	0.05 (b)		
	331	0.11	∿0.07 (b)	∿0.2
	385	0.10 (b)	0.06 (b)	∿0.08
	408	0.55	0.67	(a)
	413	0.078		0.1
	421	0.35	0.42	0.57
	425	0.95	0.97	0.87
	447	0.26	0.28	0.40
	468	0.08 (b)	<0.02 (c)	
	485.8	0.11	0.12	
	512.5	∿0.1		
	548.5	∿0.05		
	567	0.05		

E_i (KeV)	E_j (KeV)	C_{ij}	C_{ji}	$C_{expected}$
172.7 Cont.	601	0.15		
	607.5	0.26		0.08
	618	0.16		∿0.1
	627	0.11	∿0.09	(a)
	631.5	0.095		
	668	∿0.06		
	709	0.057		
	767	0.09		∿0.15
	802	∿0.07 (b)	(c)	
	833	∿0.16		
191.6	226	∿0.035 (b)	0.069	
194	56 (K_α)	0.86		
	64 (K_β)	0.22		
	214	0.35	0.48	0.55
	234	0.06		0.06
	249	0.05 (b)		
	385	0.07	0.06	0.1
	413	0.13		0.11
	447	0.31	0.28	0.48
	485	0.04 (b)		0.05
	618	0.15		∿0.1
	627	0.06 (b)	∿0.05 (b)	∿0.03
	768	0.08 (b)		∿0.07

E_i (KeV)	E_j (KeV)	C_{ij}	C_{ji}	$C_{expected}$
194 Cont.	802	<0.1 (b)	(c)	
214	88	0.15		
	234	0.10		0.23
	249	0.05		
	367	0.22	0.13	0.23
	485	0.06		
	628	≈0.04	(c)	
	708.4	≈0.08 (b)		
	768	0.09 (b)		0.12
225.7	54	0.9		
	64	0.24		
	110 (d)	0.05		
	163	0.11		0.18
	229	0.39	0.43	0.52
	246	1.9	2.2	1.4
	263	0.46	0.58	0.45
	270 (e)	0.08		
	273 (e)	0.08		
	301	0.14	0.10 (b)	(a)
	337	0.07 (b)		0.08
	344	0.10		
	368	0.25		0.12
	408.7	0.46	0.40	0.5 (h)
	508.9	0.18	0.15	(a)
	533	0.14		0.18

E_i (KeV)	E_j (KeV)	C_{ij}	C_{ji}	$C_{expected}$
225.7 Cont.	537	0.12	∿0.04 (b)	∿0.23
	554.4	0.08	∿0.08	(a)
	576	0.16	0.17	0.21 (f)
	647	0.10	∿0.08	(a)
	756	0.08		
	783	0.11		
	849	0.15		
226.9	337	∿0.07		∿0.08
246.0	163	0.08		0.18
	263	0.74	0.75	0.56
	270 (e)	0.05		∿0.06
	273 (e)	0.05		
	301 (b)	<0.10 (c)	0.11	(a)
	337	0.07 (b)		
	344	0.09		
	368	0.28	0.25	0.12
	533 (e)	0.11		0.13
	537 (e)	0.19	0.06 (b)	∿0.3
252	447		∿0.06 (b)	
263	105	0.05		
	270	0.10		

E_i (KeV)	E_j (KeV)	C_{ij}	C_{ji}	$C_{expected}$
263 Cont.	344	0.19		
	472	0.11		∿0.06
	533	0.13		0.17
331	133	0.04		∿0.12
	425	0.34	0.35	∿0.4
	460.7		0.06	
	465	∿0.06	0.08	∿0.12
	472	∿0.09		
367	385		∿0.05 [b]	
	447	0.09	0.21	0.24
	472			
	802 [b]	<0.15		
399	337	∿0.7		0.63
408	234	0.15		0.17
	252	∿0.10		∿0.1
	485	0.09	0.16	0.06
425	154		<0.01 [c]	
	157		0.04 [c]	
	468	0.12 [b]	<0.03 [c]	
461	465	0.25	0.19	
	602	0.08		

E_i (KeV)	E_j (KeV)	C_{ij}	C_{ji}	$C_{expected}$
465	133	0.22		0.16
	156	0.04 (b)		
	221	0.06 (b)		
	246	0.06 (b)		
	287	0.17		0.2
	347	0.07 (b)		
	467	0.2 (i)		0.2

(a) I_j found from C_{ij}.

(b) At limit of detection.

(c) Not observed

(d) $^{19}F(n,n')$

(e) Unresolved.

(f) Intensity from delayed coincidence experiment used for determining $C_{expected}$.

(g) K_α contribution already subtracted.

(h) Contribution of 408.3 component subtracted before determining $C_{expected}$.

(i) 465-467 and 467-465 coincidence observed in peak; therefore C_{ij} only half the observed value.

Figures 6.27-6.32

γ-γ coincidence spectra associated with transitions populating the isomeric states.

(u) indicates a line of unknown origin.

(r) indicates a transition having reduced relative intensity in the γ-γ-γ_{delayed} spectrum; the transition, therefore, does not feed either isomer.

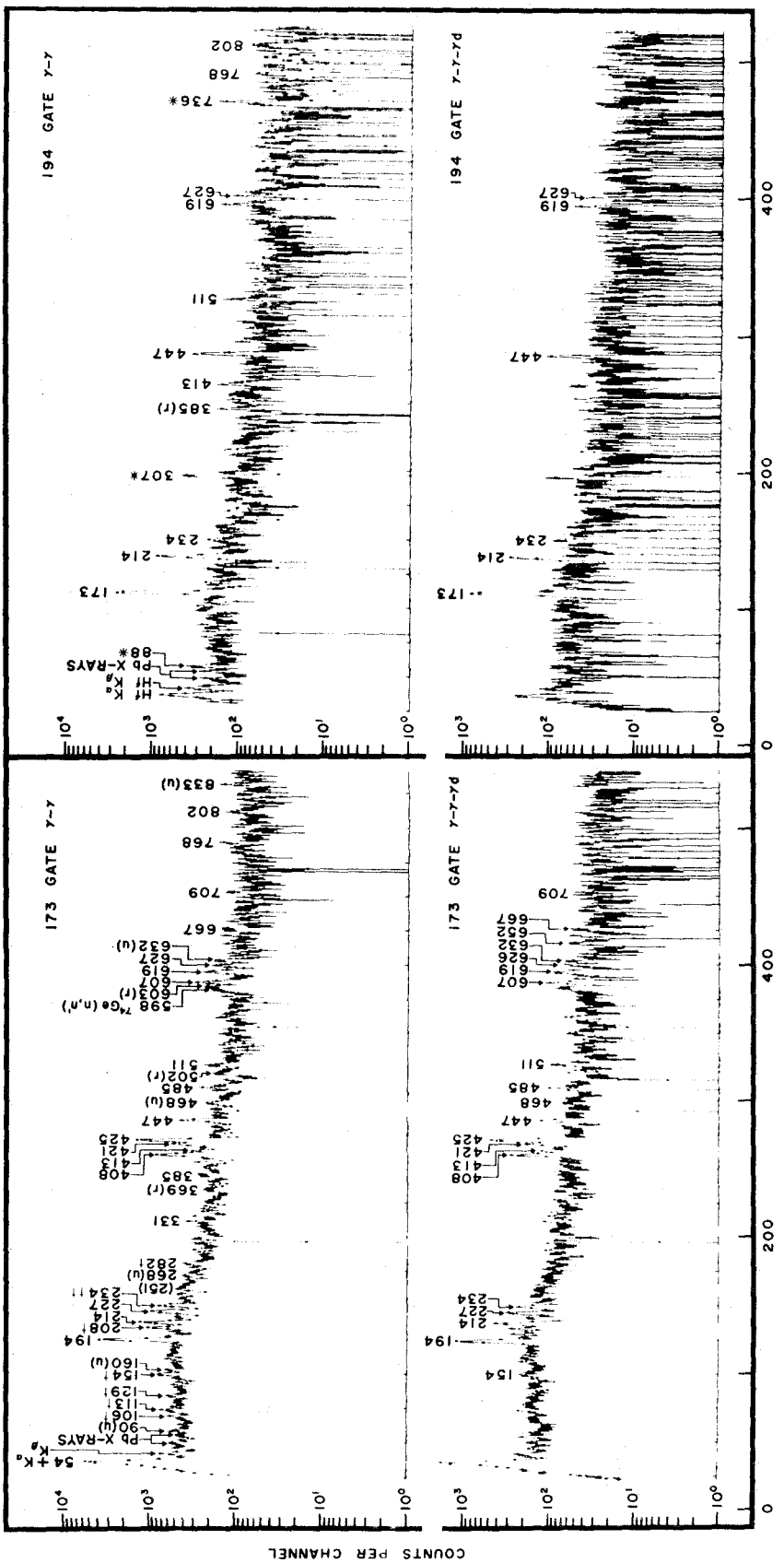

Figure 6.27

† $^{177}_{Hf}$; †† $^{176}_{Hf}$ and $^{177}_{Hf}$; * From tail of 202 keV transition in gate.

The statistics obtained in this experiment were poorer than those from the corresponding gate in the simple γ-γ coincidence experiment, so that in the case of weak peaks it was often impossible to use this criterion.

6.10 The γ-γ and $(\gamma$-$\gamma)$-$\gamma_{delayed}$ Coincidence Data

Figures 6.27 to 6.32 present spectra in coincidence with a selection of gates obtained in the γ-γ and $(\gamma$-$\gamma)$-$\gamma_{delayed}$ coincidence experiment (sections 4.6(ii) and 5.6). These data provide the essential evidence for the level scheme which was finally adopted. Many other gates were analysed and provided confirmatory evidence. The complete results are summarised in table 6.8, where the experimental and expected C_{ij}'s are compared in the manner outlined in section 6.4. The level scheme (which will be discussed in detail in Chapter 7) is reproduced in Fig. 6.33 to facilitate the discussion of the data presented.

Figure 6.27 shows the spectra coincident with the 173 and 194 keV gamma rays. These are the lowest two cascade transitions in the rotational band built on the 1333 keV isomer (labelled B in Fig. 6.33). In the 173 keV gates, the lines at 194, 214, 234, 251, 408, 447 and 485 keV are transitions within band B. Transitions between bands A and B appear at 413, 421, 607 and 619 keV. The peaks at 331, 385 and 425 keV are associated with transitions in band C and between

levels in C and B. The transition at 227 keV (which was an unresolved member of a triplet in the in-beam singles spectrum) proceeds from a level at 1732 keV. The gamma rays of energy 627, 667, 768 and 802 keV proceed from tentatively identified levels. The transitions marked with a dagger (†), which appear with reduced intensity in the $(\gamma-\gamma)-\gamma_{delayed}$ spectrum, are due to coincidences in ^{177}Hf. While the gamma ray at 234 keV also appears in ^{177}Hf, the peak in this gate is too strong and must contain a component belonging to ^{176}Hf. This is confirmed by the fact that its intensity is not reduced in the $(\gamma-\gamma)-\gamma_{delayed}$ spectrum. The 511 keV annihilation line arises from pair production caused by high energy gamma rays. Unclassified weak peaks which appear with reduced intensity in the $(\gamma-\gamma)-\gamma_{delayed}$ spectrum have been labelled "r"; these are unrelated to the isomers. Peaks whose origins are completely unknown are indicated by the symbol "u".

Finally, the 54 keV transition connecting the 1559 and 1506 keV states is evident in this gate (cf. 194 gate). The K_α contribution to this line may be obtained from the $\frac{K_\alpha}{K_\beta}$ ratio observed in the 194 keV gate. The efficiency of the detector in the 50 keV region was obtained from the X-ray intensities of the g.s.b. gates, in a manner similar to that outlined in section 6.6. From the measured coincidence

probability, the value of α_T may be deduced* as $\lesssim 0.7$. This value is consistent with the E1 assignment made in section 6.6 (see table 6.7).

The spectra coincident with the 194 keV transition confirms the deductions made from the above gates; the lines which are present in both gates feed the band B at the 1700 keV or some higher level. The 88, 307 and 736 keV gamma rays are due to a contribution in the gate from the tail of the strong 202 keV g.s.b. transition. The relative intensities of these lines are, therefore, reduced in the $(\gamma\text{-}\gamma)\text{-}\gamma_{delayed}$ spectrum. Also the 385±1 keV transition appears to be reduced in intensity in the $(\gamma\text{-}\gamma)\text{-}\gamma_{delayed}$ spectrum; however the fact that it is in coincidence with both the 173 and 194 keV transition suggests that it feeds the 1700 keV member of the band B. This appears to be the same transition as the 386.3±0.6 keV gamma ray identified in the delayed coincidence experiment.

Figure 6.28 presents spectra in coincidence with three transitions within band B (214, 367 and 408 keV). The 214 keV gate shows the expected peaks at 173, 194, 234, 367 and 485

---

* $$T_{54} < T_{173} - \sum_i T_i \sim 18-7 = 11,$$

where T represents the total transition intensity, and where the summation over i is for all the observed transitions feeding the 1506 keV level.

$$1 + \alpha_T = T_{54}/I_{\gamma_{54}}$$

$$\alpha_T \lesssim (11/6.4)-1 = 0.7$$

keV arising from transitions in band B. The 768 keV peak, which appeared also in the 173 and 194 keV gates reveals coincidence probabilities consistent with its assignment as a transition to the 1914 keV level, defining a state at 2682 keV. The gate also contains a number of peaks arising from ^{177}Hf and ^{178}Hf. The 88 keV peak is unexplained.

The 367-368 keV gate contains two gamma rays. The 367 keV transition brings up the 214 and 447 keV peaks of band B and the 413 keV transition from band A to band B. The 368 keV transition is a transition from band E to band D (see Fig. 6.34) and is in coincidence with the 226, 246 and 472 keV members of band D. The 202 and 417 keV peaks are unexplained. The 408-409 keV gate also includes two gamma rays. The 408 keV component is responsible for the peaks at 173, 234 and 485 keV of band B. The 409 keV component is a transition from band E to D and brings up the 226 keV line in the latter band.

Fig. 6.29 presents the spectra in coincidence with gates set at 425 and 465 keV. The former gate contains the 425 keV transition between band C and band B, a 426 keV transition in ^{177}Hf and a 427 keV transition in ^{178}Hf. The 425 keV component is responsible for the 173 keV transition of band B and the 331 keV gamma ray of band C. The peaks marked with a dagger belong to ^{177}Hf while those with a double dagger are associated with ^{178}Hf. The origins of the weak peaks at 137, 155+157, and 467 are unknown. The 465 and

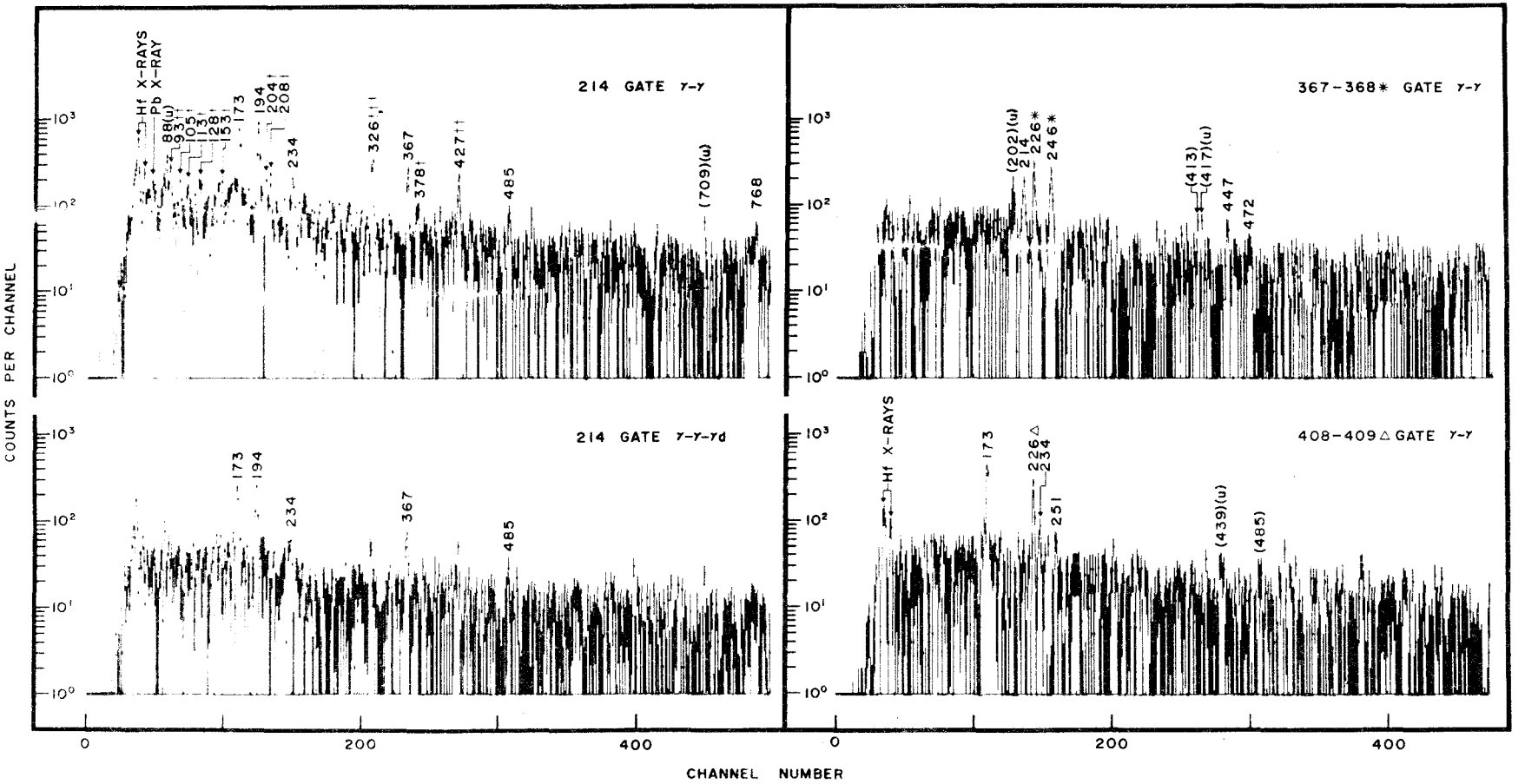

Figure 6.28

† ^{177}Hf; †† ^{178}Hf

* and Δ indicates coincidences between similarly labelled lines

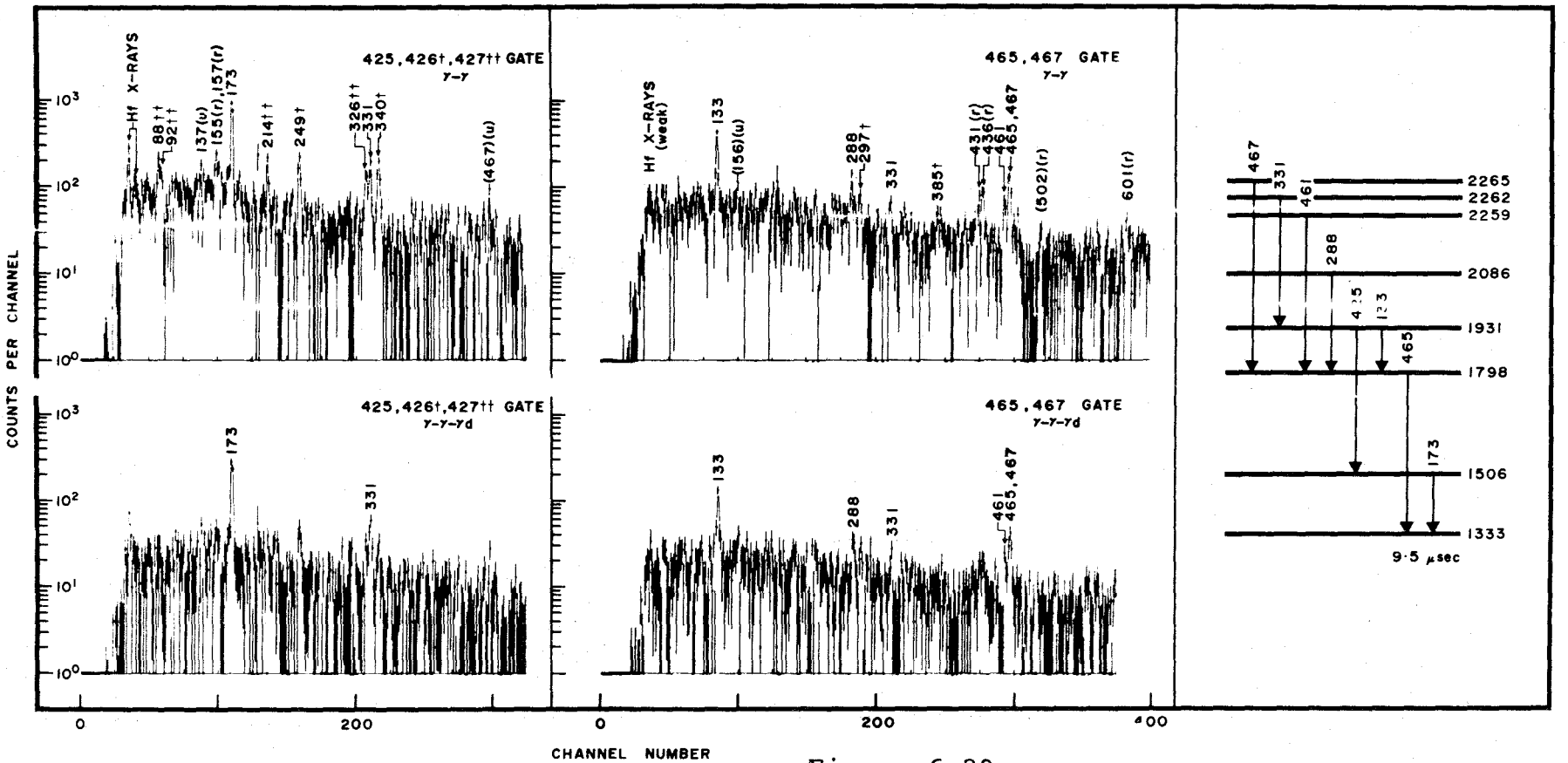

† ^{177}Hf †† ^{178}Hf

Figure 6.29

467 keV gamma rays are in direct cascade and both are contained in the gate. The 465 keV transition is responsible for the 133, 288 and 331 keV transition of band C, as well as the 461 and 467 keV transitions which define levels at 2259 and 2265 keV. The 297 and 385 keV lines are due to a 466 keV line in ^{177}Hf. The remaining lines are of unknown origin. The presence of 467 keV lines in the 173 and 425 keV gates appear to contradict the decay scheme shown in Fig. 6.33 and in the insert. However, the coincidence probabilities deduced from these three 467 keV peaks show that the 465-467 keV cascade is at least five times stronger than either the 467-173 or 467-425 keV cascades. Moreover, the 465 keV gate shows no evidence for either a 173 or 425 keV peak. We conclude that the 467 keV lines appearing in the 173 and 425 keV gates are due to statistical fluctuations. Similar arguments can be made with respect to the weak 156 keV peak which appears to define a 156-467 keV cascade. However, since no 467 keV peak appears in the 156 keV gate, its reality is subject to doubt.

Fig. 6.30 presents the spectra in coincidence with the 226 and 246 keV transitions in band D. The 226 keV gate brings up the 246, 263, 270 and 509 keV transitions within band D, the 163, 229, 344, 368 and 409 keV transitions between bands E and D, and the 783, 537 and 554 keV transitions which feed the 1785 and 2031 keV states of band D and the 2014 keV state of band E.

The 576-226 and 647-226 keV cascades are observed in the 226 keV and reverse gates and define levels at 2361 and 2433 keV. The weak 192 keV transition is seen only in the 226 keV gate and in the delayed coincidence experiment and tentatively defines a level at 1977 keV. The 273 and 302 keV gamma rays from triple cascades with the 246 and 226 keV transitions and are also seen in the reverse gates. They therefore define levels at 2304 and 2333 keV,respectively. The evidence for 246-302 keV coincidences in Fig. 6.30 is very marginal but is clearer in the reverse gate (not shown) where the 307 keV peak is absent. If one discounts the evidence for 302-246 keV coincidences, the 302-226 keV data would place the 302 keV transition between the 2086 keV member of band C and the second member of band D.

The 533 keV transition is part of the 533-263-246-226 keV cascade and thus defines a level at 2827 keV. It also fits between the 2564 and 2031 keV levels of band D but the coincidence data indicate that essentially all of its strength feeds the 2294 keV state.

The 173 and 337 keV peaks are associated with the levels at 1732 and 2070 keV. Much stronger support for these levels is presented in the 400 keV gated spectrum of Fig. 6.32.

The 88, 202 and 307 keV peaks of the 246 keV gate arise partially because of an incomplete subtraction of the background and partially because the Compton edge of the 401

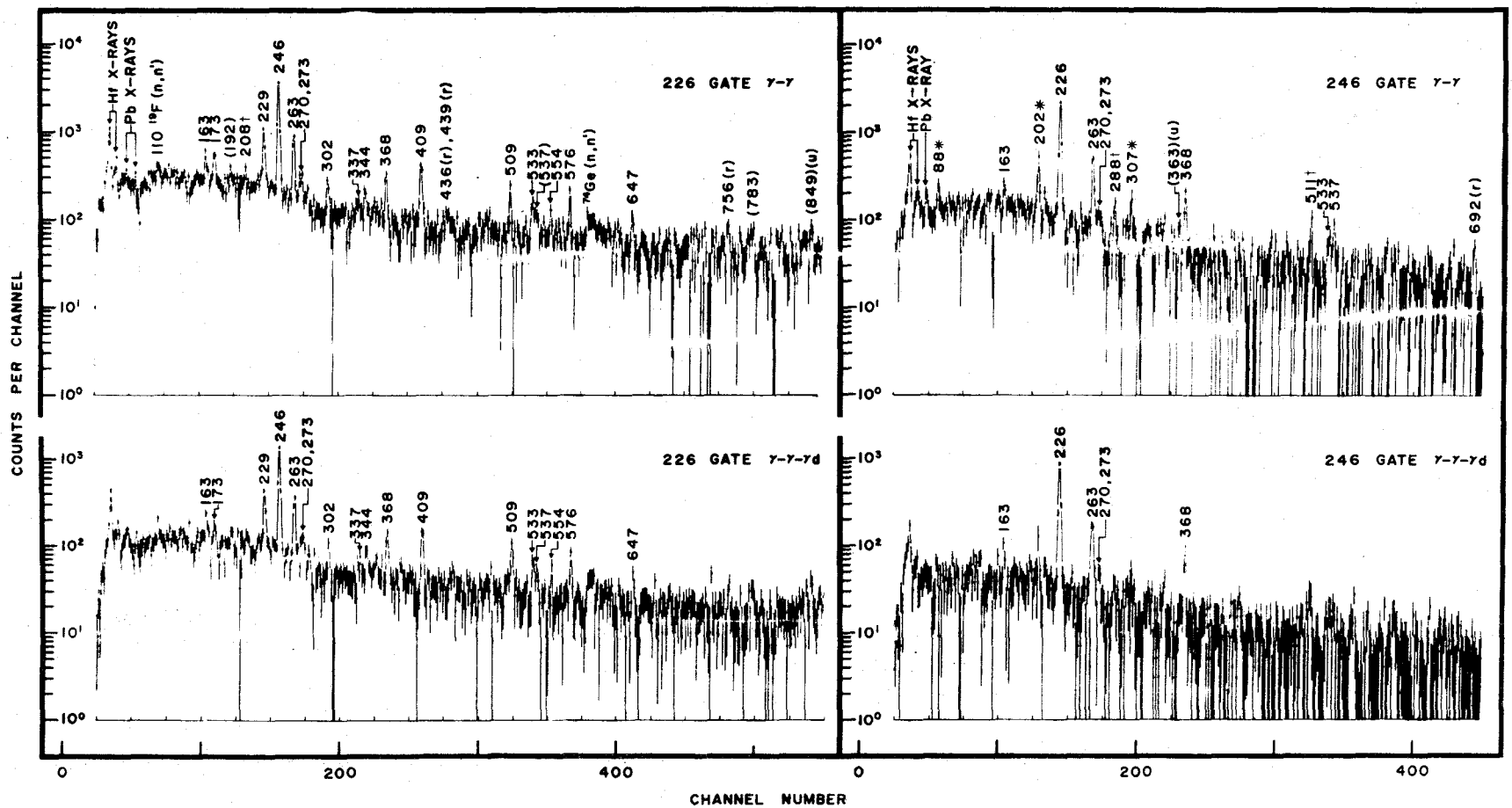

Figure 6.30

*Due to incomplete background subtraction or Compton edge of 401 keV line

†^{177}Hf

keV g.s.b. transition falls within the window.

The spectrum in coincidence with a gate set on a window at 264 keV is shown in Fig. 6.31. This gate contains the 263 keV transition of band D and two other gamma rays not related to the isomers. The 263 keV gamma ray is responsible for the peaks at 226, 246, 270, 472 and 533 keV. The 264 and 265 components bring up the 1023, 1225 and the 1188 keV components respectively and are jointly responsible for the members of the g.s.b. (see insert of Fig. 6.31). The 344 keV peak has been used to identify the level at 2638 keV. This gamma ray is also seen in coincidence with the 226 and 246 keV members of band D with coincidence probabilities of $\sim$ 0.1, roughly half of the value for the 263-344 keV cascade. This discrepancy suggests that there may be a second very weak 344 keV line in coincidence with either the 264 or 265 keV transitions in the gate.

Fig. 6.32 shows the spectrum obtained by setting a gate on the lower side of the strong 401 keV g.s.b. transition. The lines at 196 and 337 keV which are accentuated in the $(\gamma-\gamma)-\gamma_{delayed}$ spectrum are coincident with the 399 keV gamma ray included in the gate. A comparison of this spectrum with that of Fig. 6.13 derived from a gate set squarely on the 401 keV peak, shows that all the other peaks in Fig. 6.32 are associated with 401 keV component. The 337-399 keV cascade, together with the relative intensities of these two transitions establishes levels at 1732 and 2070 keV. The 1732 keV state is supported

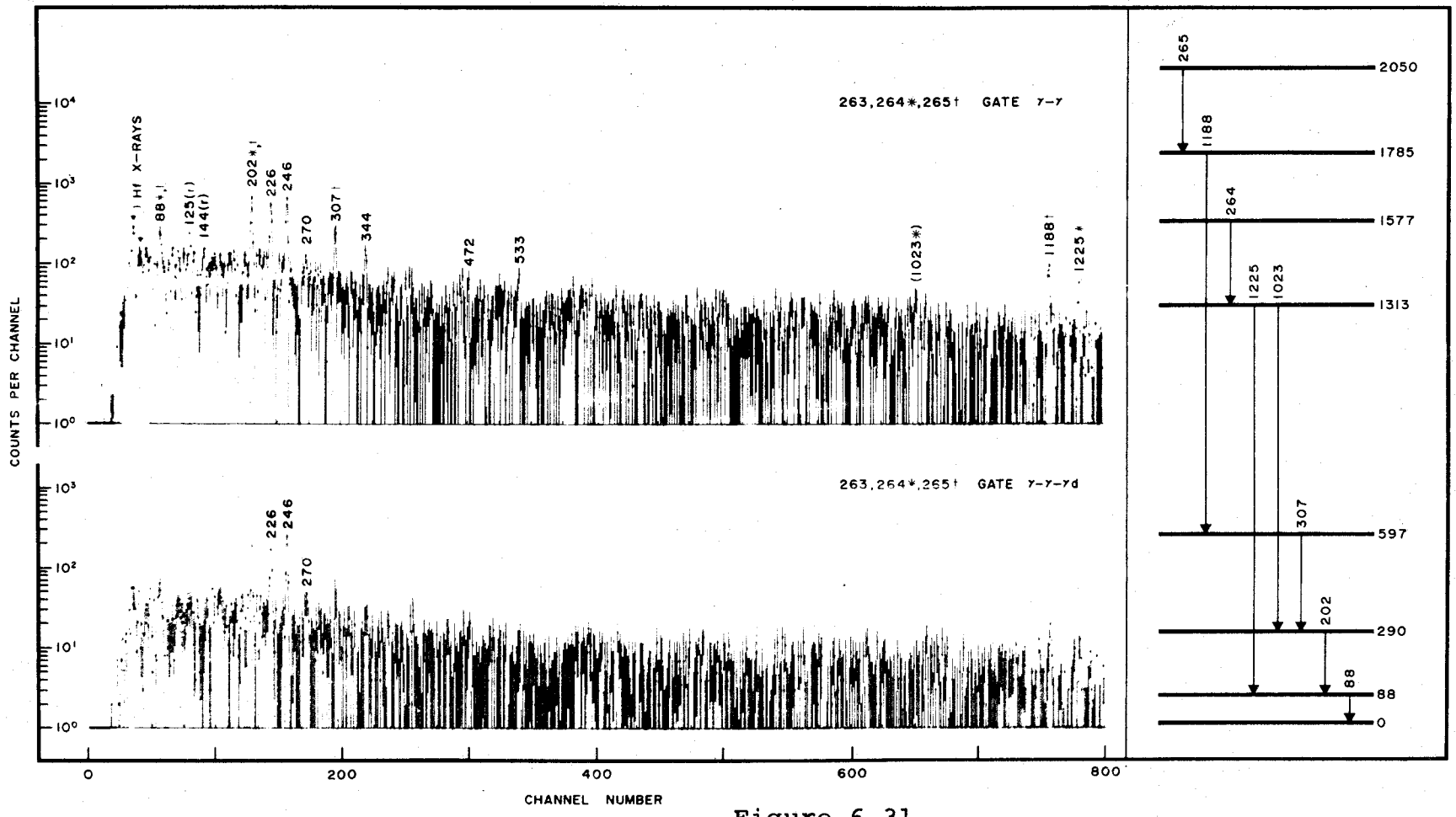

Figure 6.31

*, † Identically labelled lines are in coincidence

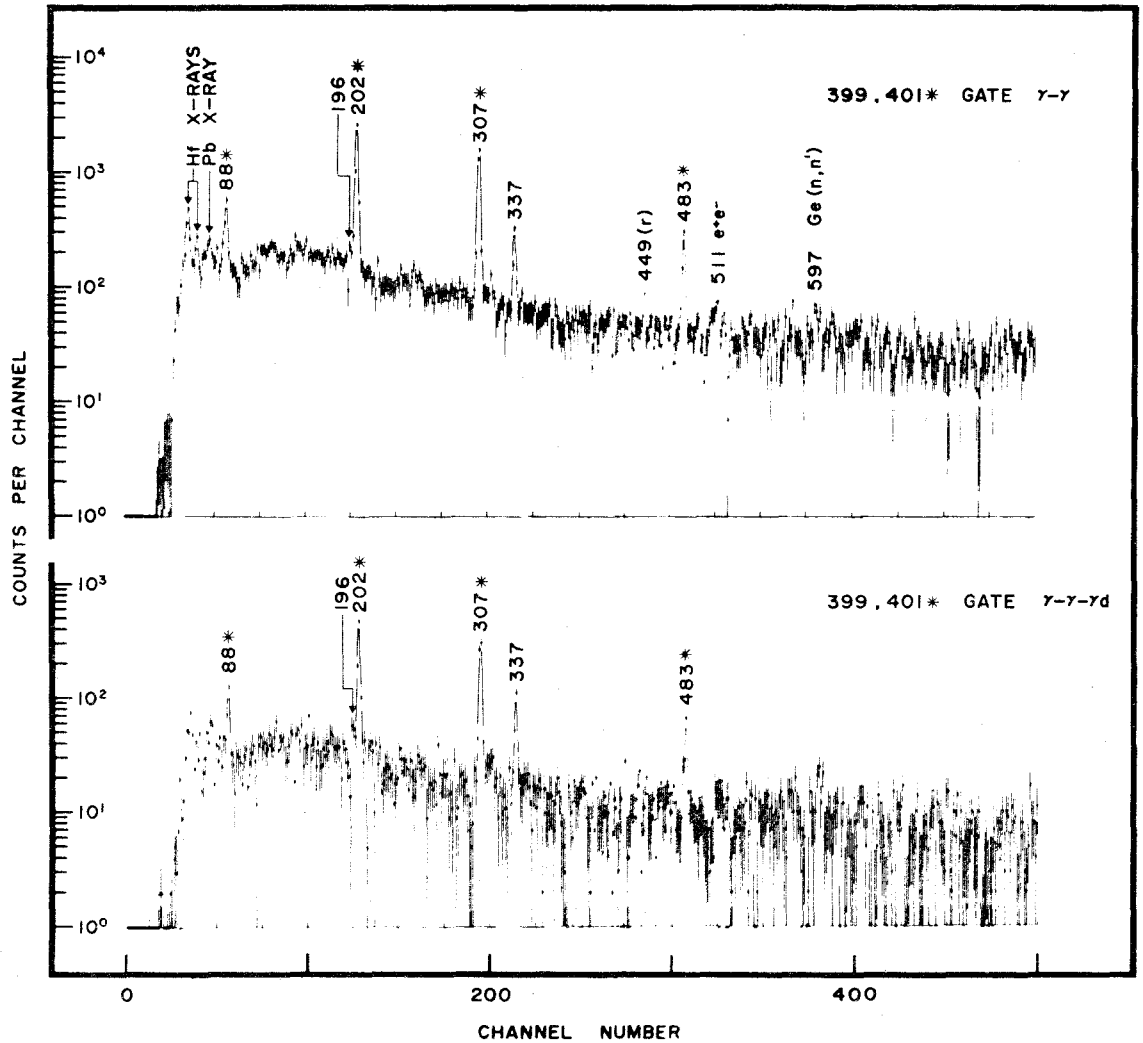

Figure 6.32 : * Identically labelled lines are in coincidence

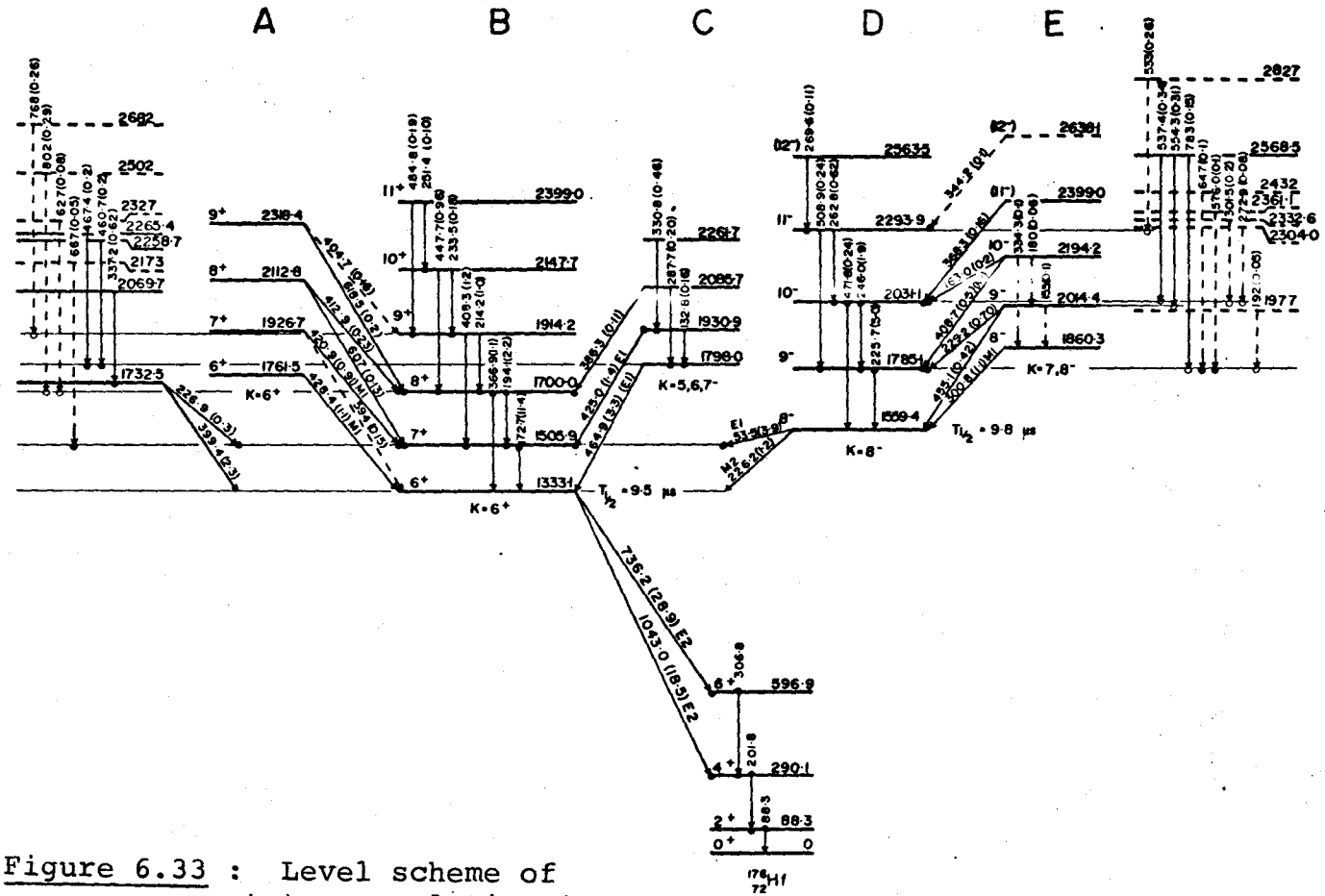

Figure 6.33 : Level scheme of states populating isomers

by the 227 keV gamma ray (see Fig. 6.30). The 196 keV transition appears to deexcite the 2265 keV level which has been established by means of the 467-465 keV cascade (see Fig. 6.29).

CHAPTER 7

DISCUSSION OF THE LEVELS IN ^{176}Hf

7.1 Introduction

In this study of ^{176}Hf, approximately 90 levels have been identified. About 60 of these have been interpreted in varying degrees in terms of the unified model. These include the members of (a) the ground state band up to spin 12, (b) a $K = 0^+$ band at 1150 keV up to spin 10, (c) a $K = 2^-$ octupole band up to spin 9, (d) a $K = 3^{(+)}$ band up to spin 8, (e) a second $K = 0$ band of which only two members have been identified, (f) three high K bands which decay to the 1333 keV isomer, and (g) two high K bands which decay to the 1559 keV isomer. In addition a number of high K states which feed the isomers have been located.

Those bands which feed the ground state band directly are shown in Fig. 7.1, while those which feed the isomers are illustrated in Fig. 7.2. These level schemes also include a number of levels of unknown character which decay to one of the bands. Other levels which have not been grouped into bands are not shown in a usual level scheme, but instead, are listed in Table 7.1. This table gives the energy of the level, the states to which it decays and the corresponding transition energies and intensities.

Figure 7.1

Level scheme of states in ^{176}Hf which decay promptly to the ground state band. (See table 7.1 for additional levels not included in this scheme). A filled circle at the end of a transition (at the arrow head) indicates that the transition was observed in a γ-γ coincidence gate set on a transition following it. A filled circle at the beginning of a transition indicates that the transition was observed in a gate set on a transition immediately preceeding it. Unfilled circles denote tentative coincidence evidence.

176
72 Hf
1Kπ
0+
2+
4+
6+
8+
10+
12+
10+
8+
6+
4+
2+
0+
0
88.32(26.5)
201.82 (100)
306.78 (69.5)
400.99 (19.2)
483.33(5.1)
553.6 (1.0)
2034.8
1481.2
1297.2 (0.5)
813.8 (0.3) E0 + E2 + M1
362 (0.14)
133.9 (1.1)
93.8 (0.6) E0 + E2 + M1
45.8 (0.08)
1338.6 (1.8)
1031.7 (1.4) E0 + E2 + M1
630.7 (0.2)
1301.8 (1.3)
1099.9 (1.6) E0 + E2
793.5 (0.57)
1227 ((1.4)
1138.1 (1.1) E0 + E2 + M1
1150 (0.004) E0
1150
2264
990.1
1628.6
1942.7
2295.0
1301.8 (1.9)
1290.8 (1.2)
1293 (0.04) E0
1208.8 ((0.6)
1293
1379.1
159.9
1287.1 (0.4)
1499.8 (1.0) (M1)
1100 (0.3)
1571.6 (1.2) M1/E2
1265.2 0.9)
1437.7 (1.6)
1130.4 (0.5)
1250.1 (1.0)
1357.4 (2.8) M1/E2
1155.6 (0.7)
1341.3 (1.8)
1252.6 (2.1)
1341
1448.7
1540.2
1727.7
1861.9
2096.7
2285.0
1509.7 (1.2)
1108.7 (0.5)
1347.4 (1.2)
268.6 (0.18)
1508 (2.0)
1201.8 (0.4)
289.6 (0.11)
1588.3 (0.58)
1385.7 (2.1)
271.8 (0.09)
1489.0 (4.2) (E2)
1287.1 (0.4)
264.0 (0.3)
1577.3
1675.8
1798.4
1944.3
2106.6
1939.4 (1.1)
655.3 (0.15)
319.6 (1.3)
1188.1 (4.0) E1
787.1 (1.0)
276.4 (0.14)
1055.8 (0.34)
248.6 (4.2) (E2)
144.5 (0.19)
1218.4 (5.0)
911.8 (1.8) E1
196 (0.2)
1114.2 (2.3) E1
156.8 (2.7) E2
91.1 (0.4)
1224.9 (7.3) E1
1023.0 (3.2) E1
1159.2 (10.6) E1 + E3 + M2
1247.5
1313.2
1404.3
1508.6
1652.9
1785.0
1992.5
2137.3
196.3 (0.15)
265.2 (0.40)
146.3 (0.24)
311.1 (1.1)
1614.2 (2.0)
1306.8 (2.6)
462.0 (0.3)
1866.3
1903.7
1964.0
2050.2
2160.3
8832
2901.4
5969.2
9979

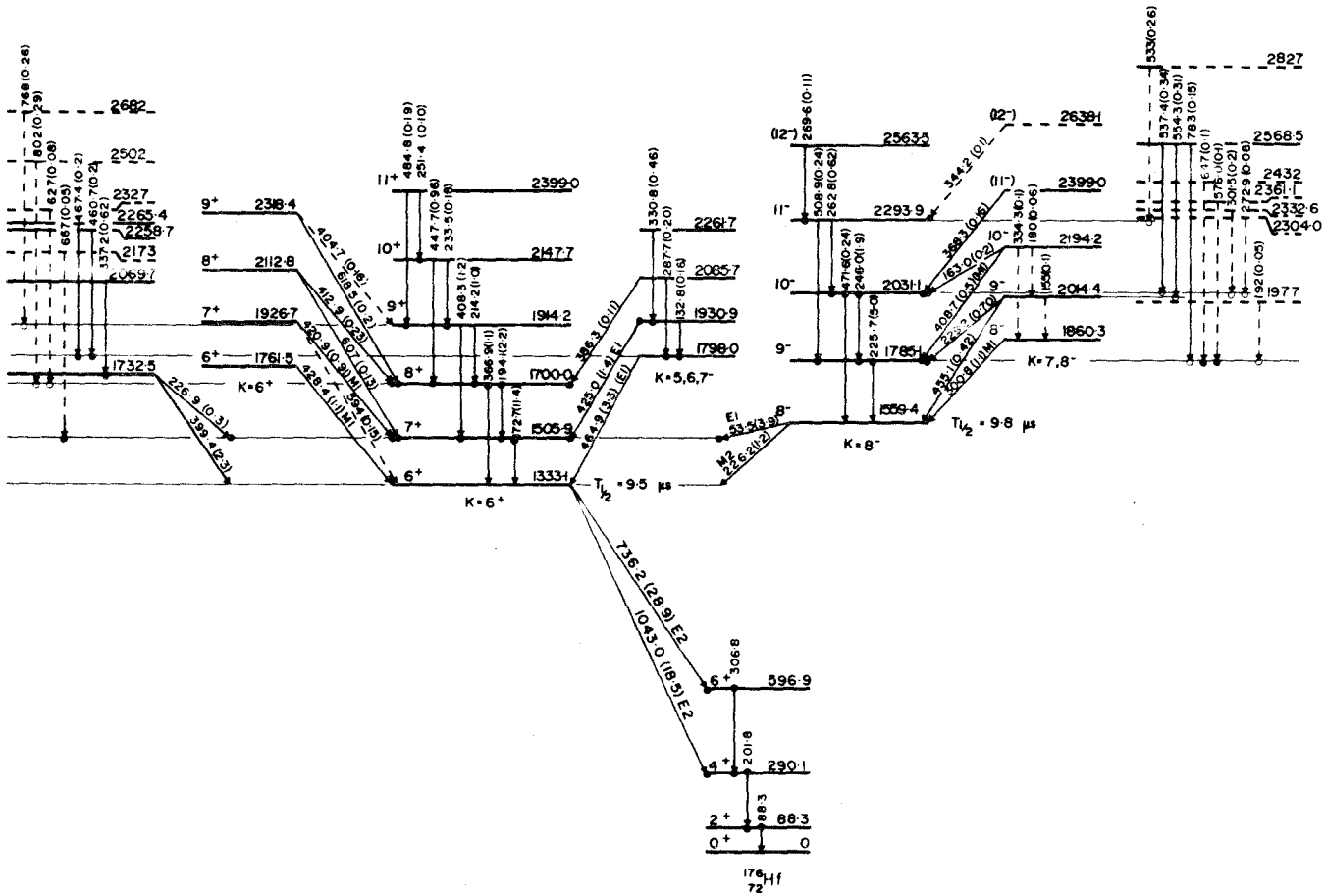

Figure 7.2: Level scheme of states in $^{176}_{72}Hf$ which decay through the isomers For an explanation of the circles connected with the transitions see caption of Fig. 7.1.

Table 7.1

Additional levels in ^{176}Hf (not shown in level scheme)

Level Energy Initial State (a)	Final State	Transition Energy	Intensity
([1454.0]	596.9)	857 ± 1	0.33
1532.5	596.9	935.8 ± 0.5	0.8[c]
([1609.3]	997.9)	611.4 ± 0.33	0.33
([1643.4]	88.3)	1555.6 ± 0.4	0.9
(	0)	1642.8[b] ± 0.6	0.54
1709.7	290.1	1419.6 ± 0.2	1.08
	88.3	1621.3[b] ± 0.3	0.85
1766.8	290.1	1476.7 ± 0.2	1.2
([1775.0]	596.9)	1177.7[c] ± 0.8	0.3[c]
1815.2	596.9	1218.4 ± 0.8	0.5[c]
	290.1	1525.0[c] ± 0.5	0.4[c]
1830.3	290.1	1540.2 ± 0.5	0.4
1853	290.1	1563 ± 1	0.9
([1878]	596.9)	1281 [c] ± 1	0.45[c]
([1906]	997.9)	908 ± 1	0.2
([1924.6]	1313.2)	611.4 ± 0.6	0.2[c]
([1959.6]	596.9)	1362.7 ± 0.2	0.9[c]
(	290.1)	1670.1[b] ± 0.4	0.7
2024.0	596.9	1427.1 ± 0.2	1.0
2116.9	596.9	1520.0 ± 0.3	1.2
2305	997.9	1307 [c] ± 1	0.4[c]

(continued next page)

Table 7.1 (continued)

Level Energy Initial State (a)	Final State	Transition Energy	Intensity
([2446.9]	997.9)	1448.0 ± 0.6	0.8
([2458.1]	997.9)	1460.2 ± 0.7	0.8
2557	997.9	1559.5 ± 0.8	0.3
2565	997.9	1567 ± 1	0.2

a) A square bracket [] indicates that the level assignment is tentative; a curved bracket between two levels indicates a tentative transition assignment.

b) Assigned on the basis of energy fits only; no γ-γ coincidence information available.

c) Obtained from γ-γ coincidence data.

Each of the identified bands will be discussed in turn. The notation adopted to represent the spin, angular momentum projection (on the nuclear symmetry axis) and parity of a level is $I\ K^{\pi}$.

7.2 The Ground State Band

(i) Identification

The members of the ground state band (g.s.b.) are strongly populated in the $(\alpha,2n)$ reaction and are, therefore, fairly easy to identify. The members up to spin 12 have been observed in this study. Previous studies by Borgreen et al. (1967) and Bernthal et al. (1971), on the ^{176}La(p,n) ^{176}Hf reaction and the ^{176}Ta decay to ^{176}Hf, respectively, have established the g.s.b. levels up to spin 6. The energies of the levels determined by the latter are in excellent agreement with those measured in this work. That the levels at 997.91, 1481.24 and 2034.8 keV are indeed the I=8, 10 and 12 members of the g.s.b. is supported by the fact that the 400.99, 483.33, 553.6 keV transitions are E2 in character. Secondly, the excitations of these transitions (see Fig. 6.6) show that they originate from levels of increasing spin. Thirdly, the ordering of the transitions is unambiguous from the coincidence data of Fig. 6.11, 6.12 and 6.13. Finally, the energy spacing is characteristic of a rotational band, as shown below.

(ii) Discussion

The rotational energy of a K = 0 band is, to first order given by

$$E_o = AI(I+1) \qquad (7.1)$$

where $A = \frac{\hbar^2}{2\mathcal{J}}$ is referred to as the rotational parameter ($\mathcal{J}$ is the effective moment of inertia). When higher order coupling effects, e.g. rotation-vibration coupling, are included, the energy may be written as a series expansion in I(I+1) (Nathan and Nilsson, 1965):

$$E = A\ I(I+1) + B\ I^2\ (I+1)^2 + C\ I^3(I+1)^3 \qquad (7.2)$$

The members of the rotational band have been fitted to eq. (7.2) by a least squares procedure. Two fits were made, one with C set at zero and the other with C treated as a free parameter. The procedure yields, in the first case:

$$A = 14.72 \text{ keV and } B = -11.11 \text{ eV} \qquad (7.3a)$$

and, in the second case,

$$A = 14.80 \text{ keV}, B = -14.56 \text{ eV and } C = +0.0216 \text{ eV}. \qquad (7.3b)$$

These results are shown in columns 3 and 4 of table 7.2a. It is clear that the inclusion of the C term improves the fit significantly.

Table 7.2 also includes the predictions of the variable moment of inertia model (VMI) of Mariscotti et al. (1969) which leads to the expression:

$$E_I\ (\mathcal{J}) = \frac{1}{2}C\ (\mathcal{J} - \mathcal{J}_o)^2 + \frac{\hbar^2}{2\mathcal{J}}\ I\ (I+1) \qquad (7.4)$$

TABLE 7.2

Experimental and Predicted Energies for bands in ^{176}Hf

(All energies in keV)

TABLE 7.2a

Ground state band

I	E_{expt}	Calculated Energies 2 parameter fit (a)	3 parameter fit (b)	VMI fit (c)
0	0	0	0	0
2	88.32±0.05	87.92	88.26	88.1
4	290.14±0.07	289.96	290.28	289.6
6	596.92±0.08	598.63	597.37	596.2
8	997.91±0.09	1002.24	997.85	998.3
10	1481.24±0.10	1484.74	1480.05	1486.5
12	2034.8±0.14	2025.97	2035.6	2052.3

a) A = 14.72 keV B = -11.11 eV

b) A = 14.80 keV B = -14.56 eV C = +0.0216 eV

c) Least squares fit by Mariscotti et al. (1969), see text.

TABLE 7.2b

K = 0' band at 1150 KeV

I	E_{expt}	Fit (d)
0	1150	1151.2
2	1226.4	1225.0
4	1390.2	1389.6
6	1628.6	1629.9
8	1932.7	1932.0
10	2295.0	2295.1

(d) 4 parameter fit A = 12.47keV B = -29.76 eV

C = +0.099 eV E_o = 1151.2 keV

TABLE 7.2c

K = 6^+_ℓ band

I	E_{expt}	Fit (e)
6	1333.12	1333.3
7	1505.86	1505.7
8	1699.98	1699.8
10	2147.69	2147.8
11	2399.0	2398.9

(e) A = 12.94 keV B = -6.30 eV E_o = 801.0 keV

TABLE 7.2d

$K = 6_u^+$ band

I	E_{expt}	Fit (f)
6	1761.5	1761.5
7	1926.7	1926.7
8	2112.8	2112.8
9	2318.4	2318.4

(f) A = 12.38 keV B = -5.93 eV E_o = 1251.8 keV

(N.B. The experimental and calculated energies are identical)

TABLE 7.2e

$K = 8_\ell^-$ band

I	E_{expt}	Fit (g)	Fit (h)
8	1559.36	1559.4	1559.26
9	1785.1	1784.8	1785.4
10	2031.1	2031.4	2030.9
11	2293.9	2293.7	2294.0
12	2563.5	2563.5	2572.7

(g) A = 11.49 keV B = +15.74 eV C = -0.0767 eV

E_o = 679.4 KeV

(h) A = 13.78 B = -7.52 eV E_o = 578.9 spin 12 member excluded in fit

TABLE 7.2f

$K=7^-$ and/or 8^-_u

I	E_{expt}	Fit (i)
8	1860.3	1860.13
9	2014.4	2014.9
10	2194.2	2193.8
11	2399.0	2399.1
12	2638.1	2633.2

(i) A = 7.10 keV B = +9.22 eV E_o = 1301.0 keV

Spin 12 excluded in the fit.

TABLE 7.2g

$K=(6^-$ and/or $7^-)$

I	E_{expt}	Fit (j)
7	1798.0	1797.9
8	1930.9	1931.2
9	2085.7	2085.4
10	2261.7	2261.8

(j) A = 7.47 keV B = 6.73 eV E_o = 1358.2 keV

for the energy of the band member with spin I. The first term expresses the increase in potential energy associated with increasing angular momentum. The second term is the usual rotational kinetic energy expression. The value of $\mathcal{J}$ appropriate to each spin value is the value which makes E_I a minimum, i.e. the value defined by the equation

$$\frac{\partial E_I(\mathcal{J})}{\partial \mathcal{J}} = 0. \qquad (7.4a)$$

There are two adjustable constants in this model: $\mathcal{J}_o$ which is regarded as the ground state moment of inertia and C which is the "restoring force constant". In the paper by Mariscotti et al., values of E_I predicted from the model are tabulated for a wide range of nuclei, using the experimentally known energies to obtain the parameters $\mathcal{J}_o$ and C. For ^{176}Hf, the energies of the members up to spin 8 were used in their fitting procedures and the energies of the states up to I=16 predicted from the model. The discrepancy between the prediced and experimental values amount to 5 and 18 keV for the 10+ and 12+ states respectively.*

In order to test if a drastic breakdown of the rotational spacing occurs for higher spin members, it would be of interest to excite these members with higher energy alpha beams (> 27 MeV) or heavier projectiles. Such a breakdown, due to the Coriolis anti-pairing effect, was predicted by

*The experimental energies available to them were not as well known as those given in Table 7.2. However, the discrepancies in energy are sufficiently small that it would not have significantly altered their predictions.

Mottelson and Valatin (1960) and seen in other deformed nuclei (e.g. ^{158}Dy, ^{160}Dy and ^{162}Er (Johnson et al., 1971)). This is a phase transition effect, occurring above a certain critical spin, at which the Coriolis force breaks down the effect of the pairing force and allows the nucleus to rotate as a rigid body.

7.3 The $K = 0^+$ band at 1150 keV

(i) Identification

The construction of the levels of this band, based on coincidence evidence has already been discussed in section 6.4 (Fig. 6.15). The pure EO character of the 1150 keV transition unambiguously defines a $IK^{\pi} = 00^+$ assignment for the level at that energy. The large EO admixtures in the 1138.1, 1099.9, 1031.7, 934.8 and 813.8 keV transitions, together with the coincidence data, definitely establish the spin sequence of the levels at 1226.4, 1390.2, 1628.6, 1932.7 and 2295.0 keV as 2, 4, 6, 8, 10, respectively, all with positive parity. The assigned spins are confirmed by the relative excitation functions of the above mentioned transitions. The rotational spacing of the level energies suggests that the levels are indeed members of the same $K = 0^+$ band. The energies may be fitted (within < 1.4 keV) to an expression of the form of equation (7.2) with the addition of

a constant term E_o, as shown in Table 7.2b.

The I=0 and 2 members of this band have also been observed in decay studies (Bernthal et al., 1971).

(ii) Mixing between the beta and ground state bands

The beta vibration and the ground state band are expected to mix through the rotation-vibration interaction (Nathan and Nilsson, 1965; Ejiri and Hagemann, 1971). A sensitive indicator of this mixing is provided by the E2 transition rates between the bands. The reduced rates for such transitions are given by:

$$B(E2\ I'0' \rightarrow I0) = \langle I'200|I0\rangle^2 |Q_{\beta g}(I'I)|^2\ e^2 \qquad (7.5)$$

where $Q_{\beta g}(I'I) = \sqrt{\frac{5}{16\pi}} \langle g|O(E2)|\beta\rangle$.

In this notation, the intrinsic quadrupole moment of the ground state would be defined as $Q_o = \sqrt{\frac{16\pi}{5}}\, Q_{gg}$.

In the presence of mixing, the wave functions of the ground state and beta bands, are given by $\psi_u(I)$ and $\psi_\ell(I)$ in equation 3.82 if one replaces "a" by "β" and "b" by "g". The interband quadrupole matrix element (see eq. 3.83a) is given by

$$Q_{\beta g}(I'I) = Q^o_{\beta g}\left[1 + (\alpha_I - \alpha_{I'})\frac{Q^o_{\beta\beta}}{Q^o_{\beta g}} + \alpha_{I'}\left(\frac{Q^o_{\beta\beta} - Q^o_{gg}}{Q^o_{\beta g}}\right) - \alpha_I\alpha_{I'}\right]\left[N_I N_{I'}\right]^{-1/2} \qquad (7.6)$$

where $Q^{o}_{\lambda',\lambda}$ are the unperturbed matrix elements; N_I is the normalizing constant $(1+\alpha_I^2)$ and α_I is the mixing coefficient given by eqn. 3.81. For the case where the interaction matrix element is much smaller than the unperturbed energy separation, i.e.

$$H_{\beta g} << E^{o}_{\beta} - E^{o}_{g}$$

first order perturbation theory is applicable, giving

$$\alpha_I \sim - \frac{H_{\beta g}}{E^{o}_{\beta} - E^{o}_{g}} \quad . \tag{7.7a}$$

The interaction matrix is usually expanded (Ejiri and Hagemann, 1971) as a simple power series of I(I+1). Therefore, to first order,

$$H_{\beta g} \sim h_o \, I(I+1) + \ldots$$

and

$$\alpha_I \sim - \frac{h_o \, I(I+1)}{E^{o}_{\beta} - E^{o}_{g}} \quad . \tag{7.7b}$$

Substituting into equations 7.6, one obtains

$$Q_{\beta g}(I'I) \sim Q^{o}_{\beta g} \{1 + [I(I+1) - I'(I'+1)] [\frac{h_o}{E^{o}_{\beta} - E^{o}_{g}}] \frac{Q^{o}_{\beta\beta}}{Q^{o}_{gg}}\} \tag{7.8}$$

where the last two terms in eqn. 7.6 have been dropped since $Q^{o}_{\beta\beta} \sim Q^{o}_{gg}$ and $\alpha_I \alpha_{I'}$ is a second order term.

It is obvious that when I' = I, $Q_{\beta g}(I'I')$ reduces to the unperturbed matrix element $Q^{o}_{\beta g}$. Moreover, $Q_{\beta g}(I'I)/Q_{\beta g}(I'I')$ is approximately a linear function of [I(I+1)-I'(I'+1)] in this

first order perturbation treatment. Ejiri and Hagemann (1971) have shown that this expression describes the beta and ground state band mixing (up to spin 6) in ^{174}Hf. It is of interest to see if this simple treatment is applicable to ^{176}Hf.

The ratio $Q_{\beta g}(I'I)/Q_{\beta g}(I'I')$ may be related to the observed gamma ray transition intensities I_γ and $I_{\gamma'}$ through the expression

$$\frac{Q_{\beta g}(I'I)}{Q_{\beta g}(I'I')} = \left[\frac{I_\gamma(I'I)/E_\gamma^5}{I_{\gamma'}(I'I')/E_{\gamma'}^5}\right]^{1/2} \frac{\langle I'200|I'0\rangle}{\langle I'200|I0\rangle} \left[1 + \frac{1}{\delta^2}\right]^{1/2} \qquad (7.9)$$

where $$\delta^2 = I_{\gamma'}(E2)/I_{\gamma'}(M1) \ .$$

The last factor in eqn. 7.9 thus corrects for the presence of an M1 component in the $I' \rightarrow I'$ (i.e. the $\Delta I=0$) transition.

Table 7.3 presents the energies and intensities of the interband transitions from which the ratios $Q_{\beta g}(I'I)/Q_{\beta g}(I'I')$ of column 4 were obtained. The table also shows the values of $(1/\delta^2)$ which were deduced in a manner to be described in section (iii) below.

$Q_{\beta g}(I'I')/Q_{\beta g}(I'I')$ has been plotted versus $I(I+1) - I'(I'+1)$ in Fig. 7.3. The data points have been derived using both the present data and that of Bernthal et al (1971). Although the error bars are rather large, the points do fit quite well to a straight line of slope 0.012. Thus

$$-\frac{h_o}{E_\beta^o - E_g^o} \cdot \frac{Q_{\beta\beta}^o}{Q_{\beta g}^o} = 0.012 \pm 0.005. \qquad (7.10)$$

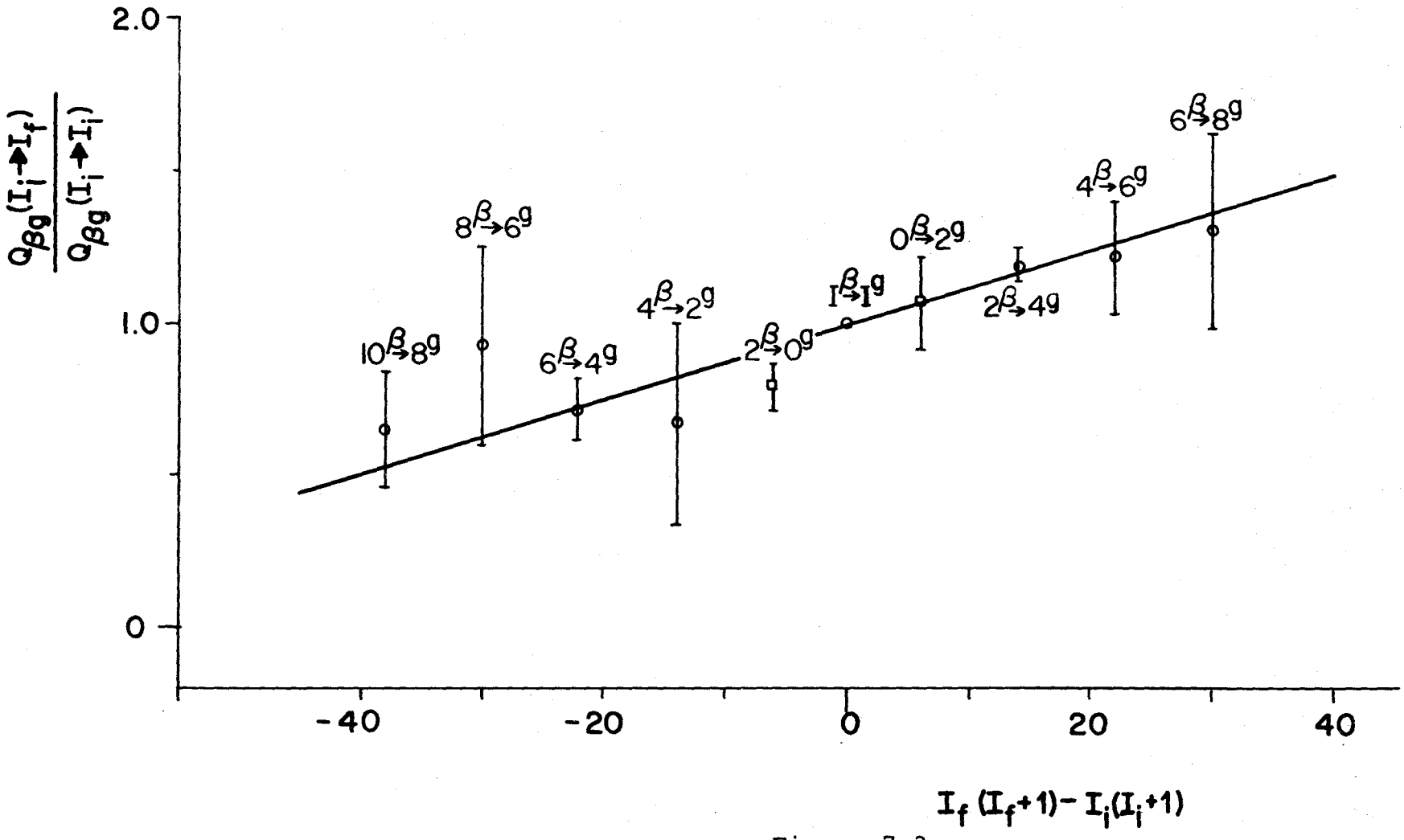

Figure 7.3

The ratio of the interband E2 transition matrix elements $Q_{\beta g}\ (I_i I_f)/Q_{\beta g}\ (I_i I_i)$ plotted as function of $[I_f\ (I_f+1) - I_i(I_i+1)]$

The ratio $Q^o_{\beta\beta}/Q^o_{\beta g}$ can be found by comparing the intensity of the I' → I'-2 intraband transition to that of the I'→I' interband transition. In the present work, the only intraband transition observed with certainty is that corresponding to I' = 10. A comparison of the intensities of the 362 and 814 keV transitions in Table 7.3 leads to

$$\frac{Q^o_{\beta\beta}}{Q^o_{\beta g}} = 8.6 \pm 1.3 \qquad (7.11)$$

and hence, using eqn. 7.10, to

$$h_o = -1.6 \pm 0.7 \text{ keV}. \qquad (7.12)$$

The mixing between the g.s. and beta bands causes a shift, ΔE, of the rotational energy of the I^{th} state from its unperturbed value $E_o(I) = AI(I+1)$. This shift is given by

$$\begin{aligned} \Delta E &= -H^2_{\beta g}/(E^o_\beta - E^o_g) \\ &= -h_o^2\, I^2(I+1)^2/(E^o_\beta - E^o_g) \\ &\sim 2\, I^2(I+1)^2 \text{ eV}. \end{aligned} \qquad (7.13)$$

This may be compared with the coefficient B of eqn. 7.2 which has been experimentally determined to be -11.1 eV. The interaction between the β and g.s. bands is thus only about 20% of that required to give the observed compression of the members of the g.s.b. The remainder of the compression may conceivably arise from the interaction between the ground state band and

Table 7.3

Transitions from the β-band and relative E2 matrix elements

$I' \rightarrow I$	E_γ (keV)	I_γ	$\frac{Q_{\beta g}(I'I)}{Q_{\beta g}(I'I')}$ [b]	$\frac{1}{\delta^2}$ [c]
$0^\beta \rightarrow 2^g$	1062		1.06(15) [e,g]	
$2^\beta \rightarrow 2^g$	1138	1.1(5)	1.00	0.17
$2^\beta \rightarrow 0^g$	1227	<1.4(4) [d]	<1.1	
			0.79(7)	
$2^\beta \rightarrow 4^g$	936		1.19(5)	
$4^\beta \rightarrow 4^g$	1100	1.6(5)	1.00	0.41
$4^\beta \rightarrow 2^g$	1302	1.3(5)	0.67(33)	
$4^\beta \rightarrow 6^g$	794	0.57(12)	1.21(19)	
$6^\beta \rightarrow 6^g$	1032	1.4(2)	1.00	0.79
$6^\beta \rightarrow 4^g$	1339	1.8(4)	0.71(10)	-
$6^\beta \rightarrow 8^g$	631	0.20(10) [d]	1.30(32)	-
$8^\beta \rightarrow 8^g$	935	0.40(20)	1.00	1.4
$8^\beta \rightarrow 6^g$	1336	1.1(2)	0.93(32)	-
$8^\beta \rightarrow 10^g$	(452)	0.08(4)	3.24(1.1)	-
$10^\beta \rightarrow 10^g$	814	0.30(8)	1.00	2.7
$10^\beta \rightarrow 8^g$	1297	0.50(25)	0.65(19)	-
$10^\beta \rightarrow 12^g$	not obs.			
$10^\beta \rightarrow 8^\beta$	362	0.14(2)	8.6(1.3) [f]	-

(continued next page)

Table 7.3 (continued)

(b) $\Delta I=0$ transitions corrected for M1 contributions, using estimated values of $\frac{1}{\delta^2}$.

(c) $\frac{1}{\delta^2} = \frac{I_\gamma(M1)}{I_\gamma(E2)}$ determined by assuming X constant for all spins.

(d) Complex peak.

(e) Values obtained from decay study (Bernthal et al 1971).

(f) Intraband to interband matrix element $\frac{Q_{\beta\beta}(I'I)}{Q_{\beta g}(I'I')}$.

(g) Determined from measured EO to E2 ratio:

$$\frac{X(2\to2)}{X(0\to2)} = \frac{B(EO\ 2\to2)}{B(E2\ 2\to2)} \Big/ \frac{B(EO\ 0\to0)}{B(E2\ 0\to2)}$$

$$= \frac{B(E2\ 0\to2)}{B(E2\ 2\to2)} \text{ , assuming } B(EO\ 2\to2) = B(EO\ 0\to0)$$

$$= \left[\frac{Q_{\beta g}(0\to2)}{Q_{\beta g}(2\to2)}\right]^2$$

excited bands such as the K=0+ and K=2+ (γ vibration ?) states at 1293 and 1341 keV respectively.

From the preceding analyses, it is clear that the observed E2 branching ratios of transitions from the β to the g.s.b. cannot be explained by assuming a constant interband matrix element $Q_{\beta g}$ (which corresponds to assuming Alaga's rules). For a proper explanation it is necessary to take into account the mixing (to first order) between the two bands, which leads to $Q_{\beta g}$ having a simple spin dependence. The interaction matrix element may be given by

$$H_{\beta g} \sim 1.6\ I(I+1)\ \text{keV}.$$

(iii) The relative EO and E2 interband transition rates

The nature of K=0+ excited states may be indicated by the relative strengths of the monopole and quadrupole transitions to the g.s.b. through the quantity X defined in eqn. 3.49. X is more easily obtained from eqn. 3.51, which relates it to the experimental data. Since the $\Delta I=0$ E2 interband transitions are not perturbed by band mixing (i.e. $Q_{\beta g}(I'I')=Q^{o}_{\beta g}$ in expression 7.8), only these transitions have been used for the determination of X. However, no $0'\rightarrow 0$ E2 transitions can occur, so that in this case it was necessary to also employ the $0'\rightarrow 2$ transitions. In this case there is a spin change and

$$Q_{\beta g}(o'2) = Q^{o}_{\beta g}\ \{1+6[\frac{-h_o}{E^{o}_{\beta}-E^{o}_{g}}]\ \frac{Q^{o}_{\beta\beta}}{Q^{o}_{\beta g}}\}.$$

$$= 1.07\ Q^{o}_{\beta g}\ .$$

For this case, the value of X given by eqn. 3.51 must be increased by $(1.07)^2$.

Table 7.4 and Fig. 7.4 present the results obtained from the present data and compares it with Bernthal's results. In deriving the values of X in the table, $\Delta I=0$ gamma-ray transitions have been assumed to be pure E2. The effect of M1 admixtures in these transitions is to reduce X below the true values. Such M1 admixtures have been observed in similar transitions in ^{174}Hf (Ejiri and Hagemann, 1971) and ^{178}Hf (Nielsen et al, 1968). In ^{174}Hf, the M1 admixtures were observed to increase with spin.

In the rotational model, X is expected to be independent of spin, and has been found to be so in ^{174}Hf. The apparent decrease in X with increasing spin in Fig. 7.4 may thus be attributed to the effect of not correcting for the M1 component. If one assumes that X is in fact constant and that it has the value given by the $0'\rightarrow 0$ transitions, Fig. 7.4 may be used to calculate the relative intensity of the M1 component, i.e. $\frac{1}{\delta^2}$. The derived values of $\frac{1}{\delta^2}$ are given in the last column of Table 7.4.

For a spheroidal charge undergoing quadrupole oscillations about a permanent deformation, Rasmussen (1960) showed that $X = 4\beta^2$. In the same article, using a microscopic model he showed that $X = 9\beta^2$. Since for $^{174, 176, 178}$Hf $\beta^2 \sim 0.3$ (Stelson and Grodzins 1965) X is expected to lie between 0.36 and 0.81, a factor of at least two larger than the experimental value of 0.19 for the 1150 keV band in ^{176}Hf.

Table 7.4

Relative reduced EO and E2 rates for the β-band

Transition $I'^{\beta}\rightarrow I^{g}$	E_c (keV)	$I_e(EO)^{a)}$ $\times 10^{-3}$	I_γ (tot)	$\Omega^{b)}$ $\times 10^{-11}$	This Work	Bernthal et al	$\frac{1}{\delta^2}$
0'→0	1150	4(2)	0.41(1)[e]	1.90	0.21(8)[f]	0.19(4)[f]	-
2'→2	1138	12	1.1 (5)	1.88	0.08(5)	0.19(4)	0.17
4'→4	1100	29(5)	1.6 (4)	1.82	0.10(4)		0.41
6'→6	1032	32(4)	1.4 (2)	1.70	0.10(2)		0.79
8'→8	935	19(5)	0.40(20)	1.55	0.14(8)		1.4
10'→10	814	8.8(2.0)	0.30(10)	1.38	0.05(4)		2.7

a) $I_e(EO) = I_e(\text{expt.}) - [\alpha_K(E2) + \frac{1}{\delta^2}\alpha_K(M1)]I_\gamma$.
In obtaining $I_e(EO)$, it has been assumed that $\frac{1}{\delta^2} = 0$, i.e. the M1 component has been neglected. The error caused by this assumption is negligible since the EO contribution in I_e(expt) is the predominant component.

b) From Church and Weneser (1956).

c) $X = 2.53\times10^{12}\, E_\gamma^{5}\Omega_K^{-1}\, [I_e(EO)/I_\gamma(E2+M1)]\langle I'200|I0\rangle^2$
The use of $I_\gamma(E2+M1)$ instead of $I_\gamma(E2)$ leads to an underestimation of X.

d) $\frac{1}{\delta^2}$ determined by assuming X independent of spin and given by X(0'→0).

e) $0'0^+\rightarrow 2_0^+$ transition used (E_γ = 1062 keV)

f) Corrected for band-mixing effects (see text).

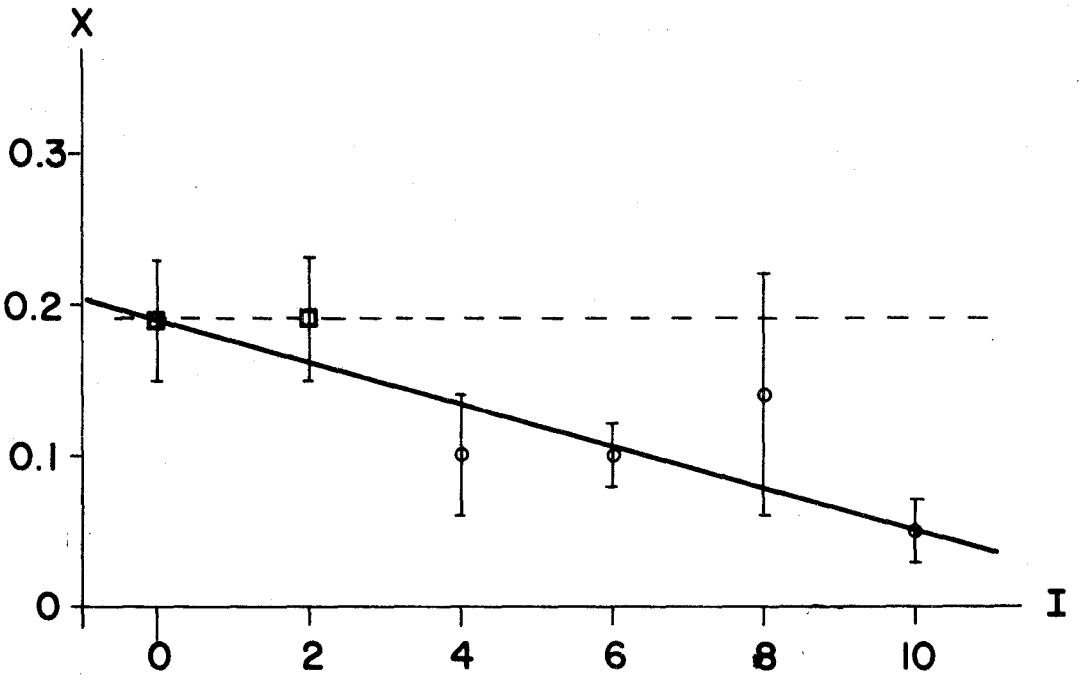

FIGURE 7.4

X = B(EO)/B(E2), determined from transitions between the K=0+' band at 1150 keV and the g.s.b. I is the spin of the initial state. X is expected to be independent of spin; the apparent gradual decrease is due to the presence of M1 components in the $\Delta I=0$ gamma transition (see text).

Figure 7.5

$K = 0^+$ states in $^{174,176,178}Hf$

References a) Ejiri and Hagemann (1971)

b) This work

c) Bernthal et al (1971)

d) Nielsen et al (1967)

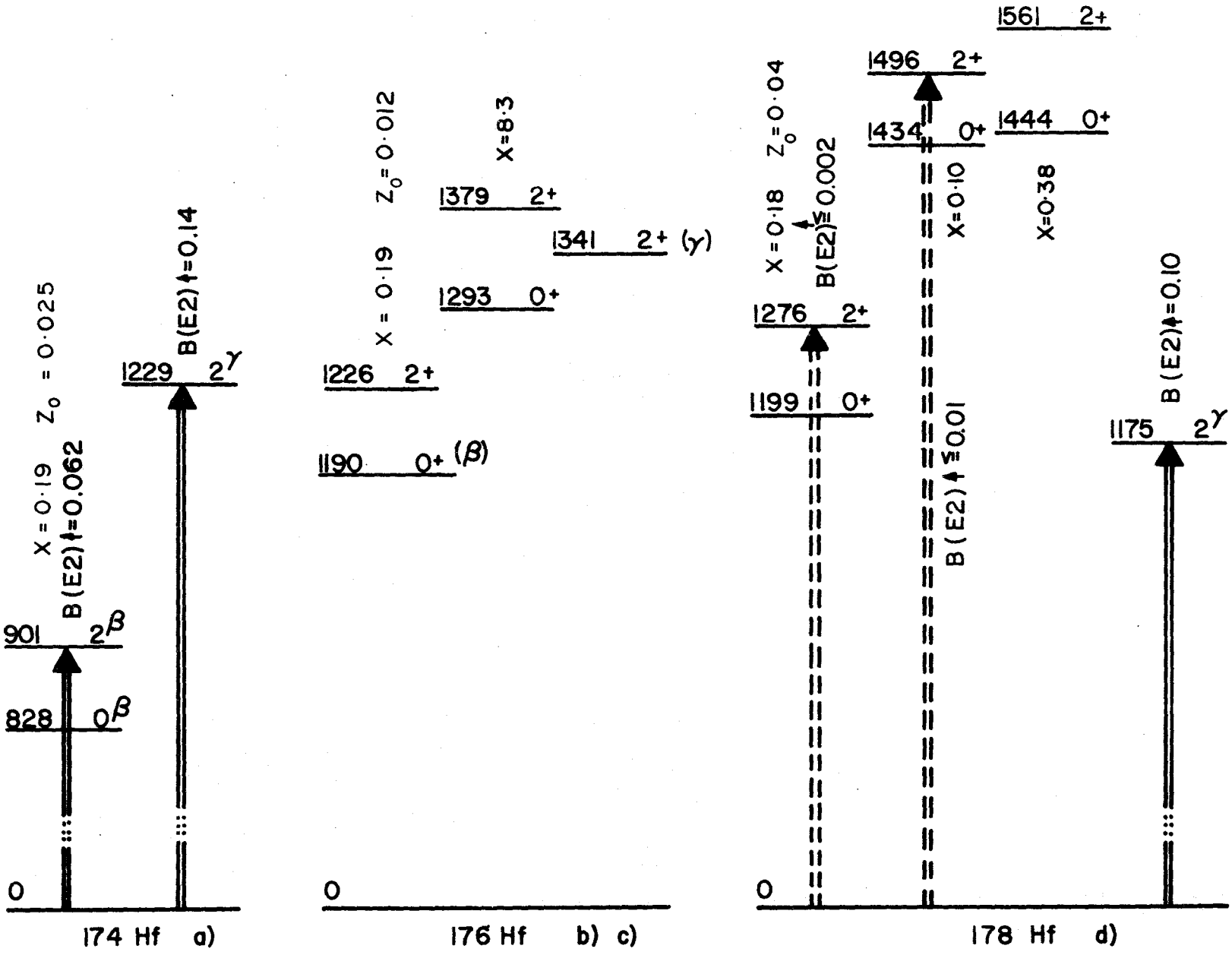

Figure 7.5

$K = 0^+$ states in $^{174, 176, 178}_{Hf}$

A comparison of the X and B(E2) values for a number of K=0 states in ^{174}Hf, ^{176}Hf and ^{178}Hf is presented in Fig. 7.5. It is seen that the values of X are almost identical for all the K=0+ bands, with the exception of the 1293 keV state in ^{176}Hf. X values have been traditionally used as a criterion for identifying beta bands.

The B(E2) value for the 901 keV state in ^{174}Hf is strongly enhanced ($\sim$ 2.9 spu) suggesting that this is a beta vibration. On the other hand, none of the O+ states in ^{178}Hf appear to have the enhanced B(E2) required of a beta vibration. It thus appears that the value of X does not provide a good criterion for identifying beta bands. It would thus be enlightening to measure the B(E2) values for the states in ^{176}Hf.

7.4 The $K=0^+$ band at 1293 keV

(i) Identification

In radioactive decay studies, Bernthal et al (1969, 1971) identified an $IK^{\pi} = 00^+$ state at 1293 keV by means of the strong EO transition to the ground state of ^{176}Hf. They also proposed that the 1379.2 keV state, which deexcites to the 2+ member of the ground state by a 1291 keV transition with a strong EO component, was the 2+ member of this K=0 band. These states are populated in the present work which supports their conclusions both from electron and γ-γ coincidence measurements. The resolution in the present electron measurements was insufficient to separate the 1291K and 1293K-conver-

sion lines. On the basis of the rotational spacing, the state at 1591.9 keV may be tentatively regarded as the 4+ member of this K=0 band. The transition from this state to the 4+ member of the ground state band has an energy of 1301.8 keV. Since the K-conversion line of this transition is only partially resolved from the strong 1293K line, and the gamma ray is itself an unresolved doublet, no meaningful statements can be made concerning the multipolarity of this transition. If it were a 4→4 interband transition, one would expect to find a significant EO component in the conversion line. None of the other high-lying rotational members have been identified. Their absence is somewhat of an enigma, particularly since the K=0 band at 1150 keV is populated up to the I=10 member.

In an inconclusive attempt to isolate the intraband transitions feeding the 1293 keV state, an e-γ coincidence experiment was carried out to obtain the gamma ray spectrum associated with the EO transition from the 1293 keV state. In the resulting spectrum, which was marred by rather poor statistics, only the 88, 202 and 307 keV members of the g.s.band were observed. This could imply that the rotational spacings in the 1293 keV band are identical (within $\sim$ 1 keV) with those of the g.s.b. A more attractive interpretation lies in the realization that the gate set on the 1293 K-conversion line by the magnetic spectrometer was about 12 keV wide and therefore contained a number of other conversion lines

associated with transitions which feed the 2+, 4+ and 6+ states of the ground state band.

(ii) Discussion

As has already been pointed out in Fig. 7.5, the value of X for the 1293 keV state is a factor of $\sim$ 50 times larger than X for the other 0^+ band in ^{176}Hf. Bernthal et al have pointed out that this state may be the ^{176}Hf analogue of a 0^+ non-collective state calculated by Soloviev in ^{178}Hf. This state is formed of a roughly 50-50 mixture of the "two-quasi-proton" excitations in each of the 7/2+[404] and 9/2-[514] orbitals, and Bernthal's calculations suggest that it should have a large EO/E2 ratio for transitions to the ground state band, in contrast to the much smaller ratios expected for the other O+ states. If this description is valid, the enhanced X ratio is probably due to a retardation of the E2 rate below that expected for a collective beta vibration rather than to an enhanced EO rate. A lifetime measurement of the 1293 keV state would provide a critical test of this interpretation.

Recently, in collaboration with R. O'Neil , the proton transfer reaction, ^{175}Lu(α,t)^{176}Hf, has been studied to gain further insight into the ^{176}Hf structure. These experiments show that the 1293 and 1379 keV states together receive $\sim$ 27% of the total $K=0^+$ population with $\sim$ 61% going to the $K=0^+$ ground state band and $\sim$ 12% to the 1150 keV beta

band. This distribution in strengths is roughly compatible with the above interpretation. Since the ground state of ^{175}Lu is the 7/2+[404] orbital, the only way that one can populate a K=0 band in the α,t reaction is by transferring a second 7/2+[404] proton. The fact that all three of these K=0 bands are excited in this reaction means that each of them contains a component of a pair of 7/2+[404] protons.

7.5 The 1341.0 keV (gamma) band

The bandhead at 1341.0 and the state at 1445.7 keV were identified by Bernthal et al (1971) and assigned IK^{π} values of 22^{+} and 32^{+} respectively. The parity assignment for the upper level was very tentative. Both these states have been observed in the present work (see Fig. 7.1) and the measured conversion coefficient of the 1357.9 keV transition indicates that the 1445.7 keV state has positive parity. It thus seems probable that these two states form the first two members of a K=2+ band. Since no two quasi-particle K=2+ configurations are expected at this low energy, it is probable that this is the γ-vibrational state.

If the 1445.7 keV state is the 3+ member of the γ band the energy separation implies a rotational parameter of 17.4 keV, which is much larger than that of the g.s. band. Such a large rotational parameter implies considerable perturbation of the band, probably by the nearby K=0 band at 1293 keV.

Such a perturbation would cause a relative displacement of the odd and even spin members of the band since the K=0 band can perturb only the even spin members of the K=2 band. By taking such an odd-even shift into account, it has been possible to identify a sequence of levels at 1341.0, 1445.7, 1540.2, 1727.7, 1861.9, 2096.7 (or 2106.8) and 2285.0 keV with an appropriate level spacing. No intraband transitions have been observed within this sequence but each level de-excites to two members of the ground state band. The observed transitions correspond to $\Delta I = 2$ and $\Delta I = 0$ for the even spin members of the sequence and to $\Delta I = -1$ and $\Delta I = +1$ for the odd members, if one assigns spins 2,3,4,5,6,7,8 and positive parity to the sequence listed above. In addition, the conversion electron data for the 1499.8 and 1571.6 keV transitions from the 2096.7 and 1861.9 keV levels respectively indicate that they are M1 and/or E2 in character. This accords with their assignment as 7→6 and 6→4 transitions in terms of the sequence above.

7.6 The $K=2^-$ octupole band at 1247.5 keV

(i) Identification of the band members

Bernthal et al (1971) proposed that the state at 1247.5 keV is the band head of the $K=2^-$ octupole band. Their evidence for this assignment was based on the presence of transitions to the 0, 2 and 4 members of the g.s.b. with

multipolarities of M2, E1+M2, and M2+E3 respectively. They also identified a 3-state at 1313.2 keV and suggested that this was the 3- member of this band. Broda et al (1970) and Löbner et al (1971) have independently determined the half-life of the 1247.5 keV state to be 4.46±0.10 ns, a value which implies that the predominantly E1 transition to the 2+ member of the ground state must be K forbidden. This plus the fact that no 1^- state of appropriate energy has been observed provide strong evidence for this K=2- assignment.

The 1247.5 keV state is strongly populated in the $(\alpha,2n)$ reaction and the present work confirms the E1+M2 character of the $2^- \rightarrow 2^+$ transition of energy 1159.2 keV. The higher background characteristic of these experiments made it not possible to detect the $2^- \rightarrow 0^+$ and $2^- \rightarrow 4^+$ transitions seen by Bernthal. However, the rotational members of the $K=2^-$ band have been identified up to spin 9, as presented in Table 7.5 which presents the energies, intensities and multipolarities of the transitions deexciting these states, together with the proposed spin assignments.

The energies of the initial states in Table 7.5 are approximately those expected from the rotational model, with a small even-odd shift characteristic of interband coupling. The plot of $\frac{E_I - E_{I-1}}{2I}$ versus I^2, which is presented in Fig. 7.6, shows this effect clearly since in the absence of such an

Table 7.5

Transitions involving the $K=2^-$ octupole band

Initial State	Final State	Transitions			Proposed Spin Assignment
		Energy	Intensity	Multipolarity	
1247.5	0 0+	1247.7	0.20 [a]	M2 [a]	2-
	2 0+	1159.3	10.6	E1+M2 [a]	
	4 0+	957.4	0.24 [a]	E3 [a]	
1313.2	2 0+	1224.9	7.3	E1	3-
	4 0+	1023.1	3.2	E1	
1404.3	4 0+	1114.2	2.2	E1	4-
	2 2-	156.8	2.7	E2 [a]	
	3 2-	91.1	0.4		
1508.6	4 0+	1218.4	5.0	[b]	5-
	6 0+	911.8	1.8	E1	
	3 2-	196	0.25		
1652.9	6 0+	1055.8	0.3		6-
	4 2-	248.6	4.2	E2 [c]	
	5 2-	144.5	0.19		
1785.0	6 0+	1188.1	4.0	E1	7-
	8 0+	787.1	1.0	(E1)	
	5 2-	276.4 [d]	0.14		
1992.5	6 2-	339.6	2.6		(8-)
2137.3	8 0+	1139.4	1.1		(9-)
	10 0+	655.3	0.27		
	7 2-	352.4 [d]	0.2		

a) Bernthal et al, 1971

b) conversion line part of unresolved multiplet

c) evidence not included in thesis

d) assignment on energy fitalone

Figure 7.6

Illustration of the odd-even energy shift in the $K=2^-$ octupole band. If the level energy were given by the usual rotational formula $E_I=E_o + AI(I+1)+BI^2(I+1)^2$, then

$$(E_I - E_{I-1})/2I = A + 2BI^2,$$

in which case one straight line should have been obtained.

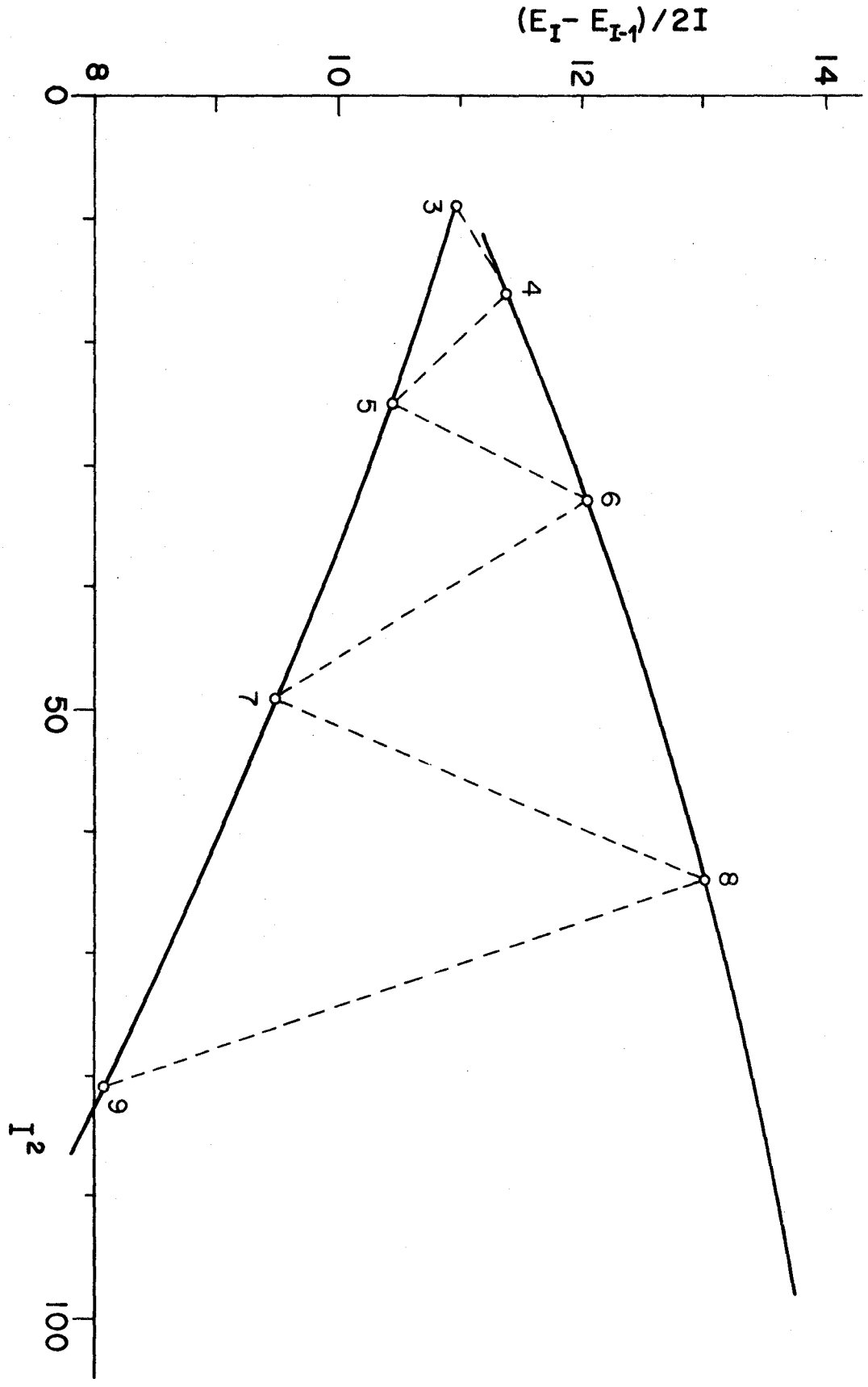
$(E_I - E_{I-1})/2I$
8
10
12
14
0
50
100
I^2
3
4
5
6
7
8
9

effect all the points should have fallen on one rather than on two smooth curves.

The deexcitation pattern for the states within this band is quite abnormal. The even members of the band deexcite strongly within the band with relatively weak $\Delta I=0$ transitions to the g.s.b. whereas the odd members of the band deexcite weakly within the band but proceed via relatively strong E1 transitions to the $I\pm1$ members of the g.s.b.

The identification of the 1992.5 and 2137.3 keV level with this band is somewhat less secure than the others. In fact, an alternative candidate for the 8- state is a level at 1964.0 keV which also decays to the 62- state via a 311.1 keV transition. The 1992 keV state has been chosen because it fits the rotational energy sequence better.

In this and succeeding sections, it will become clear that this band has a mixed character. It is thus not strictly correct to call it a K=2- band. Nevertheless, because its dominant component is $K=2^-$, it will be convenient to continue to label it in this fashion.

(ii) Deduced properties of the 22^- state at 1248 keV

The lifetime and deexcitation pattern of the 22^- state may be used to deduce the reduced transition probabilities for transitions to the ground state band shown in Table 7.6. The transition to the ground state must be pure

TABLE 7.6

B(λ) for transitions from the 1247 keV state

Transition	E_γ (MeV)	I_γ [a]	λ	I_λ	Composition	Partial [b] $T(\sigma\lambda)$ (10^6 sec^{-1})	$B(\sigma\lambda)$ [c]	Retardation Factor [d]	$\frac{B(\sigma\lambda)}{\langle 2\lambda 2-2 \mid I'O\rangle^2}$ [c]
$22^- \rightarrow 00^+$	1.248	8.5	M2	8.5	100%	2.77	6.7×10^{-2}	1.1×10^{3}	0.34
$22^- \rightarrow 40^+$	0.957	10.6	M2	0.16	1.3%	0.051	0.48×10^{-2}	2.2×10^{5}	0.34
			E3	10.5	98.7%	3.42	0.81×10^{4}	0.73	5.7×10^{4}
$22^- \rightarrow 20^+$	1.159	458	E1	343	76%	113	4.55×10^{-8}	6.5×10^{7}	9.1×10^{-8}
			M2	8.4	2 %	2.74	9.7×10^{-2}	2.9×10^{3}	0.34
			E3	100	22%	32.6	2.0×10^{4}	0.29	5.7×10^{4}

a) Intensities from Bernthal et al (1971)

b) Total decay rate 1.55×10^{8} sec^{-1}

c) $B(\sigma\lambda)$ measured in units of e^2fm^2 for E1; $\mu_N^2 fm^2$ for M2 and e^2 fm^6 for E3

d) Retardation factors calculated from the following single particle rates

$$T_{E1} = 1.5\times10^{14}\ A^{2/3}\ E_\gamma^3$$

$$T_{M2} = 1.2\times10^{8}\ A^{2/3}\ E_\gamma^5$$

$$T_{E3} = 1.1\times10^{2}\ A^{2}\ E_\gamma^7$$

M2, while those to the 4 0+ and 4 2+ states are expected to be M2+E3 and E1+M2+E3 respectively. The strengths of the M2 components in these two transitions may be deduced (following Löbner et al, 1971) by means of Alaga's rules (eqn. 3.33) using the pure M2 character of the 2 2- → 0 0+ transition. Table 7.6 shows that these components are small, and hence that the 2 2- →4 0+ transition is almost pure E3. The process may be repeated, using this E3 component to deduce the E3 component in the 2 2- → 2 0+ transition and hence, by subtraction, to arrive at the E1 component in the latter. Table 7.6 presents the partial decay rates, the reduced transition probabilities and retardation factors for each mode of decay from the 1248 keV state. The entry in the last column would be the square of the transition matrix element if the state were pure.

It should be noted that the strong retardation of the K-forbidden E1 transition indicates that the 2 2- state is almost pure K=2. Alaga's rules should therefore be valid for the K-allowed M2 and E3 transitions. The enhanced E3 strength is a strong indicator of the collective octupole character of this state. With the multipole composition of the 1159 keV transition given in Table 7.6, the K-conversion coefficient is predicted to be $(2.2\pm0.3)\times10^{-3}$ in good agreement with the experimental values of $(1.9\pm0.5)\times10^{-3}$ and $(2.9\pm0.5)\times10^{-3}$ obtained in this work and Bernthal's respectively. A similar example of E1+M2+E3 mixing from a

2-state occurs in ^{182}W (Krane et al, 1971).

(iii) Reduced B(El) transition rates for the K=2- band

The reduced transition rates from the rotational members of the octupole band may be deduced by comparing their intensities with those of the E2 intraband transitions. To do this, it is necessary to assume that the quadrupole moment remains constant throughout the band and has the same value as that of the 2 0+ member of the g.s.b. i.e.,

$$Q_o(2^-) = Q_o(g) = 7.45 \text{ barns} \qquad (7.15)$$

(Stelson and Grodzins, 1965).

Using equations 3.31 and 3.41, the E2 rate may be expressed as

$$T[E2, I2^- \rightarrow (I-2), 2^-] = 6.72 \times 10^{13} E_\gamma^5 \langle I220 | I-2,2 \rangle^2. \qquad (7.16)$$

While, strictly speaking, this expression is correct only for a pure K=2 band, it can be shown that admixture of other K components with reasonable amplitudes has a negligible effect on the result.

The conversion coefficients indicate that the transitions from the K=2- to the g.s.b. are predominantly El. (The E3/El intensity ratio which is about 20% in the 2 2- → 2 0+ transition is estimated to drop to $\sim$ 1% for the 4 4- → 4 0+ transition and to be completely negligible for all the other interband transitions.)

By using equation (7.16), it can be shown that

$$B(E1,\rightarrow I2^{-}\rightarrow I'O) = \frac{I_\gamma(E1\ I2^{-}\rightarrow I'O^{+})/E_\gamma^3}{I'_\gamma(E2,I2^{-}\rightarrow I-2,2^{-})/E'^{5}_\gamma} \times 4.23\times10^{-2}\times\langle I220|I-2,2\rangle^2 \qquad (7.17)$$

Table 7.7 presents the reduced E1 transition rates for the $K=2^-$ band obtained by applying eqn. (7.17). The table also includes three columns of B(E1) values derived from the calculations of section (v) below. The striking feature of this table is the fact that the reduced E1 strengths oscillate violently as one proceeds up the K=2- band,with the B(E1) values for even spin initial states being two orders of magnitude smaller than for the odd spin initial states.

(iv) Experimental intrinsic g_K-factor for the K=2- band

The quantity $[(g_K-g_R)/Q_o]^2$ for a band can be evaluated by comparing the cross-over to cascade branching ratios, using eqns.3.44 to 3.46. Table 7.8 presents the results of these calculations applied to the 4- and 6- states for which sufficient data are available. The data in the table are consistent with g_K-g_R being a constant. Its value $\pm$ 0.060 indicates that g_K is very nearly the same as g_R for the ground state. Since the latter has been determined to be 0.27 (Ben Zvi et al, 1968), one can say that g_K = 0.27+0.06 or 0.27-0.06. (The sign of g_K-g_R cannot be given since the sign of δ is unknown.)

Table 7.7

Reduced E1 rates from the K=2- octupole band

Transition	E_γ (keV)	I_γ	B(E1)[a] Experimental From Eq.7.15	B(E1)[a] Calculated $\Delta K=0,1$[d]	B(E1)[a] Calculated $\Delta K=1$[e]	B(E1)[a] Calculated Bohr Mottelson[f]	F_W[g] (g)
$22^- \to 20^+$	1159	10.6	0.455[b]	0.455	0.455	0.455	6.5×10^7
$32^- \to 20^+$	1225	7.3	>37 [c]	46	0.72	0.65	$<5\times10^5$
$\to 40^+$	1023	3.2	>28 [c]	38	0.54	0.49	$<7\times10^5$
$42^- \to 40^+$	1114	2.3	2.9	1.6	1.6	2.0	1.5×10^7
$52^- \to 40^+$	1218	5.0	$\sim$ 320	230	1.8	1.7	$\sim1.3\times10^5$
$\to 60^+$	912	1.8	$\sim$ 280	200	1.5	1.45	$\sim1.6\times10^5$
$62^- \to 60^+$	1056	0.34	6.5	2.6	2.6	4.6	6.6×10^6
$72^- \to 60^+$	1188	4.0	$\sim$3100	510	2.6	3.3	$\sim 1.4\times10^4$
$\to 80^+$	787	0.9	$\sim$2600	440	2.3	2.9	$\sim 1.6\times10^4$
$82^- \to 80^+$	(995)	-	< 210	3.2	3.2	11.4	-
$92^- \to 80^+$	1139	1.1	$\sim$2500	760	3.2	7.6	1.2×10^4
$\to 100^+$	655	<0.89	$\sim$3000	650	2.9	6.8	1.0×10^4

a) In units of 10^{-7} e^2 fm^2

b) From Table 7.6

c) Since the E2 intensity of the $32^- \to 22^-$ transition is unknown, these B(E1)'s were obtained by comparing their intensities with the E3 intensity expected for the $32^- \to 00^+$ transition. An upper limit of 0.02 on our gamma ray scale was found in this way using Bernthal's data

d) Calculated by mixing K=0 and K=1 components, using eqn. 7.20.

e) Calculated by mixing only K=1 component.

f) From eqn. 3.35 with $\delta=0$

g) See note d of Table 7.6.

Table 7.8

Intraband transitions in the $K=2^-$ octupole band

$I_i \rightarrow I_f$	E_γ (keV)	I_γ	$1/\delta^2$	$[(g_K-g_R)/Q_o]^2$ (a)
4→2	156.8	2.7	0	6.0±1.3
4→3	91.1	(0.4)	0.12	
5→3	(196)	∿0.2	0	
6→4	248.6	4.2	0	7.2±1.5
6→5	144.5	0.19	0.14	
7→5	276	∿0.14	0	
8→6	339.6	1.3	0	

a) In units of 10^{-5} if Q_o is given in barns

Mean $[|g_K-g_R|/Q_o] = 8.1\times10^{-3}$

$Q_o = 7.45$ barns

$g_K - g_R = \pm 0.060$

Since $g_R = 0.27$ (Ben Zvi et al, 1968)

$g_K = 0.33$ or 0.21 depending on sign of δ.

(v) Interpretation of the properties of the K=2- octupole band

In the preceding sections, four characteristics of the band built on the state at 1247.5 keV have been presented: These are in turn, the enhanced B(E3) strength of the transitions to the ground state, the odd-even energy shifts in the rotational level spacings, the oscillatory nature of the E1 strengths from odd and even members of this band to the ground state band, and the fact that $g_K \sim 0.27$. To account for these characteristics we shall call on Coriolis coupling between the different octupole bands.

In a deformed nucleus, one may expect to find negative parity octupole bands with K=0, 1, 2 and 3. These may be arranged schematically as shown in the sketch. Although the level spacings in this sketch have no significance for the general argument, we have chosen to place the band heads to

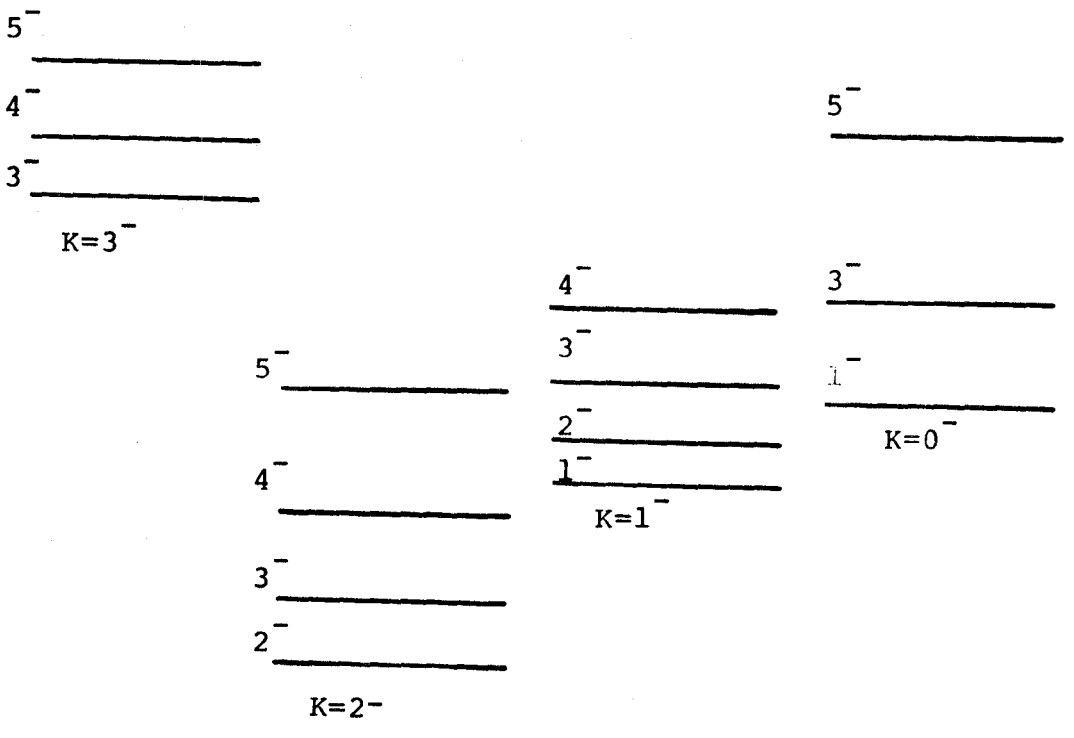

correspond roughly to the theoretical predictions for ^{176}Hf made by Neergård and Vogel (1970) whose theory will be used below. Since the Coriolis interaction will mix states of the same spin differing in K by unity, the K=2- band members will contain admixtures of the K=1 and K=3 bands in first order. While this Coriolis mixing will compress the K=2- levels it cannot create the peculiar spacing observed. However, the $K=0^-$ band, with its sequence of odd spin members will depress the odd spin members of the $K=2^-$ band through the intermediary of the $K=1^-$ band. By virtue of this indirect interaction, a small $K=0^-$ component is mixed into the wave function of the so-called $K=2^-$ band. This argument is independent of the order of the $K=0^-$ and $K=1^-$ states.

Neergård and Vogel (1970) have solved the quasiparticle random phase approximation equations to obtain all the octupole phonon states below 2.5 MeV for all the even-even rare earth nuclei from mass 152 to 190. By considering the Coriolis coupling between pairs of these states, they have derived a method of obtaining the perturbed energies and B(E3) values for these states. In their presentation, the non-diagonal Coriolis matrix elements required are expressed as

$$\langle I(K+1)^- | H_{cor} | IK^- \rangle = -\frac{\hbar^2}{2\mathcal{J}} \sqrt{1+\delta_{K0}} \sqrt{(I-K)(I+K+1)} \langle (K+1)^- | J_+ | K^- \rangle \tag{7.18}$$

in terms of the $\langle J_+ \rangle$ matrix elements and the rotational para-

meter of the g.s.b. For economy of space, their paper tabulates only the lowest $K^{\pi} = 0^-$, 1^-, 2^- and 3^- unperturbed states together with the values of $\langle J_+ \rangle$ for the Coriolis matrix elements between them. The results of the analysis using all the octupole phonon states are then presented in a series of diagrams which give the positions of the perturbed $K=0^-$, 1^-, 2^- and 3^- band members up to spin 5 for each of the nuclei considered.

In ^{176}Hf, the unperturbed $K=0^-$, 1^-, 2^-, 3^- band heads are predicted to fall at 1.67, 1.58, 1.20 and 1.84 MeV respectively. Fig. 7.7 presents the experimental data for this nucleus as obtained in our measurements and compares them with Neergård and Vogel's results. For purposes of comparison, the excitation energies presented in their paper have been normalized at the 2^- state. The agreement between their predictions and our measurements is amazing. Since they have not tabulated their complete set of unperturbed states, it is not possible for us to extend their calculations to make predictions for the higher spin members of the band found in this work.

Attempts were made to reproduce the observed structure of the band by coupling the four lowest RPA states using the matrix elements given in their paper. This calculation gave poor agreement not surprisingly, since not all the interacting states have been included. For rather collective octupole states, Bohr and Mottelson (quoted by Neergård and Vogel)

Figure 7.7

Comparison of the experimental and calculated energies of the $K=2^-$ octupole band. In the 4-band calculation[a], only the lowest RPA state of each K was included in the Coriolis coupling calculation (see text). The calculations of Neergård and Vogel[b] (1970) include all RPA states below 2.5 MeV; their results for the lowest $K=0^-$, 1^- and 3^- octupole states are also shown.

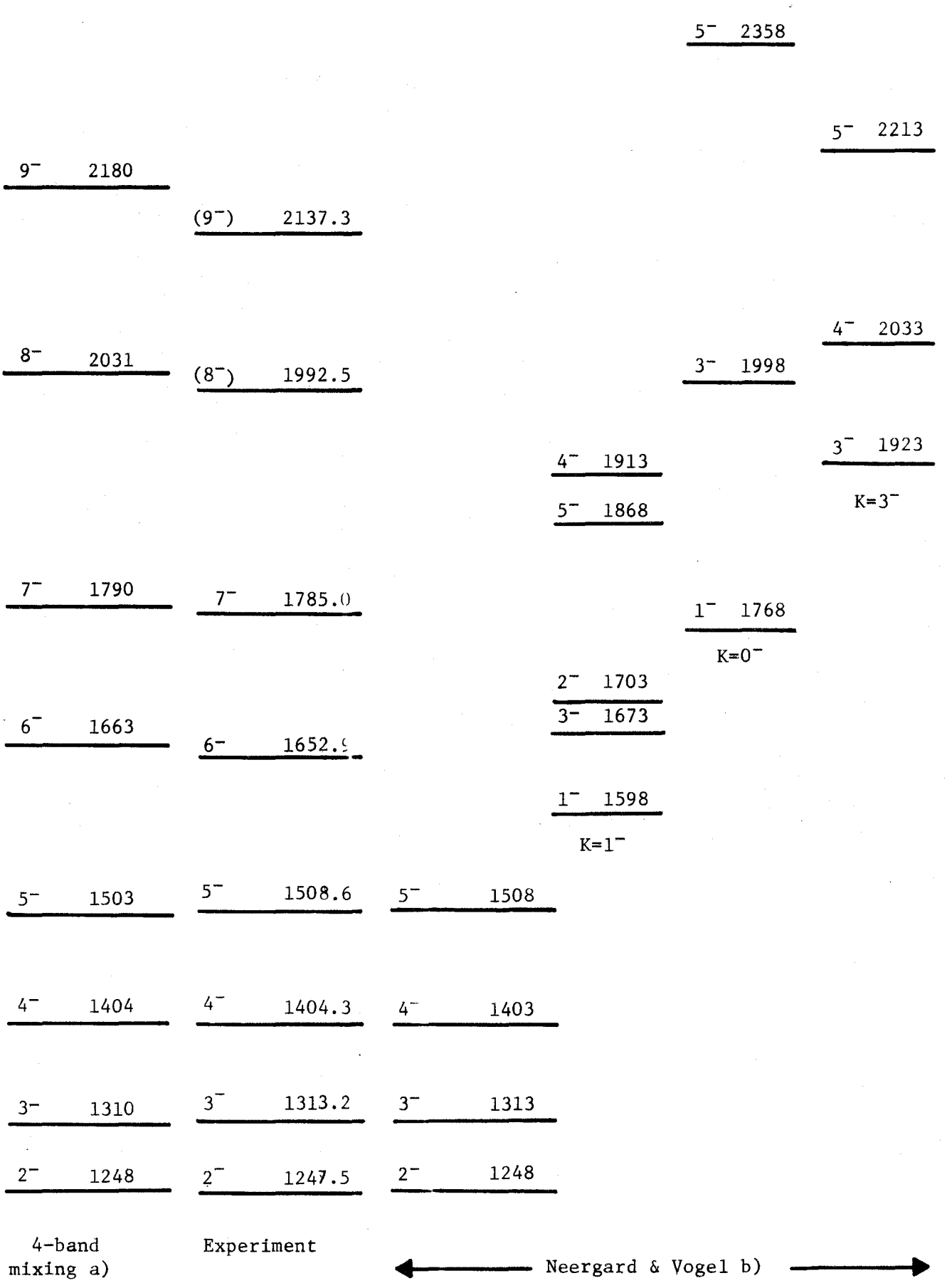
5⁻ 2358
5⁻ 2213
9⁻ 2180
(9⁻) 2137.3
4⁻ 2033
8⁻ 2031
(8⁻) 1992.5
3⁻ 1998
3⁻ 1923
4⁻ 1913
K=3⁻
5⁻ 1868
7⁻ 1790
7⁻ 1785.0
1⁻ 1768
K=0⁻
2⁻ 1703
3⁻ 1673
6⁻ 1663
6⁻ 1652.9
1⁻ 1598
K=1⁻
5⁻ 1503
5⁻ 1508.6
5⁻ 1508
4⁻ 1404
4⁻ 1404.3
4⁻ 1403
3⁻ 1310
3⁻ 1313.2
3⁻ 1313
2⁻ 1248
2⁻ 1247.5
2⁻ 1248
4-band mixing a)
Experiment
Neergard & Vogel b)

suggest that an appropriate value for $\langle J_+ \rangle$ can be obtained by using the expression for the spherical limit

$$\langle I(K+1)^- | J_+ | IK^- \rangle_{s.\ell.} = \sqrt{(3-K)(3+K+1)} \quad . \qquad (7.19)$$

While this expression was found to give quite reasonable results for ^{172}Yb (O'Neil and Burke, 1972), it overestimates $\langle J_+ \rangle$ for ^{176}Hf. Instead, it was found that matrix elements which were 75% of the spherical limit value gave a good fit to the data. The excitation energies predicted in this way were arbitrarily increased by 60 keV to normalize to the 2^- member of the band. The predictions up to spin 9 obtained in this manner are also included in Fig. 7.7. While the agreement is not as good as that from the complete calculation of Neergård and Vogel, it is still reasonable.

The amplitudes of the $K=0^-$, 1^-, 2^- and 3^- components of the wave functions of the states in this band, obtained by the diagonalization process referred to in the last paragraph, are presented in Table 7.9. It should be noted that, although the amplitude associated with the $K=2^-$ component is dominant, the components associated with $K=0^-$ and $K=1^-$ are appreciable, especially for the odd spin members of the band. The fact that the model used to get these approximate wave functions was able to predict the state energies provides some confidence that these wave functions may yield reasonable estimates of the E1 transition strengths.

Table 7.9

Amplitudes of the components of the wave function describing the $K=2^-$ band[a]

I	C_0^I	C_1^I	C_2^I	C_3^I
2	0	0.15	0.99	0
3	0.08	0.25	0.96	0.11
4	0	0.28	0.95	0.16
5	0.18	0.40	0.88	0.18
6	0	0.36	0.91	0.22
7	0.27	0.49	0.80	0.20
8	0	0 40	0.88	0.26
9	0.33	0.55	0.74	0.21
10	0	0.43	0.85	0.29

a) $\psi^I = \sum_{K_i=0}^{3} C_{K_i}^I \psi_{K_i}$

The reduced E1 transition rates are given by

$$B(E1\ I2^- \rightarrow I'O) = [C_0^I \langle I1\,0\,0|I'O\rangle \langle gs|\mathcal{O}(E1)|K=0^-\rangle + C_1^I \langle I1\,1\,-1|I'O\rangle \langle gs|\mathcal{O}(E1)|K=1^-\rangle]^2 \quad (7.20)$$

where the amplitudes are to be taken from Table 7.9.

If only the $K=1^-$ admixture is included, the first term of eqn. 7.20 disappears and one can use the measured B(E1) value for the $22^- \rightarrow 20^+$ transition from Table 7.6 to show that

$$\langle g_s|\mathcal{O}(E1)|K=1^-\rangle = \pm 2.02\times10^{-3}\ e\ fm\ . \quad (7.21)$$

With this value, it is a simple matter to calculate B(E1) rates for all the members of the band, as presented in Table 7.7. While this calculation leads to reasonable predictions for the even spin states, it fails to obtain the high B(E1) values characteristic of transitions from the odd spin states in the band.

When the $K=0^-$ admixture is included, estimates of both the matrix elements in 7.20 are required. The value of $\langle g_s|\mathcal{O}(E1)K=1^-\rangle$ can be taken from eqn. 7.21 above. From the experimental data of Table 7.7 one can write

$$\left[\frac{B(E1\ 52^- \rightarrow 40^+)}{B(E1\ 52^- \rightarrow 60^+)}\right]^{1/2} = \pm(1.08 \pm 0.07).$$

Applying this ratio to a solution of Eqn. 7.20 one obtains

$$\langle gs|\mathcal{O}(E1)|K=0^-\rangle = (0.01 \pm 0.06)\ \langle gs|\mathcal{O}(E1)|K=1^-\rangle$$

or

$$= (-18 \pm 8)\ \langle gs|\mathcal{O}(E1)K=1^-\rangle\ .$$

The first solution corresponds to the case where there is essentially no $\Delta K=0$ contribution to the B(El) transition rate. This solution, as has already been shown in Table 7.6, leads to the correct branching ratios for El transitions out of the odd spin members of the band but fails completely to reproduce the large experimental B(El) rates.

The second solution leads to

$$\begin{aligned} \langle gs|\mathcal{O}(E1)|K=0^- \rangle &= \mp(36\pm16)\times10^{-3} \text{ e fm} \\ \langle gs|\mathcal{O}(E1)|K=1^- \rangle &= \pm(2.0\pm0.2)\times10^{-3} \text{ e fm} \end{aligned} \tag{7.22}$$

and thence to the B(El) values of Table 7.7 in the column labelled $\Delta K = 0,1$. The inclusion of the $K=0^-$ component has no effect on the B(El) rates for the even spin members but causes a dramatic increase in the predictions for the odd spin members of the band, in reasonable agreement with the experimental results.

In principle, it should be possible to calculate the reduced El transition rates, using the complete wave functions of Neergård and Vogel without resorting to any empirical matrix elements. It should be of interest to perform such a calculation as a test both of their particular model and of the fundamental concepts they employ. They view nuclear excitations in terms of quasi-particles moving almost independently in a deformed Nilsson potential and interacting only through the multipole-multipole (octupole-octupole, in this case) force.

In terms of the single particle description, this concept is equivalent to thinking of the motion of single particles moving in the deformed potential and interacting through a pairing force plus an octupole-octupole interaction.

(vi) The B(E3) value for the 22^- state

The E3 transition matrix element for the $22^- \rightarrow 20^+$ transition has been experimentally determined (see Table 7.6). Thus

$$\langle gs|\mathcal{O}E3|K=2^-\rangle^2_{exp} = 5.7\times10^4\ e^2fm^6. \qquad (7.23)$$

Since the 22^- state is essentially pure $K=2^-$ with a small $K=1^-$ admixture (see Table 7.9), the experimental E3 transition matrix element may be compared with the value predicted by Neergård and Vogel for the pure RPA $K=2^-$ octupole band. From their paper we find

$$\langle gs|\ E3|K=2^-\rangle^2 = B(E3\ 00\rightarrow 32^-)\uparrow_{RPA}\ \langle 03\ 02|32\rangle^2$$

$$= 5.8\times10^4\ e^2fm^6 \qquad (7.24)$$

where we have used the fact that the $\langle 0302|32\rangle = 1$. The agreement with the experimental value is excellent.

The theoretical E3 transition matrix element for the Coriolis mixed $32^- \rightarrow 00^+$ state was found by Neergård and Vogel to be $6.8\times10^4\ e^2fm^6$, a value some 15% higher than that for the unperturbed band. The mixing of the $K=0^-$ and 3^- states has thus resulted in a small increase in the predicted B(E3) strength for the band.

(vii) The microscopic structure of the octupole states

The wave functions employed by Neergård and Vogel are not available to us at the present time. However, in the case of ^{172}Yb, earlier calculations of Soloviev (1965) led to microscopic components of the RPA wave functions nearly identical to those used by Neergård and Vogel (O'Neil, private communication). A similar situation is expected to hold for ^{176}Hf. The principal two quasi-particle components of the octupole states obtained from Soloviev's calculations as listed in Table 7.10, show that the $K=2^-$ band, before mixing by the Coriolis interaction, is formed by mixing 24% of the $\{5/2+[402]_p + 9/2-[514]_p\}$ proton state with 76% of the $\{5/2-[512]_n + 9/2+[624]_n\}$ neutron states. These two configurations are both singlet states for which $g_K \sim g_\ell$ (see eqn. 3.64a and Table 3.4) so that $g_K \sim 0$ for the 2 neutron component and ~ 1 for the 2 proton component in the admixture.

The value of g_K has been experimentally determined to be 0.27 ± 0.06 (see Table 7.8). It should perhaps be noted that in the experimental determination of g_K, the effects of Coriolis mixing were assumed to be negligible.

The experimental value of g_K implies that the $K=2^-$ state contains $\sim$ 27% of the two quasi-particle proton configuration, in excellent agreement with Soloviev's prediction.

Table 7.10

Two quasiparticle components of the octupole states[a]

	Component	Admixture
$K=0^-$	$7/2+[633]_n\ 7/2-[514]_n$	71%
$K=1^-$	$7/2+[404]_p\ 9/2-[514]_p$	∿100%
$K=2^-$	$5/2+[402]_p\ 9/2-[514]_p$	24%
	$5/2-[512]_n\ 9/2+[624]_n$	74%
$K=3^-$	(not available)	

a) Soloviev (1965).

7.7 The $K=3^+$ band at 1557.2 keV

The coincidence data establish a sequence of levels at 1577.2, 1675.8, 1798.4, 1944.3, 2106.6 and (2285.0) with a pattern of transitions to the ground state band and a rotational level spacing which together suggest that they form a band with a spin sequence 3, 4, 5 ... 8 (see Fig. 7.1). The internal conversion coefficient of the 1489 keV ($3 \rightarrow 20^+$) transition suggests that it is E2 (Bernthal et al, 1971) while the present internal conversion data for the 1385 keV ($4 \rightarrow 40^+$) transition is also consistent with E2 character. These data thus suggest that the band has positive parity. Much stronger evidence for positive parity is provided by data from the $^{177}Hf(d,t)^{176}Hf$ experiment (Casten et al, 1971), in which the first three members of this sequence are strongly populated.

It is unlikely that any $K=3^-$ band would be strongly populated in this neutron stripping reaction and Casten et al suggest this is the $K=3^+$ $\{7/2-[514]_n, 1/2-[521]_n\}$ band. The assignment of the 2106.6 and 2285.0 keV levels as the 7^- and 8^- members of this band must be regarded as being very tentative. They are both somewhat lower in energy than the value predicted from the rotational formula and the 2285 keV state also fits quite well as the spin 8 member of the $K=2^+$ band.

The 264.0 keV $33^+ \rightarrow 32^-$ transition observed in this work has been similarly assigned by Bernthal et al (1971) but no explanation for this interband transition is forthcoming from the existing data. The dotted interband transitions have been placed solely on energy fit and must therefore be treated as tentative.

7.8 The $K=6^+_\ell$* band at 1333.1 keV

(i) Identification of the band members

The 1333.1 keV state is an isomer with a measured half-life of 9.5±0.3 μsec (see Fig. 6.23). It decays to both the 4^+ and 6^+ members of the g.s.b. through pure E2 transitions and must therefore have a spin of 5 or 6 and positive parity. The recent particle transfer work in this laboratory shows that a 6^+ assignment is the most likely.

These assignments are in complete agreement with those of Borgreen et al (1967) who based their conclusions on the low lying quasi-particle states available in ^{176}Hf and

*The subscript ℓ indicates "lower" to distinguish this state from the upper $K=6^+$ state to be discussed in section 7.8.

by the recent $^{177}Hf(d,t)^{176}Hf$ reaction work of Casten et al (1970).

The rotational members of the band have been established up to 11^+ by the γ-γ coincidence measurements involving both cascade and cross-over transitions reported in Chapter 6. In addition, the 173 and 194 keV cascade transitions are M1+E2 and the 367 and 408 keV cross-over transitions are pure E2 in character, as one would expect in a well behaved band. The energies of the band members fit the rotational formula very well, as is shown in Table 7.2c.

(ii) The decay properties of the 1333.1 keV state

The partial decay rates of the 736 keV ($6\ell^+ \rightarrow 6^+$) and 1043 keV ($6\ell^+ \rightarrow 4^+$) gamma rays are 4.45×10^4 sec^{-1} and 2.85×10^4 sec^{-1} respectively. These correspond to retardation factors F_W of 7.7×10^5 and 6.8×10^6 and degrees of forbiddenness f_W of 30 and 51 respectively (see eqn. 3.38, 3.39 and the footnote* below). These factors are not unreasonable for K-forbidden transitions of order 4.

(iii) The microscopic structure of the $K=6\ell^+$ band from the particle transfer data

In the proton transfer reactions only the 1333 keV band head is populated, while in the neutron transfer reaction both this and the 1506 keV levels are populated. In the

*$\lambda_W(E2) = 1.6\times10^8\ A^{4/3}\ E_\gamma{}^5$ where E_γ is in MeV.

^{177}Hf(d,t and ^{3}He,α)^{176}Hf reactions, one starts with a neutron in the 7/2-[514$\uparrow$] orbital and excites the two neutron states produced by removing a neutron. In the ^{175}Lu(^{3}He,d and α,t)^{176}Hf reactions, one starts with a proton in the 7/2+[404$\downarrow$] orbital and adds a proton to excite the 2 proton states in ^{176}Hf. The ratio of the (α,t) to the (^{3}He,d) cross sections determined by the author in collaboration with O'Neil and Burke proved conclusively that the 1333 keV state is associated with an ℓ=2 transfer and hence is consistent with its being the band head of the K=6^{+} two proton configuration {7/2+[404$\downarrow$]$_{p}$, 5/2+[402$\uparrow$]$_{p}$}. At the same time, a second K=6$^{+}_{u}$ band at 1761 keV, whose properties will be discussed in section 7.8, was populated with an ℓ=2 transfer. The (^{3}He,d) reaction work carried out in this laboratory and the unpublished (d,t) work of Casten et al (1970) excite the same pair of K=6^{+} bands. This shows immediately that both bands have mixed proton and neutron character. The ratio $\sigma_{1333}/[\sigma_{1333}+\sigma_{1761}]$ in the proton transfer reactions yields the proton content of the 1333 keV band directly while the same ratio in the neutron transfer reactions leads to the neutron content. The results are summarized in the Table 7.11 below.

The agreement between the three independent assessments of the composition of the K=6$^{+}_{\ell}$ band is excellent. In the (^{3}He,α) experiment, the peaks due to the 1651 keV band were masked so badly that the data could not be used for this purpose.

Table 7.11

Composition of the $K=6^+_\ell$ band at 1333 keV

Reaction	proton configuration {7/2+[404↓],5/2+[402↑]}	neutron configuration {7/2-[514↓],5/2-[512↑]}
(α,t)	57%	43%
(^{3}He,d)	66%	34%
(d,t)[a]	63%	37%
Mean	62%	38%

[a] Casten's data; the resolution in the He,α experiment was not sufficient to give a meaningful ratio.

(iv) The microscopic structure of the $K=6^+_\ell$ band from gamma ray branching ratios

The composition of the band can also be deduced by comparing the M1 and E2 rates of the intraband transitions to obtain the quantity $\{|g_K-g_R|/Q_o\}$ and the mixing ratio $\delta^2 = \frac{I(E2)}{I(M1)}$, using equations 3.44, 3.45 and 3.46. The result of this analysis is presented in Table 7.12, which includes data from both the 22.5 and 24.0 MeV alpha beam experiments. The table includes values of $1/\delta^2$ and $|g_K-g_R|/Q_o$. It is clear from an inspection of Table 7.12 that $|g_K-g_R|/Q_o$ is constant, within errors, for the entire band with an average value of 0.042±0.003. If one makes the reasonable assumption that Q_o and g_R are properties of the nucleus applicable to all bands, one can use

Table 7.12

g_K-factor from transitions with the $K=^{6+}_{\ell}$ band

Transition	Energy (keV)	I_γ $E_\alpha^{b)}$=22.5	I_γ E_α=24	$\frac{1}{\delta^2}$ E_α=22.5	$\frac{1}{\delta^2}$ E_α=24	$\frac{\lvert g_K-g_R\rvert}{Q_o}$ a) E_α=22.5	$\frac{\lvert g_K-g_R\rvert}{Q_o}$ a) E_α=24
8 → 6	366.9	1.1±0.2	1.6±0.2	4.2±1.2	3.8±1.0	4.7±0.7	4.5±0.6
8 → 7	194.1	2.2±0.3	3.0±0.4				
9 → 7	408.3	1.20±0.25	2.35±0.30	3.8±1.0	3.1±0.9	4.4±0.6	3.9±0.6
9 → 8	214.2	1.0±0.2	1.7±0.2				
10 → 8	447.7	0.96±0.15	1.3±0.2	2.9±1.7	4.2±1.0	3.7±1.1	4.5±0.6
10 → 9	233.5	0.40±0.15	0.72±0.10				
11 → 9	484.8	0.19±0.08	0.87±0.30	6.1±3.6	2.4±1.0	5.3±1.8	3.6±0.8
11 → 10	251.3	0.10±0.02	0.22±0.03				

Mean$[\lvert g_K-g_R\rvert/Q_o]$ = 0.042±0.003

Q_o = 7.45 barns (Stelson and Grodzins 1965)

g_R = 0.27 (Ben-Zvi et al 1968)

Hence, $\lvert g_K-g_R\rvert$ = 0.31±0.04 c)

and g_K = 0.58±0.05 or −0.04±0.05 c)

(continued next page)

Table 7.12 (continued)

a) In units of 10^{-2} if Q_o in barns

b) E_α refers to the α-beam energy (in MeV) used in the respective runs

c) The sign of $(g_K - g_R)$ may be obtained from a measurement of δ.

the values obtained from the 20^+ member of the g.s.b. to deduce g_K, as follows:

$$Q_o^{(6+)} = Q_o^{(2+)} = 7.45\pm0.11 \text{ (Stelson and Grodzins 1965)}$$

$$g_R^{(6+)} = g_R^{(2+)} = 0.266\pm0.02 \text{ (Ben Zvi et al, 1968)}$$

$$g_K = 0.58\pm0.04 \quad \underline{\text{or}} \quad -(0.04\pm0.04) \; . \tag{7.25}$$

Since g_K=1 for the 2 quasi-proton state and g_K=0 for the 2-quasi-neutron state (see table 3.4) and since the reaction data require that the states have a two-proton component, it is clear that the second value of g_K is not acceptable. The value of g_K is 58±4% of the value expected for a pure two quasi-particle proton state indicating that the 1333 keV band is 58% two proton and 42% two neutron, in excellent agreement with the composition deduced from the neutron data.

The value of g_K deduced in this fashion should be quite reliable since we are dealing here with singlet spin states for which g_K is quite insensitive to the value of g_S used (see eqn. 3.63). It may also be shown that g_K is relatively insensitive to the deformation.

It should perhaps be pointed out that this analysis depends on the g_K factors of a mixed proton-neutron state being additive (see eqn. 3.69), and that this will only be strictly true if the non-diagonal magnetic moment matrix elements vanish. In the case under discussion, this approximation should be valid since the two "2 quasi-particle states"

which constitute the mixture share no common particle and therefore cannot be connected by the single particle magnetic moment operator.

The lack of dependence of $|g_K - g_R|$, and hence of g_K, on spin indicates that the degree of mixing between the proton and neutron components is constant for the entire band. The wave function may thus be written as

$$|K=6_\ell> = C_1|6\ pp> + C_2|6\ nn>$$

$$= 0.77|6\ pp> + 0.63|6\ nn> \qquad (7.26)$$

where $C_1^2 = 0.60$ and $C_2^2 = 0.40$ and where $|6\ pp>$ and $|6\ nn>$ represent the wave functions for the $K = 6^+$ proton and neutron configurations, respectively. The phase in eqn. 7.26 has arbitrarily been chosen to be positive. There must also be a second K=6 band, defined by $|K=6_u>$ where

$$|K=6> = 0.63|6\ pp> - 0.77|6\ nn> \ . \qquad (7.27)$$

As was indicated in the last section, this is the band located at 1761 keV and which is discussed in detail in the next section.

7.9 The $K=6^+_u$ band at 1761.5 keV

(i) Identification

The coincidence data establish a series of levels of energies 1761.5, 1926.7, 2112.8 and 2318.4 which decay to the spin 6, 7, 8 and 9 members of the $K=6^+_\ell$ band. The M1 character of the transitions from the first two of these states estab

lishestheir parities as positive and restrictstheir spins to 6, 7 or 8 and 7, 8 or 9 respectively. The energies of these levels fit the rotational formula for K=6 very well, as is shown in Table 7.2d, but the formula cannot distinguish with certainty between K=6 and a K=5 or K=7 assignment. The band is peculiar in that all the deexcitation proceeds via interband transitions while no intraband transitions are observed. As we shall see later, the anomalous behaviour is consistent with the microscopic description of this band given by equation (7.27).

The members of the band are populated in both the neutron and proton transfer experiments referred to in section 7.8 (iii) above. Although Casten et al (1970) identified this band with the $K=1^+$ coupling of the $\{7/2-[514\downarrow]_n, 5/2-[512\uparrow]_n\}$ configuration, it is clear from considering the gamma ray data presented above as well as the reaction data from this laboratory that the $K=6^+$ coupling is more appropriate. We are thus dealing with the state defined by eqn. (7.27).

(ii) Gamma ray branching from the 1761.5 keV band

An estimate of the relative intensities of the inter and intraband transitions can be made if one accepts the microscopic description of the two $K=6^+$ bands given in eqns.(7.26 and 7.27), which can be expressed algebraically as:

$$|6_\ell\rangle = C_1|6\ pp\rangle + C_2|6\ nn\rangle$$
$$|6_u\rangle = C_2|6\ pp\rangle - C_1|6\ nn\rangle\ . \qquad (7.28)$$

The electromagnetic interband matrix elements are given by

$$\langle 6_\ell|O|6_u\rangle = C_1C_2[\langle 6\ pp|O|6\ pp\rangle - \langle 6\ nn|O|6\ nn\rangle]$$
$$- C_1^2\langle 6\ pp|O|6\ nn\rangle + C_2^2\langle 6\ nn|O|6\ pp\rangle \ . \qquad (7.29)$$

Since the electromagnetic operator is a single particle operator, it cannot connect two quasi-particle states unless they share a common particle. Hence, the last two terms in eqn. (7.29) (the non diagonal terms) vanish and

$$\langle 6_\ell|O|6_u\rangle = C_1C_2[\langle 6\ pp|O|6\ pp\rangle - \langle 6\ nn|O|6\ nn\rangle] \ . \qquad (7.30)$$

Since, for the E2 operator,

$$\langle 6\ pp|Q|6\ pp\rangle \sim \langle 6\ nn|Q|6\ nn\rangle \sim Q_o,$$

the interband E2 rate vanishes identically. On the other hand, for M1 transitions (see eqn. 3.42)

$$\langle 6\ pp|M|6\ pp\rangle = (g_{K_{pp}} - g_R)K$$
$$\langle 6\ nn|M|6\ nn\rangle = (g_{K_{nn}} - g_R)K \qquad (7.31)$$

whence

$$\langle 6_\ell|M|6_u\rangle = KC_1C_2[g_{K_{pp}} - g_{K_{nn}}] \ . \qquad (7.32)$$

The values of $g_{K_{pp}}$ and $g_{K_{nn}}$ for these states have been tabulated in Table 3.4. Using these values, we find

$$\langle 6_\ell|M|6_u\rangle = 2.91. \qquad (7.33)$$

An analogous treatment of the in band M1 transitions leads to

$$\langle 6_u|M|6_u\rangle = K(C_2^2 - g_R) = 0.78$$
$$\langle 6_\ell|M|6_\ell\rangle = K(C_1^2 - g_R) = 2.0 \qquad (7.34)$$

The corresponding matrix element for the E2 in band transitions is

$$\langle 6_\ell|Q|6_\ell\rangle = \langle 6_u|Q|6_u\rangle = Q_o = 7.45 \text{ barns} \qquad (7.35)$$

These matrix elements were used, together with equations 3.41, 3.42 and 3.31, to calculate actual transition rates expected for both the interband and intraband M1 and E2 transitions. The predicted rates are compared with the experimental data in Table 7.13. The last two columns compare the predicted transition rates with the experimental gamma ray intensities. Since no lifetimes are known, one can only make comparisons for transitions originating in a common level. It is clear that, the interband transitions are expected to be several orders of magnitude stronger than the intraband transitions, in good agreement with the experimental data. The relative intensities of the observed transitions from any one level agree within the rather large experimental errors with those predicted theoretically.

(iii) <u>The unperturbed energies of the $K=6^+$ states and the interaction matrix element</u>

The excitation energies of the two $K=6^+$ bands and the amplitudes of the components in their mixed wave functions

Table 7.13

Transition rates for the $K=6^+_\mu$ band

Transition $IK^i - I'K^j$	E_γ (a) (keV)	Multipolarity λ	$\langle I\lambda 60 \mid I'6\rangle^2$	B(M1) (b) $(e\hbar/2Mc)^2$	B(E2) (c) $(10^4 e^2 fm^4)$	Transition Prob. $T(10^{12}\ sec^{-1})$	I_γ (d)
$66^u \rightarrow 66^\ell$	428.4 (o)	M1	0.857	1.73	-	2.39	1.1
$76^u \rightarrow 66^u$	165.2	E2	0.328	-	1.82	0.0027	
$\rightarrow 66^u$	165.2	M1	0.124	0.018	-	0.0014	
$\rightarrow 66^\ell$	593.6 (o)	M1	0.124	0.25	-	0.92	0.15±0.10
$\rightarrow 76^\ell$	420.9 (o)	M1	0.643	1.30	-	1.71	0.91±0.20
$\rightarrow 86^\ell$	226.7	M1	0.233	0.47	-	0.097	
$86^u \rightarrow 66^u$	351.3	E2	0.038	-	0.212	0.014	
$\rightarrow 76^u$	186.1	E2	0.353	-	1.95	0.0053	
$\rightarrow 76^u$	186.1	M1	0.206	0.030	-	0.0034	
$\rightarrow 76^\ell$	606.9 (o)	M1	0.206	0.416	-	1.64	0.17±0.06
$\rightarrow 86^\ell$	412.9 (o)	M1	0.500	1.01	-	1.25	0.23±0.04
$\rightarrow 96^\ell$	208.6	M1	0.294	0.594	-	0.095	
$96^u \rightarrow 76^u$	391.7	E2	0.081	-	0.450	0.051	
$\rightarrow 86^u$	205.6	E2	0.355	-	1.97	0.088	
$\rightarrow 86^u$	205.6	M1	0.263	0.038	-	0.0059	
$\rightarrow 86^\ell$	618.5 (o)	M1	0.263	0.531	-	2.21	0.20±0.04
$\rightarrow 96^\ell$	(404.2) (o)	M1	0.400	0.808	-	0.94	(0.16±0.08)
$\rightarrow 106^\ell$	170.7	M1	0.337	0.681	-	0.060	

(continued next page)

Table 7.13 (continued)

(a) Only transitions marked with an (o) have been observed; transition energies derived from level energies.

(b) M1 transition matrix elements: $\langle 6_\ell | M | 6_u \rangle = 2.91$

$\langle 6 | M | 6_u \rangle = 0.78$

(c) $Q_o^{(6_u)} = Q_o^{(2+)} = 7.45$ barns

(d) Only the relative intensities of transitions deexciting the same level may be compared.

may readily be used to deduce both their unperturbed energies and the magnitude of the interaction matrix element. By using eqns.(3.76) and (3.77), and the notation of eqn. (7.28) one can show that

$$(E^{o}_{nn} - E^{o}_{pp})^2/\langle nn|H_{int}|pp\rangle^2 = (1-2C_2^2)/C_2^2(1-C_2^2) \qquad (7.36)$$

and that hence

$$E^{o}_{nn} - E^{o}_{pp} = 178 \text{ keV} \qquad (7.37)$$

$$|\langle nn|H_{int}|pp\rangle| = 195 \text{ keV}$$

The energies of the pure 2-neutron and 2-proton states would then fall at 1636 and 1458 keV respectively.

7.10 The $K=8^-_\ell$ band at 1559.4 keV

(i) Identification of the Band

The 1559.4 keV member of this band was observed by Borgreen et al (1965) who showed that it decayed to the $K=6^+_\ell$ isomer by an M2 transition. The half life of the state has been measured to be 9.8±0.2 μsec (Fig. 6.21a) and the transition of energy 53.5 keV between this state and the 7^+ state of the 1333 keV band shown to be E1 (Table 6.7). The absence of an appreciable E1 component in the 1559→1333 keV transition uniquely establishes its spin and parity as 8^-.

The rotational members of the band up to spin 12 (see Fig. 7.2) have been established by γ-γ coincidence measurements and the level energies fit the rotational formula very well. The

quality of the fit to this formula is presented in Table 7.2e which shows that the 12^- term can only be fitted if one includes a small $[I(I+1)]^3$ term in the formula. Finally, a comparison of the excitation functions of the series of cascade transitions indicate that they are associated with levels of increasing spin (see fig. 6.7).

(ii) The decay properties of the 1559.4 keV state

The partial decay rates of the 226.2 keV ($88^-_\ell \rightarrow 66^+$) and 53.5 keV ($88^-_\ell \rightarrow 76^+$) gamma rays are 0.8×10^4 and 3.6×10^4 sec^{-1} respectively*. The corresponding retardation factors are 280 and 2×10^7 for the K-allowed M2 and the once K-forbidden E1 transitions respectively.

(iii) Microscopic properties of the $K=8^-_\ell$ band from gamma ray branching.

The value of g_K for this band may be deduced in the manner described for the 6^+_ℓ band in section 7.8(v). The relevant analysis is presented in Table 7.14. An inspection of this table shows that $|g_K-g_R|/Q_o$ is essentially constant for all transitions within the band and that hence the value of g_K is a characteristic of the band.

The analysis yields

---

*The transition rate for the 53.5 keV gamma ray was found from the expression $[1+\alpha_T(53.5)]^{-1}$. $[T_{172.8}/(T_{172.8}+T_{226.3})]\cdot[0.693/t_{1/2}]$ where the transition intensities required were taken from Table 6.7.

Table 7.14

g_K-factor from transitions within the $K=\frac{8^-}{\ell}$ band at 1559 keV

Transition	Energy	I_γ (b) E_α=22.5	I_γ (b) E_α=24	$\frac{1}{\delta^2}$ E_α=22.5	$\frac{1}{\delta^2}$ E_α=24	$\frac{\lvert g_K-g_R\rvert}{Q_o}$ a) E_α=22.5	$\frac{\lvert g_K-g_R\rvert}{Q_o}$ a) E_α=24
10 → 8	471.6	0.24±0.03	0.37±0.05	14.8±3.0	18.1±4.0	8.9±0.8	9.8±1.0
10 → 9	246.0	1.9 ±0.2	3.55±0.50				
11 → 9	508.9	0.24±0.12	(d)	10.3±5.6		7.2±2.2	
11 → 10	262.8	0.62±0.09	1.24±0.20				

Mean $[\lvert g_K-g_R\rvert/Q_o] = 0.091\pm0.006$

$\lvert g_K-g_R\rvert = 0.68\pm0.08$ d)

$g_K = 0.95\pm0.08$ or 0.41 ± 0.08 c)

a)-c) See Table 7.12

d) No γ-γ coincidence data available to resolve this transition from the annihilation line.

$$g_K = 0.95\pm0.08 \text{ or } 0.41\pm0.08 \qquad (7.38)$$

The predictions of the unified model indicate the existence of two $K=8^-$ configurations in ^{176}Hf (see Figs. 3.1 and 3.2). The first is the two quasi proton state, {7/2+[404↓], 9/2-[514↑[}, and the second is the two quasi neutron state, {7/2-[514↓], 9/2+[624↑]}. Both of these are singlet states for which $g_K \sim g_\ell$. The 1559.4 and 1785.1 keV members of this band are excited with full intensity in the proton transfer reactions (^{3}He,d and α,t) and not observed in the neutron transfer experiments (d,t and ^{3}He,α). This indicates very clearly that $g_K = 0.95^{\pm}0.08$ and that the state must be the two quasi proton state. When we come to discuss the 1860.3 keV band, evidence will be adduced to show that a small amount of mixing between these two states occurs. This admixture may be responsible for the compression of the 1559 keV band with increasing spin which required the introduction of an $[I(I+1)]^3$ term in the rotational formula.

7.11 The $K=7^-$ and/or 8^-_u band at 1860.3 keV

(i) Identification of the band

The five levels at 1860.3, 2014.4, 2194.2, 2399.0 and 2638.1 shown in Fig. 7.2 all show a characteristic decay pattern marked by strong transitions to the $K=8^-_\ell$ band at 1559.4 keV and weak intra band transitions. The interband transitions are all based on γ-γ coincidence measurements, the intraband transitions on energy fit. The M1 character of the 300.8 keV transition to the 1559.4 keV state establishes

the parity of the band as negative and the spin of the 1860.3 keV state as 7, 8 or 9. If the 1860 keV state is the band head, similar restrictions apply to the K quantum number. The K=9 choice is extremely unlikely since there are no K=9 configurations expected in this energy region (see Tables 3.1 and 3.2).

The spacing of the levels fits the normal rotational formula quite well (see Table 7.2f) except for the spin 12 member which requires the introduction of an $[I(I+1)]^3$ term to give a good "fit" to the data. No members of this band have been seen previously.

The levels at 1860, 2014 and 2194 keV are populated in the (^{3}He,α) neutron transfer reaction but not in the proton transfer experiments. The band must therefore arise from a two quasi-neutron configuration, with one neutron in the $7/2-[514\downarrow]_n$ orbital (the ground state of the ^{177}Hf target). Table 3.1 shows that there are only two configurations which satisfy these conditions, the $\{7/2-[514\downarrow]_n, 7/2+[633\uparrow]_n\}$ $K=7^-$ band and the $\{7/2-[514\downarrow]_n, 9/2+[624\uparrow]_n\}$ $K=8^-$ band, and hence this band must be $K=7^-$, $K=8^-$ or some mixture of the two. It will be shown in section (ii) that the cross-section for production of the I=7 member of the above K=7 configuration is very small. Thus the mere presence of a strong peak at 1860 keV in the neutron transfer spectrum proves that the spin of the state is 8^-.

(ii) The effect of Coriolis coupling on the 1860.3 keV band

The small rotational parameter (A=7.10 keV) suggests that there is a strong interaction between this band and higher lying bands. The conditions for Coriolis coupling have already been discussed in section 3.10. The strength of the interaction is given by the Coriolis matrix element (eqn. 3.87) divided by the separation of the interacting states. The ratio $R = [\langle j- \rangle / E^I_K - E^I_{K\pm1}]$, which is tabulated in Table 7.15 for interactions between a number of pairs of bands (taken from Tables 3.1 and 3.2) is a rough measure of the strength of the Coriolis interaction for each pair. For each band, the table also shows the energy of the band head and of the relevant low spin members of the band. In view of the very strong Coriolis interaction expected between the two neutron states discussed in 7.11(i) above, it seems highly likely that the 1860.3 keV band is a mixed $K=7^-$ and 8^- band.

The effect of Coriolis mixing the $K=7^-$ and $K=8^-$ bands on the differential cross-sections predicted for the $(^3He,\alpha)$ reaction is presented in Fig. 7.8. The value of $d\sigma/d\Omega$ is shown as a function of the energy separation $[E^I_8 - E^I_7]$ for separation energies from -1000 to +1000 keV for the I = 7, 8, 9, 10 members of the lower perturbed band. When $[E^I_8 - E^I_7]$ becomes $+\infty$ the calculations lead to the cross-sections for the unperturbed $K=7^-$ band shown at the right of the figure. In the same way, in the limit where $[E^I_8 - E^I_7]$ reaches $-\infty$, the calculations lead to cross-sections for the unperturbed

Table 7.15

Strength of the Coriolis Interaction between high K states of ^{176}Hf

$R^{(e)}$	$\langle j- \rangle^{a)}$	K^{π}	Configuration Neutron States		$E_{2q.p.}$ b) (MeV)	$E_{band\ head}$ c) (MeV)	E(I) c,d) (MeV)	
		8^-	7/2-[514↓]	9/2+[624↑]	1.8	1.7		1.7(8)
14	5.61							
		7^-	7/2-[514↓]	7/2+[633↑]	2.0	1.9	1.9(7)	2.1(8)
4.0	6.08							
		6^-	7/2-[514↓]	5/2+[642↑]	3.3	3.2	3.4(7)	
-1.8	-0.91							
		7^-	5/2-[512↑]	9/2+[624↑]	1.7	2.0	2.0(7)	2.2(8)
14	5.61							
		6^-	5/2-[512↑]	7/2+[633↑]	1.9	2.2	2.4(7)	
-1.8	-0.91							
		5^-	9/2+[624↑]	1/2-[521↓]	2.0	1.9	1.9(5)	
18.7	5.61							
		4^-	7/2+[633↑]	1/2-[521↓]	2.2	2.1	2.2(5)	
			Proton States					
		5^-	1/2+[411↓]	9/2-[514↑]	2.1	2.0		
		6^-	3/2 [651↑]	9/2-[514↑]	2.4	2.5		

a) $\langle j- \rangle = \langle \Omega_1 | j_{1-} | \Omega+1 \rangle$ indicates the strength of the Coriolis matrix element (see eqn. 3.87).

(continued next page)

Table 7.15 (continued)

b) unperturbed energies from Tables 3.1 and 3.2, as calculated from eqn. (3.24).

c) $E(I) = E_{2qp} + \frac{\hbar^2}{2\mathcal{J}}[I(I+1)-K^2] \pm S$ and $E_{\text{band head}}$ is obtained by setting K=I. The first two terms in this equation give the unperturbed energies for members of the band. The last term introduces the effect of the splitting due to the spin-spin interaction with the negative sign being used for the singlet and the +ve sign for the triplet state. S has been arbitrarily taken as 200 keV for this calculation.

d) The number in brackets after each energy is the spin of the state.

e) $R = \langle j- \rangle / (E^I_K - E^I_{K\neq 1})$.

$K=8^-$ band. The primed sequence of levels refer to the upper perturbed levels*, which asymptotically acquires the character of the $K=7^-$ band as $[E_8^I - E_7^I]$ approaches $-\infty$. The cross-section for the unperturbed $K=8^-$ band is much smaller than that for the unperturbed $K=7^-$ band because $V^2 = 0.3$ for the former as against $V^2 \sim 1$ for the latter.

The experimental cross-sections from the present (^{3}He,α) experiments are shown at the extreme right of figure 7.8. The spin 8 member of the band is part of an unresolved doublet in the α spectrum and therefore cannot be used as a test of mixing. The experimental cross-sections for the I=9 and 10 members are incompatible with a pure $K=8^-$ assignment but can be reconciled with any mixture which contains more than 20% of the $K=7^-$ band.

If the band were pure $K=7^-$, one would expect to find a strongly populated $I=7^-$ state in the (α,2n) reaction below the 1860.3 keV level. Although the 1732.5 keV state has approximately the predicted excitation (1723 keV) for this state, its decay properties make it quite unsuitable for a candidate. This state decays strongly to the I=6 and 7 members of the

---

*For all allowed couplings the Coriolis interaction leads to constructive interference in the population of the lower perturbed state and destructive interference in the population of the upper perturbed state.

Figure 7.8

Calculated cross-sections in the $^{177}Hf(^{3}He,\alpha)^{176}Hf$ reaction for the upper (primed) and lower (unprimed) states formed by Coriolis coupling the $K=8^-$ {7/2-[514], 9/2+[624]} and $K=7^-$ {7/2-[514], 7/2+[633]} states. Plotted as a function of the energy separation, $E_8^I - E_7^I$, between the corresponding spin members,of the unperturbed $K=8^-$ and $K=7^-$ bands. The cross sections are given by the expression

$$\frac{d\sigma}{d\Omega} = N \sum_j \sigma_\ell [a_7 c_{j\ell} V_{7/2} < 7/2\ j\ 7/2\ 7/2 | I_f 7 > +$$

$$a_8 c_{j\ell} V\ 9/2 < 7/2\ j\ 7/2\ 9/2 \mid I_f\ 8 >]^2$$

$N = 49.0$

$c_{j\ell} = c_{13/2^6} \sim 1$ (only 1 term included in the sum)

a_7 and a_8 are the amplitudes of the $K=7^-$ and $K=8^-$ components respectively, obtained from a Coriolis mixing calculation using eq. 3.87.

The other parameters are defined as usual (e.g. see O'Neil and Burke, 1972).

*Doublet peak.

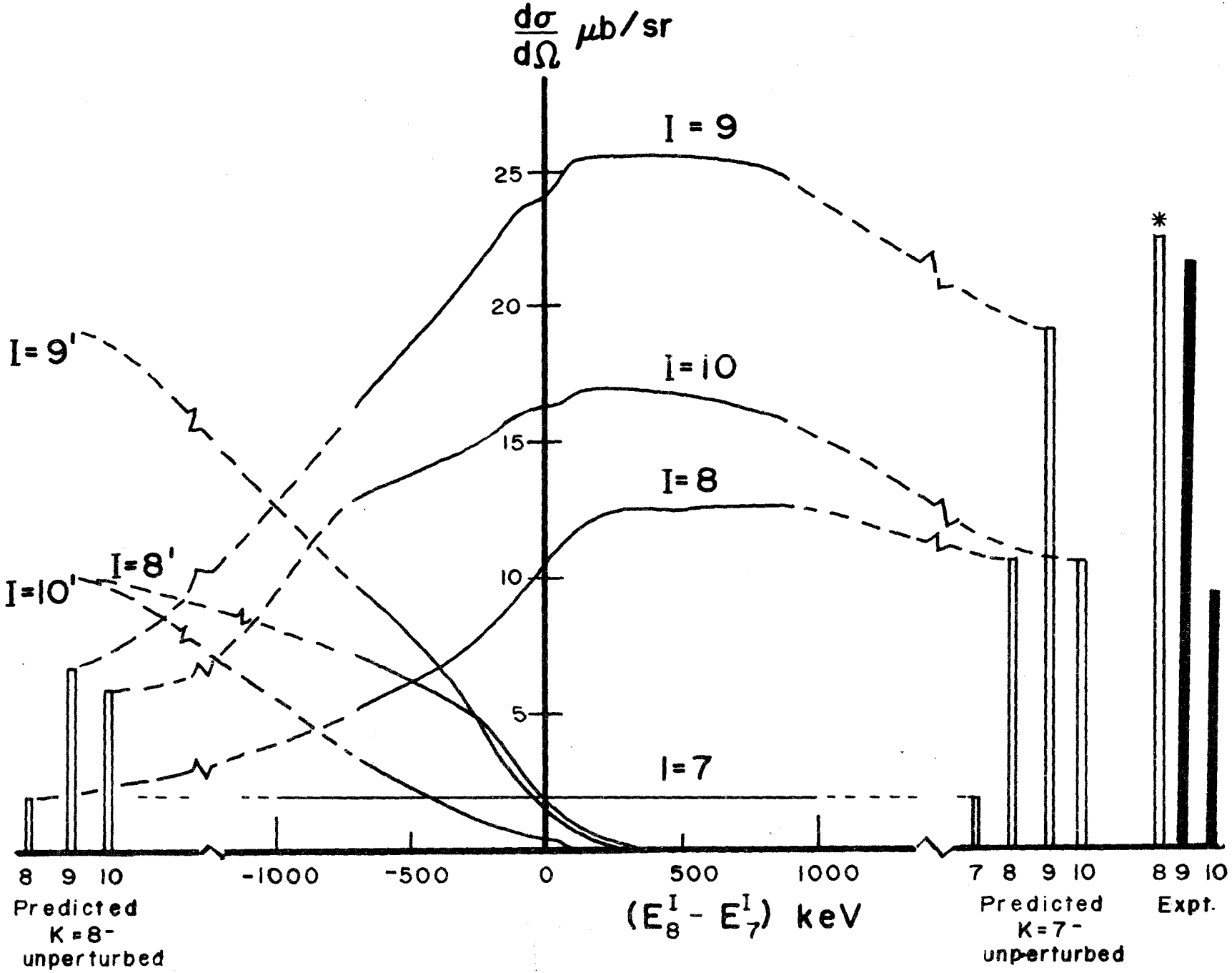
dσ/dΩ μb/sr
I = 9
I=9'
I=10
I=8
I=8'
I=10'
I=7
25
20
15
10
5
*
8 9 10
Predicted
K=8⁻
unperturbed
-1000
-500
0
500
1000
(E_8^I - E_7^I) keV
7 8 9 10
Predicted
K=7⁻
unperturbed
8 9 10
Expt.

$K=6^+_\ell$ band whereas the members of the 1860 keV band prefer to decay to the $K=8^-_\ell$ band with no observable transitions to the $K=6^+_\ell$ band. The absence of a suitable candidate provides strong grounds for rejecting predominant $K=7^-$ component, and we therefore propose that this band is predominantly $K=8^-$ with a significant $K=7^-$ component.

(iii) Configuration mixing between the two $K=8^-$ bands

It has been shown in section 7.10(iii) that the $K=8^-$ band at 1559 keV is the two quasi proton state with the configuration {7/2+[404↓], 9/2-[514↑]} and in section 7.11(ii) that the band at 1860.3 keV is a two quasi neutron state with the predominantly $K=8^-$ configuration {7/2-[514↓], 9/2+[624↑]}. Since there is no particle common to these two configurations, transitions between them are expected to be retarded, in contradiction to the strong interband transitions observed. It is thus reasonable to propose, in analogy with the two $K=6^+$ bands, that there is some mixing between the $K=8^-$ two proton and two neutron states.

In the $K=6^+$ case, the interaction matrix element was found to be independent of the spin, and this will be assumed to be true for the $K=8^+$ case also. However, because the rotational parameters are significantly different for the two $K=8^-$ bands, the mixing may be expected to become larger as the energy separation between corresponding spin states decreases with increasing I.

In order to simplify the band mixing calculations to be described, the $K=7^-$ component in the two-neutron band has been assumed to be zero. This assumption should not affect the results substantially. Secondly, since the lower $K=8^-$ was found to be almost a pure two-quasi Proton configuration, it has been assumed that the unperturbed band head energies and rotational parameters are very close to those obtained from the I=8 and I=9 members of each band. Finally, the interaction matrix element $\langle nn|H_{int}|pp\rangle$ was adjusted to give the "best fit" to the observed level energies. The results are tabulated in Table 7.16. The upper part of the table tabulates the unperturbed band heads and rotational parameters, and the interaction matrix element used. The central portion compares the predicted and experimental energies of the states in each of the bands. It is seen that agreement is quite satisfactory. The wave functions of the members of the two bands are given by

$$\begin{aligned} |I8^-_\ell\rangle &= C_1^I|nn\rangle + C_2^I|pp\rangle \\ |I8^-_\mu\rangle &= C_2^I|nn\rangle - C_1^I|pp\rangle \end{aligned} \qquad (7.39)$$

where the coefficients are now functions of the spin. The values of C_1^I and C_2^I for the two bands are tabulated in the lower part of Table 7.16

Using the wave functions of Table 7.16, the transition rates for the inter and intra band transitions may be calculated in the manner described in section 7.9(ii). The results are

Table 7.16

Configuration mixing between the $K=8^-_\ell$ and $K=(8^-_u)$ bands

E^o_{pp} = 1564 keV E^o_{nn} = 1853 keV

A_{pp} = 12.5 keV A_{nn} = 8.79 keV

$\langle nn|H_{int}|pp\rangle$ = 40 keV

Energy (keV)

Spin	2-proton			2-neutron		
	Unperturbed	Perturbed	Expt.	Unperturbed	Perturbed	Expt.
8	1564	1559	1559	1853	1858	1860
9	1788	1781	1785	2011	2018	2014
10	2037	2027	2031	2187	2197	2194
11	2315	2296	2294	2380	2399	2399
12	2612	2644	2638	2591	2559	2564

Amplitude [a]

Spin	Lower band		Upper band	
	C_1	C_2	C_1	C_2
8	.15	.99	.15	.99
9	.17	.985	.17	.985
10	.24	.97	.24	.97
11	.43	.90	.43	.90
12	-.79	.61[b]	.79	-.61[b]

(continued next page)

Table 7.16 (continued)

a) The wave functions are written as

$$|8_\ell\rangle = C_1|nn\rangle + C_2|pp\rangle$$

$$|8_u\rangle = C_2|nn\rangle - C_1|pp\rangle$$

b) Note the change in sign of the phases; the unperturbed level order is reversed from that of lower spin members.

Table 7.17

Transition rates from the band at 1860 keV[a)]

Transition	Energy	Multi-polarity	$\langle 8_\ell \lvert M \rvert 8_u \rangle$ [b)]	B(M1) $(e\hbar/2Mc)^2$	λ $(\times 10^7 sec^{-1})$	I_γ [c)]
$8_u \to 8_\ell$	300.8	M1	-1.19	0.30	144	1.1
$9_u \to 8_u$	154.1	E2 [d)]	-	-	1.4	0.09±0.03
$\to 8_u$	154.1	M1	-1.95	0.090	5.8	
$\to 8_\ell$	455.1	M1	-1.30	0.040	66.2	0.42±0.06
$\to 9_\ell$	229.2	M1	-1.34	0.305	64.6	0.70±0.11
$10_u \to 8_u$	334.3	E2	-	-	7.2	0.10±0.03
$\to 9_u$	179.8	E2	-	-	4.2	0.06±0.02
$\to 9_u$	179.8	M1	-1.82	0.135	13.8	
$\to 9_\ell$	408.7	M1	-1.74	0.124	149.	0.50±0.08
$\to 10_\ell$	163.0	M1	-1.86	0.481	36.7	0.20±0.05
$11_u \to 9_u$	384.6	E2	-	-	33.0	
$\to 10_u$	204.8	E2	-	-	8.8	
$\to 10_u$	204.8	M1	-1.29	0.089	13.5	
$\to 10_\ell$	368.3	M1	-2.90	0.452	397.	0.16±0.02
$\to 11_\ell$	105.1	M1	-3.10	1.11	22.7	
$12_u \to 10_u$	443.9	E2	-	-	18.9	
$\to 11_u$	239.1	E2	-	-	104.5	
$\to 11_u$	239.1	M1	+3.17	0.64	154.	
$\to 11_\ell$	344.2	M1	-3.58	0.82	586.	
$\to 12_\ell$	74.6	M1	-3.86	1.46	10.7	

a) The band is assumed to be pure $K=8^-$ for the purpose of this calculation.

b) M1 transition matrix element calculated using eqns. (7.29) and (7.31); the amplitudes in the wave function were obtained from Table 7.16

c) Since no life-times are known, only the relative intensities of transitions deexciting the same level may be compared with the predicted values.

d) E2 rates calculated assuming $Q_o^{(8^-)} = Q_o^{(2^+)} = 7.45$ barns.

presented in Table 7.17. Since none of the lifetimes are known, it is only possible to compare experimental and predicted branching ratios from each level. While the agreement between the observed intensity ratios and the predicted transition rate ratios is only qualitative, it is rather gratifying considering the assumptions that have been made in the calculations.

7.12 The 1798 keV band with K = 6 and/or 7^-

The rotational spacing and decay pattern of the 1798, 1931, 2086 and 2262 keV levels suggest that these are members of the same rotational band (see Table 7.2). The presence of E1 transitions from the two lower members to the 66^+_ℓ and 76^+_ℓ states suggest that the band has a K value of 5^-, 6^- or 7^-.

No mixing can occur between the 1798 and 1333 keV bands since they are of opposite parity. The occurrence of transitions between the bands indicates that their configurations share at least one of the $7/2-[514]_n$, $5/2-[512]_n$, $7/2+[404]_p$ or $5/2+[402]_p$ quasi particle states which constitute the $K=6^+_\ell$ state. An inspection of the states with appropriate K value given in Table 7.15 shows that there is no suitable $K=5^-$ candidate and that this configuration must be one or more of the following:

$$\{7/2-[514]_n,\ 5/2+[642]_n\}\ K=6^-$$

$$\{5/2-[512]_n,\ 7/2+[633]_n\}\ K=6^-$$

$$\{5/2-[512]_n,\ 9/2+[624]_n\}\ K=7^-$$

The first of these is predicted to lie at an excitation above 3 MeV and is therefore a very unlikely candidate. The remaining configurations are predicted to fall at 2.2 and 2.0 MeV respectively, and are expected to couple strongly through the Corliolis interaction between the two N=6 particles. In fact this band could well be a mixture of these two configurations. This coupling would explain the small rotational parameter for the 1798 keV band.

One might speculate that the 1732.5 keV state is the I=6 member of the band under discussion with an anomalously small spacing between it and the 1798 keV state which would then have I=7. Such an anomaly might be explained if the unperturbed 76^- state were close to the unperturbed 77^- state, since this will tend to reduce the I=7 to I=6 spacing more than any of the others. Against this interpretation is the fact that the 1798 keV state is more strongly populated than the 1732 keV state, in direct opposition to the trends in all other bands. At the moment, it does not appear possible to draw any further conclusions.

CHAPTER 8

SUMMARY AND PROPOSALS FOR FURTHER STUDY

8.1 Summary

Although for the past seven years odd-A nuclei have been successfully studied with (α,xn) reactions, this work represents one of the earliest extensive studies of this type for an even-even deformed nucleus. In spite of the rather voluminous amount of data one might expect to handle, we now feel that such an undertaking is certainly feasible. In our study we have employed a variety of spectroscopic techniques in performing both in-beam and out-of-beam (pulsed) gamma ray and electron measurements. In the process, a number of novel techniques involving pulsed beams have been developed. We have also recently examined in some detail unpublished data from single neutron or proton transfer reactions. The results of these transfer reactions have complemented those obtained from the (α,2n) studies in a very heartening fashion.

A total of ∿ 90 levels in ^{176}Hf have been established, mainly on the basis of extensive γ-γ coincidence data. It is gratifying that a number of the levels established here have also been observed in the recent radioactive decay studies of Bernthal et al (1969,1971). The decay of ^{176}Ta and ^{176}Lu populates, with three exceptions, only states with spin $\lesssim$ 3, whereas the (α,2n) reaction employed here populates states with

spins as high as 12. Nevertheless, the spin and parity assignments of Bernthal et al have proved very helpful in the interpretation of our low K-states.

An advantage of spectroscopic studies employing the $(\alpha,2n)$ reaction is that it allows the observation of an extended rotational sequence. This provides information not only on the intrinsic structure of the band but also on its interactions with other states. In this study we have been able to characterize, to some extent, more than sixty of the observed levels in terms of the unified model.

Perhaps the most interesting apsect of this study concerns the observation of five high K-bands which decay through the two isomers in ^{176}Hf. The intrinsic nature of these bands is reasonably well understood; we have determined that there is a high degree of configuration mixing between the two quasi-proton and two quasi-neutron $K=6^+$ bands, which accounts for the highly unusual behaviour displayed by one of these bands.

The other highlight of the study concerns a $K=2^-$ octupole band whose properties are remarkably predicted by a simple model (Neergård and Vogel 1971) which includes the Coriolis coupling among the negative parity octupole states. Even the most unusual uneven distribution of E1 strengths from the odd and even spin members can be accounted for on the basis of this model.

8.2 Proposals for further study

To begin, a number of the experiments described in this work might be profitably repeated with alpha beams of higher energy (27 - 30 MeV) in order to accentuate transitions from the higher spin members. A reexamination of the high energy (> 700 keV) portion of the gamma spectrum is suggested by the availability of detectors with a resolution almost twice that of the particular large volume detectors used in this work. It might then be possible to unravel the many complex peaks occurring in this energy region. Although the results from these suggested measurements are not expected to alter the proposed level scheme, they should provide more accurate transition intensities.

Unique spin and parity assignments have not been possible for many of the identified levels. The situation would be improved through more precise measurements of the conversion coefficients. We were severely limited, partly by the intrinsic resolution of the orange magnetic spectrometer. One way to overcome this would be to use high-resolution Si(Li) detectors for measuring the electron spectrum. In order to maintain a tractable background level (caused by, for instance, inelastically scattered projectiles and "delta rays"), it would be necessary to deflect only the desired electrons to the detector. A suitable arrangement would be to locate the detector at the focus of the orange spectrometer. From such a

system, one might expect a resolution of better than 2.5 keV at 1 MeV, compared to the present attainable value of $\sim$ 7 keV.

A complementary, or alternative, method for determining the transition multipolarities consists of measuring the angular distribution of the emitted gamma rays. An asset in such a measurement is provided by the superior resolution of the Ge(Li) detector compared to the basic magnetic electron spectrometer. In addition, the signs of the mixing parameters, δ, and hence of transition matrix elements could be obtained. The careful measurement of angular anisotropies is, however, made quite difficult by the extreme complexity of the spectrum.

Perhaps one drawback of this work is the fact that our sensitivity diminishes for detecting low spin states of high excitation energy. Transitions from such states (to the low spin members of the g.s.b.) necessarily have large energies and therefore are difficult to observe in the presence of the high continuum background. The use of ultra-high resolution detectors in γ-γ coincidence experiments might alleviate the problem of identifying such states. Another approach would be to reeaxmine the decay of ^{176}Ta using e-γ and γ-γ angular correlation measurements to obtain spin assignments for more of the low spin states. It is expected that many of these are the lower rotational band members of states observed in the (α,2n) study.

The measurement of the intrinsic g_K-factor has led to quantitative information regarding the microscopic structure of a number of states. These g_K's have been determined from cascade-crossover branching ratios. A direct measurement of the magnetic moment would provide an independent measurement of g_K. Perturbed angular correlation (PAC) measurements may be performed on the $K=2^-$ band head at 1248 keV which has a half-life of 4.5 ns. The very strong 710-1159 keV cascade which follows the decay of 8-hr ^{176}Ta is well-suited for such an experiment. Alternatively, the PAC measurements may be performed with a pulsed alpha beam bombarding a ^{174}Yb target. The magnetic moment of the $K=6^+$ and $K=8^-$ isomers may also be determined by either the IMPAC or the stroboscopic method of Christiansen et al (1968,1970). The relative long half-life of 10 μsec requires the use of a liquid Yb target or some suitable liquid matrix, which presents considerable experimental difficulties.

One of the interesting facets of this work is the observation of almost complete configuration mixing of the two proton and two neutron $K=6^+$ states. This mixing may be further examined by direct reactions in which both a neutron and a proton are transferred. Interference effects between the two states will be revealed in the cross-section and should yield the sign of the interaction matrix element. The

$^{176}Lu(^{3}He,t)^{176}Hf$ reaction might be employed in such an experiment.

The observed configuration mixing of the $K=6^{+}$ states poses an interesting theoretical question since it finds no explanation in terms of the models in common use. It has been suggested by Volkov (priv. commn.) that the interaction might arise from terms present in pairing Hamiltonians which have been ignored in calculations performed so far. Such calculations must also be able to account for the behaviour of the two $K=8^{-}$ configurations: these are essentially pure in ^{176}Hf, and also in ^{180}Hf (Körner et al. 1971), whereas they are highly mixed in the nucleus ^{178}Hf (Gallagher and Nielsen 1962; Helmer and Reich). A systematic experimental study of the high-K states in these and other even-even Hf nuclei might shed some light on the problem, besides being an interesting project in its own right.

Finally, the remarkable success with which we can explain the properties of the $K=2^{-}$ octupole band in ^{176}Hf (in terms of the fundamental model of Neergård and Vogel) prompts further research into the octupole states. The $B(E3,0^{+}\rightarrow 3^{-})$ value for the $K=2^{-}$ band could be checked by means of inelastic scattering (d,d' or α,α') or Coulomb excitation measurements. The B(E3) and location of the $K=3^{-}$ band, which is predicted to be collective, may also be determined simultaneously. (Valuable information on the $K=0^{+}$ bands

at 1150 and 1293 keV will also be determined at the same time.) Octupole states in other nuclei in the deformed region (e.g. ^{172}Yb or ^{182}W) may be also explored along the lines described in section 7.5.

REFERENCES

Alaga, G., Alder, K., Bohr, A. and Mottelson, B.R. (1955), Kgl. Danske Videnskab. Mat. Fys. Medd. 29, No. 9.

Alexander, P., Boehm, F. and Kankeleit, E. (1964), Phys. Rev. 133, B 284.

Bardeen, J., Cooper, L.N. and Schrieffer, J.R. (1957), Phys. Rev. 108, 1175.

Barneoud, D., Foin, C., Baudry, A., Gizon, A. and Valentin, J. (1970), Nucl. Phys. A154, 653.

Ben-Zvi, I., Gilad, P., Goldring, G., Hillman, P., Schwartzschild, A. and Vager, Z. (1968), Nucl. Phys. A109, 201.

Bernthal, F.M. (1969), Ph.D. Thesis, Lawrence Radiation Laboratory, University of California, Berkeley. UCRL Report 18651.

Bernthal, F.M., Rasmussen, J.O. and Hollander, J.M. (1971), Phys. Rev. C3, 1294.

Bès, D.R. and Broglia, R.A. (1966), Nucl. Phys. 80, 289.

Bès, D.R., Federman, P., Maqueda, E., Zuker, A. (1965), Nucl. Phys. 65, 1.

Bès, D.R. and Sorensen, R.A. (1969), Adv. in Nucl. Phys. Vol. 3, Edited by Baranger and Vogt, Plenum Press, New York.

Bodansky, D. (1962), Ann. Rev. Nucl. Sci. 12, 79.

Boddendijk, H.G., Idzenga, S., Kleimeer, G. and Verheul, H. (1969), Nucl. Phys. A134, 442.

Boddendijk, H.G., Idzenga, S., Timmerman, T. and Verheul, H. (1971), Nucl. Phys. A165, 441.

Boehm, F., Goldring, G., Hagemann, G.B., Symons, G.D., Tveter, A. (1966), Phys. Lett. 22, 627.

Bohr, N. (1936). Nature 137, 344.

Bohr, A. (1952), Kgl. Danske Videnskab. Mat. Fys. Medd. 26, No. 14.

Bohr, A. and Mottelson, B.R. (1953), Kgl. Danske Videnskab. Mat. Fys. Medd. 27, No. 16.

Bohr, A. and Mottelson, B.R. (1963), Atomn. En. 14, 41.

Borggreen, J., Hansen, N.J.S., Pedersen, J., Westgaard, L., Zylicz, J. and Bjørnholm, S. (1967), Nucl. Phys. A96, 561.

Brandi, K., Engelmann, R., Hepp, V., Kluge, E., Krehbiel, H. and Meyer-Berkhout, U. (1964), Nucl. Phys. 59, 33.

Broda, R., Walus, W., Zvolsky, I., Molnar, J., Nenov, N., Ryndina, E.Z., Fainer, U.M., Shoshev, P., (1970), Preprint P6-5094 Joint Inst. for Nucl. Res. Dubna.

Bunker, M.E. and Reich, C.W. (1971), Rev. Mod. Phys. 43, 348.

Casten, R., Kleinheinz, P., and Elbek, B. (1971) Private Communication.

Chase, R.L. (1968), Rev. of Sci. Inst. 39, No. 9, 318.

Chasman, C., Jones, K.W. and Ristinen, R.A. (1965), Nucl. Inst. and Meth. 37, 1.

Chi, B.E. (1966), Nucl. Phys. 83, 97.

Chi, B.E. (1967), State Univ. of New York (Albany) Publication.

Christiansen, J., Mahnke, H.-E., Recknagel, E., Riegel, D., Weyer, G. and Wittuhn, W. (1968), Phys. Rev. Lett. 21, 554.

———————————— (1970), Phys. Rev. C1, 613.

Church, E.L. and Weneser, J. (1956), Phys. Rev. 103, 1035.

Dzhelepov, B.S. and Shestopalova, S.A. (1968), "Nuclear Structure", Proc. of the Dubna Symposium, p. 39.

Ejiri, H., Ishihara, M., Sakai, M., Inamura, T., Katori, K. (1966), Nucl. Phys. 89, 641.

Ejiri, H. and Hagemann, G.B. (1971), Nucl. Phys. A161, 449.

Ewan, G.T., Graham, R.L. and McKenzie, I.K. (1966), IEEE Trans. Nucl. Sci. NS-13, 297.

Feshbach, H. (1960), Nuclear Spectroscopy, ed. F. Ajzenberg-Selove, Academic Press , New York.

Fossan, D.B. and Herskind, B. (1963), Nucl. Phys. 40, 24.

Gallagher, C.J. Jr. and Moszkowski, S.A. (1958), Phys. Rev. 111, 1282.

Gallagher, C.J. Jr., Nielsen, H.L. and Nielsen, O.B. (1961), Phys. Rev. 122, 1590.

Gallagher, C.J. Jr. (1962), Phys. Rev. 126, 1525.

Gallagher, C.J. Jr. and Nielsen, H.L. (1962), Phys. Rev. 126, 1520.

Gallagher, C.J. Jr. and Soloviev, V.G. (1962), Mat. Fys. Skr. Dan. Vid. Selsk. 2, no. 2.

Gedke, D.A. and McDonald, W.J. (1967), Nucl. Inst. and Meth. 55 (2).

Geiger, J.S. (1965), AECL Report CRGP-1214 (unpublished).

Graham. R.L., MacKenzie, I.K. and Ewan, G.T. (1965), Report IEEE 12th Nuclear Science Symposium, San Francisco, Oct.

Graetzer, R., Hagemann, G.B., Hagemann, K.A. and Elbek, B. (1966), Nucl. Phys. 76, 1.

Grover, J.R. (1967), Phys. Rev. 157, 832.

Grover, J.R. and Gilat, J. (1967a), Phys. Rev. 157, 802.

Grover, J.R. and Gilat, J. (1967b), Phys. Rev. 157, 814.

Grover, J.R. and Gilat, J. (1967c), Phys. Rev. 157, 823.

Günther, C., Kleinheinz, P., Casten, R.F. and Elbek , B. (1971), Nucl. Phys. A172, 273.

Hager, R.S. and Seltzer, E.C. (1968), Nuclear Data 4, 1.

Halpern, I., Shepherd, B.J. and Williamson, C.F. (1968), Phys. Rev. 169, 805.

Hammer, T. and Hagemann, G.B. (1971), Private Communication.

Harmatz, B., Handley, T.H. and Mihelich, J.W. (1960), Phys. Rev. 119, 1345.

Hashizume, A. and Tendow, Y. (1963), J. Phys. Soc. Japan 18, 1107.

Haverfield, A.J., Bernthal, F.M., Hollander, J.M. (1967), Nucl. Phys. A94, 337.

Helmer, R.G. and Reich, C.W. (1968), Nucl. Phys. A114, 649.

Hjorth, S.A., Ryde, H., Hagemann, K.A., Løvhøiden, G. and Waddington, J.C. (1970), Nucl. Phys. A144, 513.

Hooke, W.M. (1959), Phys. Rev. 115, 453.

Hübel, H., Günther, C., Krien, K., Toschinski, H., Spiedel, K.-H., Klemme, B., Kumbartzki, G., Gidefeldt, L. and Bodenstedt, E. (1969), Nucl. Phys. A127, 609.

Hübel, H., Naumann, R.A. and Spejewski, E.H. (1971), Phys. Rev. C4, 2272.

Jägare, S. (1967), Nucl. Phys. A95, 481.

Johnson, A., Ryde, H. and Sztarkier, J. (1971). Phys. Lett. 34B, 605.

Jones, H.D. (1969), Ph.D. Thesis, Florida State University (reproduced by Univ. Microfilm, Ann Arbor, Michigan).

Kerman, A.K. (1956), K. Danske Vidensk. Selsk. mat.-fys. Medd. 30, No. 15.

Kofoed-Hansen, O., Lindhard, J., Nielsen, O.B. (1950), Mat. Fys. Medd. Dan. Vid. Selsk. 25, No. 16.

Körner, H.J., Wagner, F.E. and Dunlap, B.D. (1971), Phys. Rev. Lett. 27, 1593.

Krane, K.S., Sites, J.R., and Steyert, W.A. (1971), Bull. Am. Phys. Soc. 16, 1146.

Lederer, C.M., Hollander, J.M. and Perlman, I. (1968), Table of Isotopes, 6th edition.

Leigh, J.R., Stephens, F.S. and Diamond, R.M. (1970), Phys. Lett. 33B, 410.

Lindgren, I. (1965), Arkiv för Fysik. 29, 553.

Löbner, K.E.G. (1968), Phys. Lett. 26B, 369.

Löbner, K.E.G., Smith, H.A. and Bunker, M.E. (1971), Bull. Am. Phys. Soc. 16, 1145.

Lönsjö, O. and Hagemann, G.B. (1966), Nucl. Phys. 88, 624.

Løvhøiden, G., Waddington, J.C., Hagemann, K.A., Hjorth, S.A. and Ryde, R. (1970), Nucl. Phys. A148, 657.

Malov, L. A., Soloviev, V.G. and Fainer, U.M. Contributions to the International Symposium on Nuclear Structure, Dubna. (1968), p. 78.

Marion, J.B. (1968), Nuclear Data 4, 301.

Mariscotti, M.A.J., Scharff-Goldhaber, G. and Buck, B. (1969), Phys. Rev. 178, 1864.

Mayer, M.G. and Jensen, J.H. (1955), Elementary Introduction of Nuclear Shell Structure, New York.

Mikhailov, V.M. and Mikhailova, M.A. (1966), Izv. Akad. Nauk. U.S.S.R. 30, 1337.

Mikoshiba, O., Sheline, R.K. and Udagawa, T. (1967), Nucl. Phys. A101, 202.

Morinaga, H. and Gugelot, P.C. (1963), Nucl. Phys. 46, 210.

Moszkowski, S.A. (1965), Alpha-, Beta-, and Gamma-Ray Spectroscopy, Vol. 2, Ed. by Kai Seigbahn, North Holland Publ. Co. Amsterdam.

Mottelson, B.R. and Valatin, J.G. (1960), Phys. Rev. Lett. 5, 511.

Nathan, O. and Nilsson, S.G. (1965), Alpha-,Beta-, and Gamma-Ray Spectroscopy, edited by K. Seigbahn, Vol. 1, p. 601, North Holland Publ. Co., Amsterdam.

Neergård, K. and Vogel, P., (1970), Nucl. Phys. A145, 33.

Newton, J.O., Stephens, F.S., Diamond, R.M., Kotajima, K., Matthias, E. (1967), Nucl. Phys. A95 (1967).

Newton, J. O. (1969), Prog. in Nucl. Phys. Vol. 2, Ed. by Brink, D.M. and Mulvey, J.H., Pergamon Press, Oxford.

Newton, J.O., Stephens, F.S., Diamond, R.M., Kelly, W.H. and Ward, D. (1970), Nucl. Phys. A141, 631.

Nilsson, S.G. (1955), Kgl. Danske Vidensk. Selsk. Mat.Fys. Medd. 29, No. 16.

Nielsen, H.L., Wilsky, K., Zylicz, J. and Sorensen, G. (1967), Nucl. Phys. A93, 385.

Ogle, W., Wahlborn, S., Piepenbring, R. and Fredriksson, S. (1971), Rev. Mod. Phys. 43, 424.

Olschewski, L. and Otten, E.W. (1967), Z. Physik. 200, 224.

O'Neil, R.A., Burke, D.G. and Alford, W.P. (1971), Nucl. Phys. A167, 481.

O'Neil, R.A, and Burke, D.G. (1972), Nucl. Phys. A182, 342.

Preston, M.A. (1962), Physics of the Nucleus. Addison-Wesley Publ. Co. Inc., Massachusetts.

Pyatov, N.I. (1967), Arkiv för Fysik.36, 667 (1967).

Rasmussen, J.O. (1960), Nucl. Phys. 19, 85.

Recknagel, E., (1971), Hyperfine Interactions in Excited Nuclei. Vol. 1, Ed. by Goldring, G. and Kalish, R., Gordon and Breach, New York.

Reddoch, A.H. and Ritter, G.J. (1962), Phys. Rev. 126, 1493.

Rezanka, I. (1971), Private Communication.

Robertson, R.G.H. (1971), Ph.D. Thesis, McMaster Univ.

Rusinov, L.J. (1961), Sov. Phys. Usp. 4, 282.

Ryde, H. (1971), Private Communication.

Sauer, E., Matthias, E. and Mössbauer, R.L. (1968), Phys. Rev. Lett. 21, 961.

Shirley, S. (1971), Hyperfine Interactions in Excited Nuclei. Vol. 4, Ed. by Goldring, G. and Kalish, R., Gordon and Breach.

Skånberg, B., Hjorth, S.A. and Ryde, H. (1970), Nucl. Phys. A154, 641.

Soloviev, V.G. (1965), Atomic Energy Rev. 3, 117.

Soloviev, V.G. (1965a), Preprint # D2157, Joint Inst. for Nuclear Research, Dubna.

Stelson, P.H. and Grodzins, L. (1965), Nucl. Data 1, 21.

Valentin, J. and Santoni, A. (1967), Nucl. Phys. 47, 303.

Varnell, L., Hamilton, J.H. and Robinson, R.L. (1971), Phys. Rev. C3, 1265.

Vergnes, M.N. and Rasmussen, J.O. (1965), Nucl. Phys. 62, 233.

Verheul, H., Buoy, H.M.W., Okel, J.G.R. and Blok, J. (1973), Nucl. Phys. 42, 551.

Wagner, H.F. and Lange, J. (1971), Z. Physik, 242, 292.

Wapstra, A.H. and Gove, N.B. (1971), Nucl. Data Tables A9, 303.

Weisskopf, V.F. (1937), Phys. Rev. 52, 215.

Weisskopf, V.F. in Theoretical Nuclear Physics (Wiley, New York, 1952) by Blatt and Weisskopf.

Williamson, C.F., Ferguson, S.M., Shepherd, B.J. and Halpern, I., (1968), Phys. Rev. 174, 1544.

Winter, G., Funke, L., Hohmuth, K., Kaun, K.H. and Sodan, H. (1970), Nucl. Phys. A151, 337.

Yamazaki, T. and Ewan, G.T. (1969), Nucl. Phys. A134, 81.